COMBUSTION KINETICS MODEL DEVELOPMENT & FLUID PROPERTY EXPERIMENTAL INVESTIGATION FOR IMPROVED DESIGN OF SUPERCRITICAL CO_2 POWER CYCLE COMPONENTS

FINAL REPORT

BY

Principal Investigator (PI): Prof. Subith Vasu[1]

Co-PIs: Prof. Jayanta Kapat[1], Prof. Artem Masunov[1], Dr. Scott Martin[2], Prof. Ron Hanson[3]

[1]University of Central Florida, Orlando, FL
[2]Embry-Riddle University, Daytona Beach, FL
[3] Stanford University, Stanford, CA

DE-FE0025260

Duration: 10/1/2015-09/30/2021

A Final Report Submitted to U.S. Department of Energy for the Project DE-FE0025260

(2021)

ABSTRACT

Supercritical carbon dioxide (sCO_2) cycles are being investigated for the future of power generation and will contribute to a carbon-neutral future to combat the effects of climate change. These direct-fired closed cycles will produce power without adding significant pollutants to the atmosphere. For such cycles to be efficient, they will need to operate at significantly higher pressures (e.g., 300 atm for Allam Cycle) than existing systems (typically less than 40 atm). There is limited knowledge on combustion at these high pressures and with a high dilution of carbon dioxide. Also, various experimental and computational investigations and model developments have been performed by the University of Central Florida (UCF), Embry-Riddle Aeronautical University (ERAU), and Stanford University (S.U.) to improve the current knowledge base and support the design and development of sCO_2 combustors. This project's technical aspects include chemical kinetics development, fundamental sCO_2 combustion, combustion model and sub-model development, supercritical fluid injection characterization, and heat transfer characterization.

The funding provided as a part of this cost-shared project supported 4 faculty researchers, 8 graduate students, 5 postdocs, and 6 undergraduate students at UCF. Additional students, faculty, and postdocs were supported at Stanford and ERAU. More than 50 journal and conference articles were published and disseminated to the public as a result of this project. Additionally, results from this work helped the industry establish tools and design strategies for direct-fired sCO_2 combustors. Also, this project acted as a basis for extending its impact to assist industry stakeholders in improving direct-fired sCO_2 combustion systems design and development.

TABLE OF CONTENT

CHAPTER 1: INTRODUCTION

1.1 Background

The current growth in globalization, transportation, and advancement in human civilization combined with rapid growth in the world's population demands a high growth in electrical energy production. The World Energy Outlook (WEO) New Policies Scenario 2018 expects that global energy needs to rise by over 25% by 2040. Aside from the challenges of meeting expected energy demand, the rapid rise in greenhouse gases such as CO_2, CH_4, N_2O, and Fluorinated gases are alarming the future of this planet. The largest source of CO_2 from human activities in the United States is burning fossil fuels for electricity [1], as shown in Figure 1. As per NOAA Earth System Research Laboratory, annual average CO_2 levels are higher than at any point in at least the past 800,000 years [2].

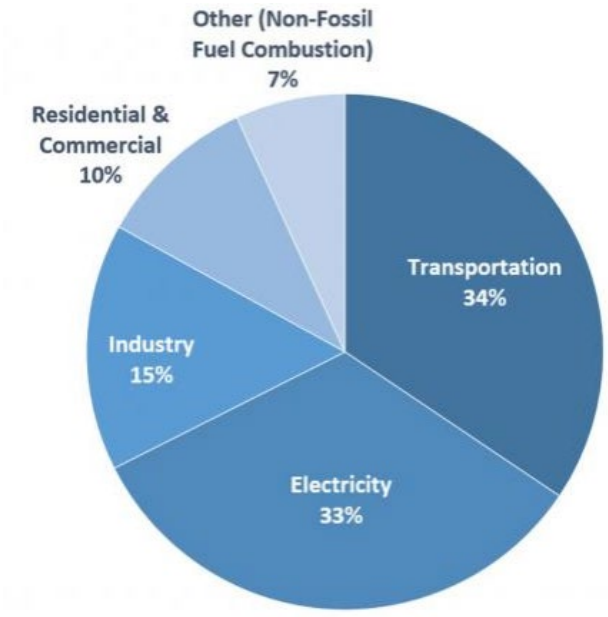

Figure 1: CO_2 emission by source in the USA in 2017 [1]

Hence, governments and industries have started exploring various technologies which could address both the energy demands and environmental concerns. The conceptual supercritical CO_2 (sCO_2) power cycles are gaining the attention of government, academic institutions, and industries due to their remarkable theoretical promise of efficiency, compactness, and eco-friendliness. Numerous studies have shown that the sCO_2 power cycles have the potential to attain significantly higher efficiencies than the conventional steam Rankine cycle [3, 4] due to the attractive characteristics of sCO_2 above its critical point. CO_2 has high density, low viscosity, and high specific heat near the critical point, as shown in Figure 2 to Figure 5 [5].

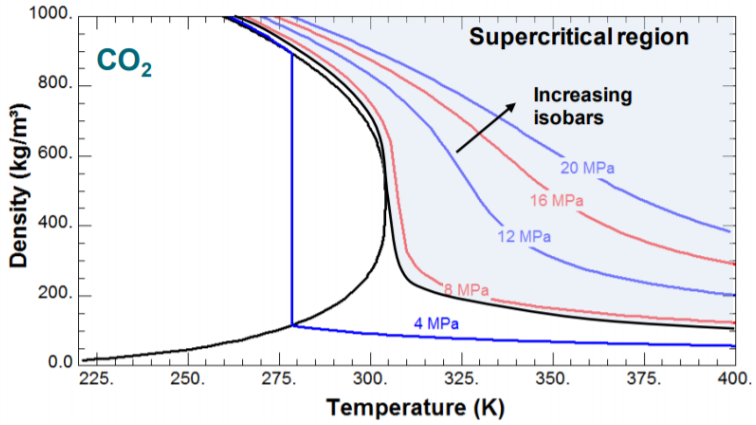

Figure 2: Variation of CO_2 density near critical point [5]

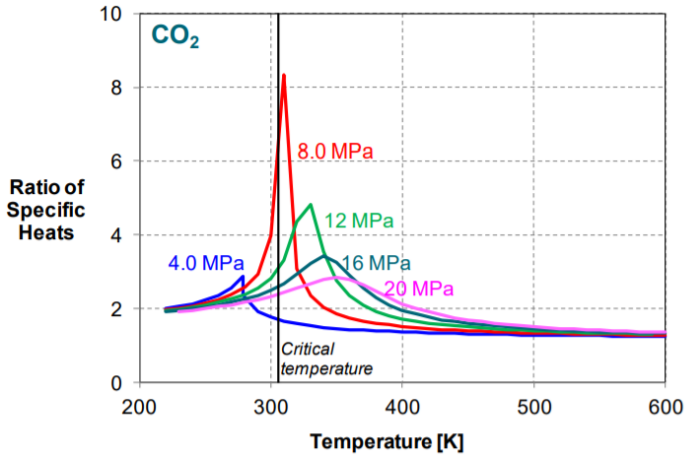

Figure 3: Variation of the ratio of specific heats of CO_2 near critical point [5]

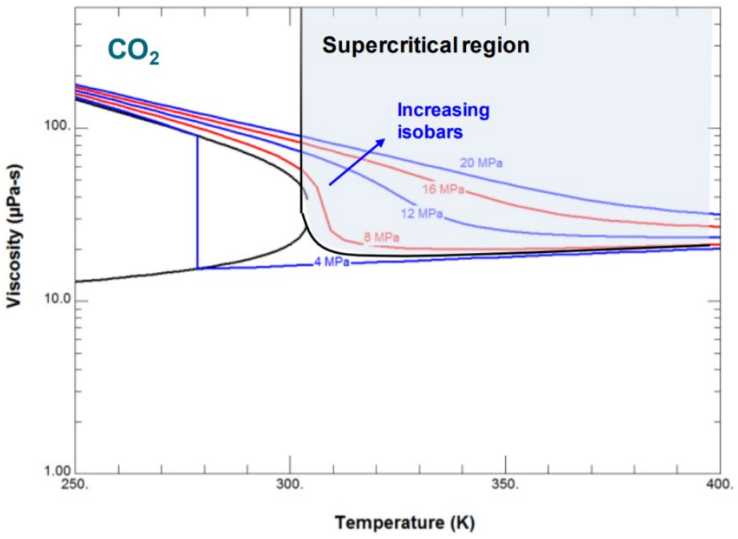

Figure 4: Variation of viscosity of CO_2 near critical point [5]

The high density reduces the required compressor power and allows compact turbomachinery due to low volumetric flow, and low viscosity reduces transmission loss in the compressor. High specific heat reduces the temperature change due to enthalpy. This characteristic of sCO_2 could reduce the number of inter-cooling and reheating stages. These characteristics add additional points to the sCO_2 cycle on an efficiency scale [4]. Also, various studies have shown that the cost of operation of sCO_2 cycles is economically impressive [6-10]. Further, the specific selection of CO_2 as the supercritical fluid allows the power cycle to be easily paired with a range of heat sources that include conventional fuel, nuclear, and renewable energies due to its critical point temperature being closer to the ambiance (31.10^o C). The wide range of sCO_2 cycle applicability based on source temperature and corresponding thermal efficiency can be seen in Fig. 1-5 [11]. Therefore, various government and industrial funding agencies across the globe are dynamically sponsoring the research related to sCO_2 power cycles.

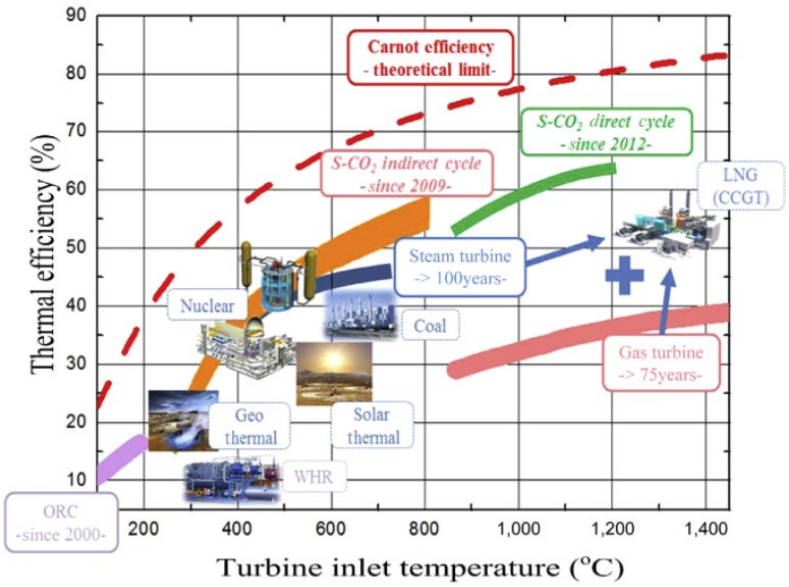

Figure 5: Thermal efficiencies of sCO_2 cycles at various source temperatures [11].

The current work focuses mainly on the combustion aspect of the direct-fired sCO_2 cycles. Here, fuel (natural gas or syngas) and oxygen are burnt directly in the cycle in the presence of sCO_2. The wide availability of natural gas across the globe is one crucial positive driving force for this technology apart from many other promising features such as higher thermal efficiency, complete carbon capture without additional cost, compact footprint, zero greenhouse gas emissions, viable to install at desert areas, and the possibility of supplying excess sCO_2 in the cycle for other commercial applications. Also, it is estimated that a 300 MW direct-fired sCO_2 plant could produce one million gallons of water per day [12]. Therefore, direct-fired sCO_2 cycles are an attractive alternative for current high source temperature and high power cycles.

The layout of this cycle is shown in Fig 6 [12]. This figure shows that oxygen will be separated from the Air Separation Unit (ASU). The quality and quantity of the air separation process are very crucial for huge power oxy-combustion applications. However, it is interesting to know that several advancements have been made by [13, 14] to demonstrate the feasibility of oxygen separation at a higher rate as per the need for oxy-combustion systems. The pure oxygen

supply from ASU burns along with natural gas or syngas in the combustion chamber in the presence of sCO_2. At the downstream of the combustor, the post-combustion stream (majorly consisting of CO_2 and H_2O) is expanded through the turbine, heat exchanger and then gets condensed. Further, H_2O (liquid) and CO_2 (gas) will be separated in a water separation unit. The remaining CO_2 will be re-circulated back to the combustion chamber via the heat exchanger. The excess CO_2 produced in the loop will be used for other commercial purposes.

The theoretical thermal efficiency of these cycles is remarkable, and it is around 58% [10, 15]. However, the operating conditions of the combustion chamber are unconventional and challenging. As per the current state-of-art (as shown in Table 1), the operating temperature of the combustor is between 760° C-1150° C, and pressure is 300 bar approximately. Also, the sCO_2 dilution is more than 95% by mass.

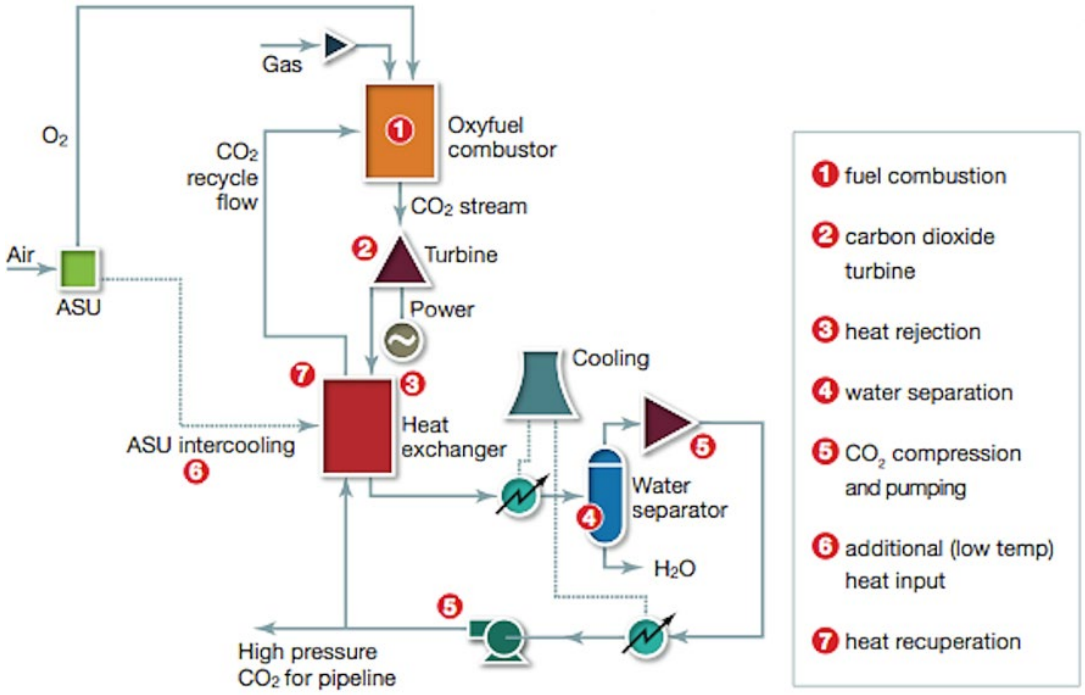

Figure 6: The layout of the Allam cycle [12]

Table 1: Operating conditions of the direct-fired sCO_2 combustor

Parameter	**Operating conditions**
1) Fuel	Natural gas/ Syngas
2) Oxidizer	Oxygen
3) Operating temperature	760-1150 ^oC
4) Operating pressure	300 bar
5) Percentage of sCO_2 dilution	> 95% by mass

Though the potential and benefits of the direct-fired sCO_2 cycle are superior to many of the trending energy production technologies, the operating conditions are stumbling blocks to its design and development. Any experimentation on combustion phenomenon at ~300 bar pressure and 95% CO_2 dilution are expensive, time-consuming, and even dangerous. Hence, accurate modeling of the sCO_2 combustion phenomenon would help developers significantly in the initial design and development process.

It is known that combustion is a complex physical phenomenon that involves fluid flow, chemical kinetics, and heat transfer. Importantly, the interaction between these three phenomena. Due to the nature of the involved complexity and limitation of the computational power, most of the theories and models in combustion are built based on certain underlying assumptions. For example, one of the commonly seen fundamental assumptions in conventional combustion modeling is the 'ideal gas assumption.' In this assumption, it is assumed that the mean free path between the molecules is large, and hence there are no intermolecular forces. Although no gas has this property at very high temperatures and low pressures, many of the gas's behavior

can be closely estimated with this assumption. However, at supercritical pressures where the molecules are closely packed, this assumption is no longer valid. Therefore, it is very important to understand the fundamental characteristics of the sCO_2 combustion before choosing an appropriate model for combustion simulation. Hence, this work primarily focuses on exploring chemical kinetics, combustion and heat transfer characteristics, and other models needed for sCO_2 combustion simulations.

Chapters 2-8 are organized and presented based on the research task conducted. Also, conclusions for each chapter are presented at the end of those chapters. Appendices provide specific analysis of sCO_2 combustors and recommendations for design strategies by the team. More detailed descriptions and presentations of some of the work and continued effort in the direct-fired sCO_2 can be found in our published articles [16-47]. Additional papers resulting from this project are currently undergoing the peer-review process, and those will be published in the near future.

CHAPTER 2: LOW AND HIGH-PRESSURE OXY-SYNGAS IGNITION STUDIES

2.1 Introduction

Synthesis gas, or syngas, is a fuel resulting from the gasification of coal or biomass that offers the potential for cleaner-burning in a power plant. A simplified model of syngas is a fuel primarily consisting of hydrogen and carbon monoxide. It has been demonstrated [48] that syngas composition is widely variable as well, complicating the design of the gas turbines. A need for experiments with a change in θ is needed as gasification results in varied fuel composition from location and processes [49]. Studies have been done to measure the ignition delay times of various compositions of oxy-syngas combustion in the air [49, 50]; however, very little has been done to see the effects that CO_2 has on the combustion process. Some studies [51-53] examined the effects of CO_2 diluted syngas at a CO_2 concentration up to 30% CO_2. Furthermore, [54, 55] examined the effects of CO_2 on oxy-methane combustion at dilution up to 60% and observed an increase in ignition delay time. Therefore, it is unknown of the effects of high concentrations of CO_2 on syngas combustion and experimentation must be done.

In recent years there has been increased interest in synthesis gas as a clean combustion fuel. Synthesis gas, or syngas, is a fuel resulting from the gasification of coal or biomass that offers the potential for cleaner-burning in a power plant. A simplified model of syngas is a fuel primarily consisting of hydrogen and carbon monoxide. It has been demonstrated [48] that syngas composition is widely variable as well, complicating the design of the gas turbines. A need for experiments with a change in the ratio between hydrogen-to-carbon monoxide, θ, is required as gasification results in varied fuel composition from location and processes [49]. Additionally, syngas is being investigated for use as a fuel in hydrogen turbines that operate near 40atm and in

supercritical CO_2 (sCO_2) power generation cycles. For these sCO_2 power cycles to operate, the chemical kinetics of syngas in CO_2 diluted environments must be well understood to pressures as high as 300 atm [56], implying the need for data at higher pressures. Also, accurate experimental data is crucial for the development and validation of chemical kinetic mechanisms used in high CO_2 combustor design codes. There is much to be developed before full operations with supercritical CO_2 power cycles can begin. Another benefit of a supercritical CO_2 cycle is that it will eliminate NOx emissions that results from combustion in air due to the CO_2 cycle being closed. This novel design, oxy-fuel combustion in supercritical CO_2 with combined CCS (carbon capture and storage), is being developed by National Energy Technology Laboratory (NETL) and private industry [57, 58].

In the literature, studies have been conducted to measure ignition delay times of various compositions of oxy-syngas in the air (see [49, 50]); however, very little has been done to assess the effects that CO_2 has on the combustion process. Some studies [51-53] examined the effects of CO_2 diluted syngas at a CO_2 concentration up to 30% CO_2—furthermore, refs. [35, 54, 55, 59] examined the effects of CO_2 on oxy-methane combustion at dilution up to 89.5%/vol. and observed an increase in ignition delay time relative to other bath gasses. Work at low pressures of about 1 atm during syngas combustion in CO_2 diluted environments up to 85%/vol. dilution [41] found large discrepancies between ignition delay times data and predictions. Therefore, more investigation is needed

2.2 Low-Pressure Ignition Study

Low-pressure measurements examined the ignition delay time of oxy-syngas combustion in a shock tube with CO_2 dilutions from 60%-85%. This study looked at the effects of changing ϕ, the equivalence ratio, from 0.33-1.0 as well as changing θ, the fuel ratio of hydrogen to carbon monoxide, from 0.25-4.0. The study was performed at 1.61-1.77 atm and a temperature range of 1006-1162K. The experimental data were compared with two combustion chemical kinetic mechanisms GRI-Mech v3.0 [60] and AramcoMech v2.0 [49]. In addition, high-speed imaging of the experiments was taken at the end wall of the shock tube to compare with different methods of determining the ignition delay time.

Table 2. The syn gas mixtures at around 1 atm that were investigated.

Mixture	**ϕ**	**θ**	**% H_2**	**% CO**	**% O_2**	**% CO_2**	**% Ar**
1	0.5	1.02	1.75	1.72	3.47	0	93.06
2	0.5	1.00	5	5	10	60	20
3	0.5	1.00	5	5	10	80	0
4	0.33	1.00	5	5	15	75	0
5	1.00	1.00	5	5	5	85	0
6	0.5	4.00	8	2	10	80	0
7	0.5	0.25	2	8	10	80	0

All the mixtures of experiments presented can be found in Table 1. It begins with the replication study mixture. The rest of the mixtures capture the change of ϕ from 0.33-1.0. It also covers a change of θ from 0.25-4.0.

2.2.1 Validation Study

In order to validate our shock tube for syngas experiments, a study was done to replicate a set of experiments performed in [49]. The measurement for ignition delay time was described as

the time between the initiation of the system by the reflected shock wave and the occurrence of the [OH] maximum. The replicated tests were the data points at 1 atm. The mixture that was created was slightly different from that study. The study had a θ value of 1.0, while the mixture I made was 1.02. In both mixtures, a ϕ of 0.5 was consistent.

2.2.2 High-Speed Image Processing

The high-speed imaging provides insight into the homogeneity of combustion in the shock tube to compare to standard methods (e.g., pressure, emissions), which assume homogenous ignition. The light sources from this reaction are the oxy-hydrogen flame and the carbon monoxide oxidation flame. The oxy-hydrogen flame emits light primarily from the 200 nm to 400 nm range, mainly due to strong OH band emissions at 306.36nm, 306.76nm, and 309.04nm [61]. The carbon monoxide oxidation flame primarily is in the 350nm to 450 nm range due to forming CO_2 emissions at 402.6 nm [61]. However, it is heavily driven by OH formation. The camera used, the Phantom V710, was designed to operate in the visible light range, 390 nm - 700 nm. The quantum efficiency (i.e., the effectiveness of the camera to see the light at a specific wavelength) quickly declines at lower wavelengths and is reported to be 15% at 350 nm [62]. Below this value, the efficiency was not recorded by the manufacturer. Even considering the broadening of emissions due to increases in temperature and pressure, the emissions are in wavelengths below the camera's design parameter.

The emissions detector is designed to see light emissions from 150 nm to 550 nm. Signal intensity was very low when a bandpass filter was placed in front of the detector because CO2 dilution makes emission intensity go down significantly. Therefore, no filter was used. When ignition starts, the concentrations of the radicals (e.g., OH) make a peak. The intensity of the emission is directly proportional to the number density of the OH molecules, which is not captured

by the camera operating in the visible light. After the radical concentration makes a peak, there is a dramatic decrease in fuel concentration due to the reactions between those radicals and other molecules. Since the camera cannot detect light in the UV range, the images recorded correspond to a time slightly later than the onset of ignition. Therefore, only images at the onset of combustion until the peak of emissions determined from the emissions detector are considered.

2.2.3 Ignition Delay Times of Replication Study

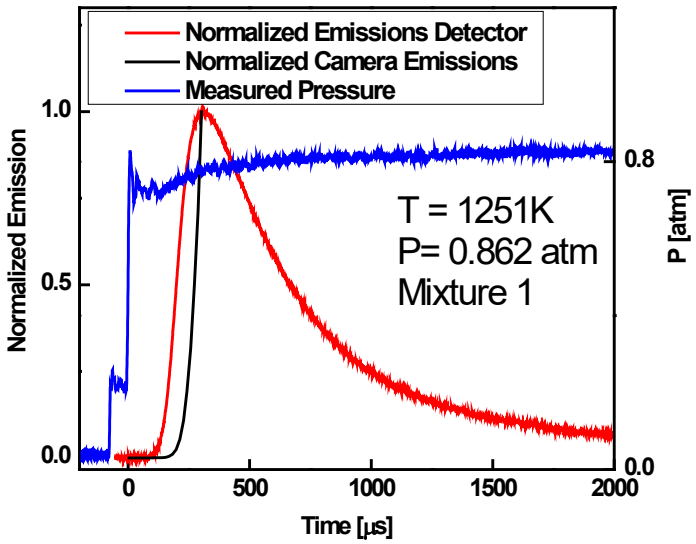

Figure 7. Pressure trace of replication study including emissions detector and camera emissions.

Figure 7 is a single experiment pressure trace of the replication study done. The main combustion event does not provide a large change in the pressure of the system. Also included with the pressure are the normalized emissions detector trace as well as the normalized camera emissions. The camera emissions are slightly behind the emissions detector due to it being unable to see OH emissions. The same method for calculating the ignition delay time using the peak of emissions was used as described in the study.

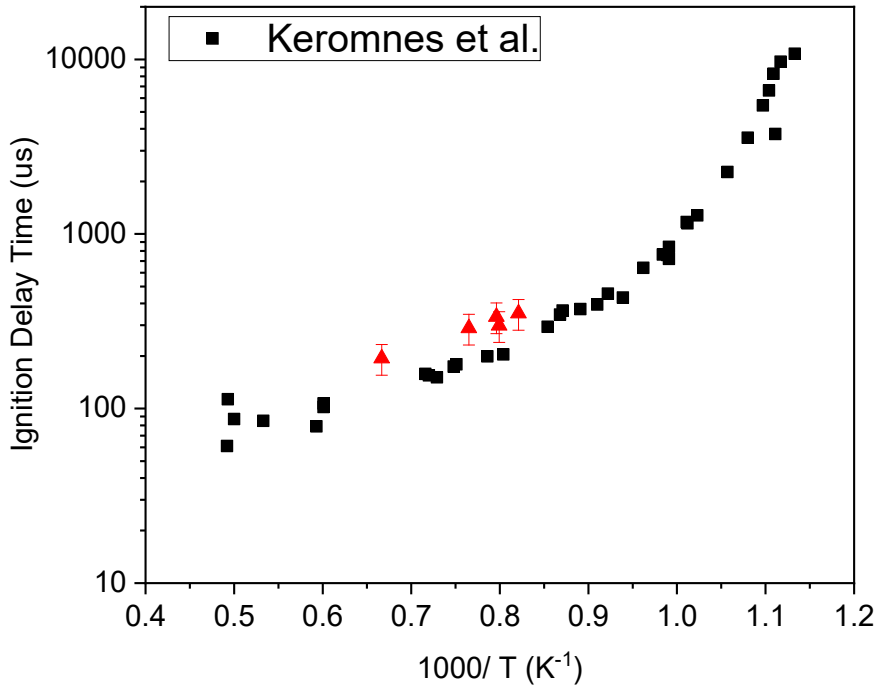

Figure 8. The data points with 20% uncertainty in our study compared to the provided data points in [49].

As seen in Figure 8, the data points of our study were at slightly higher ignition delay times compared with the data points of the previous study. However, the trends are similar, and the differences are within the limits of the uncertainties of the measurements. There were a few differences in the mixture that were noted previously.

2.2.4 Increased CO_2 Dilution in Syngas Mixtures

Mixtures 2 and 3 have similar fuel and oxygen compositions. However, mixture 2 has 60% CO_2 dilution compared to the 80% CO_2 dilution in mixture 3. Bifurcation of the shock wave due to the CO_2 dilution is noticeable in the pressure traces between the incident and reflected shocks of the experiment and the other mixtures of this paper. This phenomenon is properly documented for these dilutions [54, 63].

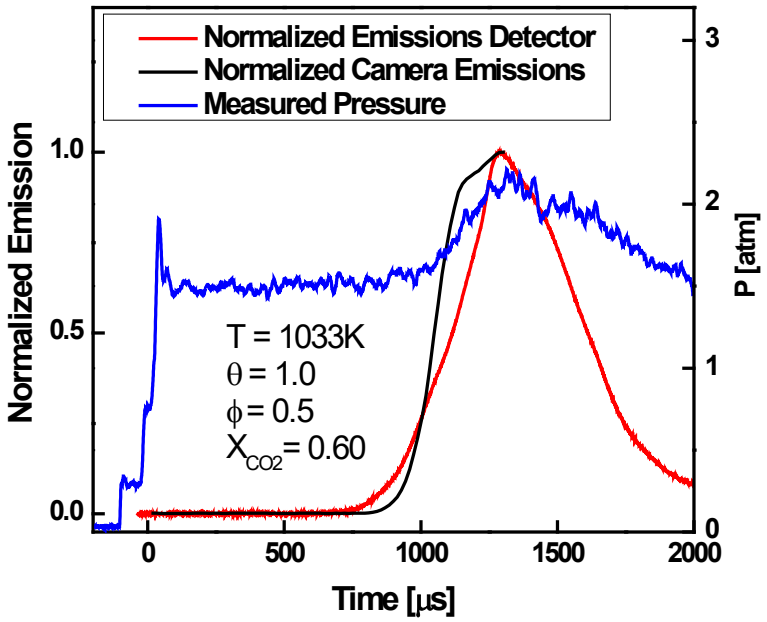

Figure 9. Pressure trace of an experiment using mixture 2, including emissions detector and camera emissions.

Figure 9 is a pressure trace of the 60% CO_2 experiment. An apparent pressure rise is seen in the experiment that matches the emissions detector. The high-speed camera was able to capture the ignition event as well. The end wall emissions from the camera are slightly behind compared to the emissions detector. However, it eventually observes more light (down the length of the shock tube) than the detector, as evident from the steeper rise of the slope compared to the camera emissions.

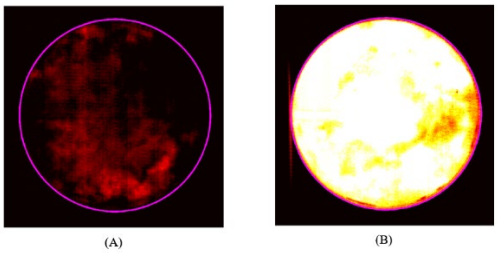

Figure 10. These images were from the experiment plotted in Figure 3. Image (A) refers to the end wall emissions at 943.92 μs. The slope method determined ignition at 947 μs. Image (B) refers to the end wall emissions at 1286.85 μs. The peak method determined ignition at 1288 μs. An artificial ring was placed to show the circumference of the shock tube.

Using two methods for determining ignition delay time, Figure 10 shows images of the flame using both the slope method (A) and a bright image at the peak of emissions (B). A completely homogenous combustion event is observed at the emissions peak throughout the entire shock tube cross-section.

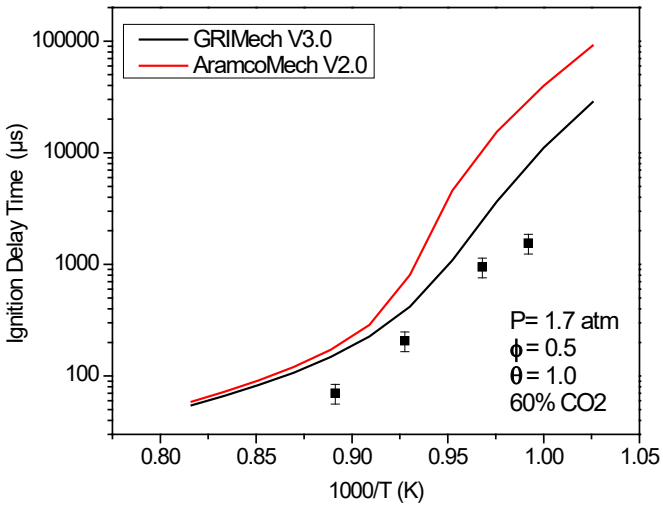

Figure 11. Mixture 2 experimental data points with 20% uncertainty are compared with two combustion kinetic models.

The data points collected using the slope method are compared with two combustion chemical kinetic mechanisms in Figure 11. The data does not match up well with these predictions; however, it follows a similar trend.

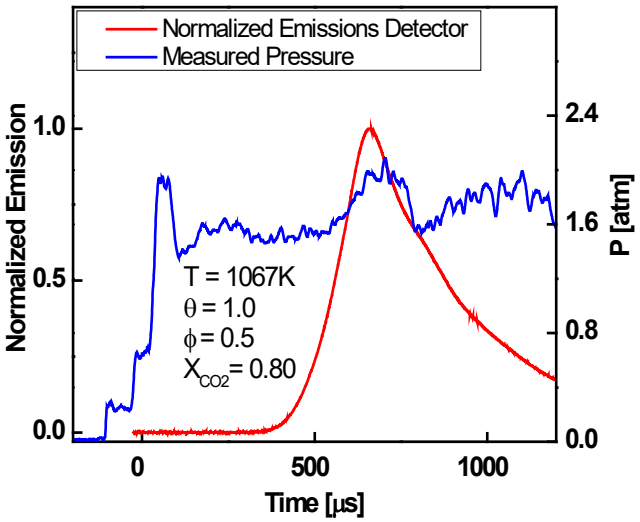

Figure 12. Pressure trace of an experiment using mixture 3, including emissions detector.

Figure 12 is a pressure trace of an 80% CO_2 experiment where ϕ =0.5. A pressure rise is visible at the same time as the emissions detector. No camera data was taken of this mixture for comparison. The chemical kinetic mechanisms were compared to these experiments of mixture 3 and are presented later in this report.

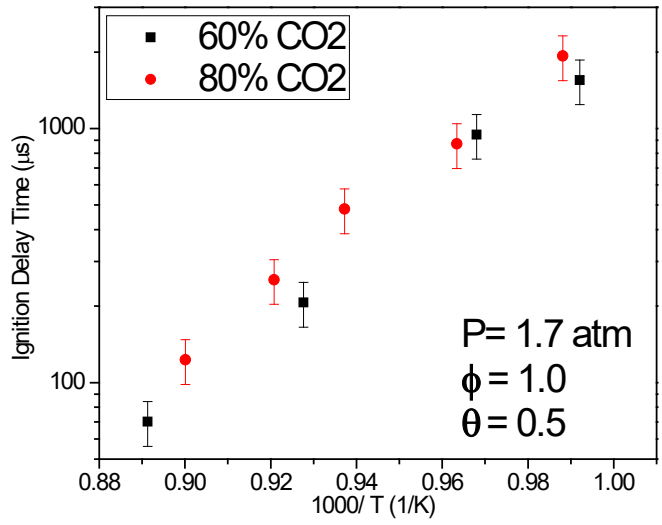

Figure 13. Ignition delay time comparison between mixture 2 and mixture 3 experiments.

It is expected that with an increase in CO_2 amount from mixture 3, an increase in the ignition delay time was observed. The primary reactions that are impacted are as follows:

$CO + OH \rightleftharpoons CO_2 + H$ (R1)

$H + O_2 \rightleftharpoons O + OH$ (R2)

It has been observed that CO_2 is not an inert bath gas in the ignition of syngas combustion. CO_2 competes for H radicals through the reverse reaction, which decreases the concentration of the H radicals that participates in the chain branching reaction given by R2. This is consistent with previous observations [64] of the chemical effect of CO_2 on methane and hydrogen flames. In the same shock tube facility, similar observations were confirmed utilizing methane as the fuel instead of syngas [54, 63].

Although within the uncertainty of the experiments from Figure 13 that compares the ignition delay time for mixtures 2 and 3, it is expected that an increase in CO_2 concentration increases the ignition delay time for the same oxy-syngas composition at these test conditions. The purpose was to study syngas combustion in CO_2 dilution and compare these with current chemical kinetic models. It will be shown throughout this publication that ignition delay times are lower than predictions by models due to CO_2 interaction.

2.2.5 Change of the Equivalence Ratio ϕ

Here, ϕ was changed between 0.33, 0.5, and 1 (mixtures 4, 3, and 5, respectively).

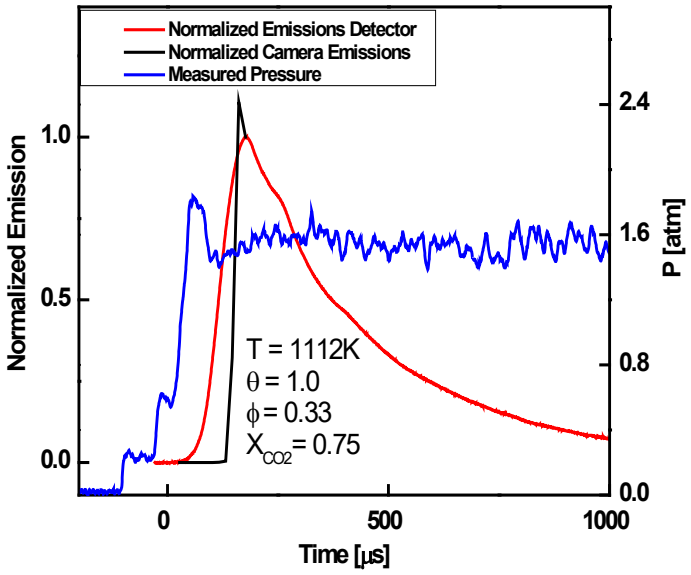

Figure 14. Pressure trace of an experiment using mixture 4, including emissions detector and camera emissions.

Figure 14 is a pressure trace of an experiment with a ϕ of 0.33 in mixture 4. The fuel-lean mixture 4 did not exhibit a pressure rise typically seen with combustion. A similar observation was seen for CO_2 diluted mixtures in methane and [55, 63]. The measurement results quantified using the camera images initially fell behind those of the emissions detector. However, more light was observed from the camera measurements downstream of the tube, resulting in higher maximum intensity. This was seen since the normalized camera emissions were greater than unity at a time before the peak of the emissions detector at the 2 cm location.

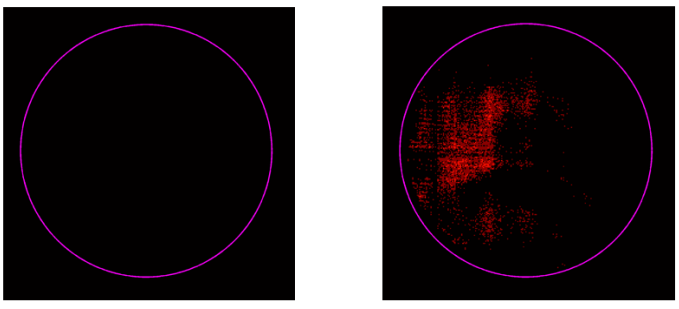

(A) (B)

Figure 15. These images were from the experiment plotted in Figure 9. Image (A) refers to the end wall emissions at 72.23 µs. The slope method determined ignition at 78 µs. Image (B) refers to the end wall emissions at 176.6 µs. The peak method determined ignition at 176 µs. An artificial ring was placed to show the circumference of the shock tube.

The images of combustion in Figure 15 show non-homogenous combustion with a very weak flame event. Compared to Figure 11B, where the combustion event consumes the entire cross-section of the shock tube, this was not observed for this mixture at critical ignition times. Bifurcation of the shock due to the CO_2 dilution has been previously observed with high-speed imaging to disrupt the homogeneity of the shock wave during ignition [63, 65]. This effect is increased with higher CO_2 dilutions. In Figure 9, the camera failed to detect light at the time of ignition determined by the slope method (A) but observed light at the time of the peak of emissions (B).

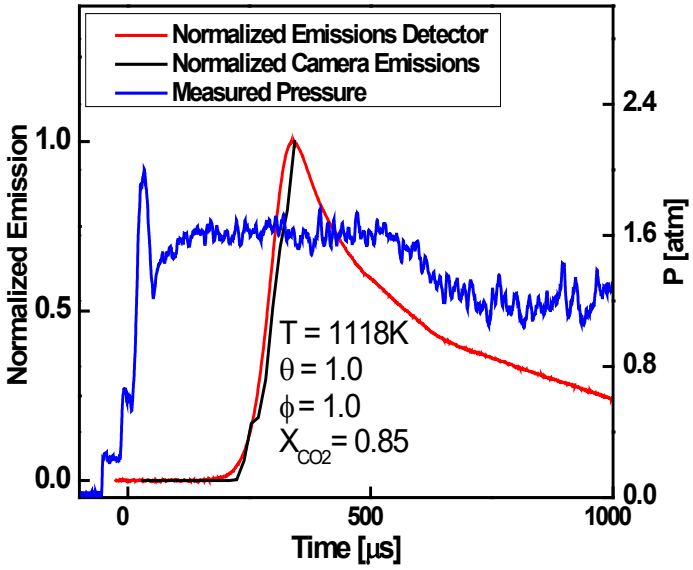

Figure 16. Pressure trace of an experiment using mixture 5, including emissions detector and camera emissions.

Figure 16 is a pressure trace of an experiment with a ϕ of 1.0 in mixture 5. A similar temperature from Figure 15 was chosen for Figure 17 to distinguish the difference in the ignition delay time. There was not a noticeable rise in the pressure from combustion in this mixture. The camera emissions were slightly behind the emissions detector in this mixture, however, it provided insight into the flame characteristics.

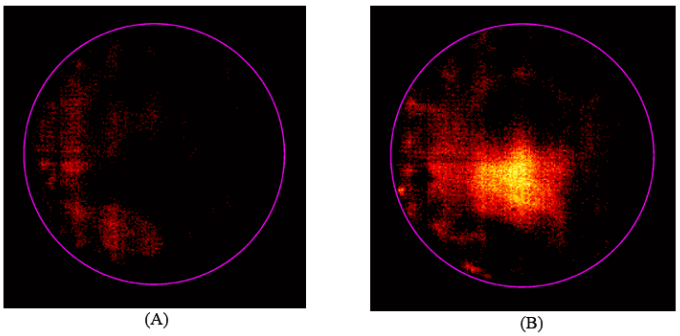

Figure 17. These images were from the experiment plotted in Figure 10. Image (A) refers to the end wall emissions at 239.24 μs. The slope method determined ignition at 245 μs. Image (B) refers to the end wall emissions at 343.61 μs. The peak method determined ignition at 340.5 μs. An artificial ring was placed to show the circumference of the shock tube.

In Figure 17, a flame is visible in the ϕ = 1.0 mixture 5 experiments correlating to the slope method (A) for determining the ignition delay time as well as the peak method (B). The flame is non-homogenous, similar to the lean fuel mixture in Figure 16. The effect of CO_2 addition on the homogeneity of both the fuel-lean (Figure 15) and ϕ = 1.0 (Figure 17) mixtures are apparent when compared to a lower CO_2 dilution (Figure 11).

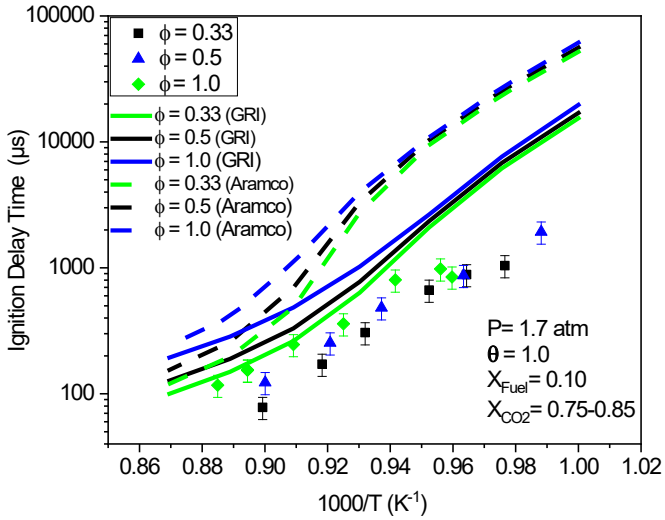

Figure 18. A plot of mixtures 3, 4, and 5 experiments. A change of ϕ resulted in differences in ignition delay time. These plots are compared to GRIMech v3.0 and AramcoMech V2.0.

Figure 18 compares the predictions of the two combustion chemical kinetic mechanisms with measurement results obtained using the mixtures of 3, 4, and 5. Neither model accurately predicted the ignition delay times, considering a 20% uncertainty in the ignition delay time measurements. The fuel-lean mixture had a shorter ignition delay time. This was primarily because of a higher concentration of free radicals, including OH, the radical involved in the primary reaction mechanism of hydrogen and carbon monoxide combustion (i.e., R1 and R2). Although incorrect in estimation for all three mixtures, the models did provide accurate trends. These trends in the temperature match previous findings [49, 50, 52], for a change in ϕ in syngas mixtures.

2.2.6 Change of the Hydrogen-to-Carbon Monoxide Ratio, θ

A change of the fuel ratio was also performed at a fixed equivalence ratio of ϕ = 0.5. This allows better insight on the contributions of each fuel to combustion.

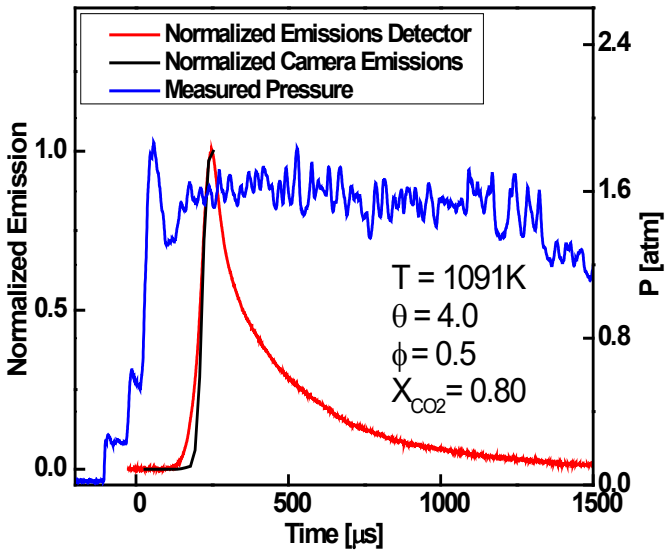

Figure 19. Pressure trace of an experiment using mixture 6 including emissions detector and camera emissions.

Figure 19 is a pressure trace of an experiment with a change of θ from 1.0 to 4.0 in mixture 6 compared to mixture 3. A large pressure rise was not seen during combustion with this mixture. Camera emissions matched well with the emissions detector but with some initial delayed response.

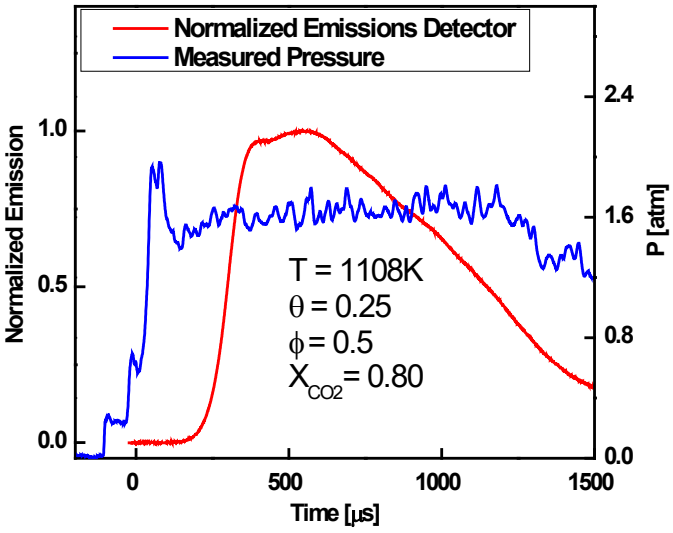

Figure 20. Pressure trance of an experiment using mixture 7, including the emissions detector.

In mixture 7, where θ was decreased from 1.0 to 0.25, there were noticeable changes. Camera imaging was not taken for mixture 7. In Figure 20, a pressure trace is given as well as the emissions detector trace. This mixture, with a larger carbon monoxide percentage, had a slower energy release as compared to other mixtures, as seen in the emissions detector. This is to be expected as carbon monoxide combustion is a much slower reaction as compared to the hydrogen combustion reaction and was previously observed [49].

For mixture 6, θ = 4.0, the models did not accurately predict the trend at colder temperatures. Both models predict an increased ignition delay time at lower temperatures. However, the observed ignition delay time does not substantially change from 1000 K to 1050 K. This was observed with a θ greater than 1.0 [49, 52]. It is explained that at low temperatures, competition between the chain branching reaction (R3) and chain termination reaction (R4) occur:

$H + O_2 = OH + H$ (R3)

$H + O_2 (+M) = HO_2 (+M)$ (R4)

The former dominates the ignition chemistry at high temperatures while the latter dominates at intermediate to low temperatures [52].

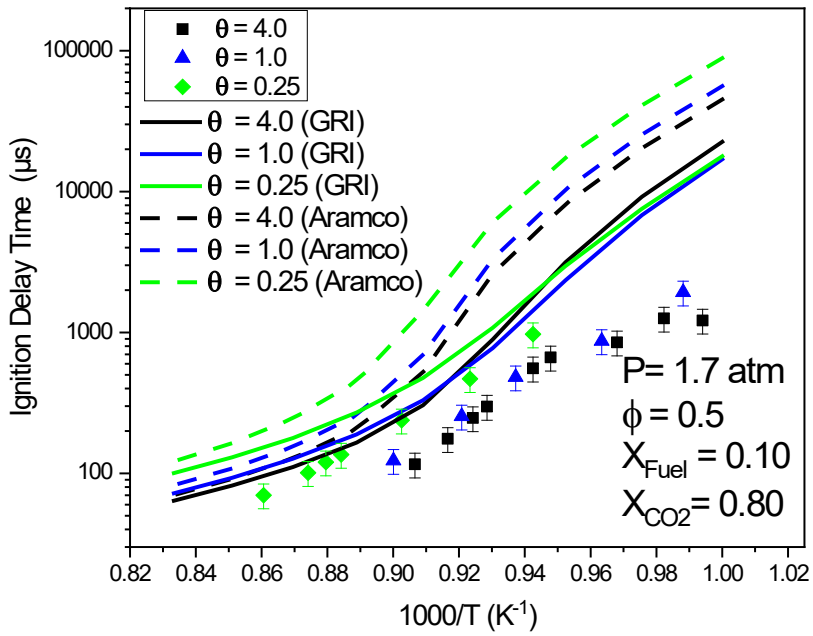

Figure 21. A plot of mixtures 3, 6 and 7 experiments. A change of θ resulted in differences in ignition delay time under similar conditions.

Figure 21 compares predictions of two combustion chemical kinetic mechanisms with data for mixtures 3, 6, and 7. None of the mechanisms accurately predicted the ignition delay times for the mixtures tested. The trends in mixtures 6 and 7 are expected and match what was observed by [50, 52] for a change in θ, with a minor exception to low temperatures in the mixture with θ = 4.0.

Mixtures with a larger value of θ had a shorter ignition delay time due to the presence of more hydrogen. Hydrogen has a much faster ignition chemistry relative to those of carbon monoxide combustion (which relies on hydroxyl formation). There was a little difference in the ignition delay time of mixtures 3 and 6, where θ changes from 1.0 to 4.0. The free radical formation for both mixtures satisfied the CO reaction to form CO_2. Whereas in mixture 7, with θ = 0.25, much less hydrogen existed to be able to form necessary free radicals for the same reaction to occur, resulting in the noticeable increase in the ignition delay time. Similar observations were

made in previous studies [49, 50, 52, 53, 63]. Present work highlights the importance of collecting experimental data in syngas mixtures so that kinetic mechanisms can be validated in mixtures with high CO_2 dilution.

2.2.7 Conclusions for low pressure

This is the first comprehensive experiment on the effects of adding high levels of CO_2 to syngas ignition delay times in a shock tube. This work measured the ignition delay time of oxy-syngas combustion in a shock tube with CO_2 dilutions from 60%-85% between 1006-1162K. Different mixtures of H_2/CO were used to see the effects of changing ϕ as well as θ. The ignition delay times had a positive correlation with ϕ showing that as the equivalence ratio decreased, the ignition delay times became shorter. Shorter ignition delay times were seen with an increase in changing θ. The mixture variations are necessary to observe trends in the ignition behavior under real-world conditions where the combustor could be operating over a wide range of settings. The experimental data were compared with two combustion chemical kinetic mechanisms GRI-Mech v3.0 and AramcoMech v2.0. In general, these models did not accurately predict the ignition delay time but generally predicted the trends seen in parametric variations in T, ϕ, etc. In addition, high-speed imaging of the experiments was taken at the end wall of the shock tube to compare with different methods of determining the ignition delay time. The high-speed camera images revealed insights into the non-homogeneity of the combustion events within the shock tube for large CO_2 dilutions but had some shortcomings to be addressed in future work.

The data suggests that there is a significant limit to the models at predicting the ignition delay time of syngas with variations in compositions with high dilutions of CO_2. Current experiments were performed around 1.7 atm. More analysis must be done at higher pressures to evaluate the effects of CO_2 within the entire range of operating conditions of a sCO_2 combustor.

In addition, modifications for the camera must be added in order to observe light at a lower wavelength. Present data would serve as crucial validation steps needed for the development and refinement of future combustion kinetic models.

2.3 Mid Pressure Ignition Study

This work offers new ignition delay time (IDT) data at higher pressures in oxy-syngas mixtures in a shock tube with high CO_2 dilution (which was fixed at 85%/vol.) and at an equivalence ratio, φ, = 1.0. Also, this research investigates changing θ, the fuel ratio of hydrogen-to-carbon monoxide, in the range 1.0-0.11. The study was performed at a range of pressures from 34.58 to 45.50 atm and temperatures from 1113 K to 1275 K. Additionally, the data was compared to the performance of 12 literature mechanisms against current data as well as with our previous measurements near 1atm [41]. The experimental data presented here will guide the development of future syngas kinetic mechanisms needed for cleaner power plants while the performance comparisons provide suggestions on existing mechanisms and their accuracy under these conditions.

2.3.1 UCF Study

2.3.1.1 Introduction

In the literature, studies have been conducted to measure ignition delay times of various compositions of syngas in the air (see [49, 50]); however, very little has been done to see the effects that CO_2 has on the combustion process. Some studies [51-53] examined the effects of CO_2 diluted syngas at a CO_2 concentration up to 30% CO_2. Furthermore refs. [35, 54, 55, 59, 66] examined the effects of CO_2 on oxy-methane combustion at dilution up to 89.5% and observed an increase in ignition delay time relative to other bath gasses. Previously, we conducted work at low pressures

of about 1 atm during syngas combustion in CO_2 diluted environments up to 85% dilution [41]. That study found large discrepancies between ignition delay times data and predictions.

This study provides new ignition delay time (IDT) data at higher pressures in oxy-syngas mixtures in a shock tube with high CO_2 dilution (which was fixed at 85%) and at an equivalence ratio, φ, = 1.0. Also, this research investigates changing θ, the fuel ratio of hydrogen-to-carbon monoxide, in the range 1.0-0.11. The study was performed at a range of pressures from 34.58 to 45.50 atm and a range of temperatures from 1113 to 1275 K. Additionally, we compared the performance of 12 literature mechanisms against current data as well as our previous measurements near 1 atm [41]. The experimental data presented here will guide the development of future syngas kinetic mechanisms while the performance comparisons provide suggestions on existing mechanisms and their accuracy under these conditions.

3.3.1.2 Results and Discussion

3.3.1.2.1 Shock Tube Simulations

Typically, shock tube experiments are modelled using a homogenous, constant-internal energy and constant-volume assumption [51, 54]. Because CO_2 is used as the diluent, there are unique challenges when modelling current experimental data. It has been well understood that CO_2 causes bifurcation of the shock wave due to boundary layer effects, shown both numerically [67] and experimentally [35, 41]. Bifurcation causes the shock wave to detach from the walls of the shock tube as it is reflected, causing turbulence and non-stagnant flow. Although this effect occurs, it has been shown to not impact the homogeneity of the core region of the mixture experimentally in our facility with a high-speed camera [41, 54]. With large amounts of CO_2 dilution, it has been experimentally observed for both syngas and methane mixtures that a significant pressure rise does

not occur from ignition and therefore it is more appropriate to use a constant-pressure assumption for modelling current experiments.

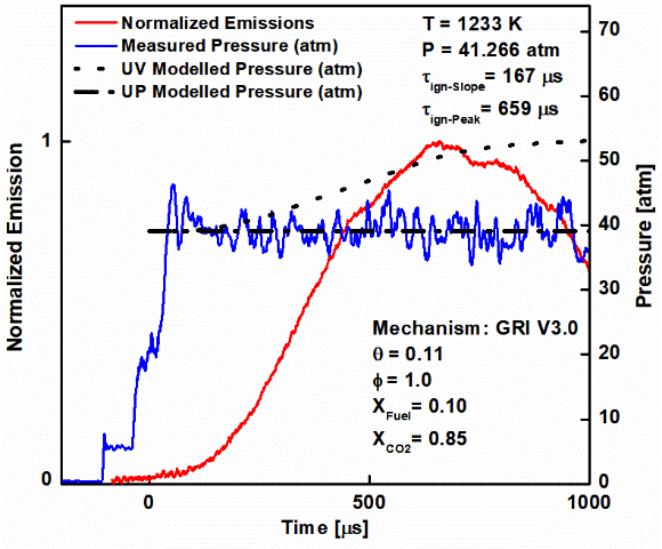

Figure 22. Pressure and emissions traces for a typical experiment near 40atm. The pressure traces for two modeling assumptions are also shown. The unsteadiness in the test pressure is due to bifurcation effects where pressure is measured.

As seen in Figure 22, the test pressure does not rise substantially when ignition occurs, which can be explained due to the higher specific heat capacity of CO_2 compared to argon (a typical diluent in shock tube experiments), which increases the specific heat of each mixture. Therefore, using a constant-pressure assumption rather than the constant-volume assumption is preferred.

Ignition delay times for the shock tube experiments evaluated were at mid-range temperatures (1000K-1250K); however, the ignition delays were on the order of 1.5 ms or less. Experiments at longer ignition delay times may encounter facility effects that increase reaction pressure over time that occur on the order of multiple ms. Additionally, impurities in the system

can cause ignition delay time measurements to depart from expected behavior, especially for CO mixtures. Common impurities were avoided, such as iron pentacarbonyl, which Dryer et al. [68] suggested may cause systematic over-predictions. These were avoided by utilizing research-grade CO in a pressurized aluminum tank rather than a carbon-steel tank.

Table 3. New data detailed mixtures compositions (%).

Mixture	**ϕ**	**θ**	**H_2**	**CO**	**O_2**	**CO_2**
1	1.0	1.00	5	5	5	85
2	1.0	0.67	4	6	5	85
3	1.0	0.25	2	8	5	85
4	1.0	0.11	1	9	5	85

Table 3 presents mixtures that are investigated in this study. The CO_2 dilute percentage was fixed at 85%, and ϕ was fixed at 1.0. These mixtures primarily compare a change of θ from 1.0-0.11.

3.3.1.2.2 Methodology for Comparison of Data with Predictions by Mechanisms

The methodology in this work adopts suggestions by Olm et al. [69] to perform a similar evaluation and review of ignition delay time measurements to model predictions. In this work, the agreement of experimental and simulation results is investigated using the following objective function:

$$E_i = \frac{1}{N_i} \sum_{j=1}^{N_i} \left(\frac{y_{ij}^{\mathrm{sim}} - y_{ij}^{\mathrm{exp}}}{\sigma\left(y_{ij}^{\mathrm{exp}}\right)} \right)^2 \quad (1)$$

$$E = \frac{1}{N} \sum_{i=1}^{N} E_i \quad (2)$$

Here, N is the number of datasets and N_i is the number of the data points in the *i*th dataset.,(1) is the error function of a given dataset, $y_{ij}^{\mathrm{sim}}$is the simulated ignition delay time measurement from the corresponding kinetic mechanism. $y_{ij}^{\mathrm{exp}}$and $\sigma\left(y_{ij}^{\mathrm{exp}}\right)$ are the j-th data point

and its uncertainty. Error function values E_i and (2) are expected to be near unity if the chemical kinetic model is accurate, and deviations of the measured and simulated results are caused by the scatter of the experimental data only. E is the total average error function averaged across all datasets. The average error was calculated for both low and high pressure separately to determine performance for the given datasets.

3.3.1.2.3 Mechanisms Chosen for Validation

A total of 12 literature kinetic mechanisms (see Table 4) were used with the CHEMKIN PRO [70] tool. The ignition delay time was determined from the predicted OH concentration time-histories (the excited OH* causes most of the emissions in these mixtures). The steepest rise in this plot was then extrapolated down to the baseline measurement to determine the predicted ignition delay time.

One of the aims of this part of the study was to compare the top eight overall rated mechanisms of the fifteen syngas combustion mechanisms that were evaluated for performance in the comprehensive syngas mechanism study by Olm et al. [69]. Additional four mechanisms (AramcoMech V2.0 [71], GRI V3.0 [60], FFCM-1 [72], and Varga [73]) were added to Table 3 to a total of twelve tested. The AramcoMech V2.0 [71] is a comprehensive C_1-C_4 hydrocarbon mechanism that was released in 2016. GRI Mech V3.0 [60] is a natural gas-based mechanism published in 1999, and however, due to its wide usage in syngas combustion literature, this was chosen as a reference mechanism. FFCM-1[72] is a 2016 released mechanism that was built on global optimization using available combustion data sets. Lastly, Varga [73] is an optimized syngas mechanism that was created as a result of the comprehensive syngas mechanism study by Olm et al.[69].

Table 4. List of mechanisms tested for IDT predictions in syngas/CO_2. Highlighted in green are the top three mechanisms (lower error value is better) from the current study.

No.	Mechanism	Reference	Species	Reactions	Low P Error	High P Error	Total Error
1	AramcoMech V2.0	[71]	493	2716	4106	4849	4403
2	CRECK-2014	[74]	14	33	7	684	278
3	Davis-2005	[75]	14	38	29	951	397
4	FFCM-1	[72]	38	291	1843	7075	3936
5	GRI V3.0	[60]	53	325	350	86	244
6	Keromnes	[49]	15	48	4259	6079	4987
7	Li-2007	[76]	14	37	82	612	294
8	Li-2015	[77]	21	93	760	1152	917
9	NUIG-NGM	[78]	293	1593	570	8269	3650
10	SanDiego-2016	[79]	57	268	115	1731	761
11	USC-II	[80]	111	784	1260	811	1080
12	Varga	[73]	14	44	2946	2127	2619

3.3.1.2.4 Comparison with Model Predictions

In Figure 23a, the experimental data points for a low-pressure mixture are shown compared to the twelve model predictions. Most of the models overpredict the data; however, at high temperatures, it appears that some of the predictions are close. It is seen that at colder temperatures, some models are greatly overpredicting IDTs. In Figure 23b, the same mixture at high pressure, all but one mechanism, Li-2007, is within the experimental uncertainties.

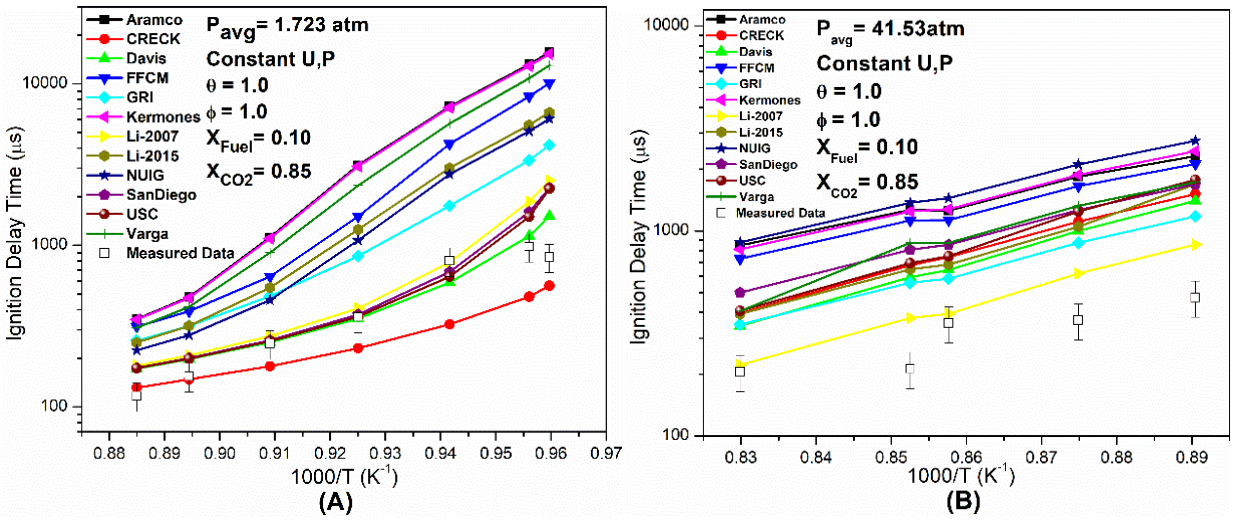

Figure 23. Measured and predicted ignition delay times for mixture 1 in Table 2 at a) low pressure (1.7atm data from [41]), and b) high pressure (42 atm, current data). The reader is referred to the PDF version of this article for interpreting different colors.

In Figure 24a, the average error function values for the low-pressure shock tube measurements are shown. The overall best mechanisms for the ignition delay times are CRECK, Davis, and Li-2007. These mechanisms can capture the behavior at lower pressures within the uncertainty for syngas diluted in a CO_2 environment. It can be concluded that even at atmospheric pressure, there are wide discrepancies in all tested mechanisms' performance. In Figure 24b, the average error function values for the high-pressure shock tube measurements are shown. All mechanisms overpredicted ignition times for all temperatures, which suggests none of the models are entirely capturing the natural chemistry occurring. All the models are, however, following a similar qualitative trend for IDT dependence on temperature. At higher pressures, GRI, Li-2007, and Davis are the best overall performers; however, none do a reasonable job at quantitatively determining the IDT. Thus, there is a large discrepancy between the tested models, which suggests the real chemistry is not being captured.

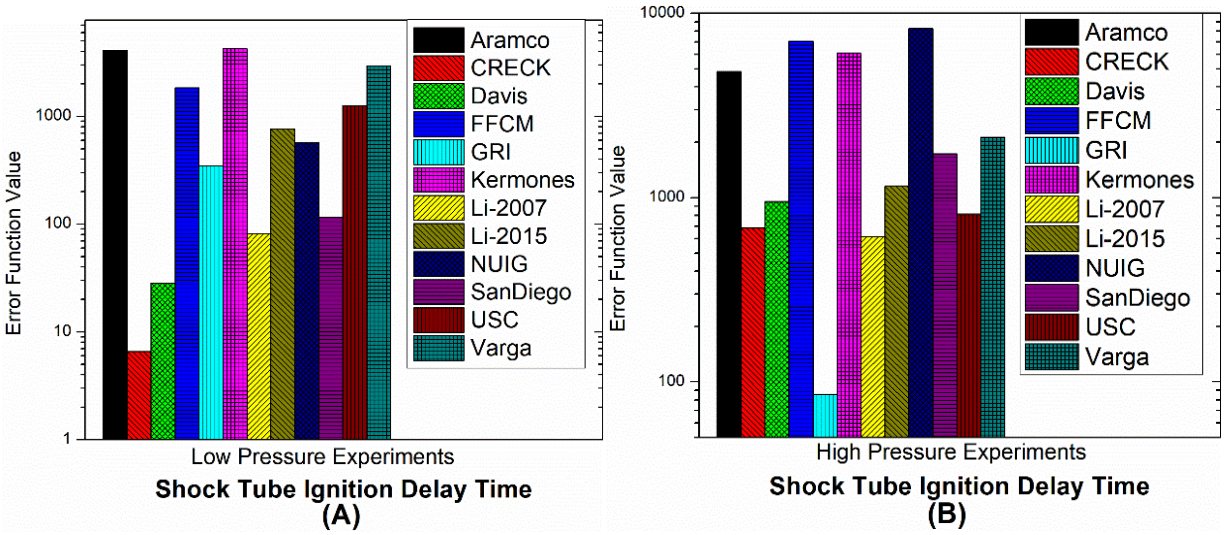

Figure 24. Error Function for the twelve mechanisms for a) low pressure (1.7 atm) and b) high pressure (42 atm) syngas experiments.

3.3.1.2.5 Pressure Dependence of IDTs with CO_2 Dilution

Earlier work performed at 1 atm has identified some of the effects of CO_2 dilution on ignition. With methane combustion, an increase in ignition delay time occurred with large CO_2 dilution [54]; however, a decrease occurred in syngas mixtures with similar dilutions and pressures[41]. Therefore, CO_2 clearly has an impact on the ignition process of oxy-syngas combustion that is not captured with the models.

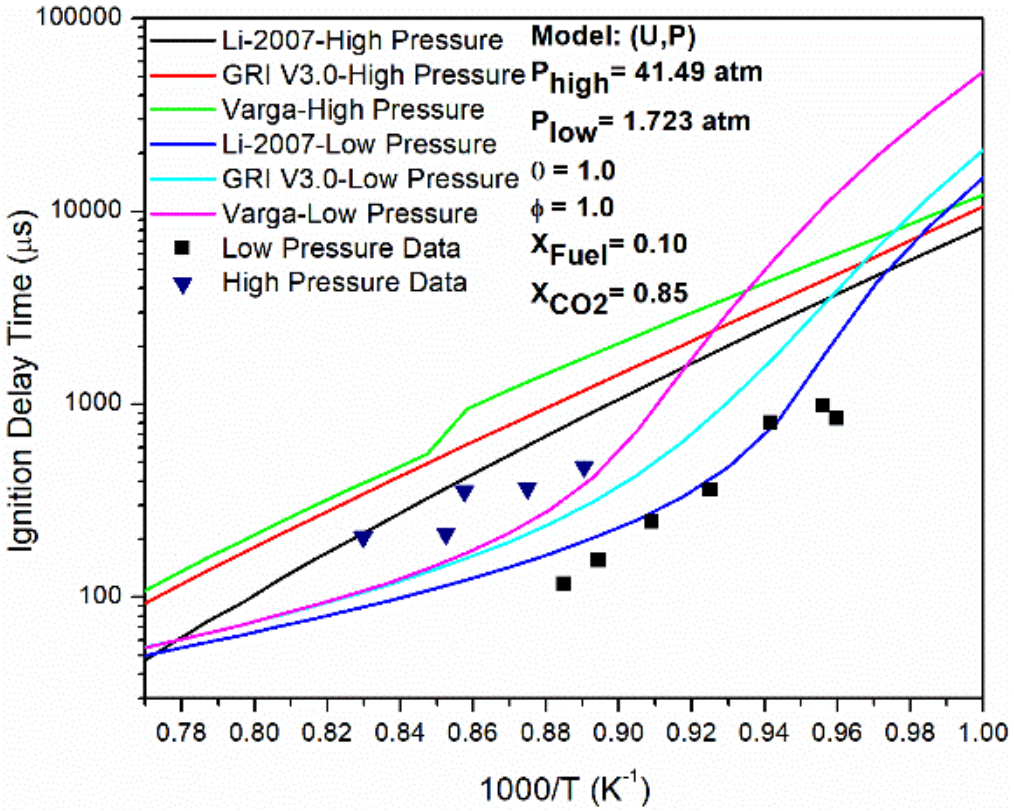

Figure 25. Pressure dependence of syngas ignition delay times along with predictions of three mechanisms. High pressure data from current work; Low pressure data from ref. [41].

Previous low pressure [41] and current high-pressure syngas data are compared in Figure 25. It is observed that ignition delay times increase for the given temperature range at higher pressures. Interestingly, the three models are shown for comparison also predict this behavior. It should be noted that both data and models are showing a cross-over point slightly above 1000 K on the colder end and about 1350K on the hotter end. In this temperature region, high-pressure ignition is delayed relative to lower pressures.

3.3.1.2.6 Sensitivity Analysis

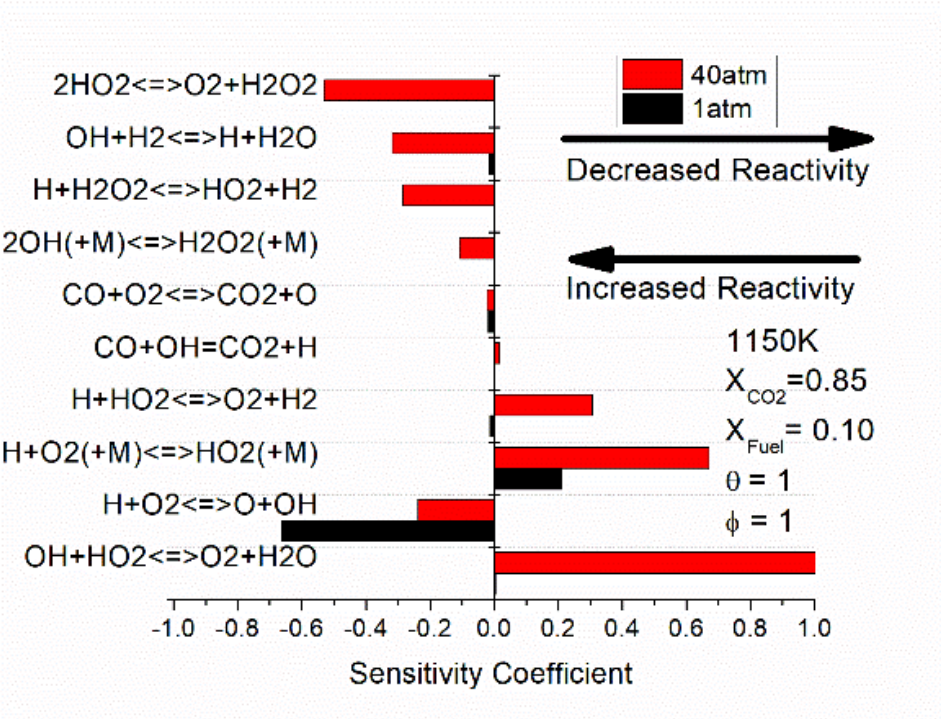

Figure 26. Sensitivity coefficients (Li-2007 mechanism) for ignition delay time on OH time-history obtained through a brute force sensitivity analysis. The top 10 reactions are shown.

A brute force sensitivity analysis for IDT was carried out for 1 atm and 40 atm for mixture 1 at 1150K. It can be seen in Figure 26 that there are competing reactions in this mixture. The top 10 reactions match the same in sensitivity studies (not shown here) done for mixtures 2, 3, and 4. As observed, these reactions have a much larger effect on the ignition delay time at 40 atm compared to 1 am.

In Figure 26, it is shown that the ignition delay time has two reactions competing for the same reactants R(1): $H + O_2 (+ M) \rightleftharpoons HO_2 (+ M)$ and R(2): $H + O_2 \rightleftharpoons OH + O$, leading to a higher termination rate relative to the chain branching rate. Indeed, a recent study on laminar flame speeds [81] of H_2/O_2 combustion in CO_2 bath gas found that at higher pressures for the same temperature,

the chain termination reaction R(1), overtakes the chain branching reaction R(2) of molecular oxygen (O_2). The chain termination reaction R(1) (due to third body M) is a strong function of pressure (the rates increase at high pressures) while it has weak temperature dependence [82]. On the other hand, reaction R(2) has a strong Arrhenius dependence on temperature [83] and a weak dependence on pressure. The competition between these two branching and termination reactions and their reaction rates' dependence on pressure and temperature is responsible for the behavior experimentally shown in Figure 25. At high temperatures, despite the increase in the reaction rate of R(2), the termination rate R(1) dominates for high-pressure mixtures (resulting in delayed ignition), while R(2) is faster for the low-pressure mixtures (hence shorter IDTs). This would explain the increase in the ignition delay time in our reported experiments at higher pressures (above 1000K). Additionally, the reaction rate for R(2) with CO_2 has only been validated up to 8 atm by Vasu et al. [51]; therefore, the high-pressure limit may not be well captured with current models at 40 atm.

CO_2 has a reduced third body collision efficiency, which will lead to different behavior, especially relative to nitrogen or argon, which are traditional bath gasses [51, 59] used in shock tube studies. CO_2 has traditionally been treated as a product of combustion; however, it has been experimentally shown that CO_2 is not an inert bath gas in the ignition of syngas combustion (i.e., CO_2 is both a reactant as well a product). Also, CO_2 competes for H radicals through the reverse reaction of R(3): $CO + OH \rightleftharpoons CO_2 + H$), which results in a decrease in the concentration of the H radicals (H radicals participate in the chain branching reaction given by R(2)). This is consistent with previous observations of the chemical effect of CO_2 on methane and hydrogen flames [64]. In the same shock tube facility, similar observations were made utilizing methane as the fuel instead of syngas [35, 54]. The collision efficiencies of CO_2 and reactions involving CO_2 will need

crucial examination in the future for improving the predictions by mechanisms for data taken in this study at high pressures.

3.3.1.3 Conclusions for mid pressure

This work measured ignition delay times of oxy-syngas mixtures in a shock tube with a high CO_2 dilution of 85% and at stoichiometric conditions. This study investigated changing θ, the fuel ratio of hydrogen-to-carbon monoxide, from 1.0-0.11. The study was performed at a range of pressures from 34.58 to 45.50 atm, and a range of temperatures from 1113 to 1275 K. Mixture variations are necessary to observe trends in the ignition behavior under real-world conditions where combustor could be operating over wide ranges of syngas compositions. To the best of our knowledge, we provide the first comprehensive experiments at elevated pressures for syngas with high levels of CO_2.

Additionally, predictions of twelve literature syngas chemical kinetic reaction mechanisms were assessed for their performance. It was found that at low pressures near 1 atm, some of the mechanisms agreed well with the data, while at high pressures, most of the models overpredicted the ignition delay times. In general, these mechanisms did not accurately capture the magnitude of experimental ignition delay time but generally predicted the trends seen in parametric variations in T, P, θ, ϕ, etc. Overall considering low and high pressures, the top three mechanisms were: GRI V3.0, CRECK-2014, and Li-2007. Both models and data indicate that ignition delay times decreased at high temperatures with increasing pressure, and there appears to be a cross-over point in temperature below which ignition delay times are faster with pressure. This trend can be explained by looking at the reaction rates of chain branching and termination reactions and their reaction rates dependence of pressure and temperature. Further measurements of reaction rates involving CO_2 bath gas at a range of temperatures and pressures must be performed and

incorporated into kinetic models. This is an area that may be improved on with future experiments to determine the high-pressure limit of R(2) for CO_2 bath gas.

Current experimental data suggests that there is a significant limitation to the literature kinetic mechanisms at predicting ignition delay time of syngas with variations in compositions under high dilutions of CO_2. More analysis must be done at higher pressures to evaluate the effects of CO_2 within the entire range of operating conditions of a sCO_2 combustor. Present data would serve as crucial validation steps needed for the development and refinement of future combustion kinetic models.

2.3.3.2 Collaboration Work

Experiments were taken in collaboration with Stanford University to compare oxy-hydrogen and oxy-methane ignition at mid-range pressures of approximately 40 atm, which culminated in a publication [46]. The purpose of this work was to determine facility effects on the collection of data. The first mixture was oxy-hydrogen with an equivalence ratio of 0.33. This mixture represents a type of syngas that contains no carbon monoxide. Future combustion systems may eliminate carbon-containing fuels. This can be achieved from extracted natural gas through a process called steam reforming [84]. In this system, no carbon emissions would form from combustion; only water would be extracted. Oxy-methane results and discussion can be found in section 4.2.1 Stanford University Collaboration Work.

Current IDT experiments for all tests above 72 atm (test mixture 2, 4, and 6 in Table A) were performed using the Stanford high-purity, high-pressure shock tube (HPST). The stainless steel driven section has an internal diameter of 5 cm and was heated to 90 C. Diaphragms were made of aluminum or steel (with cross-scribing of different depths) to allow measurements over a broad range of pressure (10 – 500 atm). In this shock tube, standard uniform test times (for non-reactive

synthetic air mixtures) are of the order of 2 ms when helium is used as the driver gas. In current high CO_2 concentration experiments, the bifurcation effect, which is a non-ideal effect caused by boundary layer build-up, is stronger and the test times for the current experiments are shorter, about 1.1 ms. High-purity methane, hydrogen, oxygen, and carbon dioxide gases were supplied by Praxair. Gas-phase fuel mixtures were prepared manometrically in a 12.8-liter stainless-steel mixing tank at 110 C. Mixtures were stirred using a magnetically-driven vane assembly for at least 15 minutes before the experiments. Current IDT experiments for all tests above 72 atm (test mixture 2, 4, and 6 in Table A) were performed using the Stanford high-purity, high-pressure shock tube (HPST). The stainless steel driven section has an internal diameter of 5 cm and was heated to 90 C. Diaphragms were made of aluminum or steel (with cross-scribing of different depths) to allow measurements over a broad range of pressure (10 – 500 atm). In this shock tube, standard uniform test times (for non-reactive synthetic air mixtures) are of the order of 2 ms when helium is used as the driver gas. In current high CO_2 concentration experiments, the bifurcation effect, which is a non-ideal effect caused by boundary layer build-up, is stronger and the test times for the current experiments are shorter, about 1.1 ms. High-purity methane, hydrogen, oxygen, and carbon dioxide gases were supplied by Praxair. Gas-phase fuel mixtures were prepared manometrically in a 12.8-liter stainless-steel mixing tank at 110 C. Mixtures were stirred using a magnetically-driven vane assembly for at least 15 minutes before the experiments.

Two diagnostics were employed during the experiments: excited OH radical (OH*) emission and sidewall PZT pressure; diagnostics in the HPST were located 1.1 cm away from the end wall. Ignition was indicated by emission near 306 nm from the $A^2\Sigma^+$ - $X^2\Pi$ ((0,0) band) of OH* that was detected using a modified PDA36A Si detector and Schott UG5 filter. Pressure time-histories are also monitored using a Kistler^{TM} piezoelectric pressure transducer. With high CO_2

dilution in the test conditions, the pressure rise during ignition is not strongly obvious in most of the cases. Results are in Figure 27 A and B along with simulation results of several literature mechanisms [46].

Table A. IDT test conditions and facilities.

Mixture	Reactant Mole Fractions				Initial Conditions		Facility
	CH_4	H_2	O_2	CO_2	T/K	P/atm	
1	0.075	0	0.15	0.775	1346-1434	27-35	UCF ST
2	0.075	0	0.15	0.775	1045-1411	100-286	SU HPST
3	0.0391	0	0.0992	0.8617	1447-1578	28-36	UCF ST
4	0.0391	0	0.0992	0.8617	1082-1453	72-269	SU HPST
5	0	0.05	0.1	0.85	1170-1270	37-40	UCF ST
6	0	0.1	0.05	0.85	1083-1291	103-311	SU HPST

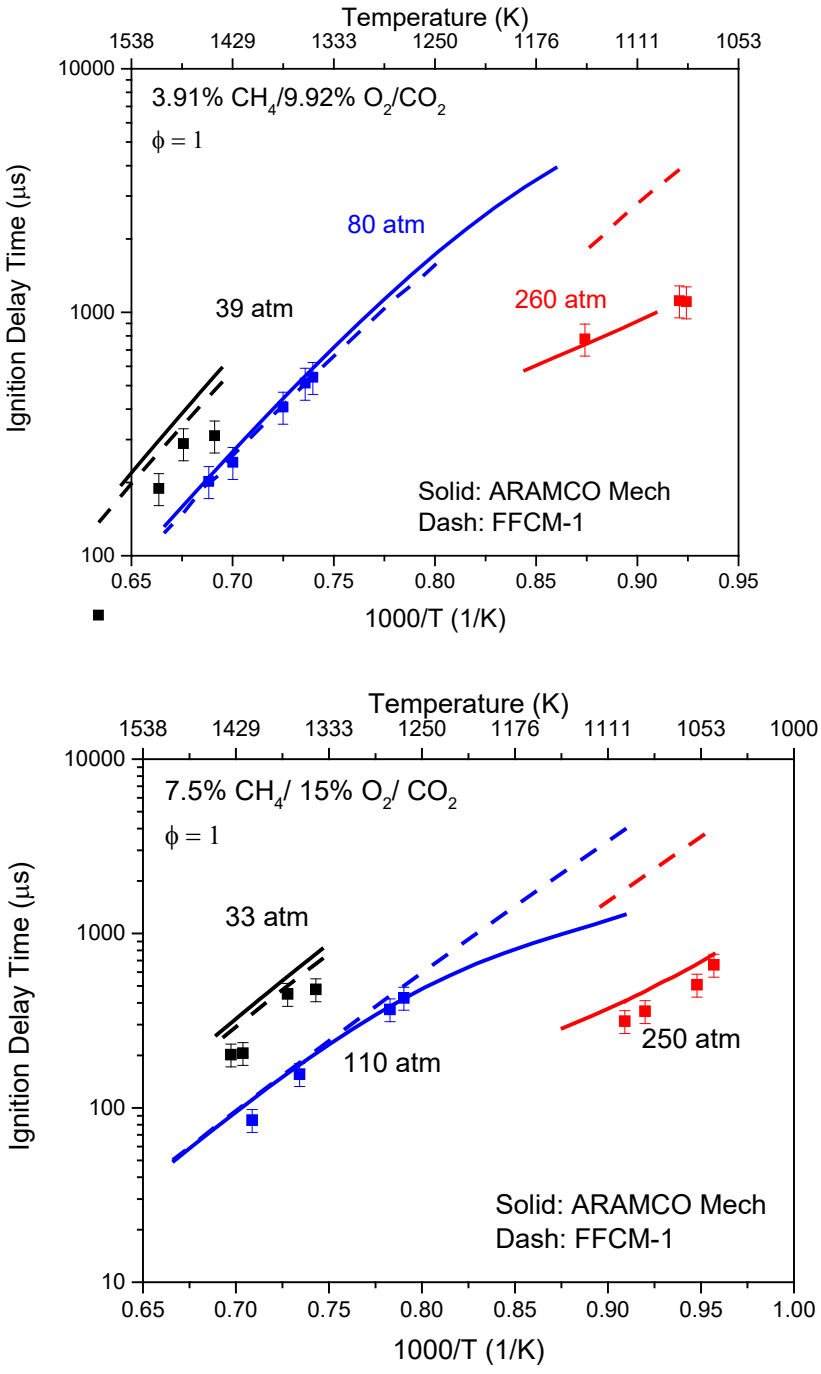

Figure 27 A. Ignition delay time measurement for $CH_4/O_2/CO_2$ mixtures

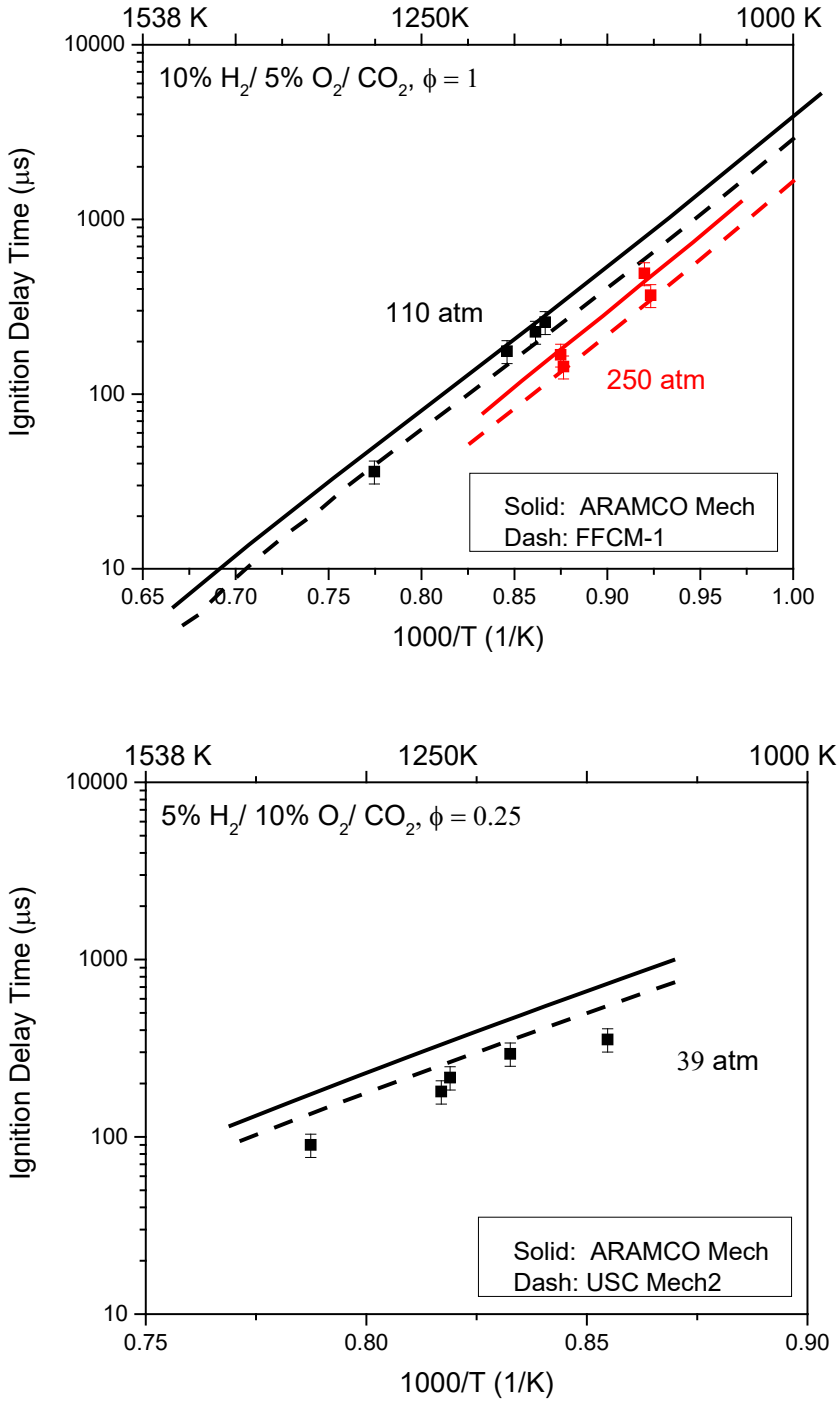

Figure 27 B. Ignition delay time measurement for $H_2/O_2/CO_2$ mixtures

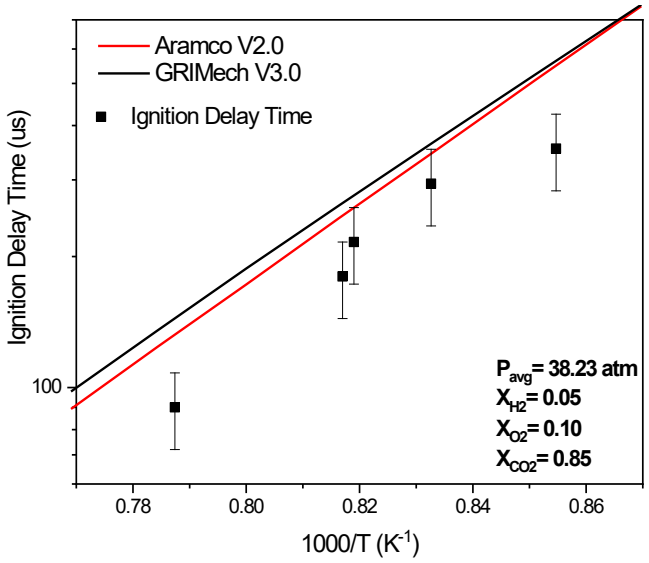

Figure 27 C. Oxy-hydrogen combustion around 40 atm in carbon dioxide bath gas.

In Figure 27C, data was collected between a temperature range of 1150 K - 1250K and an average pressure of 38.23 atm. Both Aramco and GRIMech capture the accurate trend with respect to temperature. There are two data points that match Aramco within the uncertainty, but the ignition delay time from experiments was quicker than both model predictions for all other data points. Aramco predictions were slightly better than GRIMech. These findings were expected after previous investigations, in Sections 2.2 Low Pressure Ignition Study and 2.3.1 UCF Study, found similar disagreement.

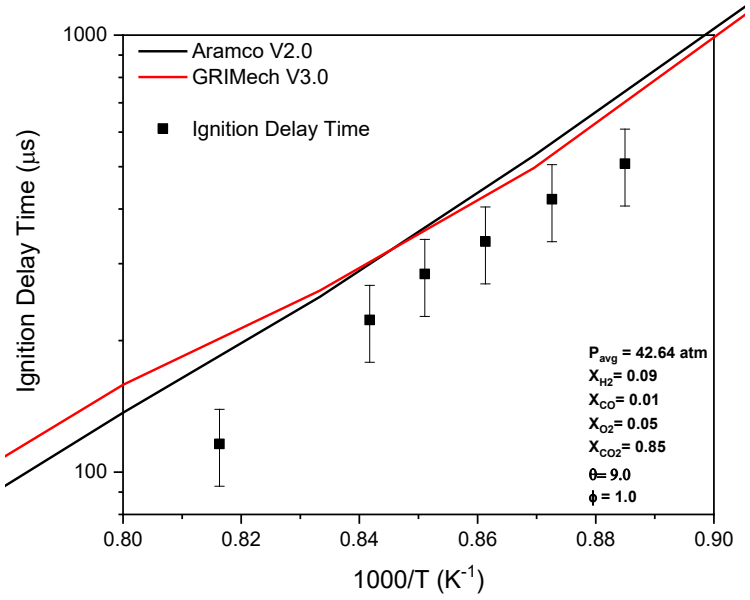

Figure 28. A high hydrogen oxy-syngas mixture at pressures around at 42 atm.

Figure 28 contains data collected and mechanism predictions for a high hydrogen oxy-syngas combustion in a temperature range of 1125 K - 1225 K and an average pressure of 42 atm. Similar to the previous figure, Figure 28, both mechanisms captured the trend with respect to temperature; however, both models overpredicted the ignition delay time. Aramco predicted a lower ignition delay time relative to GRIMech from approximately 1100- 1175 K but then crossed over at around 1175K to a more extended ignition delay time prediction. The overprediction of high hydrogen oxy-fuel combustion in heavily diluted carbon dioxide environments has been recognized in other work, in Section 2.3.1 UCF Study.

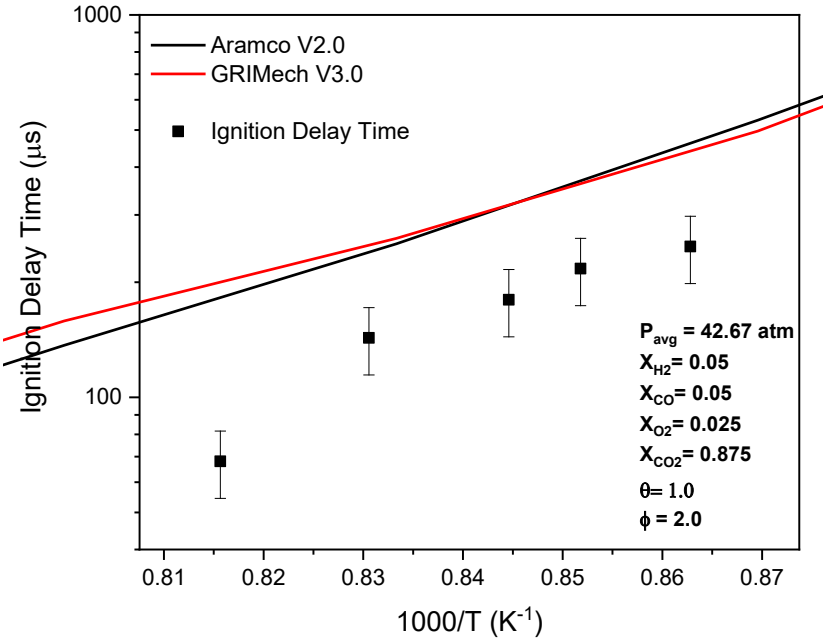

Figure 29. Oxy-syngas ignition data under rich conditions around 40 atm.

Figure 29 contains experimental data for the oxy-syngas mixture with a high equivalence ratio of 2.0. The temperature range of these experiments is 1150K - 1225K, and the average pressure is 42.67 atm. This data was compared to Aramco V2.0 and GRIMech V3.0. The experimental ignition delay times are significantly lower than the computer model predictions; however, the models can capture the trend with respect to temperature. The overprediction of the models are more significant at hotter temperatures. Mixtures of this equivalence ratio are important to test because there can be a region of higher fuel concentration in diffusion-style combustors.

2.4 High-Pressure Ignition Study

Ignition studies of oxy-syngas combustion was performed at high pressures between 70-100 atm. Mixtures. This work has a pressure range of 70-100 atm and a temperature range of 1064K – 1340K. Four separate mixtures were made.

Table 5: Summary of high-pressure syngas experimental conditions (% vol. fraction).

Mix	**θ**	**ϕ**	**H_2 (%)**	**CO (%)**	**O_2 (%)**	**CO_2 (%)**	**P_{avg} [atm]**
1	1.12	1.02	2.9	2.6	2.7	91.8	77.9
2	0.41	0.99	6.9	16.7	11.9	64.5	90.5
3	0.41	0.96	1.5	3.7	2.7	92.2	88.4
4	1.09	0.99	12.5	11.5	12.1	63.9	88.5

Table 5 reports the oxy-syngas mixtures that are presented in this study. The CO_2 dilution percentage was varied as well as θ, φ, and fuel loading. A dilution of an inert gas was not necessary to prevent detonation pressures inside the shock tube which could exceed the material limits of windows.

Time-zero for these experiments was defined as the halfway point between the end of the incident wave and beginning of the reflected shock pressure. This definition will be discussed in more detail later in this report.

The ignition delay time definition was defined as the difference in time between time-zero and the onset of the primary ignition event at the measurement location. The onset of ignition was defined as the time corresponding to the maximum slope of the emissions detector extrapolated to baseline at the same axial location (traditionally called the slope method). This method has been previously used for CO_2 diluted mixtures [35, 41, 54] and previous studies [85, 86] estimated a 20% uncertainty in the ignition delay time. This is a combination of uncertainties due to: mixture, temperature, pressure, equipment, and experimental uncertainty [54]. The amount of available test time was determined when expansion waves from the driver end reached the test location resulting

in about 1 millisecond of test time at 100 atm (without any special tailoring strategies used with shock tubes [87]).

Because of the high fuel loading in these mixtures, during experiments, there were significant pressure rises from combustion. Modelling this behavior in CHEMKIN PRO was done with constant volume, internal energy (constant V, U) model using AramcoMech V2.0 and GRIMech V3.0.

Four different mixtures were created to simulate different conditions that may be seen inside a combustor due to differences in coal gasification processes and fuel loading. Table 4 shows the mixture composition of the four different syngas mixtures. Mixtures 1 and 3 have similar, low fuel loading and equivalence ratios, but Mixture 1 has a near unity θ, while Mixture 3 has a value close to 0.40. Mixtures 2 and 4 have higher fuel loading with nearly the same equivalence ratio. Similarly, Mixture 2 has a lower θ near 0.40, meaning higher carbon monoxide fuel content. The lower fuel loading mixtures have lower overall combustion temperatures as compared to the high fuel loading ones. Experiments were taken for each of these mixtures to better understand syngas oxidation under supercritical carbon dioxide conditions. Results were compared to the predictions of Aramco V2.0 and GRI V3.0 mechanisms during this work. Overall, at low fuel loading/high CO_2 dilution conditions, and colder temperatures the Aramco 2.0 mechanism was able to predict the ignition delay times decently well.

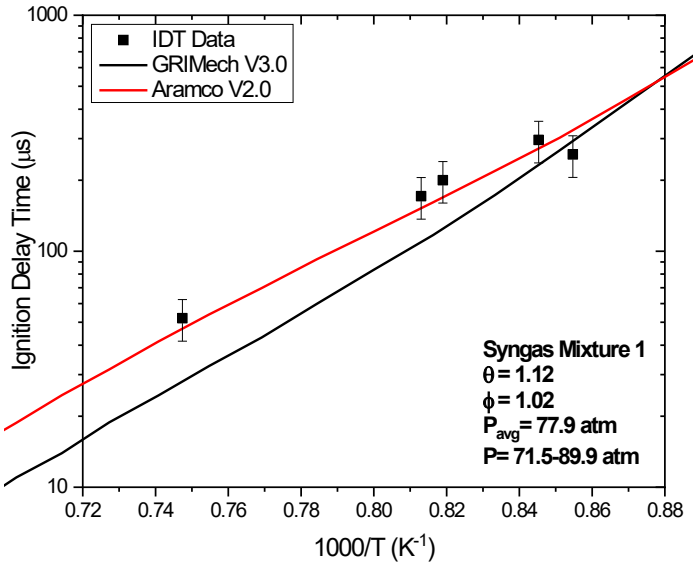

Figure 30. Experimental syngas ignition delay times and comparisons with predictions of two mechanisms ($\theta = 1.12$ and $\varphi = 1.02$). The mechanisms were run at the average pressure of 77.90 atm.

The experiments shown in Figure 31 of Syngas Mixture 1 were predicted well by the Aramco 2.0 mechanism, although with some slight disagreement with an experiment in the colder regime. The overall profile of a reduction of the ignition delay time as temperature increased was well captured. The vibrational relaxation time of this mixture was calculated and had a maximum time of 1.11 μs. This relaxation time is minor compared to the measured ignition delay times. GRI V3.0 did not perform very well at these predictions. The mixture was designed to simulate conditions in the center of the combustor and had a near stoichiometric equivalence ratio (additionally, this had low fuel loading). The Aramco 2.0 mechanism can accurately model current experimental data over all these conditions tested.

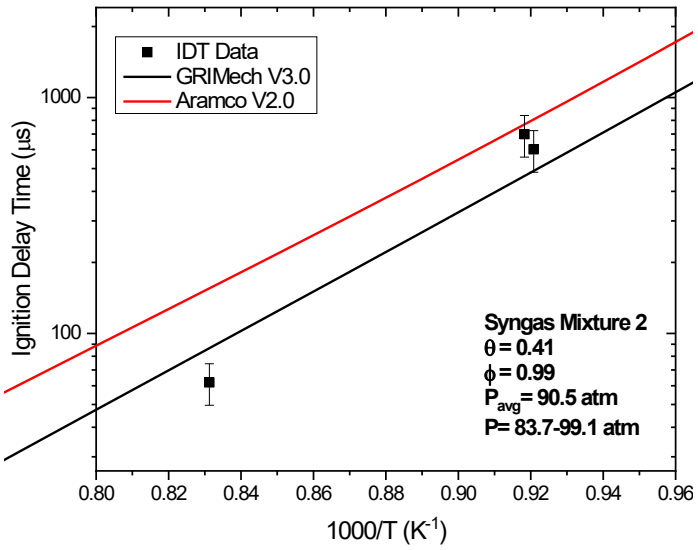

Figure 31. Experimental syngas ignition delay times and comparisons with predictions of two mechanisms ($\theta = 0.41$ and $\varphi = 0.99$). The mechanisms were run at the average pressure of 90.5 atm.

The experiments shown in Figure 31 of Syngas Mixture 2 were predicted well by the Aramco 2.0 mechanism at colder temperatures. At higher temperatures, both mechanisms did not accurately capture the real behavior. The vibrational relaxation time of this mixture was calculated and had maximum time of 0.66 μs. This relaxation time is very minor compared to the ignition delay times reported. Again, it is observed that GRI V3.0 did not perform very well at these conditions. This mixture was designed to simulate conditions in a combustor with a high carbon monoxide concentration and high fuel loading. We have previously published results at lower pressures with a similar mixture [41, 88] and had inaccurate predictions by the GRI V3.0 mechanism. We suspect updated reactions rates and newer reaction pathways not found in GRI could explain the discrepancy.

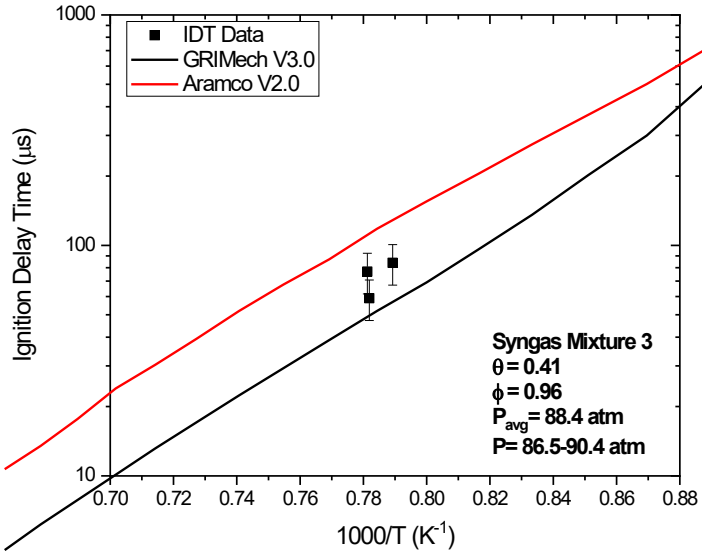

Figure 32. Experimental syngas ignition delay times and comparisons with predictions of two mechanisms (θ = 0.41 and φ = 0.96). The mechanisms were run at the average pressure of 88.4 atm.

Results shown in Figure 32 for Syngas Mixture 3 showed both mechanisms, Aramco V2.0 and GRI V3.0, did not perform very well at these predictions. The vibrational relaxation time of this mixture was calculated and had maximum time of 1.25 μs. Again, this relaxation time is very minor compared to the ignition delay times reported. The mixture was designed to simulate conditions with levels of high carbon monoxide and low fuel loading. Similarly, the experiments shown in Figure 33 of Syngas Mixture 4 were not predicted well by either the Aramco 2.0 or GRI V3.0 mechanisms over the entire temperature range. The vibrational relaxation time of this mixture was calculated and had a maximum time of 0.44 μs. This relaxation time is minor compared to the ignition delay times reported. The mixture was designed to simulate conditions in the center of the combustor and had a near stoichiometric equivalence ratio. Additionally, this mixture had a near-unity θ and had high fuel loading.

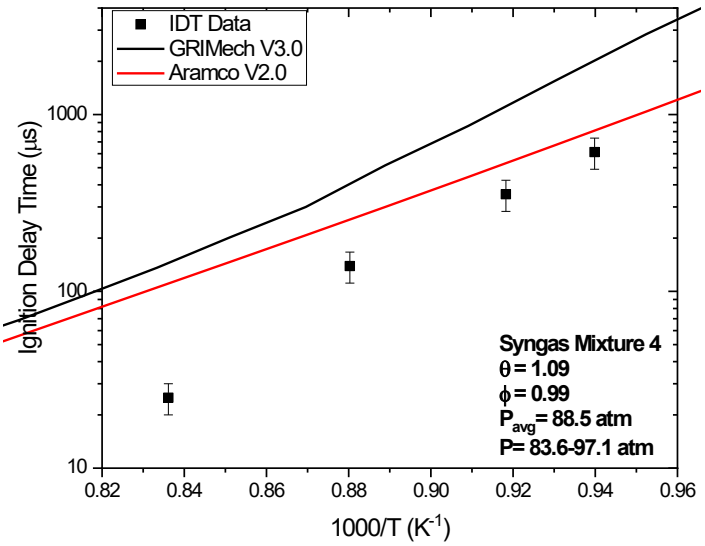

Figure 33. Experimental syngas ignition delay times and comparisons with predictions of two mechanisms (θ = 1.09 and φ = 0.99). The mechanisms were run at the average pressure of 88.5 atm.

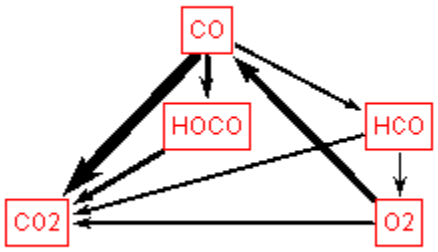

Figure 34. Reaction pathway for Syngas Mixture 1 at T= 1230 K and P= 77.56 atm (simulations with the Aramco 2.0 mechanism).

The reaction pathway for CO in syngas oxidation with highly diluted carbon dioxide is shown in Figure 35. The main pathways for CO oxidation directly into CO_2 are reactions R(4) and R(6). Accurate rate coefficient estimations or measurements for these reactions might improve the predictions of syngas ignition delay times measured in this study. More specifically, the 3rd body collision efficiencies for CO_2 may need to be further addressed. [89] Also, it is important to note that these radicals come from the decomposition of diatomic hydrogen in competing effects of

R(1) and R(2). As mentioned earlier, the pressure dependency of R(2) and its efficiency tied to the 3rd body collision efficiency of CO_2 bath gas will need future investigations as well.

CHAPTER 3: LOW AND HIGH-PRESSURE OXY-METHANE STUDIES

3.1 Introduction

Natural Gas, or NatGas, is a fuel resulting in extraction from underground wells that offers the potential for cleaner burning in a power plant. A simplified model of natural gas is a fuel primarily consisting of methane with smaller amounts of larger hydrocarbons. Depending on the extraction method and location across the world, the composition of natural gas can have variations. A 1992 nationwide survey found variations across the US of up to 14% in heating value, 14% in density, 20% in Wobbe Index and 25% in stoichiometric air-fuel ratio [90]. The issue may be more serious for places like Europe that import natural gases from outside the continent. Effects of natural gas composition variations can impact operation, performance and exhaust emissions of natural gas-powered vehicles or power generation equipment [91, 92].

Very little data exists for oxy-NatGas combustion in highly diluted carbon dioxide in literature, however, some exists for oxy-methane combustion in carbon dioxide environments [46, 54, 59, 93, 94]. Due to the complex nature and variation of fuels that may be contained in a natural gas pipeline, simplifying it in experiments to methane provides a baseline of understanding the chemical kinetics. The effects of CO_2 on oxy-methane combustion at dilution up to 60% at low pressures of 1 to 4 atm observed an increase in ignition delay time [54]. Similarly, an increase in the ignition delay time was observed at higher pressures between 6- 30 atm [59]. Therefore, it is unknown of the effects of high concentrations of CO_2 on oxy-NatGas and oxy-methane combustion at higher pressures and experimentation must be done. Comparisons with models are necessary to evaluate their ability to capture the behavior.

3.2 Mid Pressure Ignition Studies

3.2.1 Collaboration Work

Experiments were taken in conjunction with Stanford University to compare oxy-methane ignition at mid-range pressures. This work was taken in addition to the data presented in the previous chapter, in section 3.3.2 Stanford University Collaboration Work. The mixtures contain different amounts of fuel loading and equivalence ratio.

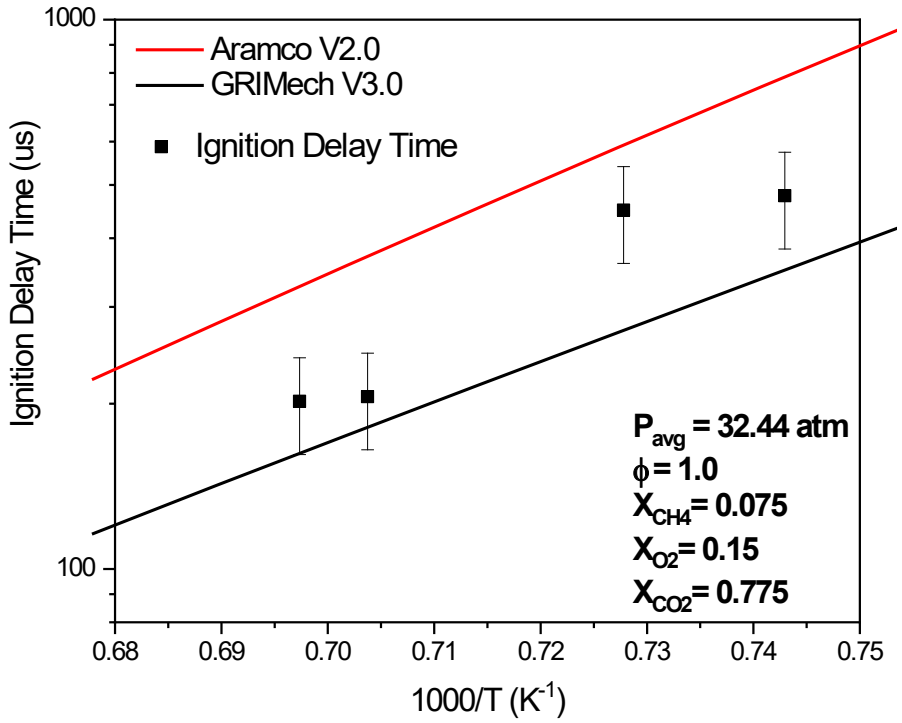

Figure 35. Oxy-methane combustion at an average pressure of 32.44 atm.

Data is presented in Figure 36 for an oxy-methane mixture with an equivalence ratio of 1.0 with a temperature range of 1340K - 1430K and an average pressure of 32.44 atm. Both models capture the trend with respect to temperature. Aramco overpredicts the ignition delay time through the entire temperature range. GRIMech underpredicts the ignition delay time at colder temperatures but has some agreement at the hotter temperatures.

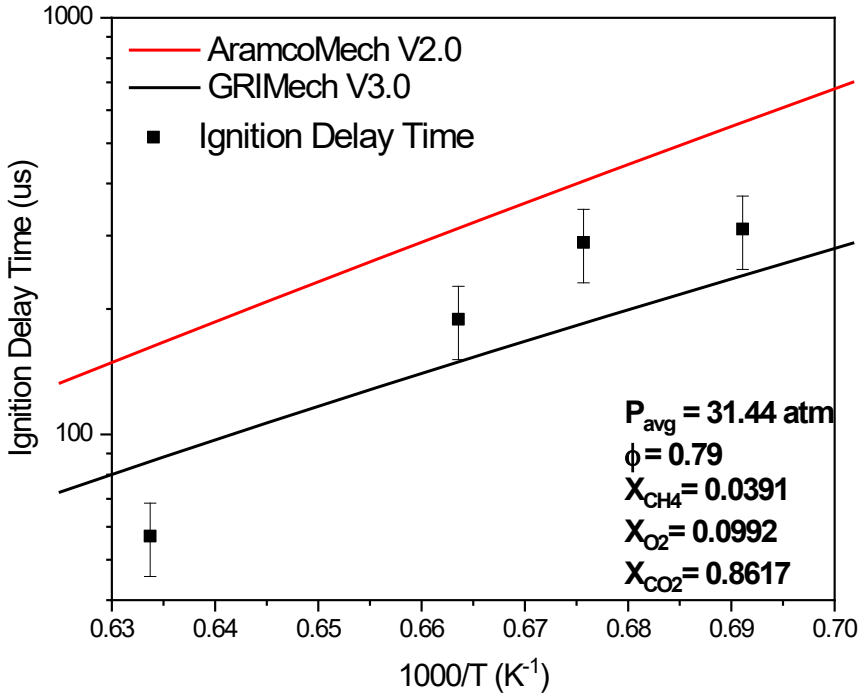

Figure 36. Oxy-methane combustion at an average pressure of 31.44 atm.

Data is presented in Figure 37 for an oxy-methane mixture with an equivalence ratio of 0.79 with a temperature range of 1425K – 1575 K and an average pressure of 31.44 atm. Both models capture the trend with respect to temperature. Aramco overpredicts the ignition delay time through the entire temperature range. GRIMech underpredicts the ignition delay time at colder temperatures but has some agreement at the hotter temperatures.

3.2.2 Oxy-Natural Gas Studies

As mentioned in the introduction, section 4.1 Introduction, natural gas has a variety of composition depending on the extraction process and location around the world. In collaboration and with additional support from with Southwest Research Institute (SWRI) combustion of an oxy-NatGas mixture in highly diluted carbon dioxide environment was investigated. This data was taken in three pressure ranges: 40, 45, and 50atm.

Table 6: Synthetic natural gas (NatGas) fuel blend used for these experiments (% vol. fraction).

NatGas Fuel	
CH_4	93.00
C_2H_6	4.75
C_3H_8	1.50
iC_4H_{10}	0.35
nC_4H_{10}	0.40

In Table 6, the composition of the natural gas is presented. This synthetic natural gas blend mostly contains methane, CH_4, but also contains small amounts of ethane, C_2H_6, propane, C_3H_8 and two isomers of butane, iC_4H_{10} and nC_4H_{10}, which captures potential liquid natural gas (LNG) gas composition. This fuel was then introduced into a mixture with an oxygen and other diluents, mostly carbon dioxide.

Table 7. This mixture of oxy-natural gas blend for SWRI experiments (% vol. fraction).

Mixture	**ϕ**	**CO_2**	**AR**	**N_2**	**O_2**	**NatGas**	**H_2O**
SWRI	1.00	85.51	6.16	3.31	3.24	1.59	0.19

The oxy-NatGas mixture presented in Table 7 contains the natural gas fuel discussed earlier and an oxygen balance for an equivalence ratio of 1.0. Additionally, small amounts of impurities are introduced: argon, nitrogen, and water, which can occur during air separation of oxygen and recycled through the closed system.

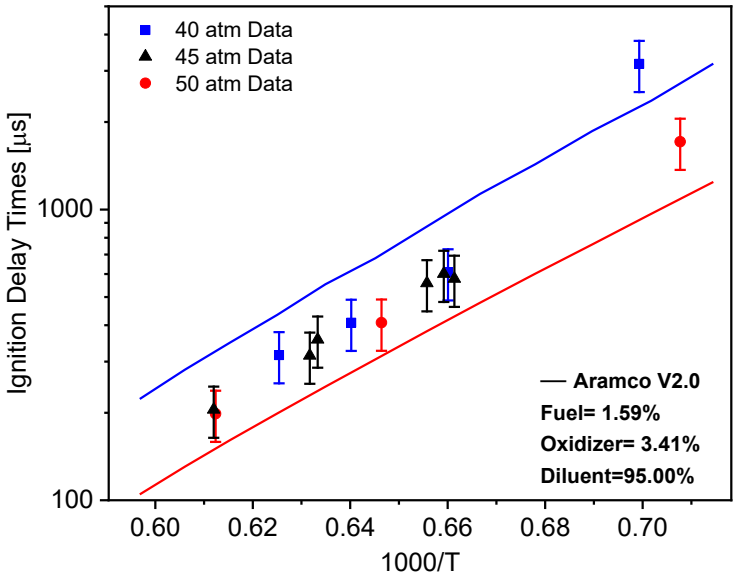

Figure 37. Oxy-NatGas mixtures investigated at multiple pressure ranges compared to model predictions. Aramco predictions at both 40 atm (blue) and 50 atm (red) are shown.

Oxy-NatGas mixture ignition delay time data at three pressure ranges: 40, 45, and 50 atm and a temperature range of 1400K - 1640K are presented in Figure 38. Aramco mechanism predictions at both 40 atm (blue) and 50 atm (red). The model captures the expected trends with respect to temperature and pressure. Most of the data lies within the two bounds of pressure model predictions and is independent of pressure in this range. At the colder range, there is some underprediction of the ignition delay time of an experiment at 40 atm.

3.3 High-Pressure Studies

3.3.1 Oxy-Methane Ignition Data

This study contains ignition delay time data for oxy-methane combustion up to 36.5% CO_2 diluted environment in a shock tube. Table 7 reports the methane mixture that was used in this study. The original mixture, without nitrogen, contains a fixed ratio of CH_4:O_2:CO_2.The ratio was maintained between the fuel, oxygen, and CO_2, while making the mixture contain 50% N_2. The

CO_2 dilution percentage was adjusted to 36.5%, and ϕ, was kept at 1.0. A dilution of nitrogen was necessary to prevent or reduce detonation possibility inside the shock tube. The ratio of the fuel loading (fuel plus oxidizer) to CO_2 concentration remained the same. Additionally, a secondary effect of adding nitrogen is a reduction in bifurcation of the shock wave during the experiments that is caused by high concentrations of CO_2 [95]. Adding nitrogen to the mixture adds an additional species for determining the full chemical kinetic effects, however; the chemical kinetic effects of nitrogen have been more frequently studied and behavior is better captured by available mechanisms [96].

Table 8: Summary of high-pressure methane experimental conditions.

ϕ	X_{CH4}	X_{O2}	X_{CO2}	X_{N2}	P_{avg} [bar]
1.00	0.045	0.090	0.365	0.500	78.0

Experiments were performed around 80 atm for methane oxidation in a CO_2 diluted environment (the composition of the mixture can be seen in Table 8). The mixture was diluted with nitrogen to prevent detonation pressures to exceed material limits behind the reflected shock wave. The maximum relaxation time of this mixture was calculated to be 6.6 μs with available literature. This relaxation time is very minor compared to the ignition delay times reported (> 300 μs). Methane relaxes itself within 0.03 μs even though other relaxation parameters were not available in literature molecules. Since methane has more than 3 atoms there are several degrees of freedom and other molecules interacting with methane will further reduce the relaxation time of the mixture.

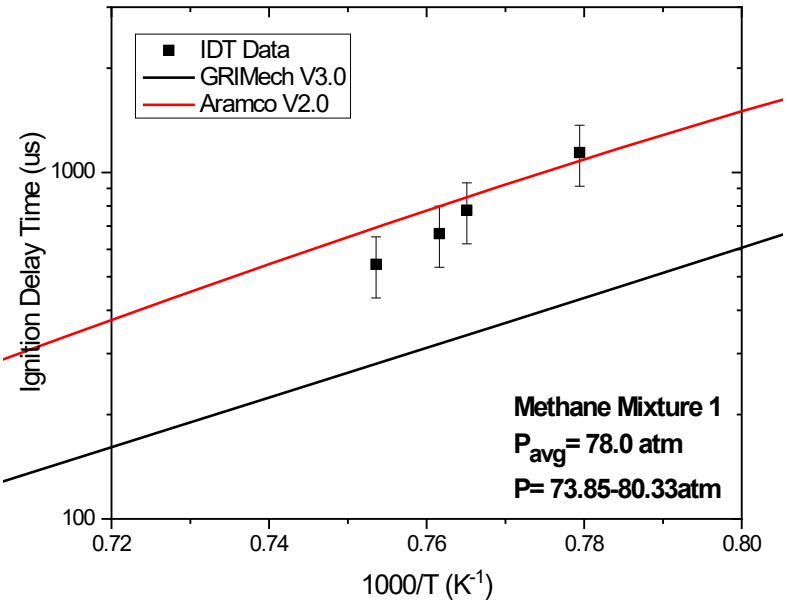

Figure 38. Experimental methane ignition delay times and comparisons with predictions of two mechanisms. The mechanisms were run at the average pressure of 78.0 atm. This mixture contains 4.5% CH_4/ 9% O_2/36.5%CO2/ 50% N2.

The ignition delay times were measured using the slope of the emissions profile for all of these experiments. The temperatures and pressures reported are before ignition occurs. Predictions of the Aramco 2.0 mechanism had very good agreement with the experimental data. At hotter temperatures, there is a deviation and the measured ignition delay time was shorter than the simulated ones. The GRI V3.0 mechanism did not perform very well at these conditions. The model underpredicted the ignition delay times throughout the entire temperature range. The mixture was designed to simulate conditions at stoichiometric equivalence ratio and low fuel loading. Similar observations regarding the Aramco 2.0 mechanism performance for methane were reported earlier at a range of pressures including the supercritical CO_2 conditions [46]. However, for syngas it is a different story [41, 88] and thus the current investigations had more syngas mixtures (see next section).

With methane combustion, an increase in ignition delay time occurred with large CO_2 dilution [54], however, a decrease in ignition delay time occurred in syngas mixtures with similar dilutions [41]. Our previous low [41] and high [88] pressure syngas data observed a shorter ignition delay time than those predicted by models. Also, data showed, contrary to Le Chatelier's principle, an increase in the ignition delay time for the same temperature at higher pressures. It was shown that in syngas, ignition delay time has two reactions competing for the same reactants leading to a higher termination rate relative to the chain branching rate (at high pressures) slowing the oxidation process.

R(1): $H + O_2 (+ M) \rightleftharpoons HO_2 (+ M)$

R(2): $H + O_2 \rightleftharpoons OH + O$

The thermal decomposition of CO_2 is encompassed by the reverse reaction of the following reaction:

R(3): $CO + O (+M) \rightleftharpoons CO2(+M)$

CO_2 decomposition reaction is largely endothermic and requires very high temperatures to impact the ignition delay time. In the range of the experimental data presented, R(3) is not a large contributor. There are several reactions where CO_2, in the reverse reaction, can consume radicals in the combustion process:

R(4): $CO + OH \rightleftharpoons CO_2 + H$

R(5): $CO + O_2 \rightleftharpoons CO_2 + O$

R(6): $CO + HO_2 \rightleftharpoons CO_2 + OH$

Of these reactions, R(5) and R(6) have relatively slow reaction rates in this temperature range, however, R(4) is found to have an impact on ignition chemistry. CO_2 competes for H radicals through the reverse reaction of R(4): $CO + OH \rightleftharpoons CO_2 + H$, which results in a decrease in the concentration of the H radicals (H radicals participate in the chain branching reaction given by R(2))[97]. This is consistent with previous observations of the chemical effect of CO_2 on methane and hydrogen flames [64]. In the same shock tube facility, similar observations were made utilizing methane as the fuel at lower pressures [35, 54]. A reaction pathway analysis of the Methane Mixture 1 shows that before ignition, the most dominant absolute rate of production of CO_2 in the system is the reverse R(4) reaction.

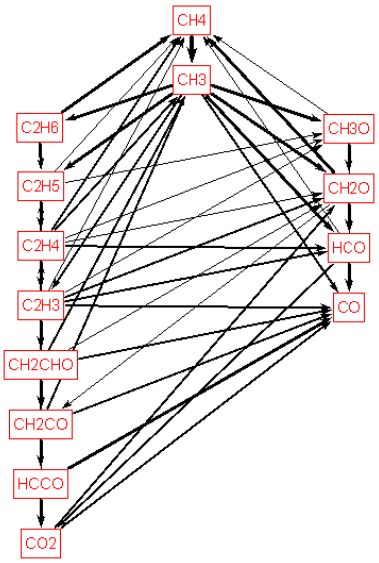

Figure 39. Reaction pathway for Methane Mixture 1 at T= 1307K and P= 79.69 atm (simulations with the Aramco 2.0 mechanism).

The reaction pathway for methane oxidation in highly diluted carbon dioxide is shown in Figure 40. The main reaction pathways for CH_4 consumption are reactions with radical species

(e.g. O, H, OH, etc). The reactions R(7), R(8), and R(9) account for most radical species that have an interaction with CH_4 (for depletion to the CH_3 methyl radical).

R(7): $CH_4 + OH \rightleftharpoons CH_3 + H_2O$

R(8): $CH_4 + O \rightleftharpoons CH_3 + OH$

R(9): $CH_4 + H \rightleftharpoons CH_3 + H_2$

From the methyl radical, two pathways exist. The first reaction is with HO_2 radical to form CH_3O and OH (strictly a temperature dependent reaction). The second reaction is the recombination reaction of two methyl radicals into C_2H_6 (ethane), which occurs as a function of pressure and is a function of the 3rd body collision efficiency of diluent gases. As previously mentioned by the authors earlier in this section and in previous work, CO_2 has a reduced collision efficiency than reported in mechanisms that some models may not fully capture.

3.3.2 Oxy-Natural Gas Studies

Following the mid-pressure natural gas experiments and mechanism predictions presented in 4.2.2 SWRI Oxy-Natural Gas Studies, further investigations were performed with oxy-NatGas at higher pressures. This study investigated several oxy-NatGas mixtures with a variety of equivalence ratios and CO_2 dilutions. Overall, there were eight mixtures with a pressure range of 80 atm – 120 atm and a temperature range of 1340K – 1620K.

Table 9. Mixtures composition of experiments near 100 atm. (% vol fraction)

Equivalence Ratio, ϕ	**1.0**	**0.5**	**1.25**	**1.5**	**2.0**	**1.0 D1**	**1.0 D2**	**1.0 D3**
Fuel	1.68	0.84	2.1	2.52	3.36	1.68		
O_2	3.62							
CO_2	44.70	45.54	44.28	43.86	43.02	29.79	14.90	59.58
Ar	50.00					68.53	83.42	38.74

The mixtures in this work are presented in Table 9; the oxygen concentration of all eight mixtures remained constant at 3.6%. The baseline mixture has an equivalence ratio of 1.0, 44.7% carbon dioxide, and 50% argon dilution. Some of the additional mixtures investigated altered the equivalence ratio by changing the fuel concentration while maintaining the same oxygen concentration from 0.5, 1.25, 1.5, and 2.0. The goal of this was to determine the impact of the equivalence ratio on the ignition delay time. Additional mixtures kept the fuel and oxygen constant with an equivalence ratio of 1.0 but changed the carbon dioxide concentration in three ways: $1/3^{rd}$ reduction of carbon dioxide, $2/3^{rd}$ reduction of carbon dioxide, and $1/3^{rd}$ increase of carbon dioxide. The goal of this was to determine the effects of carbon dioxide on the ignition delay time.

The ignition delay time measurement of the shock tube was defined as the time interval between the arrival of the reflected shockwave and the onset of the ignition at the measurement location. The arrival, or time zero, was determined as the half-way point between the incident and reflected shock waves. This corresponds well with more accurate methods, such as using a laser schlieren, as discussed in section 2.2.1.1 Bifurcation. The onset of the ignition time, also known as the slope method, was determined by evaluating the time-history of the emissions, finding the steepest rise, and then extrapolating down to the baseline measurement. This method was described in a previous study [85]. Emissions were measured using a Newport 2032 Large Area Optical Receiver with a filter centered at 307 nm for measuring OH* from combustion.

Modeling was performed using CHEMKIN PRO [98] assuming a closed homogenous batch reactor with constant volume and internal energy (V, U). The model used was AramcoMech V2.0 [96] due to it containing C4 hydrocarbons which are part of the natural gas fuel studied. GRIMech V3.0, another natural gas mechanism, only contains up to C2 hydrocarbons and therefore was not used. In CHEMKIN PRO, the ignition delay time was calculated using a similar method for calculating the ignition delay time on the shock tube experiments by using the OH concentration time-history. This method was previously used for CO_2 diluted mixtures [35, 41, 54] and in previous studies [85, 86]. A 20% uncertainty in the ignition delay time is estimated for current measurements. The amount of available test time was determined when the expansion waves from the driver end reached the test location resulting in an end to the constant temperature and pressure conditions.

3.3.2.1 Ignition Delay Time

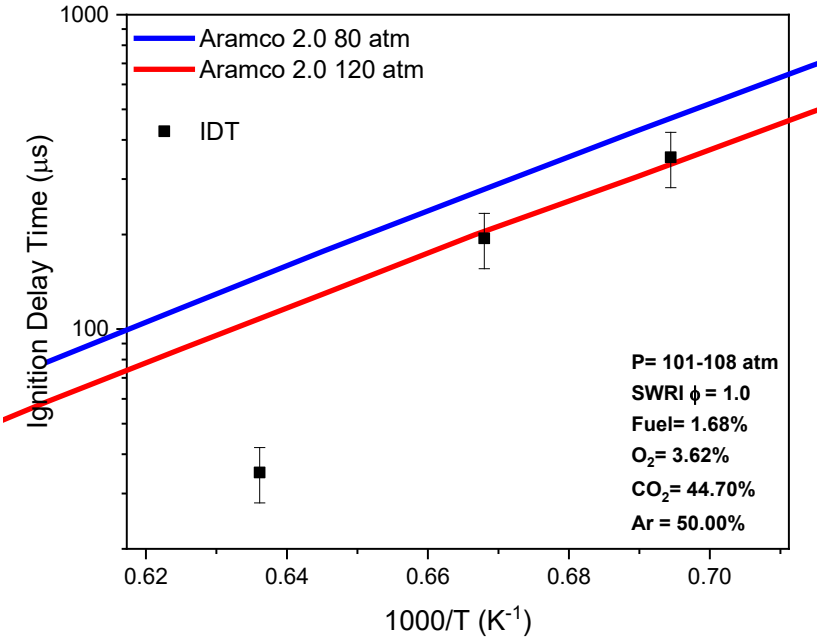

Figure 40. Baseline SWRI oxy-NatGas mixture.

Ignition delay time data was collected for the baseline mixture shown in Figure 41. The temperature range was 1440 K - 1550K and a pressure range of 101- 108 atm. Aramco model predictions were evaluated at both 80 and 120 atm to determine differences in ignition delay time due to pressure. Aramco was able to capture the expected trend with respect to temperature. At the colder range of the data, there is good agreement with the 120 atm predictions and within the uncertainty range, in between the two models. At the hottest data point, the models overpredict the ignition delay time.

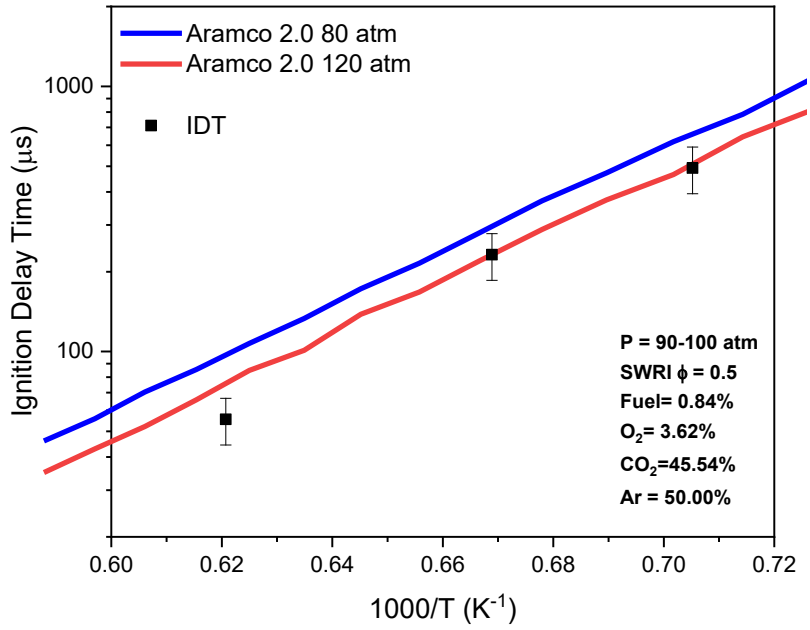

Figure 41. Equivalence ratio = 0.5 oxy-NatGas mixture.

Ignition delay time data was collected for the equivalence ratio = 0.5 mixture shown in Figure 42. The temperature range was 1400 K - 1600 K and a pressure range of 90 - 100 atm. Aramco model predictions were evaluated at both 80 and 120 atm to determine the differences in ignition delay time due to pressure. Aramco was able to capture the expected trend with respect to temperature. At the colder range of the data, there is good agreement with both models within the

uncertainty. As seen in the previous section, the hottest data point is overpredicted by both pressure models.

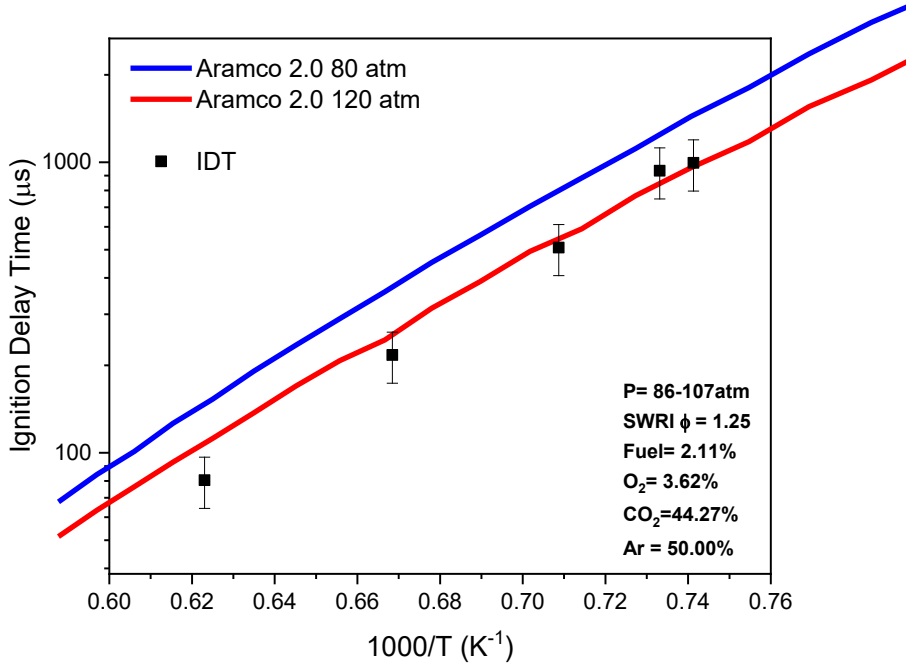

Figure 42. Equivalence ratio = 1.25 oxy-NatGas mixture.

Ignition delay time data was collected for the equivalence ratio = 1.25 mixture shown in Figure 43. The temperature range was 1350 K - 1600 K and a pressure range of 86 - 107 atm. Aramco model predictions were evaluated at both 80 and 120 atm to determine the differences in ignition delay time due to pressure. Aramco was able to capture the expected trend with respect to temperature. At the colder range of the data, there is good agreement with both models within the uncertainty. As seen in the previous section, the hottest data point is overpredicted by both pressure models.

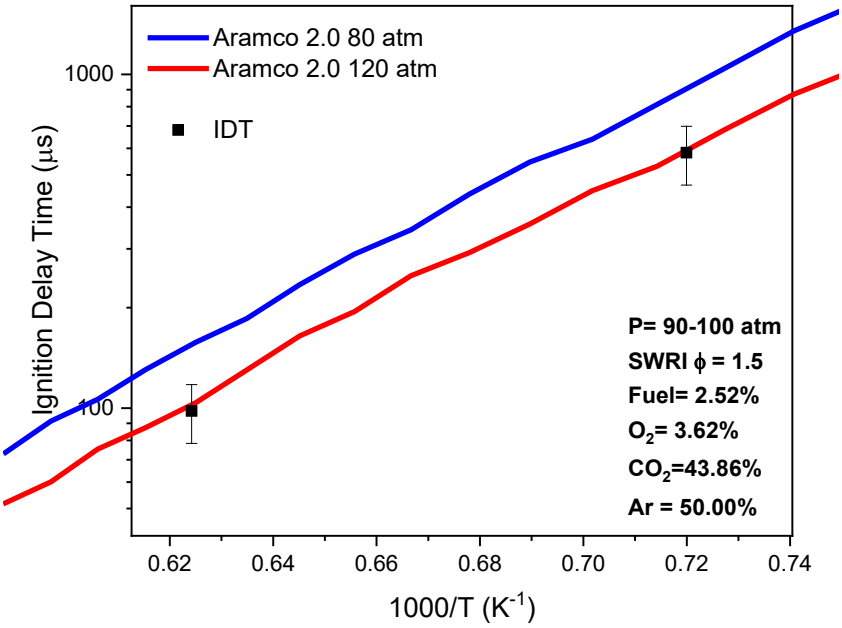

Figure 43. Equivalence ratio = 1.5 oxy-NatGas mixture.

Ignition delay time data was collected for the equivalence ratio = 1.5 mixture shown in Figure 44. The temperature range was 1400 K - 1600 K and a pressure range of 90-100 atm. The Aramco model predictions were evaluated at both 80 and 120 atm to determine the differences in ignition delay time due to pressure. Aramco was able to capture the expected trend with respect to temperature. There is good agreement with predictions by the 120 atm model and within the uncertainty for some pressure deviation.

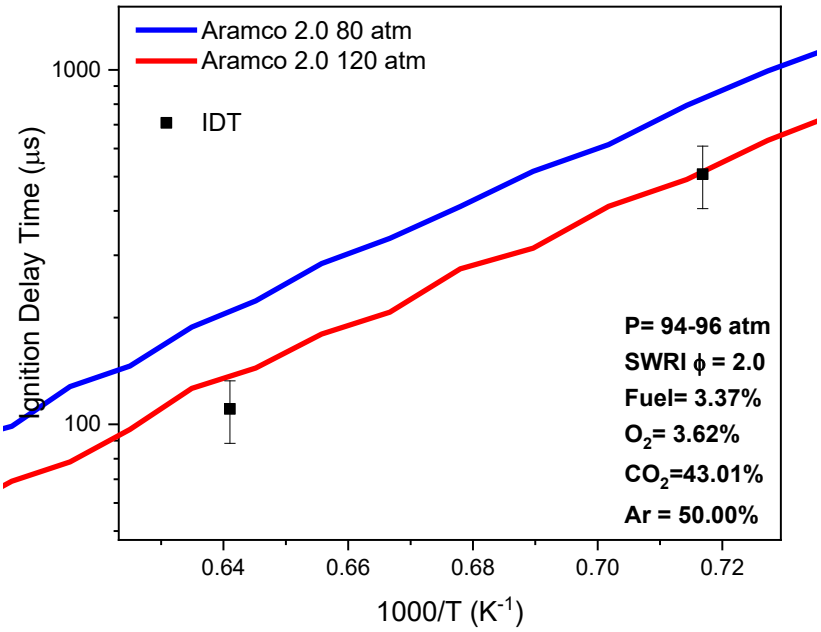

Figure 44. Equivalence ratio = 2.0 oxy-NatGas mixture.

Ignition delay time data was collected for the equivalence ratio = 2.0 mixture shown in Figure 45. The temperature range was 1400 K - 1600 K and a pressure range of 94-96 atm. The Aramco model predictions were evaluated at both 80 and 120 atm to determine the differences in ignition delay time due to pressure. Aramco was able to capture the expected trend with respect to temperature. There is agreement with the 120 atm model, however the pressure range of these experiments should align closer to the 80 atm predictions.

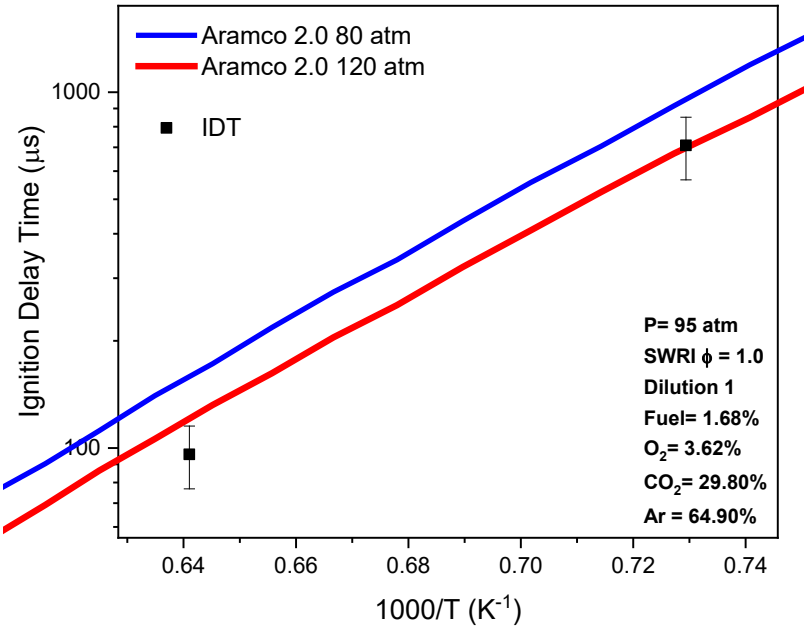

Figure 45. Dilution 1 relative to baseline oxy-NatGas mixture.

Ignition delay time data was collected for the Dilution 1 mixture shown in Figure 46. The temperature range was 1400 K - 1600 K and a pressure of 95 atm. Aramco model predictions were evaluated at both 80 and 120 atm to determine the differences in ignition delay time due to pressure. Aramco was able to capture the expected trend with respect to temperature. There is agreement with the model at both the hot and colder range with the 120 atm model, however the pressure range of these experiments should align closer to the 80 atm predictions.

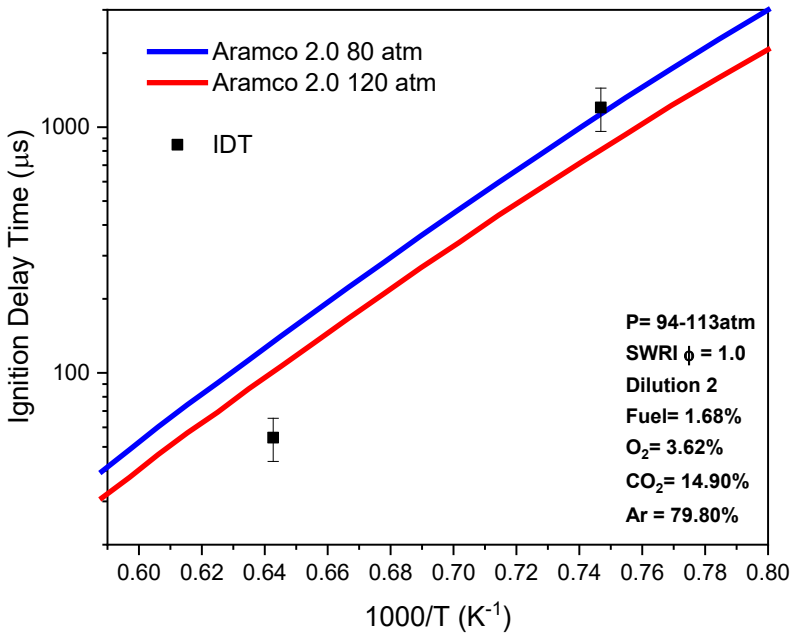

Figure 46. Dilution 2 relative to baseline oxy-NatGas mixture.

Ignition delay time data was collected for the Dilution 2 mixture shown in Figure 47. The temperature range was 1350 K - 1600 K and a pressure range of 94 - 113 atm. Aramco model predictions were evaluated at both 80 and 120 atm to determine the differences in ignition delay time due to pressure. Aramco was able to capture the expected trend with respect to temperature. There is agreement with the model at and colder range with the 80 atm model, however both models overpredict the ignition delay time for the hotter experiment.

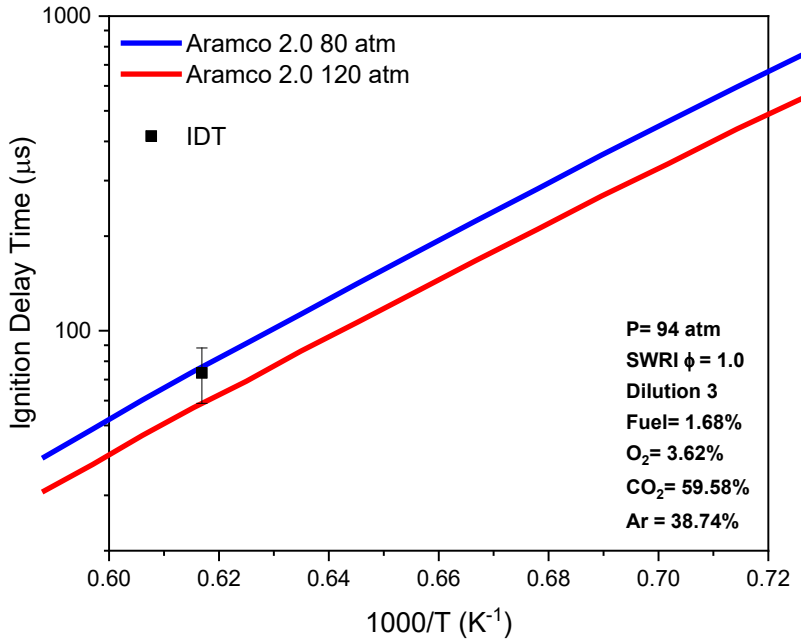

Figure 47. Dilution 3 relative to baseline oxy-NatGas mixture.

Ignition delay time data was collected for the Dilution 3 mixture (shown in Figure 48) at a temperature of 1600 K and pressure of 94 atm. The Aramco model predictions were evaluated at both 80 and 120 atm to determine the differences in ignition delay time due to pressure. Aramco was able to capture the expected trend with respect to temperature. There is agreement with the models at both 80 and 120 atm within the uncertainty.

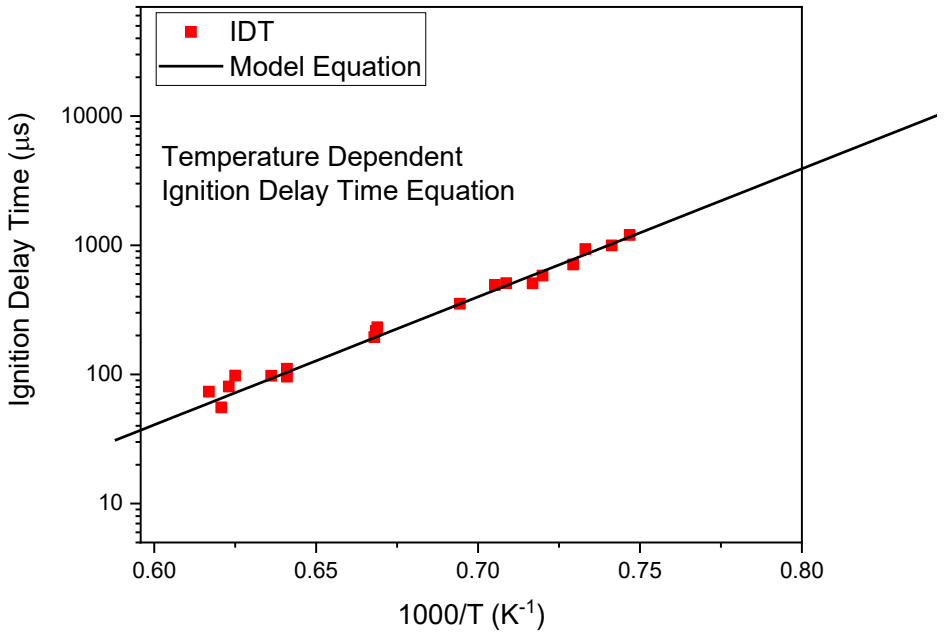

Figure 48. Modeling the ignition delay time of the SWRI experiments. Adj R^2= 0.984

The ignition delay time of the measurements was modeled using a simple exponential equation.

$$\tau_{IGN} = 4.604 \cdot 10^5 \cdot \exp(\frac{-43.35}{R_U \cdot T}) \quad (1)$$

Where R_U = $1.987 \cdot 10^{-3}$ kcal/(mol·K). This equation captures the entire behavior of all mixtures in this study with only a temperature dependence. The reason this is occurring is that the oxygen concentration primarily drives the ignition delay time. Although these data points are very similar, comparison with the model predictions was critical.

3.3.2.2 Reaction Pathway and Sensitivity Analysis

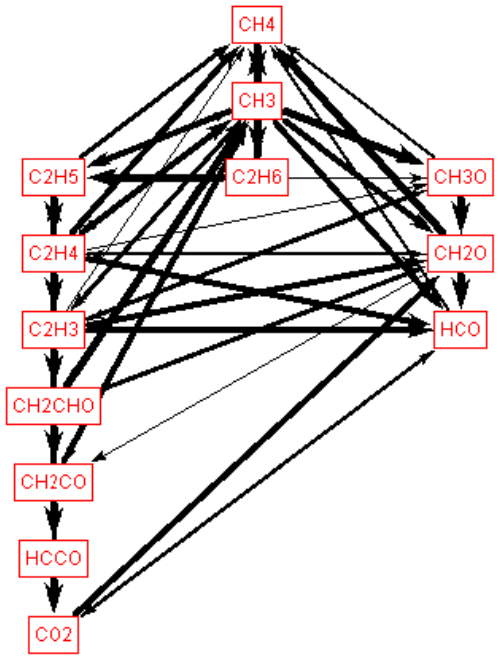

Figure 49. Reaction pathway analysis for baseline mixture at 1500K and 100atm.

With methane combustion, an increase in ignition delay time occurred with large CO_2 dilution [54], however, a decrease in ignition delay time occurred in syngas mixtures with similar dilutions [41]. Our previous low [41] and high [88] pressure syngas data observed a shorter ignition delay time than those predicted by models.

The reaction pathway for methane oxidation in highly diluted carbon dioxide is shown in Figure 50. The main reaction pathways for CH_4 consumption are reactions with radical species (e.g. O, H, OH, etc). The reactions R(7), R(8), and R(9) account for most radical species that have an interaction with CH_4 (for depletion to the CH_3 methyl radical).

R(7): $CH_4 + OH \rightleftharpoons CH_3 + H_2O$

R(8): $CH_4 + O \rightleftharpoons CH_3 + OH$

R(9): $CH_4 + H \rightleftharpoons CH_3 + H_2$

From the methyl radical, two pathways exist. The first reaction is with HO_2 radical to form CH_3O and OH (strictly a temperature dependent reaction). The second reaction is the recombination reaction of two methyl radicals into C_2H_6 (ethane), which occurs as a function of pressure and is a function of the 3rd body collision efficiency of diluent gases. As previously mentioned by the authors earlier in this section and in previous work, CO_2 has a reduced collision efficiency than reported in mechanisms which some models may not fully capture. Further investigation is warranted.

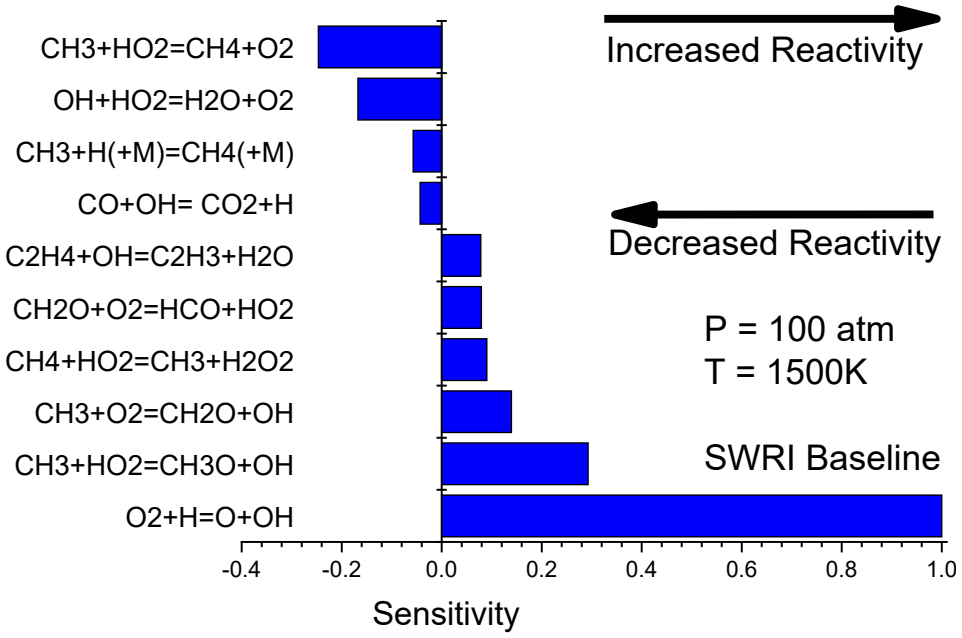

Figure 50. Normalized brute force sensitivity analysis on ignition delay time for baseline mixture at 1500 K and 100 atm.

A brute force sensitivity analysis was done to evaluate the top ten reactions for reactivity of ignition delay time on all eight mixtures. The top ten reactions determining the ignition delay time are the same for the eight mixtures, so only the baseline is shown. As shown in the previous

section, the ignition delay time is primarily a function of temperature in this range. There is only one pressure dependent reaction in the system R(4): CH_3+ H(+M) = CH_4(+M). This reaction rate has been studied in the past [99, 100] but has never been studied with high CO_2 dilution or at the pressures of these experiments.

CO_2 has a reduced third body collision efficiency, which will lead to different behavior, especially relative to nitrogen or argon, which are traditional bath gasses [51, 59] used in shock tube studies. CO_2 has traditionally been treated as a product of combustion; however, it has been experimentally shown that CO_2 is not an inert bath gas in the ignition of syngas combustion (i.e., CO_2 is both a reactant as well a product). Also, CO_2 competes for H radicals through the reverse reaction of R(3): CO + OH ⇌ CO_2 + H), which results in a decrease in the concentration of the H radicals (H radicals participate in the chain branching reactions). This is consistent with previous observations of the chemical effect of CO_2 on methane and hydrogen flames [64]. In the same shock tube facility, similar observations were made utilizing methane as the fuel [35, 54]. The collision efficiencies of CO_2 and reactions involving CO_2 will need crucial examination in the future for improving the predictions by mechanisms for data taken in this study at high pressures.

3.3.2.3 Impact of Impurities on Ignition Delay Time

Impurities in the combustion process play an important role in ignition characteristics. Many impurities are found in untreated natural gas and are typically removed before transportation [101]. Impurities can change the ignition delay time in a system and cause instabilities. Previous work on established feedstock impurities such as H_2S (hydrogen sulfide), NH_3 (ammonia), SO_2 (sulfur dioxide), and NO_2 (Nitrogen dioxide) [102-104] found significant deviation to the ignition delay time with only ppm levels introduced. In a closed cycle, such as the sCO_2 cycle, impurities can build up in a system over time altering both the performance and stability of these systems. In

the closed sCO_2 cycle, the nitrogen impurities will be introduced into the system from the oxygen feedstock which is produced from an air-separating unit (ASU). This nitrogen will undergo the thermal NO_X (sum of NO, NO_2, N_2O) chemistry and create NO_X in the combustor. Some investigations of these impurities have been done at pressures ranging up to pressures of 28 atm[105, 106], but none have been performed at near 100 atm. These studies found that N_2O impurities decreased the ignition delay time in the system.

Table 10. Mixture composition of the baseline mixture and impurity mixture.

	Baseline	**Impurity**
Fuel	1.68	1.68
O_2	3.62	3.62
CO_2	44.70	44.70
Ar	50.00	49.00
N_2O	N/A	1.00

In this work, the mixtures are presented in Table 10. The baseline mixture of the previous section was compared with a similar mixture containing 1% N_2O impurity, the difference being 1% Ar. N_2O is one of three major components of regulated NO_X emissions that is produced in high-temperature environments and must be evaluated to determine its impact on ignition delay time.

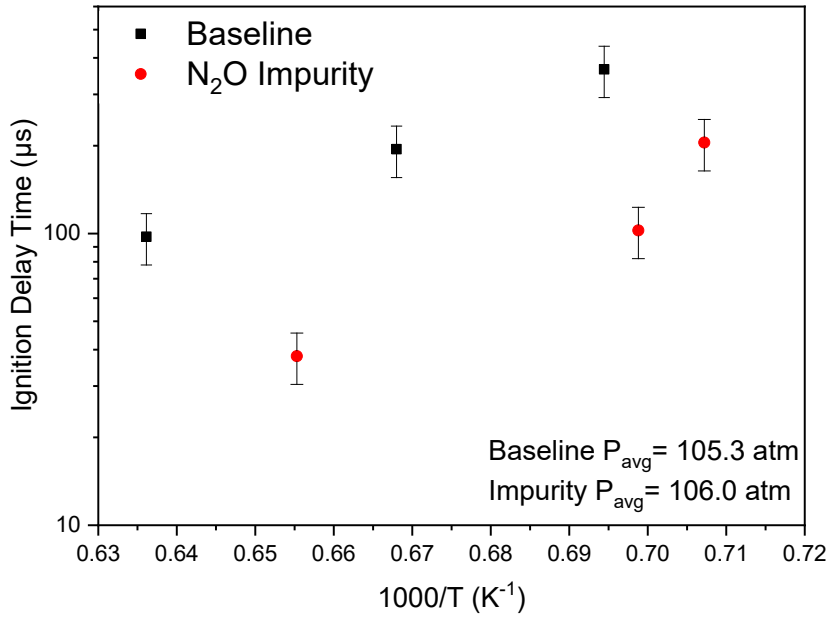

Figure 51. The ignition delay time of the baseline mixture vs. the impurity mixture.

In Figure 52, the baseline mixture has a temperature range of 1440K – 1572 K, and the impurity mixture had a temperature range of 1414 K - 1526 K, nearly 86 K of direct overlap. The average pressure of the baseline mixture was 105.3 atm, and the impurity mixture had an average pressure of 0.6%. The ignition delay time of the impurity mixture was significantly lower than the baseline mixture throughout the entire range of temperature. These results are consistent with the findings in previous studies at lower pressures [105, 106]. These authors concluded that the additional oxygen in the system due to the impurities reduced the ignition delay time by adding additional oxidation pathways for methane. Additional studies at a larger temperature range and pressures would be necessary to capture the full chemical kinetic effects. Additionally, investigations of other common impurities will be necessary for the development of accurate chemical kinetic models.

CHAPTER 4: CHEMICAL KINETIC MECHANISM FOR sCO_2 COMBUSTION

4.1 Introduction

The chemical kinetic mechanism is a record of a sequence of guessed elementary reaction paths that could take place as the reactants are converted into products. It is known that the Arrhenius constants defined in the chemical mechanisms, i.e., pre-exponential factor, temperature exponent and activation energy, are derived from fundamental experiments or detailed theoretical based calculations [107, 108]. Under the absence of such studies (calculations or experiments), the rate constants are typically estimated based on similarity with other known reactions [109]. Oftentimes, optimization of rate constants of the elementary reactions within the allowed uncertainty may be needed to match the mechanism's performance with a wide set of experiments [110]. These constants are valid only within the operating conditions in which they are defined, hence cannot be used outside the domain of validated conditions. Also, there is no assurance that the mechanism validated under certain conditions is physically correct. Therefore, a good mechanism must have physically correct rate constants along with validation with the experiments.

In fact, there are well testified chemical kinetic mechanisms for low pressure and low CO_2 diluted conditions. But, the knowledge of reactions pathways and their rate constants at sCO_2 combustor operating conditions are scanty. The current knowledge base of sCO_2 combustion kinetics can be seen in Figure 52: Current knowledge base of gas phase chemical kinetics (Source: [65]).

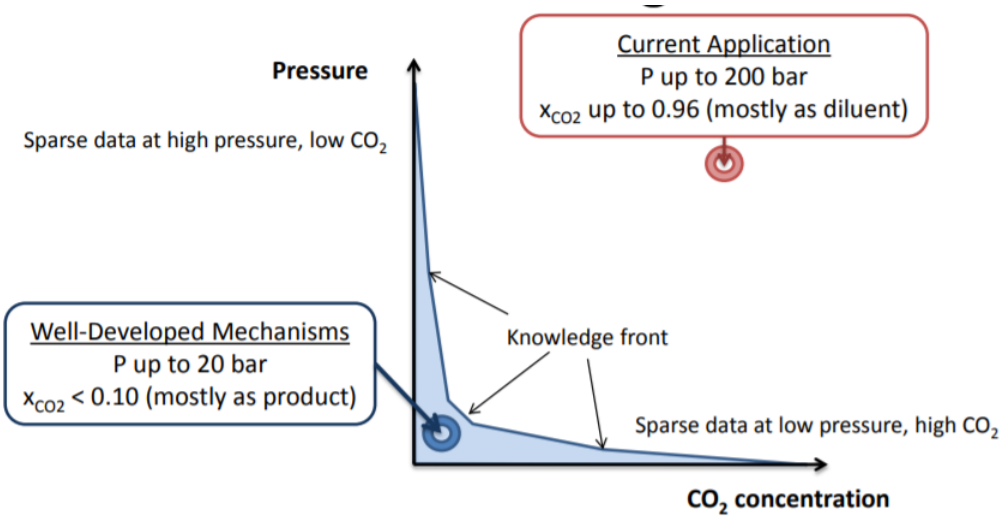

Figure 52: Current knowledge base of gas phase chemical kinetics (Source: [111])

Therefore, it is very important to develop a chemical kinetic mechanism for sCO_2 applications. In the current work, a base mechanism which closely predicts the sCO_2 combustion behavior (including supercritical solvent effects) is identified in the initial sections of this chapter and a skeletal mechanism is developed by eliminating unwanted reactions and species from that base mechanism. Finally, rate constants determined [112-115] using quantum chemistry and molecular dynamic approaches for sCO_2 conditions are implemented in that mechanism to derive a new sCO_2 combustion mechanism. Finally, a comparison is made between the performance of the base mechanism and the derived mechanism with the available sCO_2 shock tube conditions.

4.2 The effect of equation of state and base mechanism

As discussed in the previous chapter, at supercritical pressures the ideal gas assumption is no longer valid to predict the state of a system, because at these pressures the intermolecular forces are significant, and they must be accounted while calculating the chemical, thermodynamic properties and the state of the system. Therefore, choosing an appropriate EOS is very important.

In the previous chapter various equation of states are compared for a constant pressure system and in this chapter the EOSs are compared for a constant volume system. Also, the base mechanism for sCO_2 application is identified by comparing two prominent mechanism such as, GRI 3.0 [116] and Aramco 2.0 mechanisms [117, 118] with experimental shock tube ignition delay time data [119].

Comparing the chemical kinetic mechanism with IDTs of shock tube data is one standard practice to validate a chemical kinetic mechanism. However, an unanswered question in the literature is "which EOS needs to be used to simulate the IDTs of supercritical combustion?". In the current section, the IDTs are calculated by van der Waals type of EOSs by using both the Aramco 2.0 and GRI 3.0 mechanisms. Further, the calculated IDTs are compared to understand the effect of EOS on IDTs. Figure 53, shows the absolute deviation of simulated IDTs with respect to experiments [120]. Here, the constant volume reactor is simulated with CHEMKIN-RG by using various real gas EOS. In Figure 53, the left column of the plot consists of the IDTs calculated by the Aramco 2.0 mechanism while the right plot is by the GRI 3.0 mechanism. The vertical axis of each plot represents the absolute deviation of the simulated IDTs with respect to the experiments. It should also be noted that, each subplot has five absolute deviation values (for five EOSs considered) and also five mean values of those absolute deviations. Each row in this plot corresponds to a particular molar ratio of fuel and oxidizer used in the shock tube experiments.

The subplots (1,1) and (1,2) in Figure 53 corresponds to stoichiometric hydrogen mixture (mixture-1, see also Table 3-3) diluted with CO_2. Here, it must be noted that the Aramco 2.0 has better performance then GRI 3.0. For the GRI 3.0 mechanism all simulation data points are clearly beyond the uncertainty of experiments, which is reported to be 20% [119]. However, for the subplot (1,1) some of the EOSs are within the uncertainty limits except SRK EOS. Also, from both

subplots (1,1) and (1,2) it can be observed that, the estimation of each IDT is significantly different from each other.

The subplots (2,1) and (2,2) in Figure 53 represent a lean methane mixture (mixture-2, Table 3-3) diluted with CO_2. Here, both the IDTs of Aramco 2.0 and GRI 3.0 are predicting the experimental IDTs reasonably good. Also, the selection of EOS is not impacting the IDTs significantly as in the case of H_2 and O_2 mixture (mixture-1). Further, the subplots (3,1) and (3,2) in Figure 53 represents the stoichiometric methane mixture (mixture-3) heavily diluted with CO_2. It can be seen that the GRI 3.0 is poorly predicting the IDTs (compared to Aramco 2.0) and all IDTs predicted by the Aramco 2.0 mechanism are within the experimental uncertainties. Also, interestingly the IDTs are not much impacted by the selection of EOS. The maximum difference among the EOS is less than 10%, which is less than the experimental uncertainty.

The EOS has significant impact on mixture-1, but not on mixtures-2 and 3. The main combustion product of mixture-1 is H_2O and for mixture-2 and 3 it is both CO_2 and H_2O. The critical pressure of H2O (~220 atm) is approximately three times higher than the CO_2 (~74 atm). Hence, the higher amount of H_2O in the products of mixture-1 increases the resultant mixture critical point. It is known that, the van der Waal's type EOSs deviate among them largely near to critical point because close to critical point the gradients are very high. However, in the case of mixtures-2 and 3, the formation of CO_2 further reduces the overall critical point. Hence, the EOSs has smaller deviation.

Therefore, as far as the constant volume reactor IDTs are concerned (for mixture-2 and 3), the equation of state does not have a notable effect, because the deviation of real gas IDTs are within 20% from the IGA IDTs. Over all, in this section it is re-confirmed that the performance of the Aramco 2.0 mechanism is better (compared to GRI 3.0) for estimating the supercritical CO_2

shock tube experiments. Therefore, in this work, reduced skeletal mechanism are derived from the Aramco 2.0 mechanism and then the sCO_2 reaction rate constants are substituted.

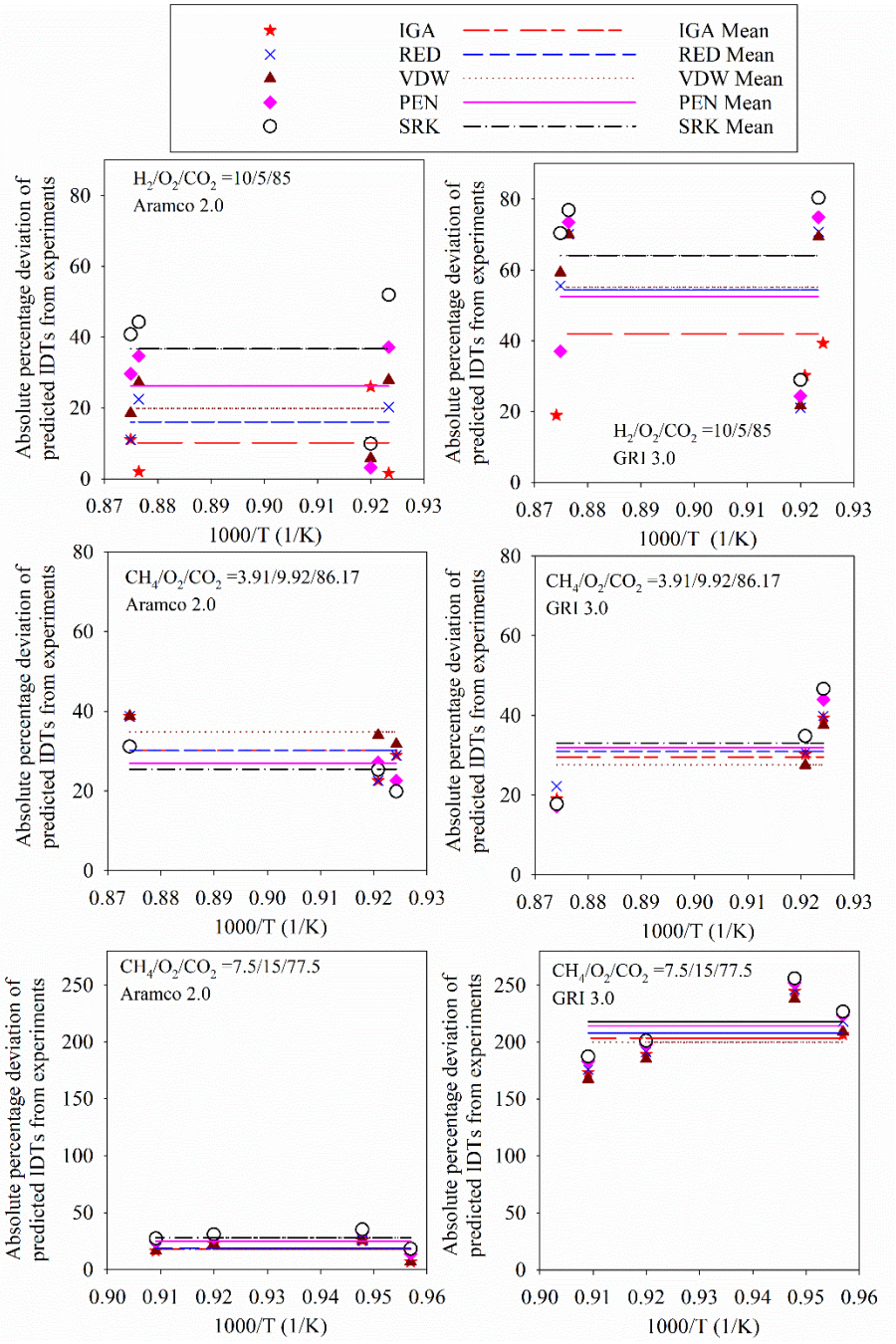

Figure 53: Comparison of sCO_2 shock tube ignition delay times [120] with the Aramco 2.0 and GRI 3.0 by various EOSs

4.3 The skeletal mechanism

As discussed in the introductory section, the usage of detailed mechanisms in CFD simulations is not practical due to associated expensive computational power. Therefore, a reduced skeletal mechanism is of much interest to the combustion CFD community. An automated computer program called CHEM-RC from the work of [121, 122] is used in order to eliminate unimportant species. This computer model uses the Multi-Generation Path Flux Analysis (PFA) method to identify the important species to the targeted species. The PFA method is an extension of Direct Relation Graph (DRG) method and Direct Relation Graph with Error Propagation (DRGEP) methods [123] and proven to capture better flux . The previous section confirms that Aramco 2.0 mechanism is better suitable for sCO_2 simulations compared to GRI 3.0. Therefore, the Aramco 2.0 mechanism is used as a source for further reduction process. The full Aramco 2.0 mechanism consists of 493 species and 2714 reactions for fuels up to C6. A total of five reduced mechanisms are generated from this detailed mechanism by using CHEM-RC by varying the threshold values (a parameter used in PFA to choose the reaction paths). The higher the threshold value the smaller will be the reduced mechanism. The detailed information on the threshold value can be found in [121]. Also, various mixtures from lean to rich and moderate to highly CO_2 diluted conditions have been given to CHEM-RC as inputs (conditions shown in Table 11). The smaller the number of species, the lower will be the computational time for CFD simulations. Therefore, initially the reduction process started with a 15-species mechanism and the threshold values in CHEM-RC were reduced gradually to obtain all the necessary species which are needed to validate the targeted mixture conditions.

Here, the performance of a reduced mechanism is compared with respect to the detailed Aramco 2.0. In the current work, the performance of the seven reduced mechanisms, namely, 15-species, 16-species, 19-species, 21-species, two 22-species and 23-species is discussed.

The species in these mechanisms are tabulated in Table 12. Here, it should be noted that, the two 22 species mechanisms as mentioned in the table are derived from the 23-species mechanism by removing C_2H_3 and CH_3OH respectively. Basically, this test has been performed to understand the importance of these species in estimating the IDTs at lean conditions.

Figure 54 shows the comparison of IDT estimation of reduced mechanisms against those of the detailed mechanism for mixture-3 (stoichiometric mixture). It should be mentioned that the IDTs are estimated based on IGA EOS. Here, IGA EOS is used because, as discussed in the previous section, significant effect of real gas EOSs is not observed for mixture-2 and 3. It should be noted that the vertical axis is shown in logarithmic scale because the IDTs of the 15-species mechanism are deviating largely from the detailed mechanism predictions. Every other mechanism is performing very close to the detailed mechanism. The 16-species and 15-species mechanisms differ only by the species hydrogen peroxide (H_2O_2) and its associated reactions. Interestingly, this one species has changed the prediction of IDTs by as much as 50 times. The main reason is that for auto ignition of hydrocarbon and oxygenated fuels, the hydrogen atom (H) abstraction by hydroperoxyl radical HO_2 (forming H_2O_2) is an important reaction class in the autoignition of fuels, particularly at low-to-intermediate temperatures in the range 600-1300 K [124]. The role of the hydroperoxide radical, HO_2, in high-pressure ignition phenomena is well established, as is the role of hydrogen peroxide decomposition [125].

A rate of production (ROP) and sensitivity analysis at stoichiometric, low temperature conditions is shown in Figure 55. It illustrates that the reaction RR-1 is the second prominent reaction for CH_4 consumption:

$CH4+HO_2 \Leftrightarrow CH_3+H_2O_2$ RR- 1

Figure 56 shows that, the H_2O_2 is formed in the constant volume reactor even before auto-ignition starts and it is due to RR-2. Therefore, the omission of H_2O_2 in the 15-species mechanism has significantly delayed the interaction of CH_4 and HO_2 and delayed the methane consumption and formation of CH_3, hence the IDTs are delayed. Also, it must be noted that the accumulated H_2O_2 reacts with "+M" to produce two OH radicals and it is responsible for the bulk of heat release at high-pressure and high-temperatures. The detailed description of this phenomenon can be obtained in [125].

$H_2O_2(+M) \Leftrightarrow OH+OH\ (+M)$ RR- 2

Therefore, the 16-species as shown in Table 12 are the minimum required in a reduced mechanism to estimate the IDTs of a highly CO_2 diluted, stoichiometric methane mixture. Also, there could be possibilities of reducing the species number further by other mechanism reduction methods than PFA (e.g., [126, 127]). But, it must be remembered that the PFA method in this analysis is considered to capture the maximum path flux during the reduction process. Hence, other methods are not explored. Further, the 15-species mechanism is not considered during IDTs comparison of lean mixture (mixture-2) and hydrogen mixture (mixture-1).

Figure 57 compares the lean mixture (mixture-2) IDTs estimated by 16, 19, 21, two 22-species and 23-species mechanism with those of the detailed mechanism. It is interesting to note that none of the reduced mechanisms below or equal to 21 species are able to predict the lean mixture IDTs. The 16 and 19-species mechanisms estimate almost similar IDTs. Further, the addition of two more species C_2H_5 and CH_2OH species to 19-species mechanism has slightly

delayed the IDTs. However, this 21-species mechanism is still far from the detailed mechanism predictions and shows faster ignition. At the same time, the 23-species mechanism is predicting the IDTs of mixture-2 almost same as the detailed Aramco 2.0 mechanism. The two additional species in the 23-species mechanism compared to 21-species mechanism are CH_3OH and C_2H_3. These two species significantly delayed auto-ignition under lean conditions and matches the 23-species mechanism prediction with the detailed Aramco 2.0 (when compared to the predictions from the 21-species mechanism).

Table 11: The parameters chosen used in CHEM-RC to reduce the mechanism

CHEM-RC parameters	Value chosen
Mixture conditions	$CH_4/O_2/CO_2$ 1. 1/2/35 (stoichiometric- high CO_2 dilution) 2. 1/2/16.5 (stoichiometric- low CO_2 dilution) 3. 1/2.5/40 (lean- high CO_2 dilution) 4. 1/2.5/20 (lean- low CO_2 dilution) 5. 1/0.84/20 (rich-high CO_2 dilution) 6. 1/0.84/10 (rich-low CO_2 dilution)
Threshold values	0.50 to 0.95
Initial temperature	800 K to 1500 K
Pressure	250 atm. to 350 atm.

Table 12: The list of species in the reduced mechanisms

Species. No	23 species	22 species (with CH3OH)	22 species (with C2H3)	21 species	19 species	16 species	15 species
1	H2	H2	H2	H2	H2	-	-
2	H	H	H	H	H	H	H
3	O2	O2	O2	O2	O2	O2	O2
4	O	O	O	O	O	O	O
5	H2O	H2O	H2O	H2O	H2O	H2O	H2O
6	OH	OH	OH	OH	OH	OH	OH
7	H2O2	H2O2	H2O2	H2O2	H2O2	H2O2	-
8	HO2	HO2	HO2	HO2	HO2	HO2	HO2
9	CO	CO	CO	CO	CO	CO	CO
10	CO2	CO2	CO2	CO2	CO2	CO2	CO2
11	CH4	CH4	CH4	CH4	CH4	CH4	CH4
12	CH3	CH3	CH3	CH3	CH3	CH3	CH3
13	CH3O2H	CH3O2H	CH3O2H	CH3O2H	CH3O2H	CH3O2H	CH3O2H
14	CH3O2	CH3O2	CH3O2	CH3O2	CH3O2	CH3O2	CH3O2
15	CH3OH	CH3OH	-	-	-	-	-
16	CH3O	CH3O	CH3O	CH3O	CH3O	CH3O	CH3O
17	CH2OH	CH2OH	CH2OH	CH2OH	-	-	-
18	CH2O	CH2O	CH2O	CH2O	CH2O	CH2O	CH2O
19	HCO	HCO	HCO	HCO	HCO	HCO	HCO
20	C2H6	C2H6	C2H6	C2H6	C2H6	-	-
21	C2H5	C2H5	C2H5	C2H5	-	-	-
22	C2H4	C2H4	C2H4	C2H4	C2H4	-	-
23	C2H3	-	C2H3	-	-	-	-

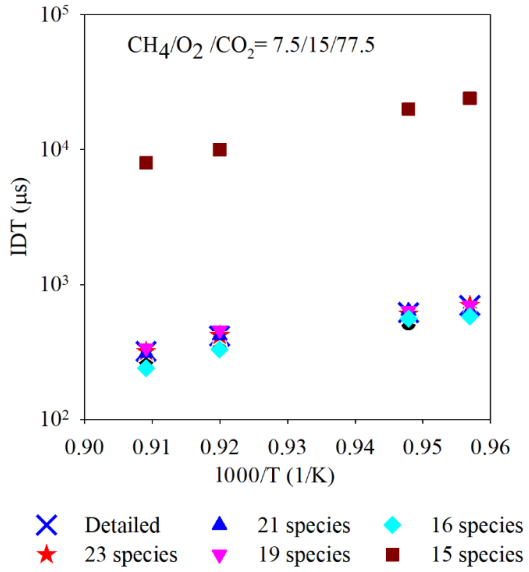

Figure 54: Comparison of IDTs (stoichiometric mixture) of the detailed Aramco 2.0 and reduced species mechanisms

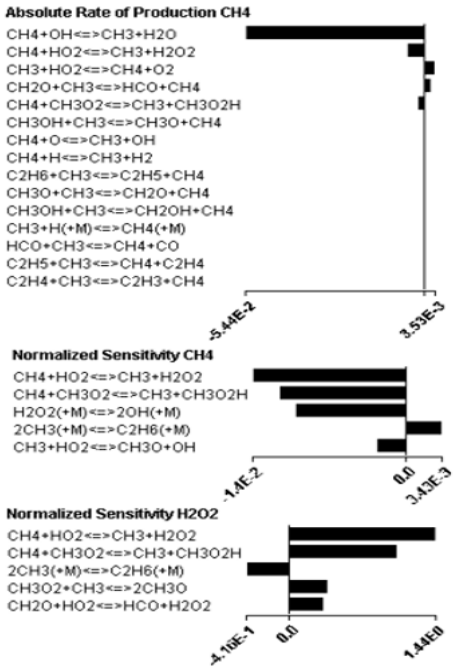

Figure 55: The absolute rate of production of CH_4 and sensitivity of CH_4 and H_2O_2 at Tinl=1100 K, Pinl=285.5 atm

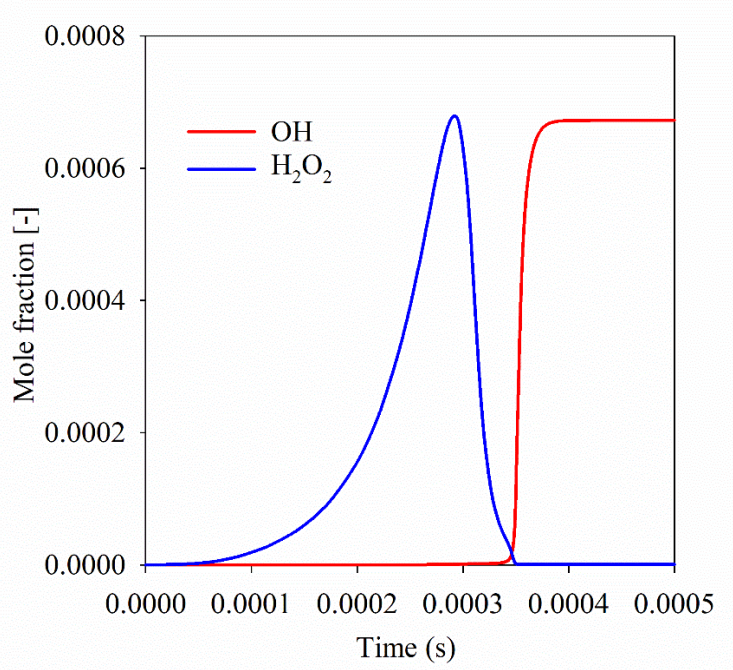

Figure 56: Production of OH and H_2O_2 during stoichiometric constant volume combustion for mixture-2 at Tinl=1100 K, Pinl=285.5 atm.

It is interesting to understand how these two species (CH_3OH and C_2H_3) are causing mixtures to ignite later. Therefore, each species is removed from the 23-species one at a time to make two new mechanisms (2-species as listed in Table 3-2). The IDTs predicted by these two 22-species mechanisms are also shown in Fig. 3-6. It can be observed that, the contribution of C_2H_3 in delaying the ignition is much more than the CH_3OH. But, as it can be observed from Fig. 3-6, the 22-species mechanism with C_2H_3 alone is not sufficient to predict IDTs within the 20% uncertainty. Therefore, it can be concluded that these two species are very important for lean sCO_2 mixtures.

Figure 58 compares IDTs of the stoichiometric H_2 mixtures with those of the detailed Aramco 2.0 predictions. The 19-species mechanism can capture IDTs on par with the detailed one. Thus the 19-species mechanism is sufficient for the H_2 mixtures selected in the current study.

From this analysis, it can be concluded that, minimum 16 species are required for predicting the stoichiometric CH_4 and high CO_2 diluted mixtures. Further, 19 species are required for supercritical H_2 mixtures and 23 species are required for lean CH_4 mixtures with high CO_2 dilution. The 23-species mechanism has better IDT prediction capabilities compared to all other reduced mechanisms discussed in this work. The average deviation of the IDTs calculated by 23-species mechanism with respect to those of the Aramco 2.0 mechanism is less than one percent.

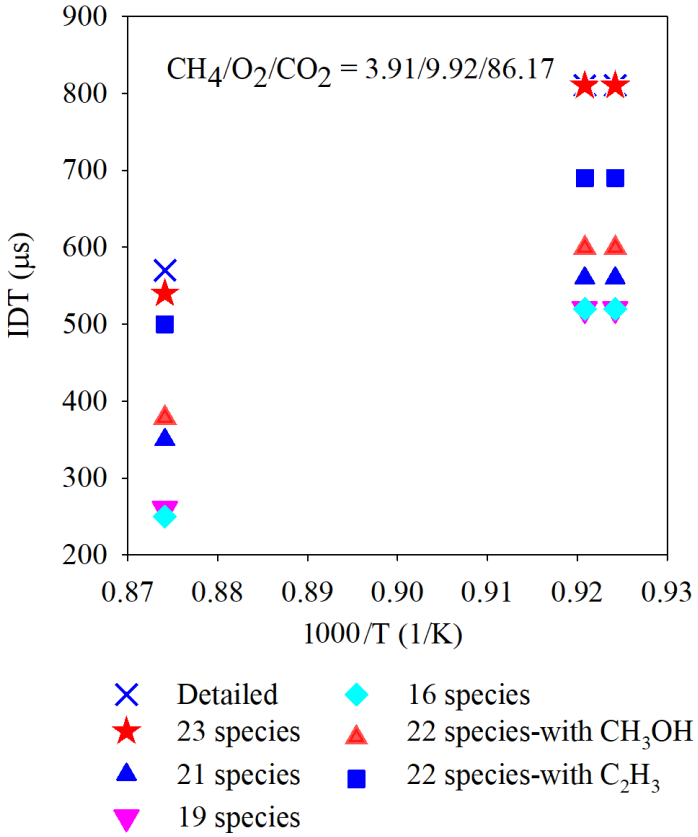

Figure 57: Comparison of lean mixture IDTs of the detailed Aramco 2.0 and reduced species mechanisms

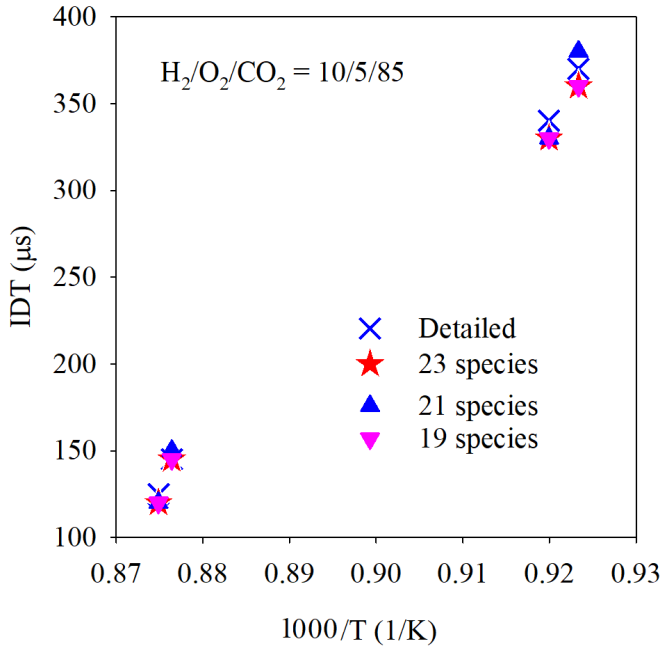

Figure 58: Comparison of stoichiometric $H_2/O_2/CO_2$ mixture IDTs of the detailed Aramco 2.0 and reduced species mechanisms

4.4 Comparison of skeletal and detailed mechanisms with perfectly stirred reactor model

From the previous analysis the 23-species mechanism is identified as the appropriate reduced mechanism for sCO_2 combustion simulations. In this section, the performance of the 23-species mechanism is compared with the detailed Aramco 2.0 mechanism while simulating a perfectly-stirred-reactor (PSR). The PSR simulation is a zero-dimensional simulation which is used as a tool for gas-turbine combustor development since the 1950s. The primary zone of the combustor can be simulated with the PSR [128]. In this section, various possible CO_2 dilution levels and methane-oxygen equivalence ratios in the primary zone are simulated by using a PSR model in CHEMKIN-II. The SRK EOS [39] is considered in the simulation by using CHEMKIN-RG. The inlet temperature of the reactor is 1000 K, pressure is 300 atm.

Figures 59 and 60 show a comparison of the detailed and 23-species mechanisms when they are applied to a PSR. The horizontal axis of Figure 59 represents the residence time in the PSR and the vertical axis represents the exit temperature of the PSR. Here, stoichiometric CH_4 and O_2 at 1000 K are diluted by 60 to 90 percent CO_2 by mass. The results show that, at all dilution levels, the predictions by both detailed and reduced mechanisms yield the same PSR exit temperature (the average deviation between the reduced and the detailed mechanisms are less than 0.5 percent).

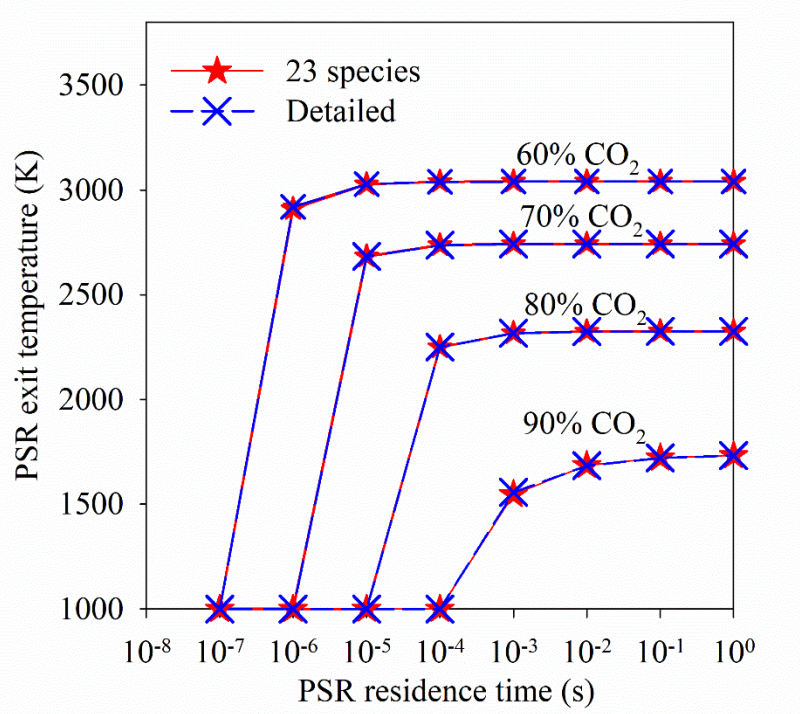

Figure 59: PSR exit temperature comparison of detailed Aramco 2.0 mechanism with the 23-species one at stoichiometric CH_4/O_2 ratio and at various CO_2 dilution levels.

Figure 60 shows the PSR simulation comparison at various equivalence ratios (ϕ). Here, at each equivalence ratio the percentage of CO_2 dilution is kept constant at 90 percent and the residence time as one millisecond. The results show that, the accuracy of 23-species mechanism is a little

less in lean conditions compared to stoichiometric and rich conditions. However, the maximum deviation is observed at ϕ=0.8 and is 2.1 percent which is not considered as significant.

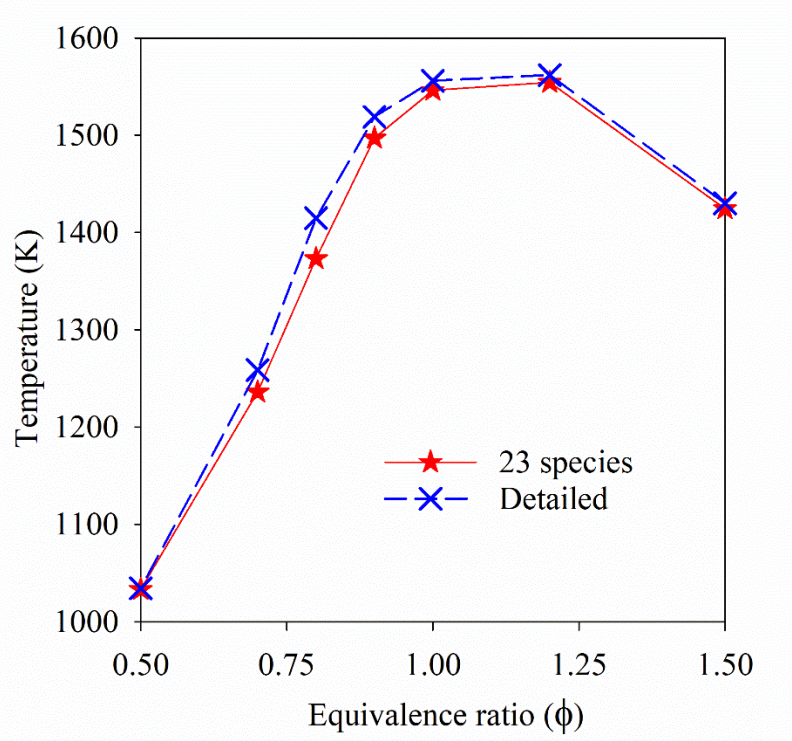

Figure 60: Comparison of detailed Aramco 2.0 mechanism with the reduced 23-species mechanism at various equivalence ratios of CH_4/O_2 at ninety percent CO_2 dilution level at one millisecond residence time

4.5 Comparison of skeletal and detailed mechanisms for turbulence chemistry interaction

Figure 61 shows the comparison of the PCMC solution with both detailed and reduced Aramco 2.0 mechanisms. The horizontal axis of each subplot in Figure 61 corresponds to the Reaction Progress Variable (RPV). The scale represents unburnt condition when RPV is zero and fully burnt condition when RPV is one. The vertical axis of each subplot represents mass fraction of a species. Here, the mass fractions of five species, CH_4, CO, CH_2O, C_2H_6 and OH has been shown with respect to the RPV. Each column in Figure 61 corresponds a species and each row corresponds to a turbulent dissipation value. Here, three turbulent dissipation values (N 1/s),

10000, 100 and 0.1 are presented. For larger N, for CH_4, the PCMC solution is just a straight line. It represents that, the reaction is following a single step pathway at higher N. However, as N decreases, the CH_4 profile is curved more implying that the CH_4 disintegration follows more complex reaction paths. Here, it must be noted that the CH_4 disintegration is very well predicted by the 23-species mechanism on par with the detailed mechanism. Also, the intermediates and radicals, CO, CH_2O, C_2H_6 and OH mass fraction are increasing as the N value deceases. These variations are also predicted well by the 23-species mechanism. However, at small values of N (N=0.1), the difference seems higher. It is because, the PFA method used in this chapter does not account the pathways at various turbulent dissipation levels.

Figure 62 shows a comparison of the source term (S_c) between the detailed Aramco 2.0 mechanism and the reduced 23-species mechanism at various turbulent dissipation values. In the PCMC, the source term represents the non-dimensional reaction energy release per second. At N value 10000, the peak of the source term is towards the right side of the plot and it represents the maximum rate of energy releases towards the end of the reaction. However, at lower N the peak value moves towards the left. This trend is very well predicted by the 23-species mechanism.

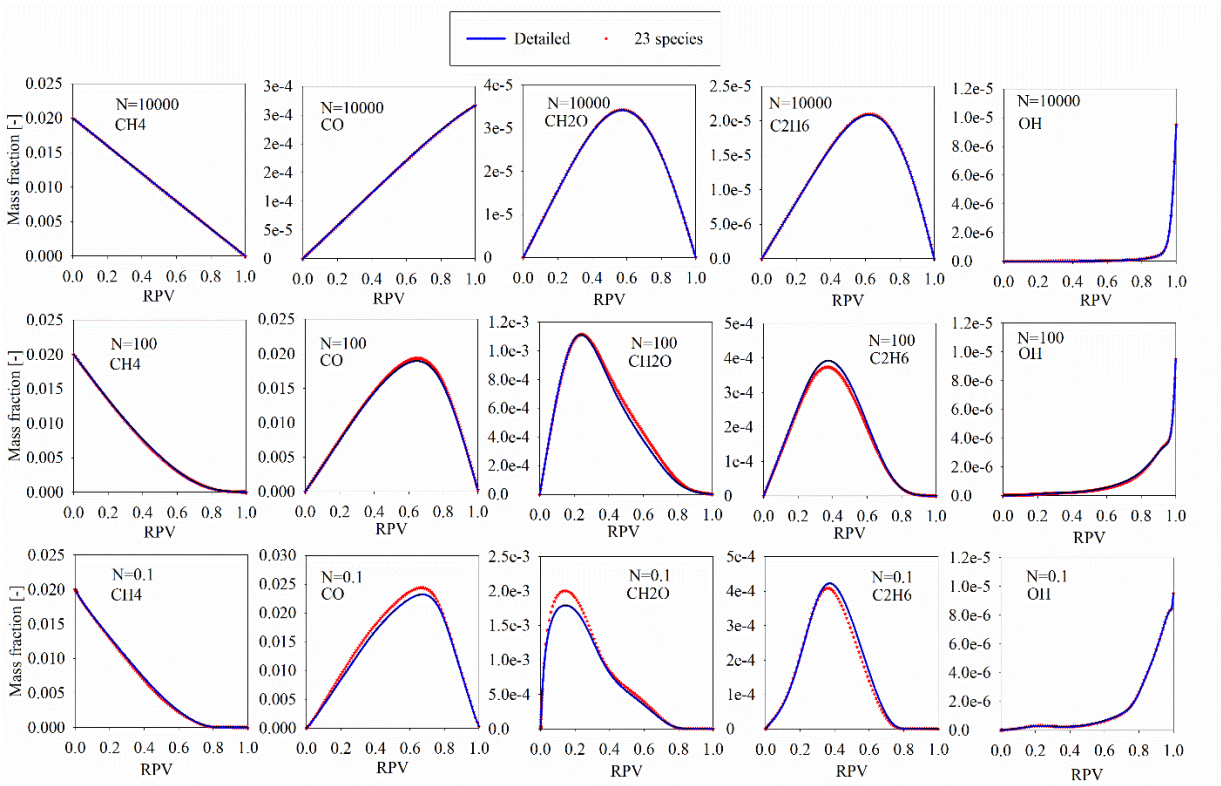

Figure 61: Comparison of detailed and reduced (23-species) Aramco 2.0 mechanisms at various turbulent dissipation values

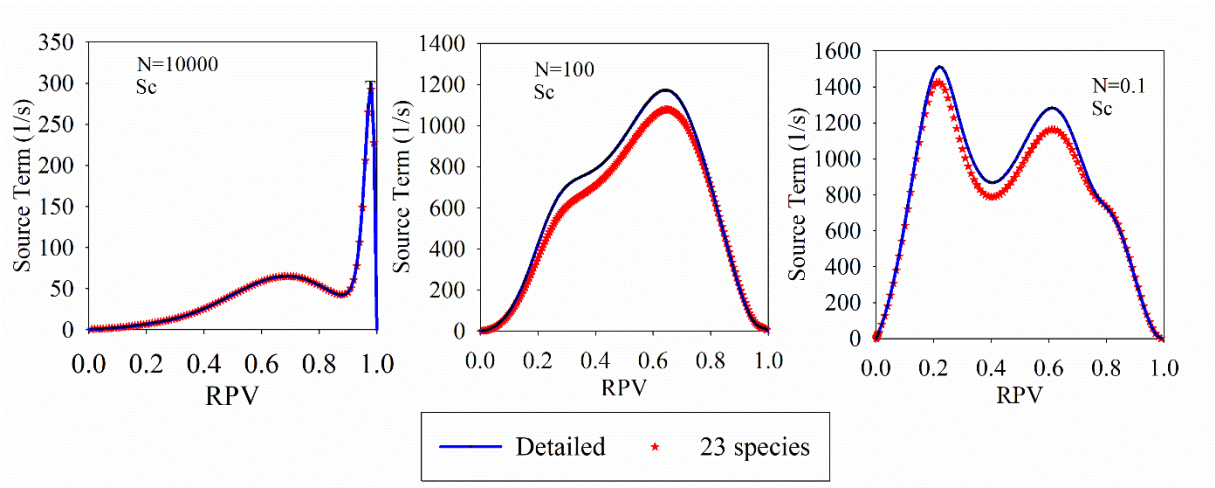

Figure 62: The comparison source term (S_c) estimated by detailed and reduced (23-species) Aramco 2.0 mechanisms at various turbulent dissipation values

4.6 Comparison of skeletal and detailed mechanisms for ignition delay times

In this section, the 23-species and detailed Aramco 2.0 mechanisms are compared by using IDTs in constant volume reactor. Here, four mixture conditions (In addition to Mixture-1,2 and 3) are considered for comparison and each mixture has five initial temperature conditions varying from 1000 K to 1500 K. The temperature range chosen here corresponds to the approximate inlet and outlet temperatures of the sCO_2 combustion chamber. Also, these mixture conditions consist of two stoichiometric ratios, one lean and rich equivalence ratio.

The IDTs are shown in Figure 63, which shows that both the detailed Aramco 2.0 and 23-species mechanisms are predicting approximately the same IDTs. The maximum difference observed between both the predictions are less than 2%.

Table 13: Mixtures considered for comparing IDTs in the constant volume combustion chamber

Initial Mixture	Mole ratios of fuel/O_2/CO_2
Mixture 1-H_2/O_2/CO_2	10/5/85
Mixture 2- CH_4/O_2/CO_2	3.91/9.92/86.17
Mixture 3- CH_4/O_2/CO_2	7.5/15/77.5
Mixture 4- CH_4/O_2/CO_2	1/2/26.7
Mixture 5- CH_4/O_2/CO_2	1/2/9
Mixture 6- CH_4/O_2/CO_2	1/4/15
Mixture 7- CH_4/O_2/CO_2	1/1.33/9

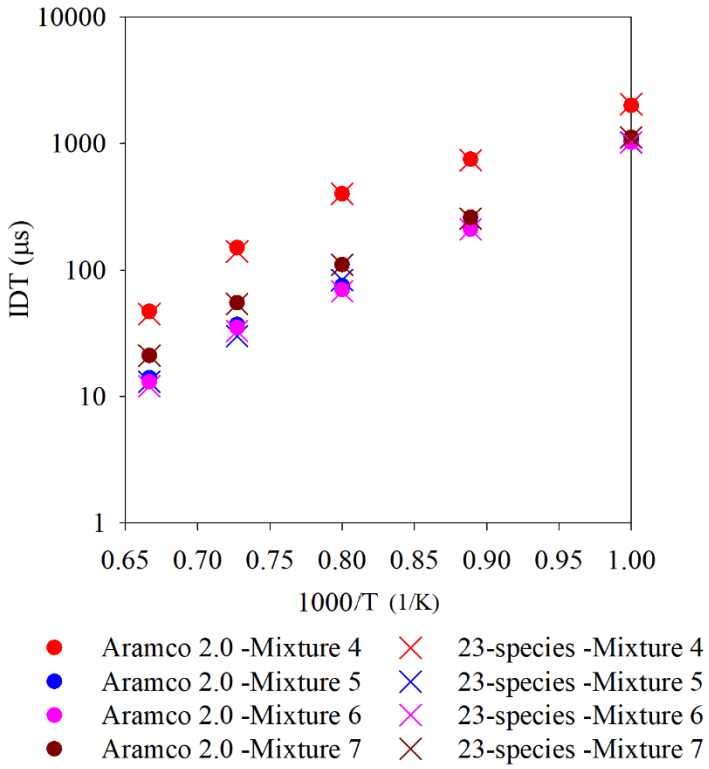

Figure 63: Comparison of the Aramco 2.0 and 23-species mechanisms in terms of ignition delay times estimation in a constant volume combustion chamber

4.7 Reaction rate constant estimate by molecular dynamic simulations

Chemical kinetics in the sCO2 environment is different from that of ideal gases [129, 130]. Arrhenius rate constants for reactions in sCO2 could be determined either by experiments or by detailed molecular level simulations. At present, experimental efforts to understand reaction rate constants in the sCO2 environment at the molecular level are rare. However, some progress has been made through Quantum Mechanical (QM) and Molecular Dynamics (MD) simulations, in combination with the theory of chemical reactivity approaches, including Rice–Ramsperger–Kassel–Marcus (RRKM) one, as discussed in this section.

4.7.1 Review of QM, MD, and RRKM reaction rate estimates in the combustion

There are several methods to calculate rate constant *k* by estimating the reaction path at molecular level. Even the apparently simple reaction may proceed through a complicated mechanism with multiple transition states and intermediate species. Also, environmental atoms and molecules may participate to form unexpected species. Transition-state theory (TST) [131] is the most common method to predict rate constant for a single step process. QM method is used to optimize geometries of the reactants and transition state (the saddle point, with one imaginary vibrational frequency). Next, Eyring-Polanyi equation (Eq. 18) can be applied to calculate *k*. In some cases, free energy barrier still exists, but there is no intrinsic potential barrier. The location of this free energy barrier, is called variational TST (VTST) [132], and it can be used to calculate *k*. Bond breaking reactions usually proceed through VTST.

One should note that TST treats elementary reactions on the assumption of fast equilibration with the bath gas molecules (strong collision limit). There are other theories, accounting for the finite collision rates to evaluate *k*. For example, the critical assumption of RRKM theory is applied to treat temperature and pressure dependence of unimolecular dissociation or isomerization. In TST there is no re-crossing of the dividing surface, meaning that trajectories passing through TS always continue on to the products. Moreover, TST requires the values of energy, rotational constants, and the vibrational frequencies at the saddle point, all of which can be provided by the quantum chemical calculation. In turn, RRKM accounts for a finite fraction of hot (not equilibrated) product molecules, recrossing TS back to the reactants basin [133, 134]. Typical RRKM calculation also includes quantum tunneling probabilities [135]. However, RRKM theory often oversimplifies reaction mechanism, ignoring other isomerization channels. Therefore, Master equation [136] can be applied in cases of multiple interconnected wells and the dissociation

of weakly-bound radicals, These processes can be presented as stochastic differential equation chain or Markovian equations:

$$\frac{dn_i(t)}{dt} = \sum_j (p_{ij} n_j(t) - p_{ji} n_i(t)) \qquad (4\text{-}1)$$

where p_{ij} is the probability per unit time of a transition from state j to i and $n_i(t)$ is the probability of finding the ensemble of molecule or population at state i at time t.

The accurate prediction of the rate constant k in sCO_2 environment may include several steps. First, the potential energy surface (PES) maps the location of the local minima, corresponding to reactants and products, as well as intermediates on the reaction path between them. The saddle point where the energy profile along the reaction path reaches its maximum is known as transition state (TS). Its elevation above the reactants is activation energy. Second, the free energy profile along the reaction also known as the potential of mean force (PMF) is produced. Two points on PMF (reactants and TS) are the most important, they determine Gibbs free activation energy of a reaction. Eyring-Polanyi equation (Eq.4-1) can be applied after evaluating this activation free energy. Free energy can be determined by quantum mechanical (QM) and molecular dynamics (MD) simulations. A high-level *ab initio* QM methods combined with a large basis set produce the most accurate results. In chemical kinetics studies, methods such as coupled-cluster (CC) theory with single (S) and double (D) substitutions and perturbational inclusion of unlinked triples [CCSD(T)] [137] is considered "golden standard", they are the most accurate while often unaffordable. Therefore, multi-configurational self-consistent field (MCSCF) [138, 139] method such as complete active space SCF (CASSCF) and perturbation theory (CASPT2) [140, 141] were used in early studies. CASSCF has a limited account for dynamic electron correlation, while CASPT2 overcome such issues, especially for hydrogen atom association with radical hydrocarbon reactions [142]. Recently, the rate constant of reactions was also predicted by a

machine learning approach to reduce QM calculation time without losing the accuracy of estimating *k* [143].

Combustion reactions include association/dissociation of atoms or molecules and bond formation/breaking. Of these reactions, methane oxidation $CH_4 \rightarrow CH_3 \rightarrow CH_2O \rightarrow HCO \rightarrow CO \rightarrow CO_2$ is one important high-temperature pathway in the combustion mixture. At low temperatures, pathways that are unimportant at higher temperatures become prominent. In a low-temperature pathway, CH_3 to CH_2O can appear through methanol (CH_3OH) or CH_3 recombine to form C_2H_6, which is a higher hydrocarbon than CH_4. The CH_3OH and C_2H_6 can ultimately be converted into CO.

Many of these radicals were studied by experimental and theoretical groups. The reaction path of radical-radical recombination is typically barrierless, and therefore tunneling effects are not important. Usually, no well-localized TS (saddle point on PES) is found, and location of variational TS (saddle point on PMF) depends on temperature, account of anharmonicity, hindered rotation, etc. Other reactions, such as hydrogen abstraction reactions and molecular decomposition/dissociation represent combustion reactions in general [144]. Hydrogen-oxygen reactions play essential roles in combustion reactions [145, 146]. One or more intermediates exist and contribute to chain-branching and chain-terminating reactions. Of all the series of hydrogen-oxygen reactions, $H + O_2 \Leftrightarrow OH+O$ reaction is the essential chain-branching reaction. Other chemical kinetics information can be obtained from the NIST Kinetics Database [147]. However, the database is still lacking many reactions under high pressure. Therefore, several computational methods have been used to estimate *k* in high pressure, high-CO_2 concentration environments. These studies are reviewed in the following.

4.7.2 A summary of MD, QM, and RRKM studies of high-pressure reactions

Chemical reactions studied at high pressures above 100 atm are relatively rare. A series of oxy-fuel combustion reactions in the sCO_2 environment were studied by QM and classical MD methods to evaluate constant rate *k*. In these studies, the CO_2 molecule was treated explicitly as a spectator molecule that may modify the reaction mechanism and reduce the activation energy barrier. The 1st important combustion reaction is:

$$CO+OH \rightarrow H+CO_2 \qquad \text{(R1)}$$

This reaction converts CO to CO_2 with significant exothermic effect. It was found in the study [148, 149], that one CO_2 molecule may covalently bind with OH radical, followed by attachment of CO molecule and formation of a new intermediate. This alternative reaction pathway lowers the activation energy [148, 149]. It was found to be autocatalytic because the reaction product CO_2 acts as a catalyst. Subsequently, the Master equation approach was applied to compare pathways with and without CO_2 molecule [150]. The rate constant with the CO_2 molecule was higher only when the temperature is lower than 370 K and when the pressure is higher than 300 atm. At 300 atm, the rate constant *k* of (R1) is in the order of 10^{-12} cm^3/molecule/s with or without catalytic CO_2 molecule. Experimental and theoretical studies of this reaction at low pressure were performed by other groups [151-155].

The 2nd and 3rd most important reactions in combustion are the transfer of hydrogen atom (H-abstraction):

$$HO_2+CH_2O \rightarrow H_2O_2+HCO \qquad \text{(R2)}$$

and the self-reaction of HO_2:

$$2HO_2 \rightarrow H_2O_2+O_2 \qquad \text{(R3)}$$

These reactions in the presence of spectator CO_2 molecule were studied to investigate the effect of covalent and van der Waals (vdW) complex formation [149, 156]. The authors concluded that the formation of covalent intermediates does not play the role of hydrogen transfer kinetics because of the higher activation barrier along that pathway. The vdW complexation of CO_2 molecule in (R2) does not affect hydrogen transfer from formaldehyde but accelerates HO_2 self-reaction (R3). It represents the catalytic effect of CO_2 molecule in (R3). Other theoretical studies of *k* of (R2) were performed [157-160] and *k* of (R3) [161-164], both at low pressure.

QM calculations and Master equation approach were also applied in the reaction of hydrogen transfer from formaldehyde to hydroxyl in our group [22, 165]:

$HO+CH_2O \rightarrow H_2O+CHO$ (R4)

Formaldehyde is an essential intermediate in oxidation reactions in both combustion and atmospheric chemistry. The role of CO_2 molecule was found to form the vdW complex under higher pressure and lower temperature, which leads to a higher rate constant of this reaction. Rate constant *k* of (R4) at 300 atm below 1,000-2,000 K is in the order of 10^{-12} cm^3/molecule/s with CO_2 molecule and of 10^{-11} cm^3/molecule/s without CO_2 molecule. These results show the importance of the solvent effect of CO_2 at room temperature. Studies of (R4) by other research groups were done by shock tube experiment [166, 167] and *ab initio* Quantum chemical calculations [168-171]. Other oxidation reactions of methyl radical $CH_3 + O_2$ were investigated as well. They include vdW or covalently bonded CO_2 molecule leading to alternative pathways and produce CH_3O, CH_2O, or CHO [165]:

$CH_3+O_2 \rightarrow CH_3O+O$ (R5)

$CH_3+O_2 \rightarrow CH_2O+HO$ (R6)

$CH_3+O_2 \rightarrow CHO+H_2O$ (R7)

All these CH_3 radical reactions (R5)-(R7) were found to be catalyzed by the CO_2 molecule [165]. Experimental studies of *k* for (R5) include shock tube [172-175] and flash photolysis [176]. Studies of *k* for (R6) include shock tube [172, 175, 177, 178] experiments at high temperature and low pressure and theoretical *ab initio* calculations [179, 180]. Reaction (R7) was studied only by shock tube experiments [181, 182]. Table 14 presents the characteristics of reactions involving explicit CO_2 molecule, studied in our group.

Table 14: Explicit CO_2 molecule-included reactions performed in our group

Reactions	Quantum calculation performed?	Master Equation included?	Hydrogen transfer?	van der Waals intermediate?	Covalent-bonded intermediate?
$CO + OH \rightarrow H + CO_2$	Y	Y	N	N	Y
$CH_3 + O_2 \rightarrow H_3CO + O$	Y	N	N	Y	N
$CH_3 + O_2 \rightarrow H_2CO + HO$	Y	N	N	N	Y
$CH_3 + O_2 \rightarrow HCO + H_2O$	Y	N	N	N	Y
$H_2CO + HO \rightarrow HCO + H_2O$	Y	Y	Y	Y	N
$H_2CO + HO_2 \rightarrow HCO + H_2O_2$	Y	N	Y	N	N
$2HO_2 \rightarrow O_2 + H_2O_2$	Y	N	Y	Y	N

Besides QM studies, classical MD simulations were performed in our group for the series of combustion reactions where large number of spectator CO_2 molecules were included to mimic the sCO_2 environment. The challenge of MD simulations of these reactions is that they include making or breaking chemical bonds. Therefore, MD needs special force field. There are various methods incorporating chemical reactions in MD simulations, including the reactive force field (ReaxFF) [183]. Modifications of the force field parameters was found to be necessary since the

original ReaxFF did not reproduce transcritical behavior of CO_2 and H_2O well [113]. PES of the most important combustion reaction CO + OH → H + CO_2 (R1) was validated by such updated ReaxFF force field parameters. Later, the same reaction was studied by MD simulations to obtain rate constant *k*. In this MD study, the combined quantum mechanical/molecular mechanical (QM/MM) method was applied instead of ReaxFF approach to describe the reactive system. The QM/MM method has been developed to simulate chemical reactions in large systems and is especially appropriate for reactions in solution [184-186]. The combination of semi-empirical modified neglect of diatomic overlap (MNDO) [187] as QM method to treat the reactive system and transferable potentials for phase equilibria (TraPPE) [188] as MM force field to treat CO_2 molecules were selected. To sufficiently sample crossing the activation barrier, boxed MD (BXD) protocol [189, 190] was applied. BXD allows to explore rare events and obtain the potential of mean force (PMF). The idea of this protocol is to divide the entire range of reaction coordinate into several intervals, called "boxes". The dynamic trajectories are locked within each box to observe a sufficient number of events, involving rarely visited regions (like barrier crossing). BXD provides free energy along the reaction coordinate. Once PMF is known, VTST is located, and is used to predict the activation free energy, and subsequently the rate constant by Eyring-Polanyi equation (Eq.18). The calculated *k* (~10^{-12} cm^3/molecule/s at 300 atm) has a similar trend to that fitted by the Master equation in the previous work [150], and it shows the validity of such delicate composite MD simulation method. In this study, rates of formation and decomposition of the stable intermediate HOCO were evaluated.

Other important combustion reactions in sCO_2 environment were studied by a similar protocol. These include methane oxidation reaction [191]:

$CH_3+HO_2 \rightarrow CH_3O+OH$ (R8)

and the decomposition of formyl radical [192]:

$HCO \rightarrow H+CO$ (R9)

The stable intermediate CH_3OOH in (R8) and HCO at a higher temperature in (R9) or vibrationally excited intermediate HCO* at lower temperature represent various reaction channels and will lead to different k in different temperature and pressure range. Other studies of k on (R8) include shock tube experiments [193, 194] and theoretical estimation [195]. Rate constant for (R9) were studied by flash photolysis [196, 197], or combined experimental and quantum chemical methods [198].

To obtain more accurate PES, than semiempirical QM methods could provide, the multi-state empirical valence bond (MS-EVB) [199, 200] method was applied in two of the important barrierless combustion reactions - ethane dissociation [201]:

$C_2H_6 \rightarrow 2CH_3$ (R10)

and hydrogen oxidation [202]:

$H+O_2 \rightarrow HO_2 \rightarrow HO+O$ (R11)

The flexibility of MS-EVB allows one to use force field tools to reproduce the accurate (predicted at high QM theory level) reactive PES in the TS region, thus bridging the gap between classical and quantum mechanics. The effect of supercritical environment on calculated free energy can be taken into account by applying the method developed by Akiya and Savage [203]. In this method the reaction free energy in the gas phase ΔG_{gas} and solvation free energy of supercritical solvent ΔG_{sol} make up the reaction free energy in supercritical phase $\Delta G^{\neq}$ at any point along the reaction coordinate r:

$$\Delta G^{\ddagger}(r) = \Delta G_{gas}(r) + \Delta G_{sol}(r) \qquad (4\text{-}2)$$

While calculation of $\Delta G_{gas}(r)$ is performed by a high-level *ab initio* QM method, $\Delta G_{sol}(r)$ is obtained by Boxed MD simulation using MS-EVB force filed (as the difference between two PMF,

predicted with and without solvent molecules). This solvation free energy eliminates the systematic error from transferring a reaction from the gas phase to the supercritical phase.

This approach was applied to reactions (R10) and (R11). The variational TST (VTST) [131, 204] was applied to predict $\Delta G^{\neq}$ in the case of (R10), while RRKM [134] was used in the case of (R11). Figures 60 and 61 show the rate constants of (R10) and (R11) in comparison with experimental and theoretical results from different groups. The composite method described above was able to evaluate k at higher pressures. The predicted k was closer to experimental results at different temperatures and pressures. Table 15 lists the summary of combustion reactions in the sCO_2 environment studied in our group. The refinement of rate constant for reaction $CH_3 + HO_2 \rightarrow CH_3O + OH$ (R8) was performed in our group, by taking into account the complex formation with CO_2. Figure 64a compares predicted k with other theoretical evaluation by VRC-TST [195] and RRKM [205] methods from other groups. Figure 64b shows the difference of k at 1, 100, and 300 atm after the correction. The result illustrates pressure independence of the reaction R8 (Figure 64a) and the usefulness of such correction (Figure 64b) to reduce deviations from experiment at lower temperatures ~1,000 K.

Table 15: Molecular dynamics simulation of combustion reactions in supercritical CO_2 environment

Reaction	ReaxFF	QM/MM	MS-EVB	CVTST	RRKM	Temperature range (K)	Pressure range (atm)
$CO + OH \rightarrow CO_2 + H$	Y	Y	N	N	N	400 - 1,600	1 - 1,000
$CH_3 + HO_2 \rightarrow CH_3O + OH$	N	Y	N	N	N	600 - 1,600	0.3 - 1,000
$HCO \rightarrow H + CO$	N	Y	N	N	N	400 - 1,600	0.3 - 1,000
$C_2H_6 \rightarrow 2CH_3$	N	N	Y	Y	N	1,000-2,000	100 - 1,000
$H + O_2 \rightarrow HO + O$	N	N	Y	N	Y	1,000 - 2,000	100 - 400

Table 16: Parameters A, n, and E_a in extended Arrhenius equation of combustion reactions at 300 atm studied in our group

Reaction	A cm^3/molecule/s	n	Ea cal/mol	Reaction	A 1/s	n	Ea cal/mol
$CO + OH \rightarrow H + CO_2$	4.30E-06	-1.310	40680				
$CH_3 + HO_2 \rightarrow CH_3O + OH$	1.53E-21	2.758	-8905				
$HCO \rightarrow H + CO$	1.02E+15	-1.254	13000	$H + CO \rightarrow HCO$	2.01E-15	0.298	-1840
$C_2H_6 \rightarrow 2CH_3$	8.44E-19	1.420	-19890	$2CH_3 \rightarrow C_2H_6$	2.41E+14	-0.200	77030
$H + O_2 \rightarrow HO_2$	5.22E-02	-2.860	7247	$H + O_2 \rightarrow HO + O$	4.23E-07	-0.730	21855

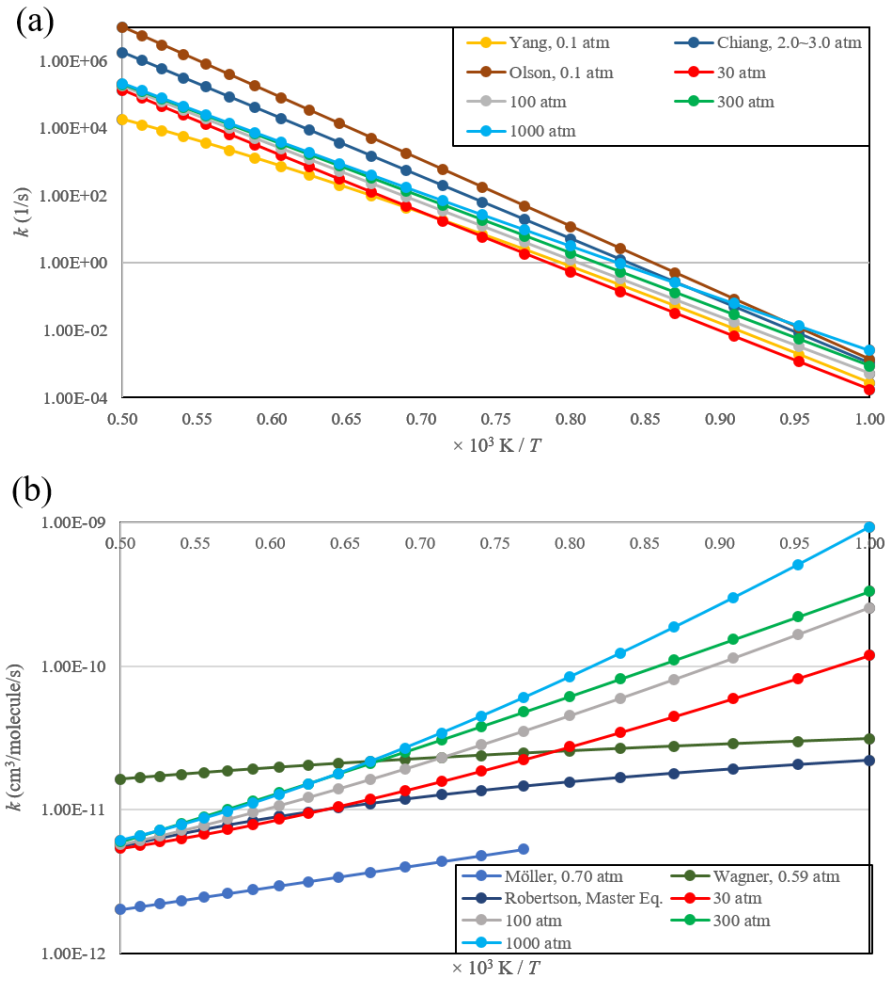

Figure 64: The rate-constant of (R10) (a) and its reverse reaction, (b) $2CH_3 \rightarrow C_2H_6$. Experimental shock tube results are from [206-208] in (R10) and from [209, 210], and theoretical comparison from [211] in the reverse reaction of (R10).

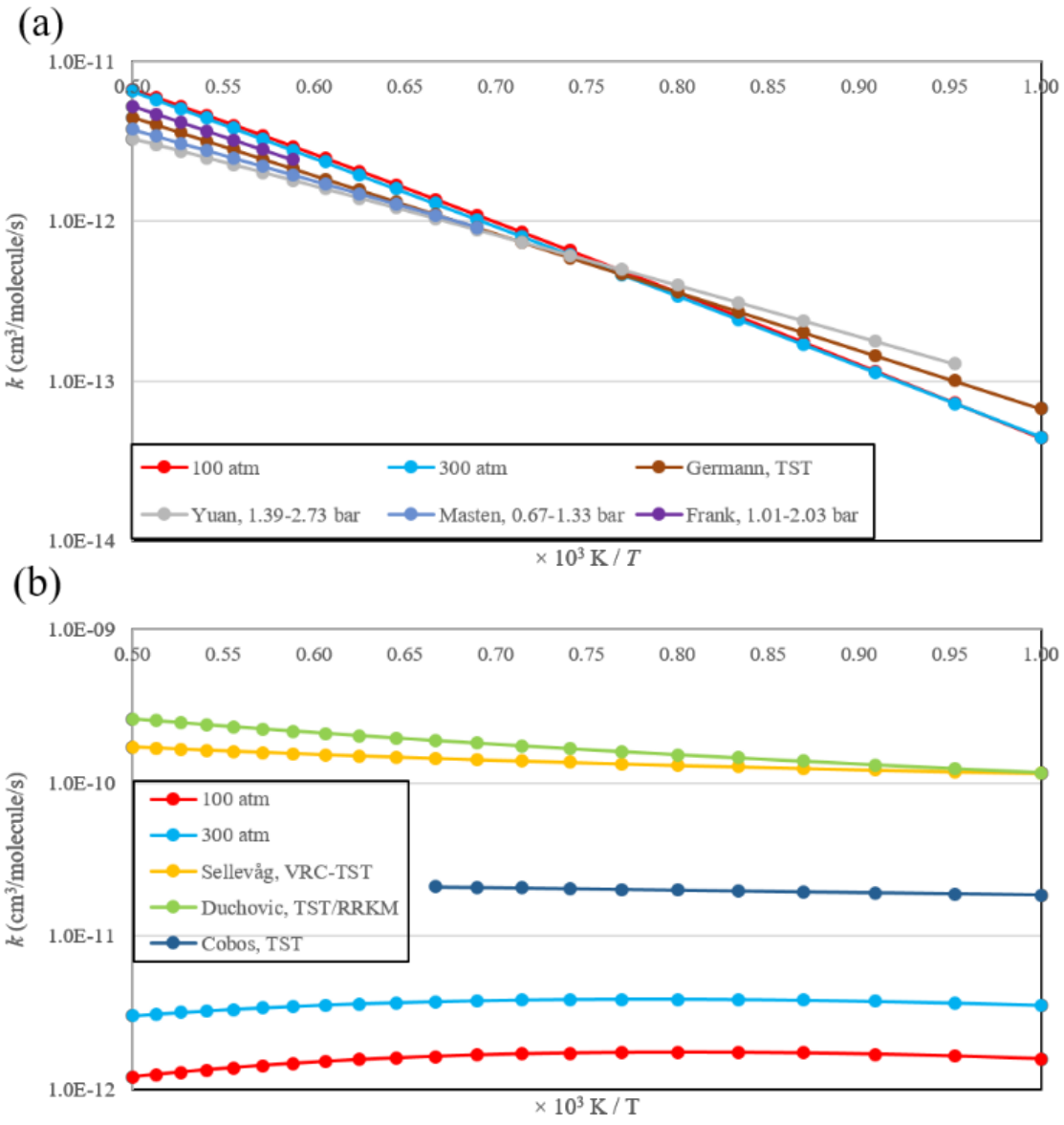

Figure 65: The rate is constant (R11) (a) and its stable intermediate reaction (b) $H + O_2 \rightarrow HO_2$. Experimental shock tube results are from [212-214], and theoretical comparison from [215-218].

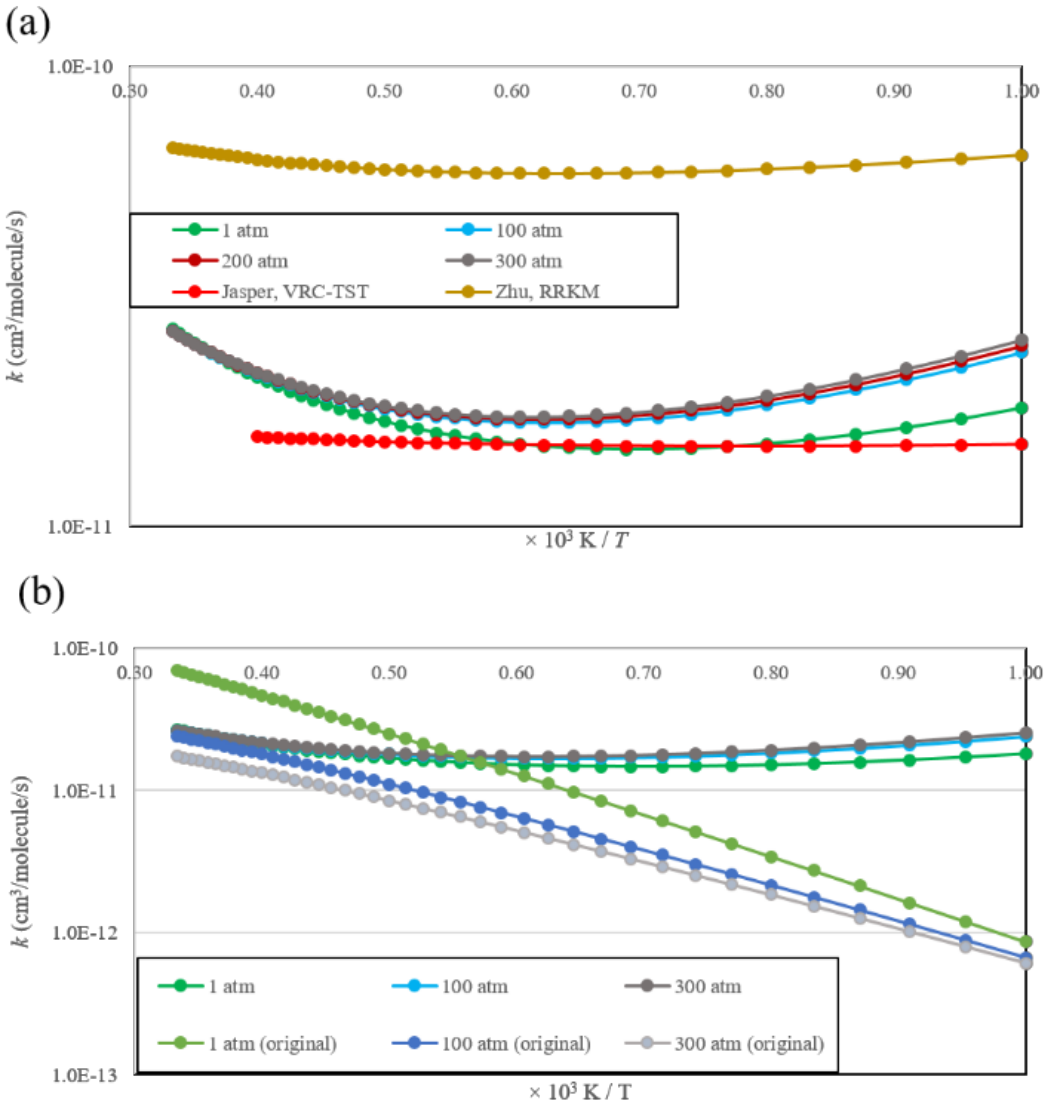

Figure 66: The rate constant k of (R8) in (a) 1 to 300 atm and by VRC-TST[195] and RRKM[205] methods; (b) 1 to 300 atm before and after solvent correction.

Table 16 presents the parameters A, n, and E_a of extended Arrhenius equation for several reactions at 300 atm predicted by MD simulations in our group. In summary, the combustion reaction in the sCO_2 environment may change the reaction path compared to that in the gas phase. Explicit representation of CO_2 molecules in simulations allows one to track the dynamic properties and the interactions between the reactants and CO_2 molecules. The correction method (Eq.4-2) by Akiya and Savage [203] allows to reduce deviations of the calculated rate constant from the experimental measurements (where available), and demonstrated that k can be predicted more accurately compared to the other theoretical studies at high pressures. The combination of QM and MD methods helped to understand the role CO_2 molecules play in the combustion reactions.

4.8 Performance of new sCO_2 mechanism

As discussed in introduction of this chapter, a mechanism must have validated with respect to experiments and the reaction rates must be physical. Hence, the rate constants of reactions determined specifically for sCO_2 combustion application is substituted in Aramco 2.0 mechanism and called as UCF 1.1 mechanism. The new reaction rates are estimated with molecular dynamics simulations are implemented in UCF 1.1 mechanism. Also, the performance of the mechanism is shown in Fig. 3-13 and 14. Here, the figures illustrates that the performance of this mechanism is better than the Aramco 2.0 mechanism under the conditions compared. Further, this mechanism is validated on other unpublished sCO_2 shock tube data which is not shown in this report.

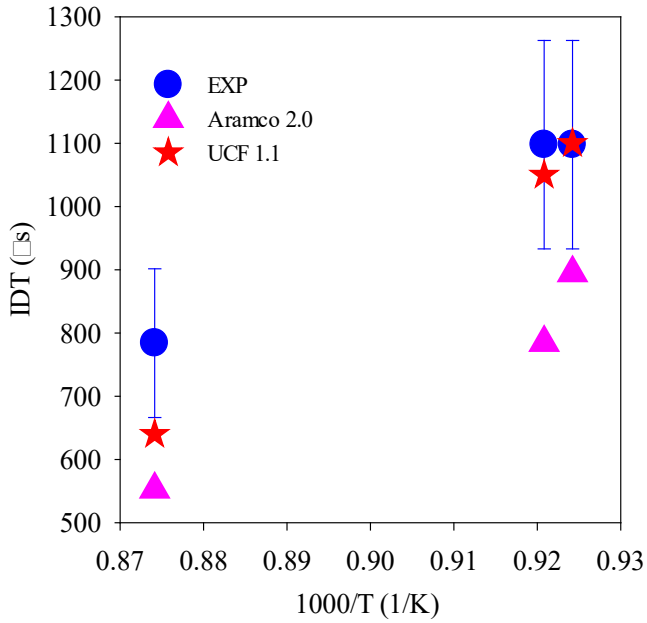

Figure 67: Comparison of lean (mixture-2) sCO_2 shock tube ignition delay times [46] with Aramco 2.0 and UCF 1.1 species mechanism

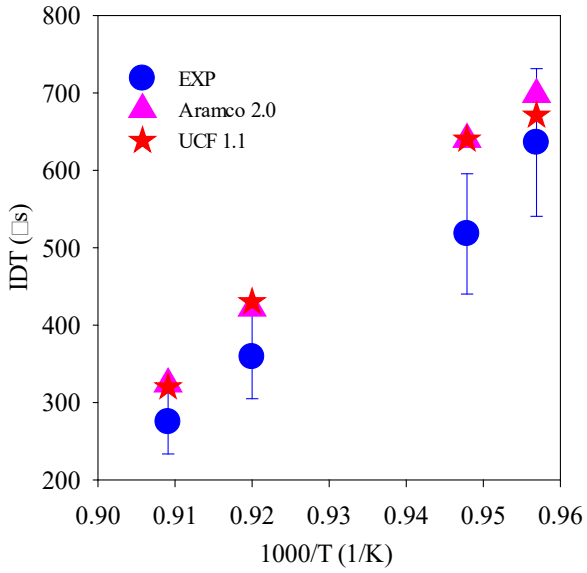

Figure 68: Comparison of stoichiometric sCO_2 shock tube ignition delay times [46] with Aramco 2.0 and UCF 1.1 species mechanism

4.9 Conclusions

In the current chapter, a comparison is made between the Aramco 2.0 and GRI 3.0 mechanism by using various van der Waal's type of equations to predict the ignition delay times of a shock tube. From this analysis, the Aramco 2.0 mechanism is confirmed to be a better accurate mechanism available for sCO_2 combustion applications. After that, a 23-species reduced mechanism has been developed from Aramco 2.0 mechanism by using the path-flux-analysis method (PFA) by employing the CHEM-RC tool. Finally, Aramco 2.0 mechanism is updated with the reaction rates specifically determined for sCO_2 conditions and shown the improvement in ignition delay time predictions.

1) The equation of state is found to have no impact on estimating ignition delay times of supercritical $CH_4/O_2/CO_2$ mixtures unlike supercritical $H_2/O_2/CO_2$ mixture considered in this work. It may be because, in $H_2/O_2/CO_2$ mixture, the main product of combustion, i.e., H_2O is shifting the critical point of the mixture towards the testing pressure.
2) The $CH_4+HO_2 \Leftrightarrow CH_3+H_2O_2$ is very crucial in the prediction of auto ignition under sCO_2 conditions, because methane decomposes into CH_3 and H_2O_2 by this reaction even before the actual ignition starts.
3) The species C_2H_3 and CH_3OH and their associated reactions are very important in predicting the lean auto ignition.
4) The 16-species mechanism identified in this work is sufficient to recognize the ignition delay times of the stoichiometric conditions. However, for identifying lean conditions at least a 23-species mechanism is required. Also, the 19-species mechanism is needed in predicting the ignition delay times of stoichiometric sCO_2 hydrogen mixtures.

5) The 23-species mechanism presented in this work is performing on par with the detailed Aramco 2.0 mechanism in-terms of ignition delay times, perfectly stirred reactor estimation under various CO_2 dilutions and equivalence ratios, and prediction of turbulence chemistry interactions.
6) Further, the mechanism (UCF 1.1) is updated with the reaction rate constants of some sensitive reactions. These reaction rate constants are specifically calculated for sCO_2 combustion by using detailed molecular level simulations.

CHAPTER 5: A GENERAL STUDY OF COUNTERFLOW DIFFUSION FLAMES FOR SUPERCRITICAL CO_2 MIXTURES

5.1 Introduction

In the current paper an attempt is made to understand the influence of CO_2 dilution and pressure on the non-premixed sCO_2 combustion by using the popular, axisymmetric counterflow diffusion flame analysis. A schematic diagram of counterflow diffusion flame is shown in Figure 69. Counterflow diffusion flames are significant in the field of non-premixed turbulent systems because the turbulent flame can be assumed as a combination of small laminar flamelets locally, therefore, the local strain effect on a turbulent flame can be studied simply by changing the strain (by changing the inlet boundary conditions) on the counterflow diffusion flame. It should be noted that, in the current work inlet velocity of both streams is kept constant at 40 cm/s.

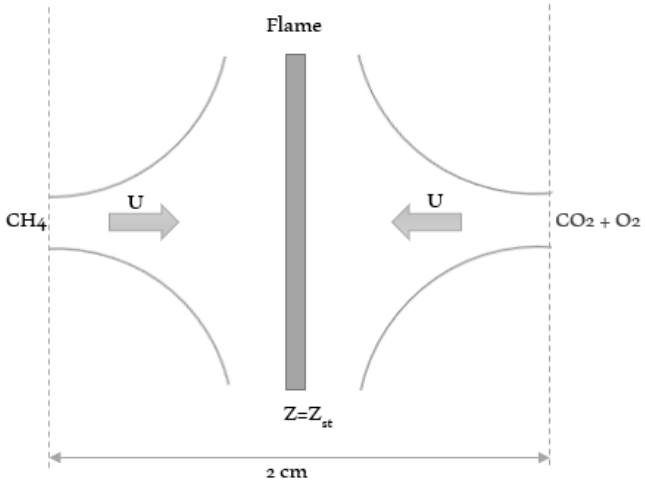

Figure 69: A schematic diagram of the counterflow diffusion flame (U is the inlet velocity boundary condition and Z_{st} is the stoichiometric mixture fraction)

A comprehensive experimental and numerical literature of counterflow diffusion flames is obtainable for ideal gases and real gases [219-224]. However, a similar analysis for sCO_2 oxy-methane combustion with real gas effects is not available. Therefore, in the chapter, attention is focused on sCO_2 mixtures.

The organization of this chapter is described as follows. Initially, the modeling section describes various real gas corrections and inputs accounted in the current simulation. Further, a comparison is made between Peng-Robinson (PEN) and Soave-Redlich-Kwong (SOV) equation of states (EOS) under various CO_2 dilution conditions and SOV EOS is chosen for further simulations. Further, this study mainly focuses on investigating a few important non-premixed combustion characteristics such as Prandtl number, thermal diffusivity, Lewis number, stoichiometric scalar dissipation rate, flame thickness and Damköhler number, etc., and their dependency on both CO_2 dilution and pressure

5.2 Modeling

As described in the introduction section, the operating conditions of sCO_2 combustors are in the supercritical regime where intermolecular forces are prominent and can alter the thermodynamic and transport properties. Therefore, simulations must account for the real gas corrections.

A pictorial representation of real gas thermal and transport property implementation into the OPPDIF [225] (a FORTRAN counterflow diffusion flame code) is shown in Figure 70. The OPPDIF is a one-dimensional Fortran program that computes the diffusion flame between two opposing nozzles by using a two-point boundary value problem solver. The two-point solver solves the discretized differential equations by adaptive finite difference schemes. The CHEMKIN

OPPDIF code for counterflow diffusion flames [225] is coupled with CHEMKIN-RG [226] to account for real gas corrections and SRK EOS is used for the simulation.

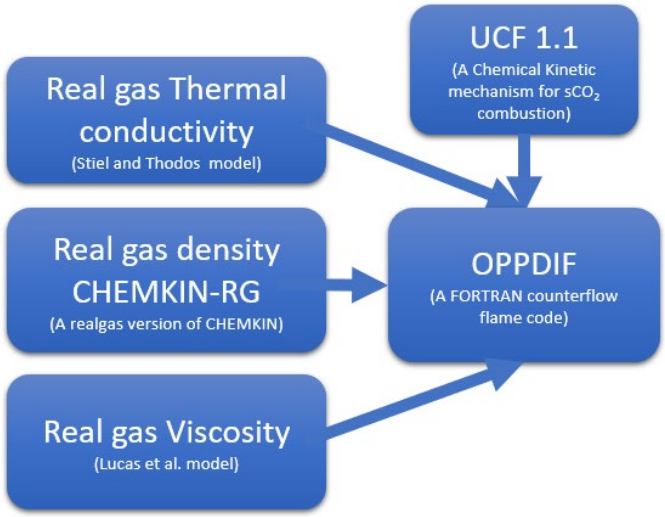

Figure 70: A pictorial representation of the real gas modeling in the current study.

5.2.1 Viscosity modeling:

Lucas et al. [227, 228] model recommend [39] for modeling sCO_2 combustion mixture viscosity, because this approach is relatively inexpensive in terms of computation, shows a good agreement with NIST when this method is applied to major species of combustion, and the predicted viscosity is closer to other supercritical viscosity models. This method does not consider the interaction between species as it is in the Chung et al. method [228]. Therefore, this model is implemented in the OPPDIF for supercritical mixture viscosity estimation along with real gas EOS.

In this method, the mixture is assumed as a single fluid and the critical properties of mixture are calculated based on the weightage of its constituent's mole fractions x_i. Please note that here suffix 'i' represents the species.

5.2.2 Thermal conductivity modeling:

Stiel and Thodos model [228, 229] is used due to its better accuracy and lesser computational time compared to Chung et al.[228] method [39]. The Stiel and Thodos method estimates the supercritical thermal conductivity by adding a correction factor to the low-pressure thermal conductivity at the same temperature. This correction factor is a function of critical properties of the mixture and its reduced density. In general, Stiel and Thodos method is not recommended for polar substances; however the work of [39] shows that at higher temperatures the thermal conductivity of H_2O (which is a major polar molecule in the sCO_2 combustion) is better predicted by this model. Therefore, this model is implemented in this work along with the real gas EOS.

5.2.3 Chemical mechanism:

The UCF 1.1 24-species mechanism is employed in this work accounts for the chemical kinetics. This mechanism is an updated version of the mechanism used in [230] and the rates of some reactions in this mechanism are updated with the rates specifically calculated for sCO_2 combustion [113-115, 231, 232].

5.3.4 Case setup

As discussed in the modeling section, the updated OPPDIF code is used to simulate the counterflow diffusion flame. The width between two jet inlets is two centimeters. It should be noted that, the fuel jet is located at $x = 0$ and the oxidizer jet is located at $x = 2$ centimeters. Three different levels of sCO_2 dilution such as thirty, sixty and ninety percent by mass in the oxidizer stream is used in the analysis. Also, four supercritical pressures, i.e. pressure which are beyond the critical point of major diluent CO_2, such as 150, 200, 250 and 300 atm. are used to investigate the influence of pressure. Also, it must be noted that only real gas simulations performed with SOV

EOS to account for the real gas corrections in transport properties as discussed in the modeling section.

5.3 The influence of equation of state

The equation of states available in literature can be categorized into virial-type, molecular-based and van der Waals type EOS [233, 234]. The virial and molecular based EOS are highly accurate and complex in their formulations. Hence, using them in combustion simulations are computationally expensive. The third category of EOS, i.e. van der Waals type EOS such as Peng-Robinson EOS (PRS) [235] and Soave-Redlich-Kwong (SOV) [236] are popularly seen in the supercritical combustion literature [237, 238]. The work of [39] reports the equivalent performance of SOV and PEN EOS for sCO_2 premixed mixture from unburnt to fully burnt condition. In the current paper, a comparison is made between SOV and PEN at different dilution levels of CO_2 at a reactor pressure of 300 atm.

Figure 71 shows the influence of EOS on the temperature profile of the counterflow diffusion flame at various levels of CO_2 dilution in the oxidizer stream and at 300 atm. pressure. The boundary conditions of this numerical experiment are shown in Table 17. Here, three different dilution levels are chosen because the oxidizer stream can have any level CO_2 dilution, so a broader range is studied. The result shows that, at thirty percent dilution, there is a clear distinction between the temperature profiles predicted by SOV and PEN, whereas, as the dilution level is increasing, the estimates of these two EOS are becoming identical. The reason for this occurrence can be explained as follows. The mole fraction of the H_2O in the products is higher at lower CO_2 dilution condition compared to a higher CO_2 dilution condition. Since the critical pressure of the H_2O is approximately 218 atm. (much higher than other major combustion products), it would

significantly increase the whole mixture critical pressure. Hence, the ratio of the operating pressure to the mixture critical pressure i.e. the reduced pressure P_r decreases. In this case, the operating pressure of the reactor is 300 atm; therefore the magnitude of P_r is closer to one at lower dilution case compared to higher dilution case. In general, the van der Waals type EOSs agree very well when P_r and T_r are far higher from unity [228] which is not the case at low CO_2 dilution condition. Therefore, from this study it is recommended to validate EOS when it is applied to a low CO_2 dilution sCO_2 combustion system. At a high CO_2 dilution and pressure case the PEN and SOV are equivalent.

Table 17: List of boundary conditions used for analyzing the influence of equation of state

	Oxidizer jet	Fuel jet
Reactants	O_2 CO_2 (varied from 30% to 90% by mass)	CH_4
Temperature (K)	1000	1000
Inlet velocity (cm/s)	40	40
Reactor pressure (atm)	300	300

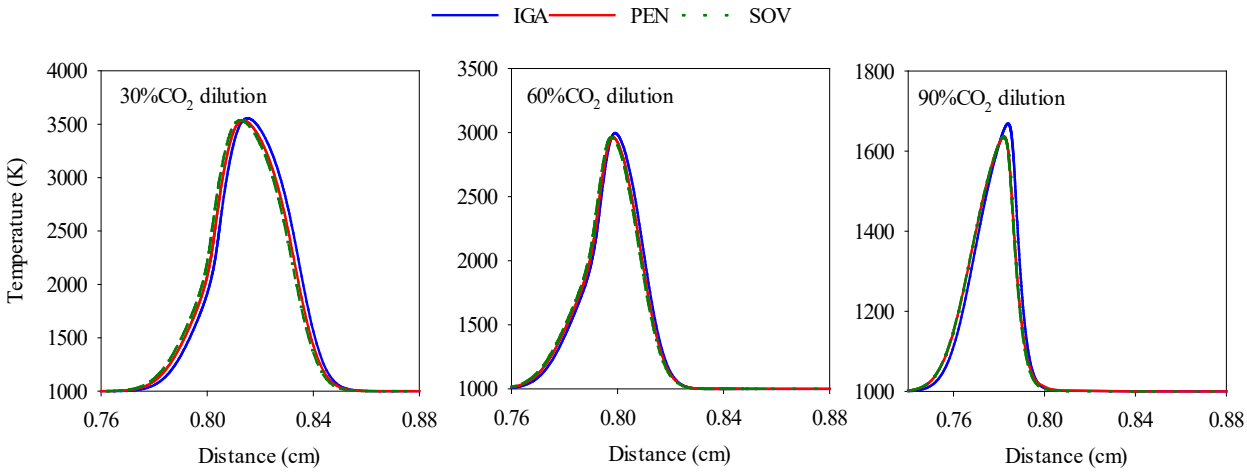

Figure 71: The Effect of EOS on flame temperature at different oxidizer CO_2 dilution levels (300 atm. pressure and U=40 cm/s)

5.4 The effect of CO_2 dilution and reactor pressure:

As discussed in the introduction section, the overall dilution of CO_2 in the sCO_2 combustor must be approximately ninety-five percent by mass. However, the level of dilution in the primary and secondary zones of the combustor will be chosen based on the design requirement [239-241] such as low-Mach number inlet, shorter combustor residence time and complete oxidation of CO before the combustor exit, etc. Therefore, it is very important to look at the non-premixed combustion characteristics at different levels of CO_2 dilution. In the current study three different levels of CO_2 dilution are considered in the oxidizer stream such as thirty, sixty and ninety-percent. Also, though the optimized pressure of direct-fired sCO_2 combustor is 300 atm. the initial test run combustors are being developed at 150-200 atm. [241]. Therefore, four reactor pressures such as 150, 200, 250 and 300 atm. are considered for analysis. The interesting investigation would be to know how dilution and pressure are influencing the important non-premixed combustion characteristic like transport of species, momentum, heat, scalar dissipation, flow and chemical time scales etc. This investigation is important because, combustion codes reasonably assume some of these characteristics to reduce the complexity and associated computational time.

Two cases as presented in Table 18 are studied to understand the influence of CO_2 dilution and reactor pressure. Also, SOV EOS is used for these simulations. In case-1, the pressure is kept constant and the CO_2 dilution is varied, whereas in case-2, dilution level is kept constant and reactor pressure is varied.

Table 18: List of boundary condition used for analyzing the influence of CO_2 dilution and pressure

		Oxidizer jet	Fuel jet
Case-1	Reactants	O_2 CO_2 (varied as 30%, 60% and 90% by mass)	CH_4
	Temperature (K)	1000	1000
	Inlet velocity (cm/s)	40	40
	Reactor pressure (atm)	150	150
Case-2	Reactants	O_2 CO_2 (90% by mass)	CH_4
	Temperature (K)	1000	1000
	Inlet velocity (cm/s)	40	40
	Reactor pressure (atm)	Varied as 150, 200, 250 and 300	

5.4.1 Influence on temperature:

Figure 72 shows the effect of CO_2 dilution (left) and reactor pressure (right) on the counter flow diffusion flame temperature. Here, the horizontal axis with the label "distance" represents the distance between the fuel and oxidizer inlets. The fuel jet is located at $x = 0$ and oxidizer jet is located at $x = 2$. The result shows that the flame temperature decreases as the CO_2 dilution increases (left) and increases as the reactor pressure increases (right). It is because as CO_2 dilution increases the mixture specific heat increases, hence the enthalpy released during the combustion process is absorbed by the CO_2 without increasing the temperature. Also, it is known that pressure can increase the combustion temperature which be seen the "inset" view of the Figure 72.

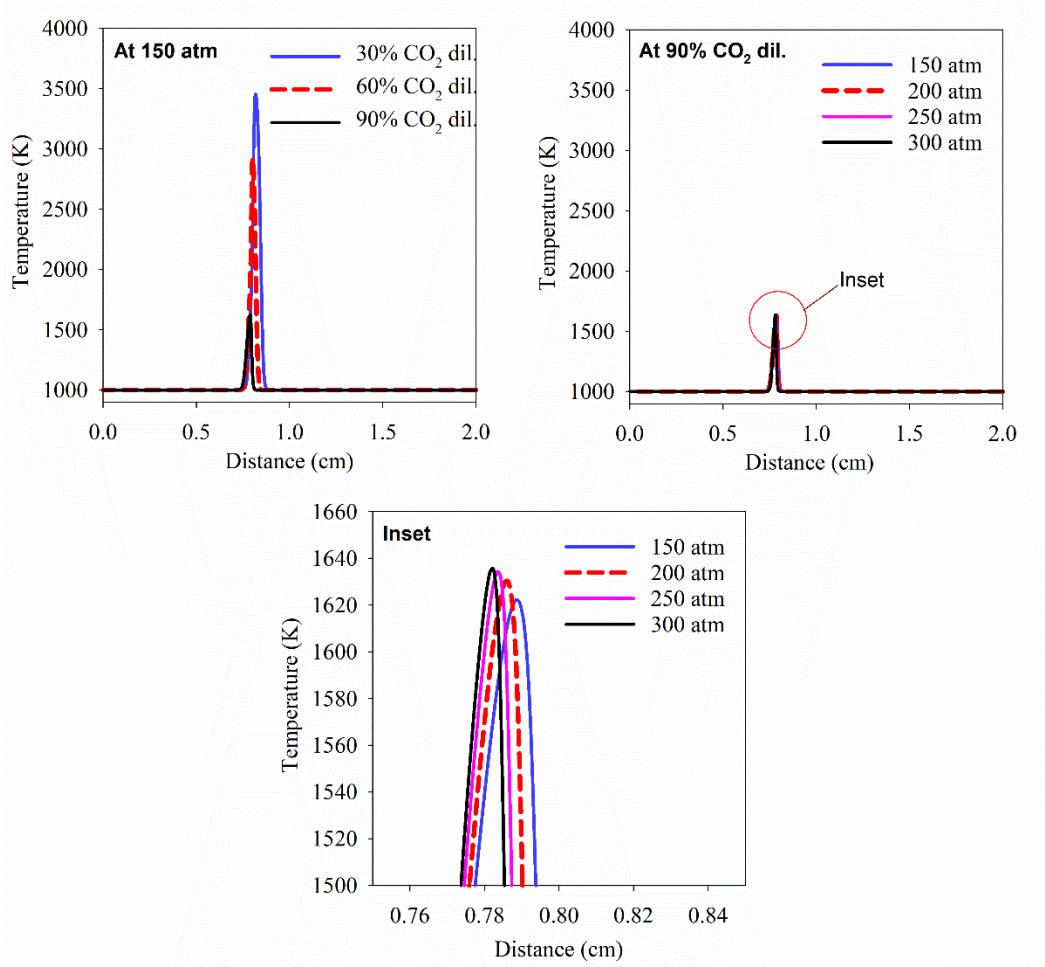

Figure 72: The variation of temperature with respect to percentage of CO_2 dilution and reactor pressure at U= 40 cm/s (Inset shows the zoomed view of temperature variation with pressure)

5.4.2 Influence on Prandtl number:

The Prandtl number compares the momentum and heat transport in a mixture. Also, this number provides insight of the sCO_2 non-premixed combustion characteristics. Prandtl number greater than unity represents that momentum is dominating the thermal diffusion rate and vice versa. The Prandtl number is defined as follows.

$$Prandtl\ numebr = \frac{\mu/\rho}{k/\rho c_p} \qquad (5\text{- }1)$$

The variation of Prandtl number with respect to CO_2 dilution and pressure is shown in Figure 73. The figure shows that, as the CO_2 dilution increases the Prandtl number on the flame (minimum value on the curve) and oxidizer stream increases. Also, pressure (right plot of Fig. 73) increases the Prandtl number on either side of jets. Here, the first observation is the overall Prandtl number in all these cases is less than one which clearly indicates that thermal diffusivity dominated momentum diffusivity in sCO_2 combustion.

Second, the Prandtl number is more influenced by the percentage of CO_2 dilution than by the pressure (note the pressure change is very high). The main reason for this change is thermal diffusivity and viscosity as shown in the Figures. 74 and 75. The thermal diffusivity and viscosity are increasing with increase in temperature however in this case the rise in thermal diffusivity is more than the viscosity so the resultant Prandtl number on flame is lowest for 30% CO_2 dilution. Also, increases in pressure reduce the diffusivity significantly more than increasing the viscosity as observed in the left side plots of Figs. 74 and 75. Hence, the Prandtl number on the jet increases.

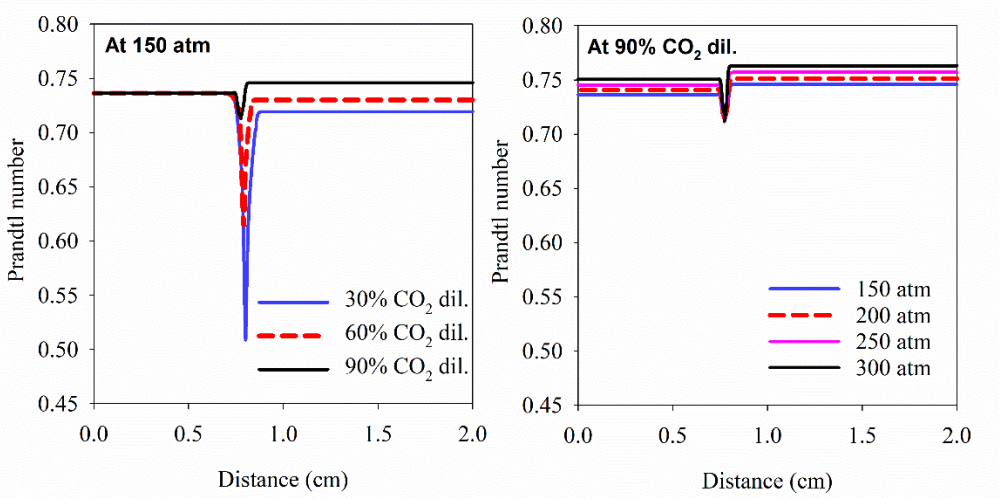

Figure 73: The variation of Prandtl number with respect to percentage of CO_2 dilution and reactor pressure (at U=40 cm/s)

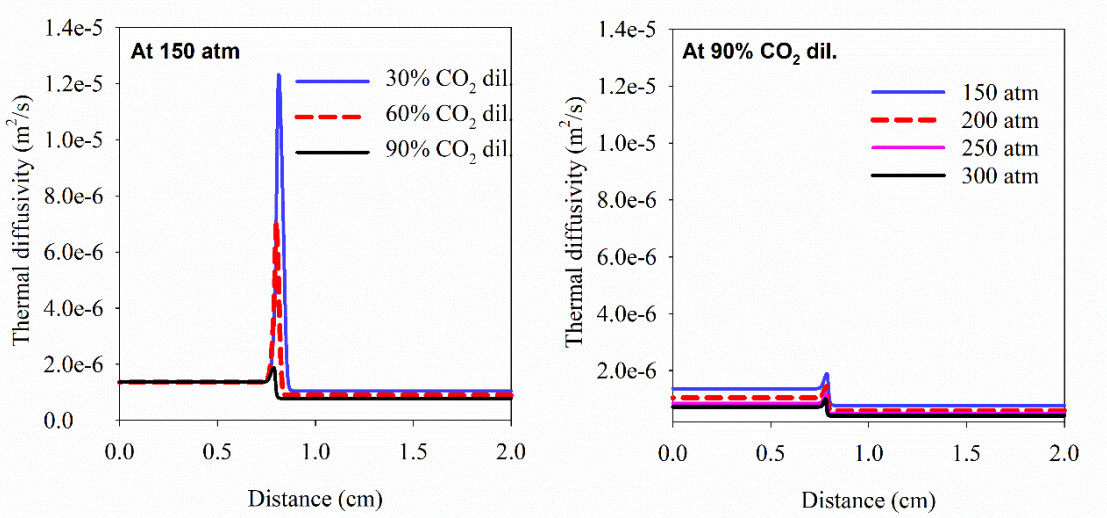

Figure 74: The variation of thermal diffusivity with respect to percentage of CO_2 dilution and reactor pressure (at U=40 cm/s)

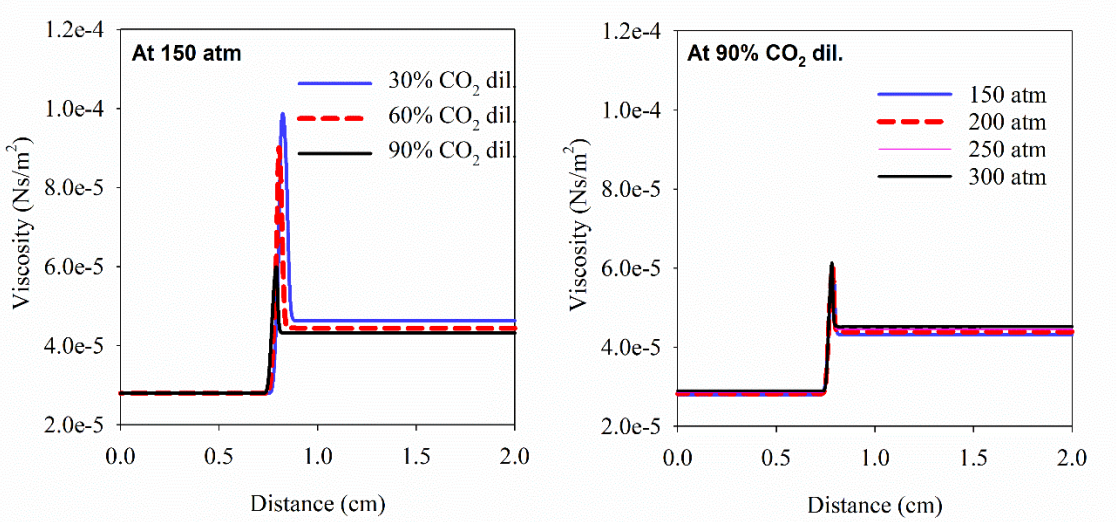

Figure 75: The variation of viscosity with respect to percentage of CO_2 dilution and reactor pressure (at U=40 cm/s)

Thirdly, the overall variation of Prandtl number between both the jets and flame is relatively very minimal for 90% CO2 dilution case. Therefore, assuming a constant value under this condition holds reasonable for simulations which accounts flame wall interactions. The average value of Prandtl number is varying only between 0.733-0.739 for all the pressure

conditions at 90% CO_2 dilution. For high fidelity of these simulations at lesser CO_2 dilution levels a variable Prandtl number approach needs to be considered.

5.4.3 Influence on the Lewis number:

The Lewis number is the ratio of thermal diffusion to the molecular diffusion as shown in the Eq. 5-2. The computation of D_k is challenging in a combustion code especially if there are many number of species are involved [242]. A most common assumption in premixed and non-premixed combustion is that this number changes very little across the flame [243] and hence assumed as constant (in general, it is assumed as one) for theoretical and model developments. This assumption may not hold good for some applications especially when the Lewis numbers are varying significantly across the flame and not equal to one. Hence, there are complex approaches available in non-premixed combustion literature which accounts the Lewis number variation [244]. Therefore, it is very important to analyze the nature of Lewis number in sCO_2 combustion before choosing an appropriate model or theoretical tool for analysis.

$$Lewis\ numebr = \frac{thermal\ diffusivity}{species\ diffusivity} = \frac{D_{th}}{D_k} = \frac{k}{\rho C_p D_k} \qquad (5\text{-}2)$$

Figures 76, 77, 78 shows the variation of Lewis numbers of CO_2, CH_4 and OH across the flame for the cases 1 and 2 as discussed previously in the Table 18. Further, Figure 79 shows the 'Lewis number on the flame' of some important species in sCO_2 combustion. Figure 76, 77, 78 shows that, the Lewis number of CO_2, CH_4 and OH towards the oxidizer side is lower compared to the fuel side. It is mainly due to lesser thermal diffusivity towards oxidizer side (can be seen in Fig. 74). Next, the Lewis number for these species are approximately same for fuel jet at all different levels of dilution whereas towards the oxidizer side Lewis number keeps decreasing with increase in the CO_2 dilution and hence increases the difference in the Lewis number across the flame. Again, this can be attributed to the decline in thermal diffusivity with dilution.

As explained earlier, Figure 79 shows the Lewis number of few important species on the flame. Here, the horizontal axis represents the reactor pressure and each subplot has Lewis number information at three different dilution conditions. The figure illustrates that, for all the species shown, the Lewis number decreases with increases in dilution. It should be noted that, on each subplot the Lewis number curves at different CO_2 dilutions are differentiated by almost same magnitude. It shows that, increase in 30% CO_2 dilution reduces the Lewis number of species approximately by 15%. Further, Lewis number is not significantly influenced by the change in the pressure.

The magnitudes of Lewis numbers of OH and H_2O shows that the molecular diffusivity of these species is slower compared to heat diffusivity whereas for rest of the species it is reversed.

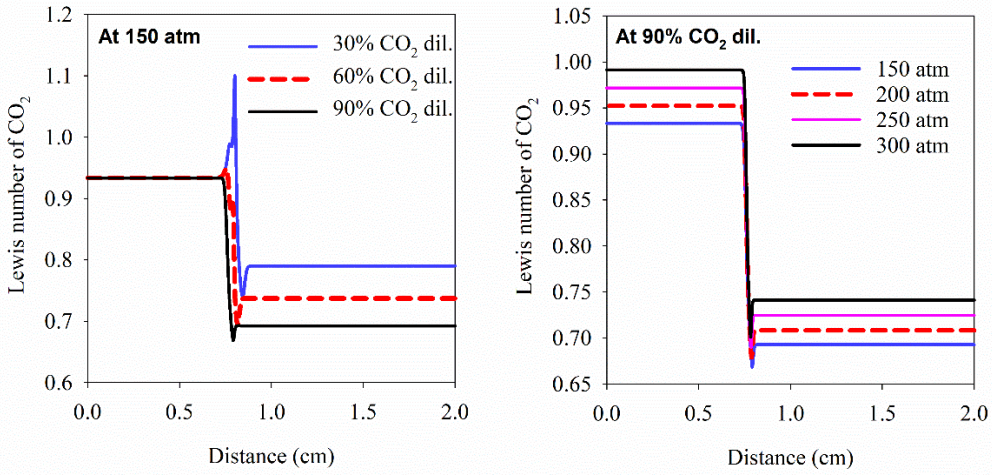

Figure 76: The variation of CO_2 Lewis number with respect to percentage of CO_2 dilution and reactor pressure (at U=40 cm/s)

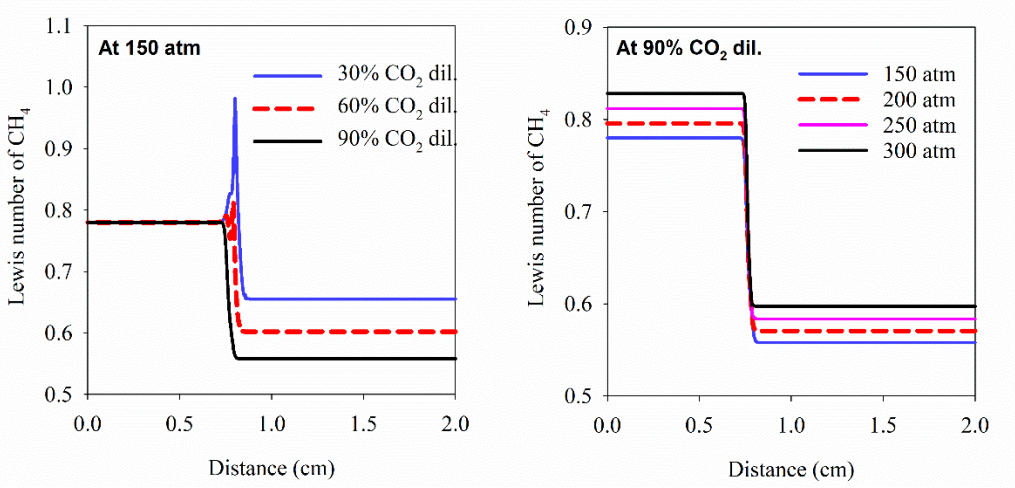

Figure 77: The variation of CH4 Lewis number with respect to percentage of CO2 dilution and reactor pressure (at U=40 cm/s)

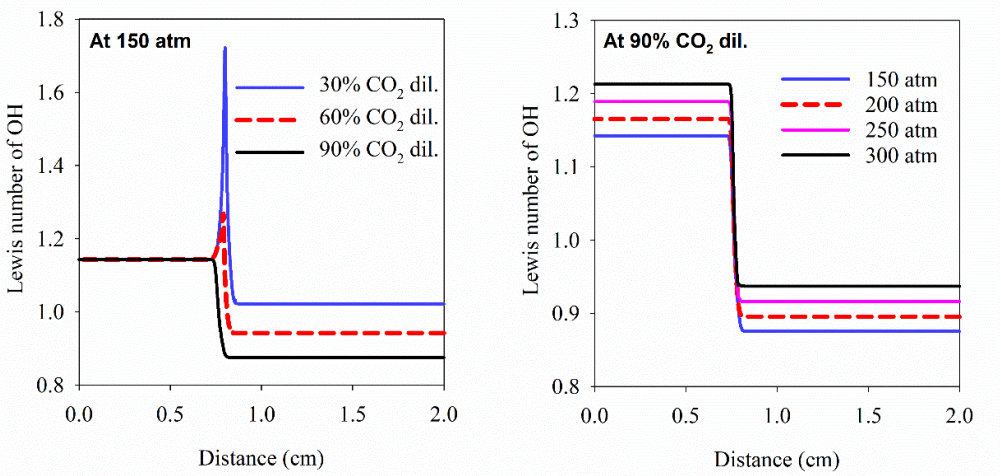

Figure 78: The variation of OH Lewis number with respect to percentage of CO_2 dilution and reactor pressure (at U=40 cm/s)

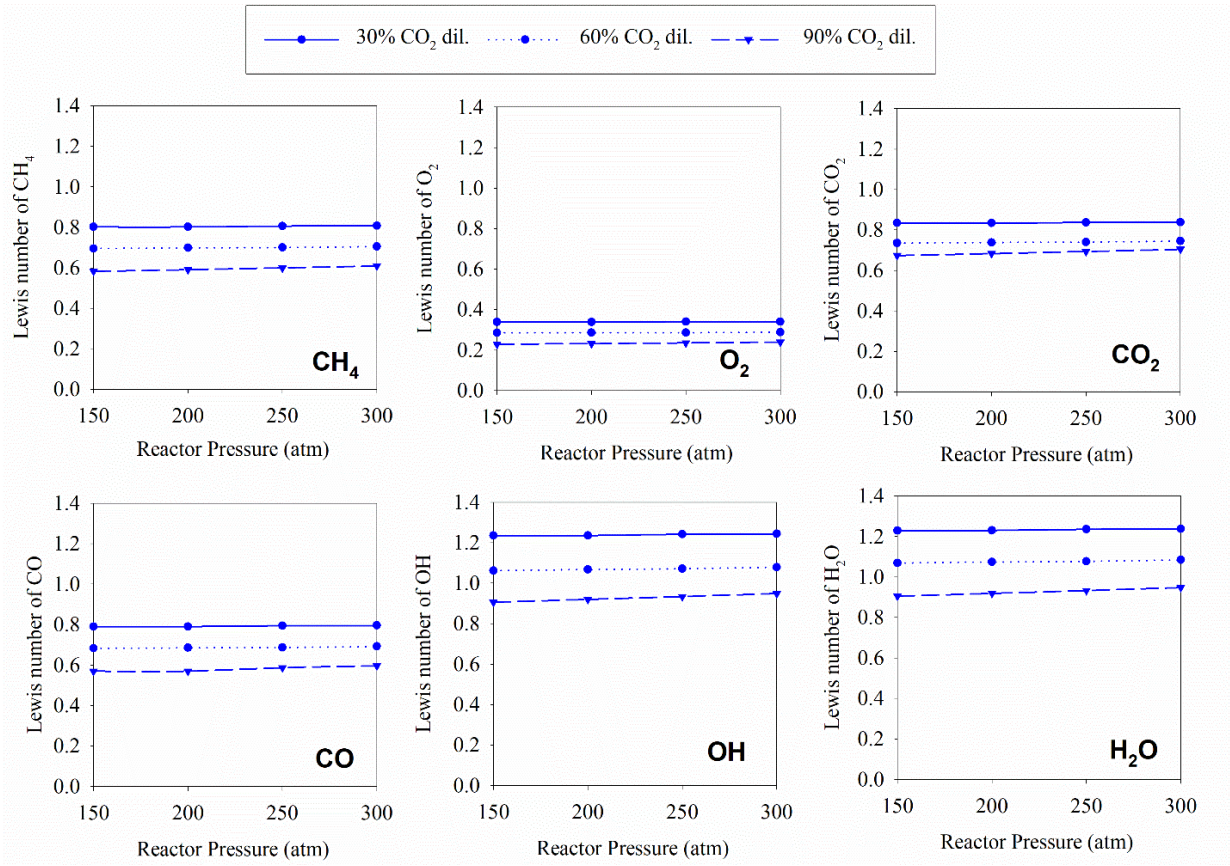

Figure 79: Variation of Lewis number on the flame of various important species in Oxy-Methane combustion with respect to percentage of CO_2 dilution and reactor pressure (at U=40 cm/s)

5.4.4 Influence on the Damköhler number:

Damköhler number is the ratio of flow time scale to the chemical time scale. Therefore, the flow and chemical effects on the diffusion flame structure are generally quantified by the Damköhler number. Some flamelet solution methodologies [242] assume that the combustion is fast i.e. Da=∞, so that that the products form instantaneously (achieves equilibrium instantaneously). Such, methodologies do not account for the dependency of scalar dissipation on the solution (or assume χ=0). However, finite rate chemistry must be accounted in the flame zone (important near to stoichiometric mixture fraction) when Damköhler number has a finite value. In

the current study, the flow time scale is taken as the inverse of the stoichiometric scalar dissipation rate $(1/\chi_{st})$ and the global chemical timescale is computed based on Eq. 5-3. Eq. 5-3 represents the inverse of non-dimensionalized energy release rate [245]. Here, h_p is obtained from the OPPDIF solution and the mixing line enthalpy is calculated based on the pure mixing (frozen chemistry) assumption.

$$Chemical\ time\ scale = \frac{h_p - h_{mixing\ line}}{\sum_i^{kk} \dot{\omega}_i h_{fi}/\rho} \qquad (5\text{-}3)$$

Here, $h_p - Enthalpy\ of\ products\ (\frac{J}{kgK})$

$h_{mixing\ line} - Enthalpy\ of\ unburnt\ reactants\ on\ pure\ mixing\ line\ (\frac{J}{kgK})$

$\dot{\omega} - molar\ production\ rate\ of\ species\ 'i'\ (\frac{mol}{m^3 s})$

$h_{fi} - Heat\ of\ formation\ in\ molar\ units\ (\frac{J}{mol})$

$kk - number\ of\ species$

$\rho - Density\ (\frac{kg}{m^3})$

Figure 80 shows the variation of Damköhler number with respect to the pressure and dilution. First, it can be observed that the Damköhler number is finite at all different levels of dilution and significantly lower at high CO_2 dilution case. Therefore, this finite value to the Damköhler number represents that sCO_2 combustion falls in finite rate chemistry regime. A more elaborate discussion on this result can be found in [246].

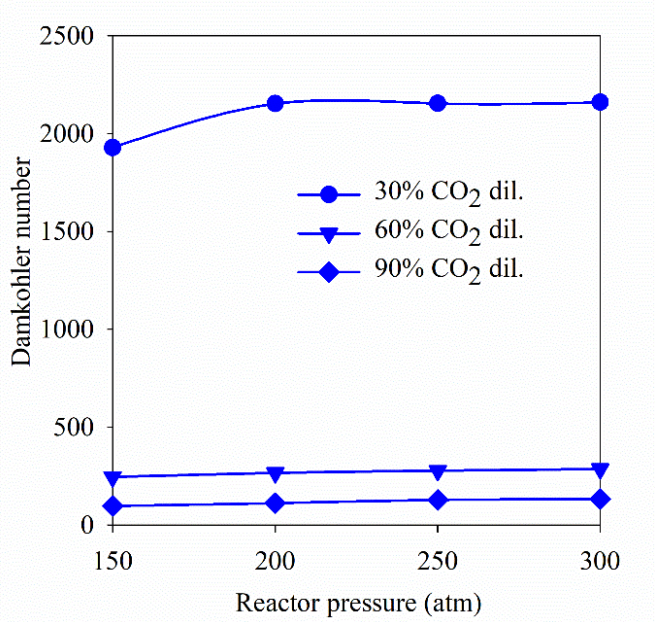

Figure 80: The variation of Damköhler number with respect to pressure and dilution (U=40 cm/s)

5.4.6 Implementation of real gas models in OpenFOAM CFD

Real gas chemical kinetics, equation of state, thermal, and transport properties are implemented in counterflow flame code and premixed conditional moment closure (PCMC) model to couple it with OpenFOAMCFD. The counterflow solution in physical space is mapped in mixturefraction space to tabulate chemistry at various values of scalar dissipation (until extinction) to simulate non-premixed sCO2 combustion. The same approach is followed for premixed sCO2 combustion simulations as well. A sample test simulation with PCMC-sCO2 CFD is shown in Figure 81.

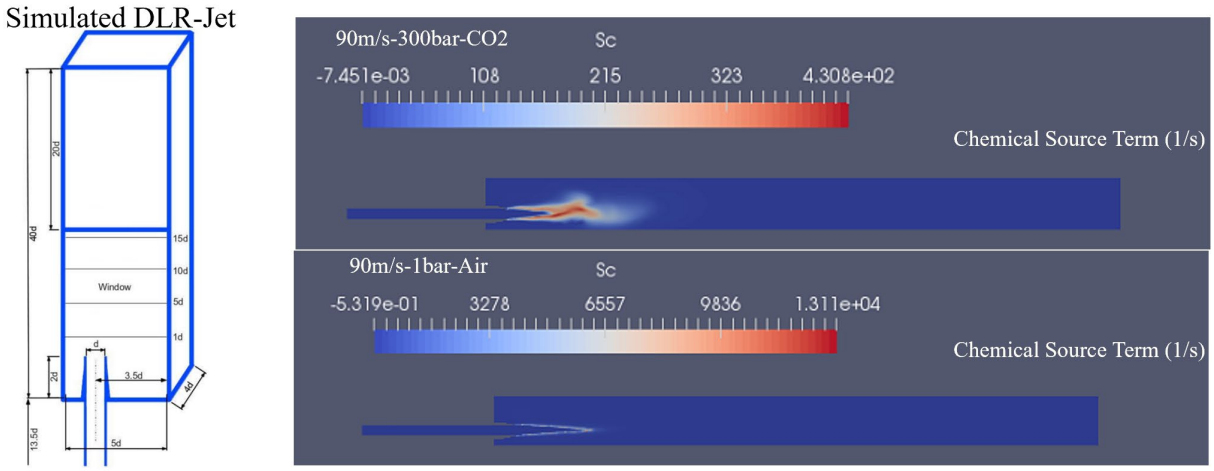

Figure 81: A sample premixed sCO2 simulation perfomed with OpenFoam CFD

5.5 Conclusions

Work presented in this chapter here is a step towards addressing the modeling challenges faced by sCO_2 combustion at high pressures. A counterflow diffusion flame analysis was performed for supercritical CO_2 combustion by using an updated OPPDIF code. This updated code accounts for the real gas effects in both thermal and transport properties. The viscosity and thermal conductivity are modelled with Lucas et al. [227, 228], and Stiel and Thodos models [229], respectively. Also, a 24-species mechanism derived from the UCF 1.1 mechanism (a mechanism developed for sCO_2 applications) is used. Further, the nature of some important non-premixed combustion characteristics such as Prandtl number, Lewis number, scalar dissipation, flame thickness, Damköhler number are investigated at various levels of CO_2 dilution (in the oxidizer stream) and supercritical pressures.

Some important conclusions from this study are as follows:

1) The Peng-Robinson and Soave-Redlich-Kwong equation of state are identical in terms of their prediction at high CO_2 dilutions (sixty and ninety percent dilutions) whereas they

differ significantly at lower CO_2 dilutions. Therefore, validation is recommended at lower dilution conditions.

2) The Prandtl number in sCO_2 combustion is always less than unity. Further, an increase in the CO_2 dilution increases the Prandtl number in the flame. At 90% CO_2 dilution the difference between the Prandtl number in the flame and the inlet streams (oxidizer and fuel streams) is very small hence a constant Prandtl number assumptions holds reasonably well. Increase in reactor pressure increases the Prandtl number but the change is not as significant as with dilution.
3) The Lewis number varies significantly across the flame due to the large difference in the thermal diffusivity of fuel and oxidizer streams. Further, the increase in CO_2 dilution towards the oxidizer side increases the difference of Lewis number across the jets. Also, the Lewis number for some important species in the flame and their variation with respect to dilution and pressure is reported. The Lewis number of species is more influenced by dilution than to pressure. Interestingly, the drop in the Lewis number with dilution follows a certain proportion. Every 30% rise in CO_2 dilution drops the Lewis number of the species by 15%. The results show that assuming Lewis number equal to unity may not hold good for sCO_2 combustion applications.
4) The increase in CO_2 dilution decreases the stoichiometric scalar dissipation χ_{st}, which implies that flow timescales (mixing) getting longer with dilution. Also, χ_{st} increases a little with an increase in pressure.
5) The flame thickness increases with an increase in CO_2 dilution and reduces with pressure.
6) The Damköhler number decreases with an increase in CO_2 dilution. Also, the CO_2 dilution influences the chemical times scale more significantly than flow time scales. Both chemical

timescale and flow time scale becomes larger with dilution, however chemical time scale increases more than flow time scale. It means that, Damköhler number drops non-linearly with respect to the CO_2 dilution. This observation is very important for the operation of sCO_2 combustor.

7) The Damköhler number is too small in high CO_2 dilution conditions and large in low CO_2 dilution conditions. Hence, overall combustion cannot be categorized as too fast or too slow as the time scale of combustion depends on the local percentage of CO_2. Hence, the turbulent combustion model for sCO_2 combustion simulation needs to be applicable in all the regimes of Damköhler number.
8) Realgas thermal, transport, kinetics are implemented in OpenFOAM CFD bu using counterflow flame and PCMC approaches.

CHAPTER 6: SUPERCRITICAL CO2 HEAT TRANSFER COEFFICIENT MEASUREMENTS

6.1 Introduction

Near the thermodynamic critical point, effects of buoyancy on sCO2 internal heat transfer have been reported by many authors. In the case of flow-through heated tubes, the temperature difference between wall and bulk flow can cause variation in density. This can generate buoyancy forces, which affect secondary flow structures and turbulence generation in the flow hence, thus affecting convection heat transfer.

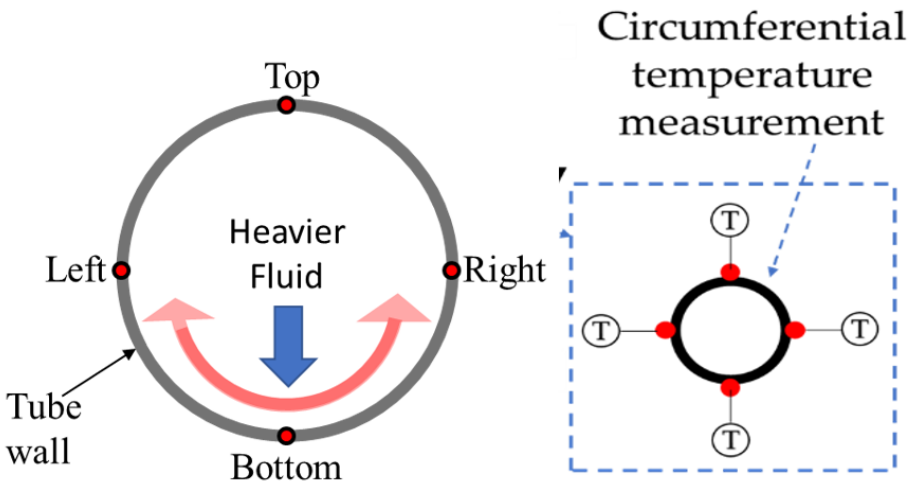

Figure 82: Schematic showing buoyancy flow formation (left) and circumferential measurement strategy for this work(right)

Most of these studies are performed for temperature and pressure near the critical point of CO_2. Study of heat transfer away from pseudocritical temperature can be valuable for the design of components of sCO_2 cycle that operate away from the critical point such as heat exchanger and

recuperators, especially for shell-n-tube type recuperators with macro sized tubes where effects of buoyancy are more probable. In addition to that, such information can be used to design turbine blade internal cooling passages. This report presents sCO_2 heat transfer in a horizontal or an inclined tube covering temperature and pressure ranges for recuperators and primary heat exchangers and provides insight into varying effects of buoyancy on heat transfer. As seen from Figure 82, non-linear variation in properties still exists till 300^oC for 200 bar pressures.

It is anticipated that the effects of buoyancy on heat transfer will gradually diminish as conditions move away from the pseudocritical point. However, more results and comparison against available heat transfer correlations are necessary to investigate exactly what the criterion is when effects of buoyancy can be neglected. The temperature at which these buoyancy effects start to disappear can depend on CO_2 pressure and testing conditions such as mass flux and heat flux. Studies reporting the exact temperature limit where buoyancy effects start to disappear have not been published yet. Detailed heat transfer experiments for this range have not been reported yet. This may be due to difficulty in performing experiments at higher temperature. Heating and cooling requirements increase substantially in order to perform these experiments since pumps in the loop operate at temperatures as low as or lower than ambient temperature. This increases size of the experimental setup, considerably increasing complexity and cost. In addition to that, experiments are limited to the highest operating temperature of the metal tube at high heat flux conditions. Experiments at such a large scale can also be vulnerable to transient effects of surrounding temperature, adding difficulty to achieve steady state results. The experimental setup for this study is designed considering all the above potential difficulties.

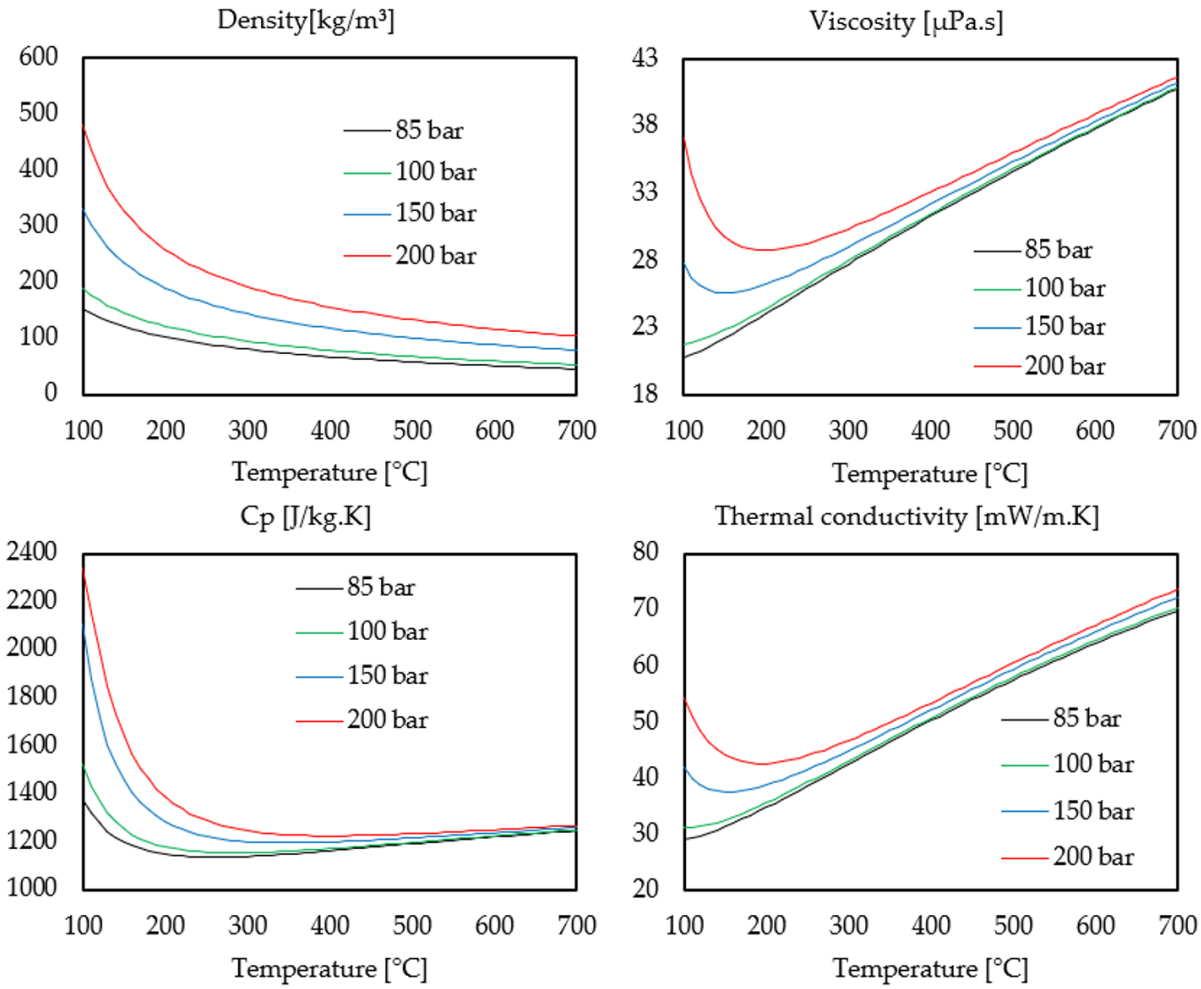

Figure 83: Property variation for CO_2 with pressure and temperature plotted using CoolProp NIST tables

6.2 Experimental rig description

The experimental loop for this study is designed with considering high pressure (200 bar) and high temperature (540ºC for Stainless steel and 700ºC for Inconel) operating conditions. Because of such high pressure and temperature conditions, the experimental approach uses electrically heated pipes, as opposed to use of heating foils transient thermal experiments for measurement of heat transfer coefficient. Since the heating is done by providing electricity to the metal tubing, the tubing cannot have any machining done for optical window access. It is not possible to create pressure taps for local pressure measurements as this machining will cause nonuniformity in heat flux. Hence for the current testing, seamless stainless-steel tubing with outside wall temperature measurements is utilized. For safe operation at such extreme conditions, ASME B31.3 Pipe Code is followed to ensure the pressure rating of the tube. The schematic of the experimental rig can be seen in Figure 84. The test loop is setup in a closed loop configuration to conserve usage of CO_2. Before filling the loop with CO_2, the loop is vacuumed to remove any air ensuring close to pure concentrations of CO_2 for testing. The loop is also equipped with an exhaust system to safely discharge the loop. CO_2 cylinder and booster pump are used in series to pressurize the loop to the desired pressure. After the filling process, the booster pump is disconnected using an ON/OFF valve from the loop.

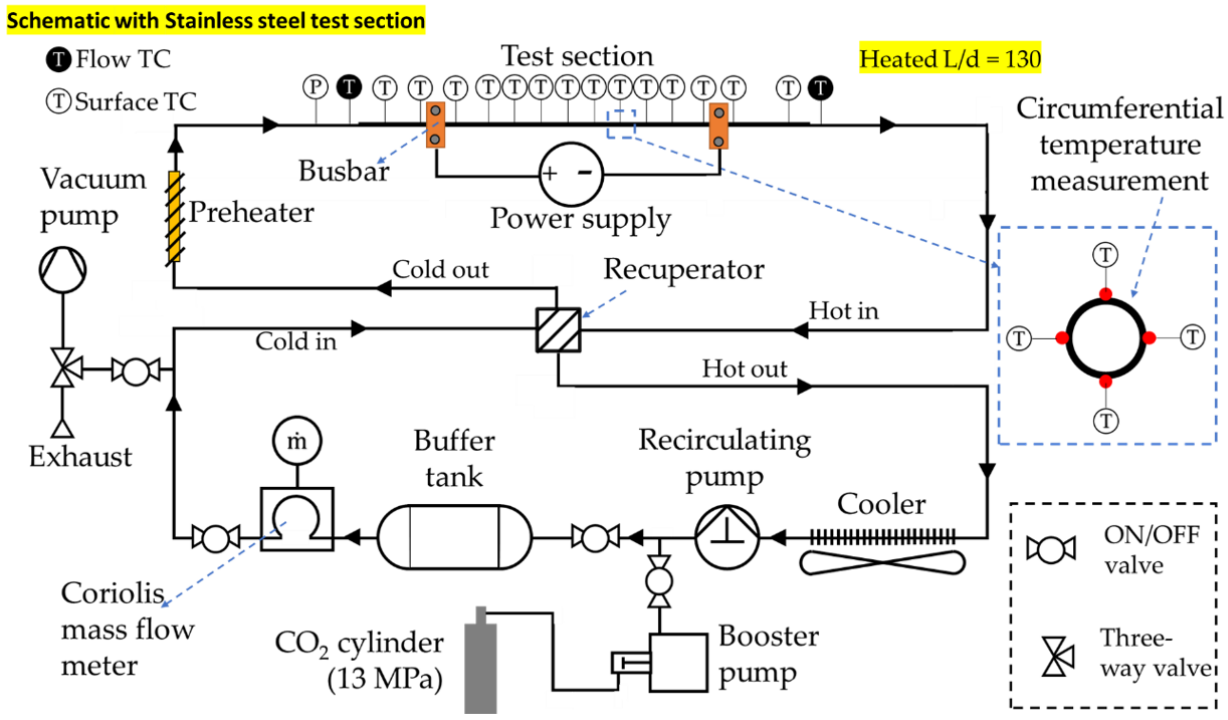

Figure 84: Schematic of the experimental setup with stainless steel test section

Sigma pump (plunger type positive displacement pump), as shown in Figure 85 is used to circulate sCO_2 through the loop with capabilities of maximum differential pressure of 4MPa and maximum operating pressure of 30MPa. A buffer tank is used downstream of the Sigma pump to absorb any possible pressure fluctuations and deliver a constant steady mass flow rate to the test section. For inclined rig setup, Micropump gear pump is used. Specifications of both pumps are shown in Figure 85. Coriolis mass flow rate meter is used to measure mass flow rate. The temperature inlet to the test section is controlled using a preheater made from wrapped around electric rope heaters and voltage controlling variacs. The heating of the test section is achieved using a DC power supply which is connected to the test section tube using machined copper busbars. These machined copper busbars ensure low contact resistance achieved from good contact with the test section tube. A busbar that is in loose contact with the tube might create a local spike in heat generation, making it difficult to account for heat transferred to the flow. sCO_2 coolers are

used downstream of the test section before the gear pump to protect gear pump, valves and Coriolis mass flow rate meter from exceeding their high temperature limit as well as to achieve overall steady state during testing. These coolers are shown in Figure 86. First cooler consists of a fan blowing ambient air on a finned stainless steel tube array to cool from high temperatures to 50-80ºC. Then sCO_2 is further cooled to 25-30ºC using cooling coils immersed in cold water. The cold water temperature is regulated using a water chiller.

The inlet flow temperature is measured using a K-type thermocouple probe inserted into the flow. Static pressure is measured at the inlet using a pressure transducer. The test section includes an unheated section with L/D_{int} = 90, heated section with L/D_{int} = 130 and unheated section L/D_{int} = 90 before measuring outlet flow temperature using a K-type thermocouple probe inserted into the flow. These values of L/D_{int} ratios are chosen based on conventional values necessary to fully develop hydrodynamic boundary layer and thermal boundary layer. The data reduction process takes into account outside wall temperatures in the test section, which are measured using K-type themocouples welded on the tube surface. At each axial location, 4 surface thermocouples are welded at 90º tangential intervals to measure temperatures at top, bottom, right and left wall locations (as shown on the right side of Figure 84). Electric heating is accounted by measuring the current provided by the DC power supply and voltage measured between two busbars. The maximum pressure limit of the test section is 24 MPa at a maximum surface temperature limit of 537ºC (1000F).

Sigma pump plunger pump

- Max inlet temperature = 37°C
- Pressure on suction inlet of the pump
  - Min 80 bar, Max 260 bar
- Pressure on discharge outlet of the pump
  - Min 120 bar, Max 300 bar
- Max differential pressure = 40 bar
- Mass flow rate range
  - 0.66-16.5 L/min *OR* 0.01-0.25kg/s @910 kg/m^3

Micropump gear pump

- Max inlet temperature = 150°C
- Maximum system pressure = 103 bar
- Max differential pressure = 8.7 bar
- Mass flow rate range
  - 3.21 L/min *OR* 0.05kg/s @910 kg/m^3

Figure 85: Recirculating pumps in the loop

- ***Each heat exchanger is custom-designed and in-house fabricated***
- Air cooler to cool CO_2 from higher temperatures to 50-80°C
- Water cooler to cool CO_2 to 25-30°C (required at inlet of recirculating pump)

Air cooler

- Finned tube bank over the fan (left bottom)
- Canopy+duct for fan exhaust out of the room
- Dielectric union is connected between air cooler and water cooler
- Flow TC between air and water cooler to monitor temperature going into water cooler below ~90°C

Water cooler

- Tube bank for CO2
- Insulated water drum with distilled water (right bottom)
- 2 re-circulating pumps inside for increased convection
  - Bottom to top and Tangential to inner side

Figure 86: Coolers in the loop

6.3 Test Section experimental and numerical Setup

In addition to experimental study, CFD study is also performed for the same test section setup. Numerical domain dimensions and instrumentation locations are identical to the test rig (Inlet/exit bulk temperature, surface temperatures, heating busbars). These are shown in Figure 87. Conjugate CFD is performed, including the stainless steel metal domain with temperature varying property tables for stainless steel along with flow domain with sCO_2. Simulations are run in ANSYS Fluent with inbuilt NIST Real Gas model tables. Meshing is done in ANSYS workbench with Multizone method. Y+ values observed throughout the domain is less than 1 in order to model convection heat transfer properly. External Wall Convective heat loss boundary expression is based on experimentally derived heat loss data. Wall heating in test section through domain source volumetric heat generation.

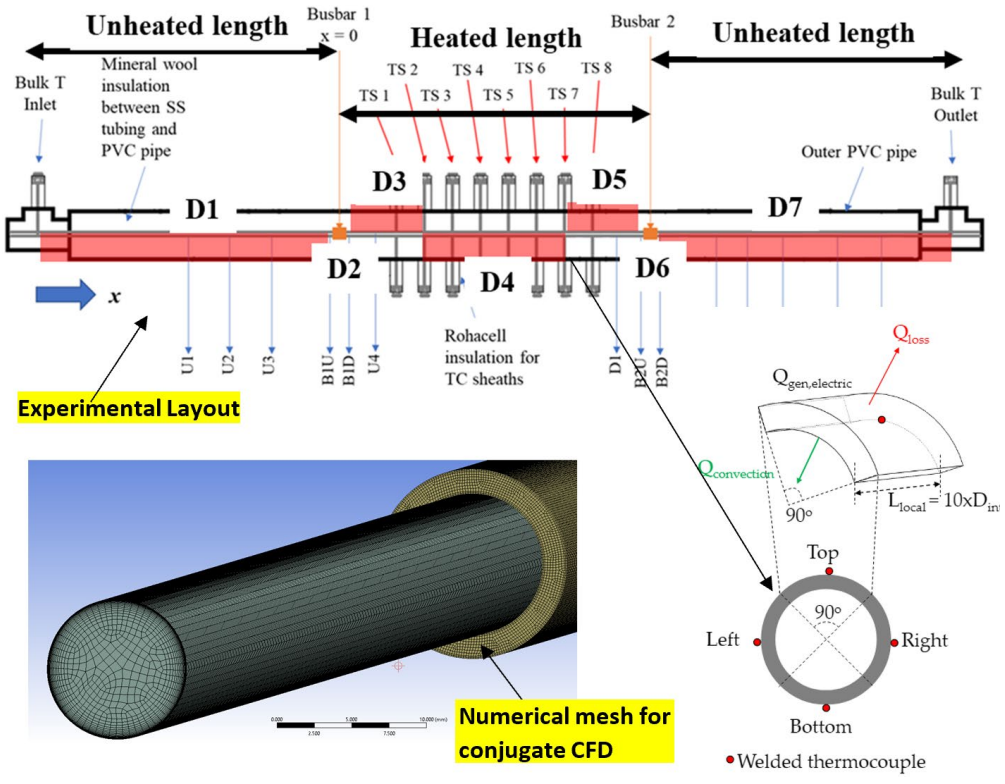

Figure 87: Test section experimental and numerical setup

6.4 Heat loss tests

Even though the stainless-steel tube is encased in an insulated duct with dimensions around 35 times of tube outer diameter, heat loss through the ceramic fiber insulation to the surrounding is imminent, especially for experiments with wall temperatures as high as 500-700^{o}C. Hence heat loss calculations are important to calculate heat transfer coefficient correctly. Heat loss from the tube to ambient is a function of the difference between tube wall temperature and ambient (T_{w-amb}), outer tube area and area specific equivalent conductance (U_{loss}[W/m^{2}K]) between outer wall of tube and ambient. The goal of heat loss tests was to calculate this equivalent conductance, U_{loss}, since the other two parameters are known. T_{w-amb} is measured using thermocouples instrumented on outer wall of tube and ambient. The local outer tube area of the required section is calculated knowing dimensions of tube and length of the section. To calculate U_{loss}, the test loop is vacuumed so that the inside wall of the tube does not experience any surface heat convection. Here, it is assumed that the axial conduction from heated section of the tube to unheated section of the tube is negligible. Four heat loss tests are performed with four different values of electric power to cover the range of T_{w-amb} expected from flow experiments. U_{loss} is calculated for each case and plotted against T_{w-amb} to obtain an expression for U_{loss}. This plot is shown including the expression for U_{loss} in Figure 88. The linear increase observed in Uloss with T_{w-amb} is due to linear increase thermal conductivity of ceramic fiber insulation with temperature.

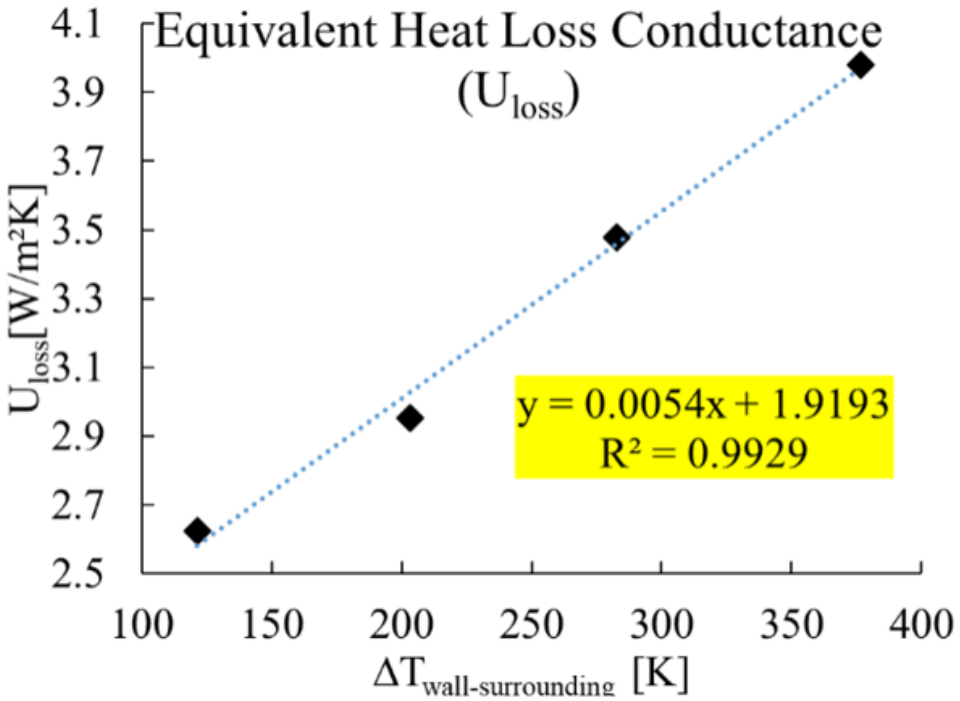

- $\text{Heat loss} = U_{loss} \times \Delta T_{wall\text{-}surrounding} \times A_{surface}$

Figure 88: Results from heat loss

6.5 Validation of experimental setup using air heat transfer

Due to the unconventional nature of experimental setup described here, it is important to validate the correctness of experimental results and data reduction process obtained from this setup. A similar experimental setup with electrically heated surface and data reduction with measurement of external surface thermocouples have been presented by several authors for sCO_2 heat transfer studies. Among these authors, only Guo et al.* have calibrated their experimental system by running single phase heat transfer experiments with de-ionized water. Their heat transfer results matched well with prediction from Dittus-Boelter Nusselt number correlation with largest error less than ±10%. For this paper, validation experiments with high pressure air were conducted to establish the baseline confidence interval for the sCO_2 tests and the data reduction procedure.

For testing air heat transfer, the loop was converted to open loop configuration by disconnecting the circulating pump and connecting high pressure air from a compressor with other open end acting as exhaust for the air. Reynolds number tested for these air validation cases are between 20,000 and 50,000. Additionally, similar Reynolds numbers were also tested at two different heat fluxes to show validity of heat transfer results. This is listed in Table 6.1 for Reynolds number of 32,000 where the two heat fluxes tested are 15 and 46kW/m^2. Even at different heat fluxes, Nusselt numbers are within good agreement of Nusselt number obtained from Gnielinsky correlation as well as with each other. Overall, for all air tests, the Nusselt number calculated from experiments fit well with predicted Nusselt numbers from Gnielinksy conventional correlations. This is shown in Figure 89. The largest error between the predicted Nusselt numbers and calculated values was less than ±4% for the range of Reynolds number tested.

Due to the unconventional nature of the experimental setup described here, it is important to validate the correctness of experimental results and data reduction process obtained from this setup. A similar experimental setup with electrically heated surface and data reduction with measurement of external surface thermocouples have been presented by several authors for sCO_2 heat transfer studies. Among these authors, only Guo et al.* have calibrated their experimental system by running single phase heat transfer experiments with de-ionized water. Their heat transfer results matched well with prediction from Dittus-Boelter Nusselt number correlation with largest error less than ±10%. For this paper, validation experiments with high pressure air were conducted to establish the baseline confidence interval for the sCO_2 tests and the data reduction procedure. For testing air heat transfer, the loop was converted to open loop configuration by disconnecting circulating pump and connecting high pressure air from a compressor with other open end acting as exhaust for the air. Reynolds number tested for these air validation cases are between 20,000

and 50,000. Additionally, similar Reynolds numbers were also tested at two different heat fluxes to show the validity of heat transfer results. This is listed in Table 19 for Reynolds number of 32,000 where the two heat fluxes tested are 15 and 46kW/m^2. Even at different heat fluxes, Nusselt numbers are within good agreement of Nusselt numbers obtained from Gnielinsky correlation as well as with each other. Overall, for all air tests, the Nusselt number calculated from experiments fit well with predicted Nusselt numbers from Gnielinksy conventional correlations. This is shown in Figure 89. The largest error between the predicted Nusselt numbers and calculated values was less than ±4% for the range of Reynolds number tested.

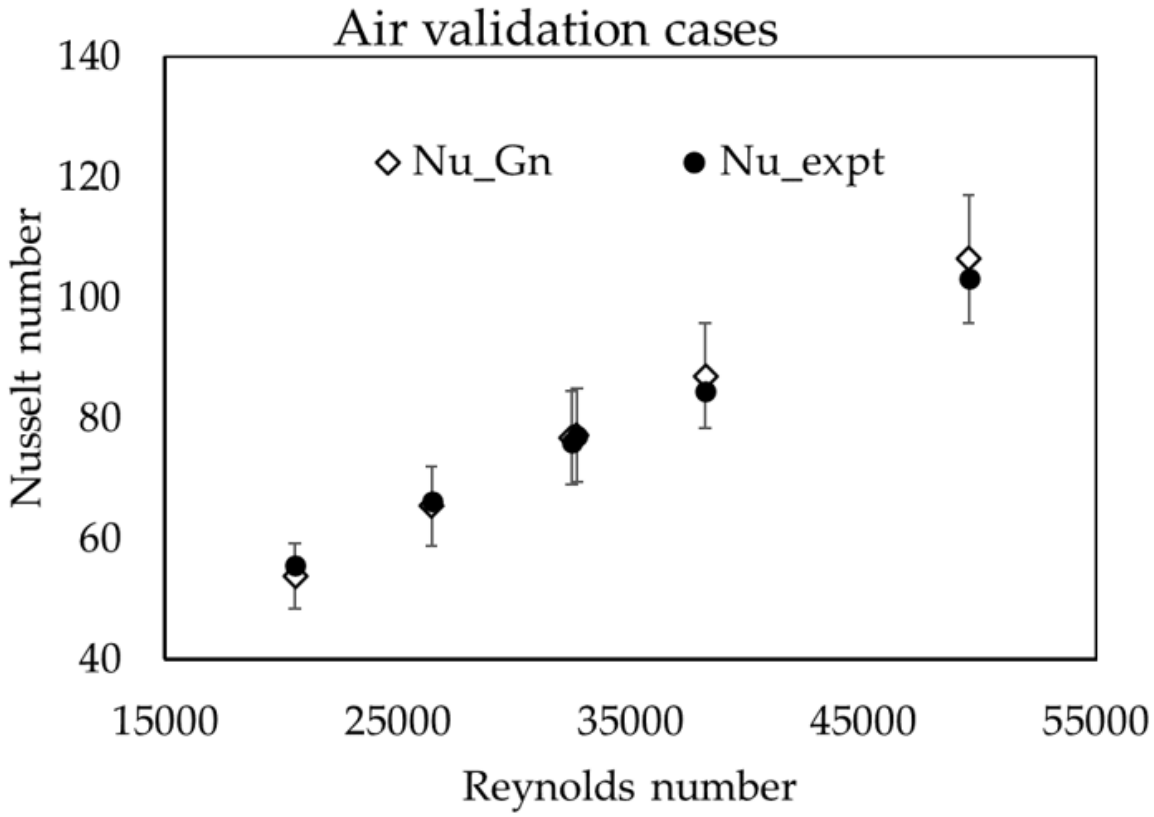

Figure 89: Results of air validation cases. Maximum deviation observed was less than 4% from Gnielinski correlation

Table 19: Validation results using air heat transfer experiments

Reynolds number	Heat flux	Nu_expt	Nu_Gn	Deviation
20581	13	56	54	-3%
26452	16	66	65	-1%
32693	15	77	77	0%
32470	46	76	77	1%
38213	45	85	87	3%
49544	27	103	106	3%

6.6 Results and Discussion: ½" Stainless steel test section

All tests performed under this study are with bulk flow inlet temperature higher than 100°C. Testing parameters are listed in Table 20. For all cases, temperatures at right wall and left wall surfaces are found to be same. Henceforth, all the results for right and left wall are plotted as a common location called side wall. Nusselt number is used as the basis to evaluate and compare amount of heat transfer at different locations and at different testing conditions. A local calculation domain for Nusselt number is shown in Figure 87 showing 90° sector of circumference of the tube. The domain also shows major heat transfer pathways. Gnielinski correlation is used to obtain Nusselt number from bulk flow properties to compare with experimental Nusselt number calculated at wall.

Table 20: Experimental parameters for testing with 1/2" Stainless steel tube

Parameter	Experimental testing range
Tube I.D.	9.4 mm
Inlet pressure	85-205 bar
Inlet temperature	100-432°C
Heat flux	47kW/m^2
Mass flux	180 kg/m^2s
Reynolds number	50,000-140,400

6.7 Repeatability and steadiness of testing

Test to test repeatability is verified by performing tests at 90 bar and varying inlet temperatures of 110, 120, 130,140ºC. Each test is repeated for three different days. Results of repeatability tests are shown in Figure 90. During these tests, maximum deviation found for mass flow rate was within 0.1%, for inlet pressure within 0.3% of average value. Inlet temperature was repeated within 0.6ºC. Figure 90 also shows plot of temperatures measured on external wall showing good repeatability.

\

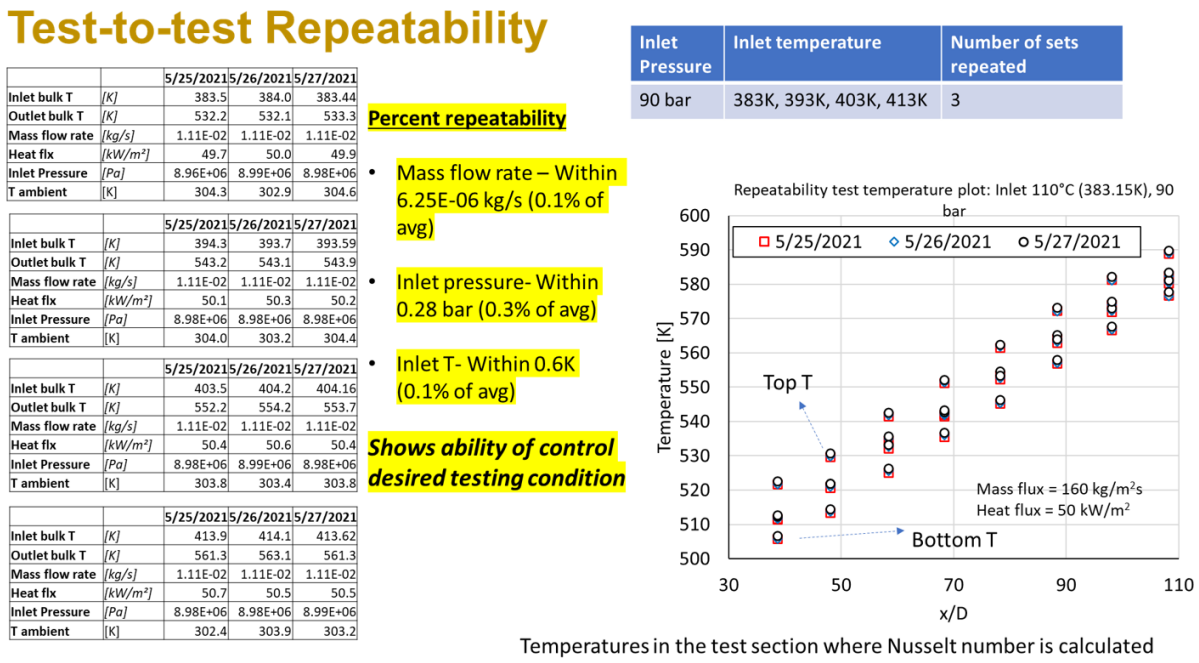

Figure 90: Repeatability tests results

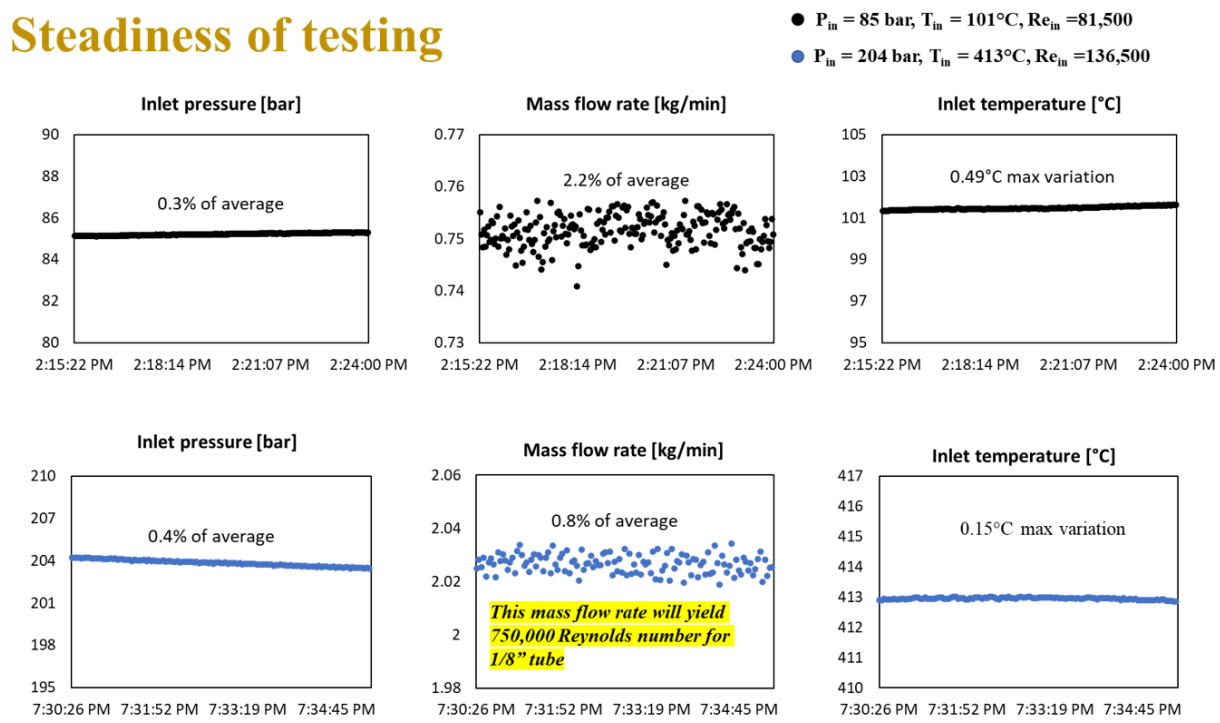

Figure 91: Steadiness of testing for steady state data acquisition

Heat transfer calculations presented in this work are for steady state results. Hence it is important to check the steadiness of testing. Figure 91 shows steady state data of two tests run at two different conditions. For test at lower pressure of 85 bar, the maximum deviation from the average value of pressure was within 0.3% while mass flow rate maximum deviation was within 2.2% of its average value. Inlet temperature was within 0.49ºC from its average value. For the test at higher pressure of 204 bar, the maximum deviation from the average value of pressure was within 0.4%, while the mass flow rate maximum deviation was within 0.8% of its average value. Inlet temperature was within 0.15ºC from its average value. This shows that the experiments reached proper steady-state so as to obtain steady-state heat transfer results.

6.8 Effects of varying pressure

To study effect of pressure on heat transfer away from critical point, experiments are performed at 85 bar, 90 bar and 100 bar with the same testing conditions. Bulk flow inlet temperature is kept constant for three tests at 100°C with a constant mass flux of 180 kg/m^{2}s and heat flux of 47 kW/m^2. For all three inlet pressure cases at 100°C inlet temperature, buoyancy effects on heat transfer can be seen from the top and bottom surface differences. Nusselt numbers are plotted in Figure 92. Even at 100°C, away from pseudocritical temperature, the observed difference between top and bottom wall Nusselt number is 17-20%. This shows that buoyancy effects on heat transfer cannot be neglected at such conditions. However, values of Nusselt numbers at all wall locations are comparable to each other for the three cases as seen from local Nusselt numbers and average Nusselt numbers as seen from Figure 92. This shows the minimal effect of pressure on heat transfer at conditions tested. This is mainly because buoyancy effects are driven by the density difference between the bulk flow. Density variation away from the critical point is more affected by temperature change compared to pressure change. However, a slight increase in buoyancy effects at higher pressure is due to the slightly higher values of density difference at higher pressure.

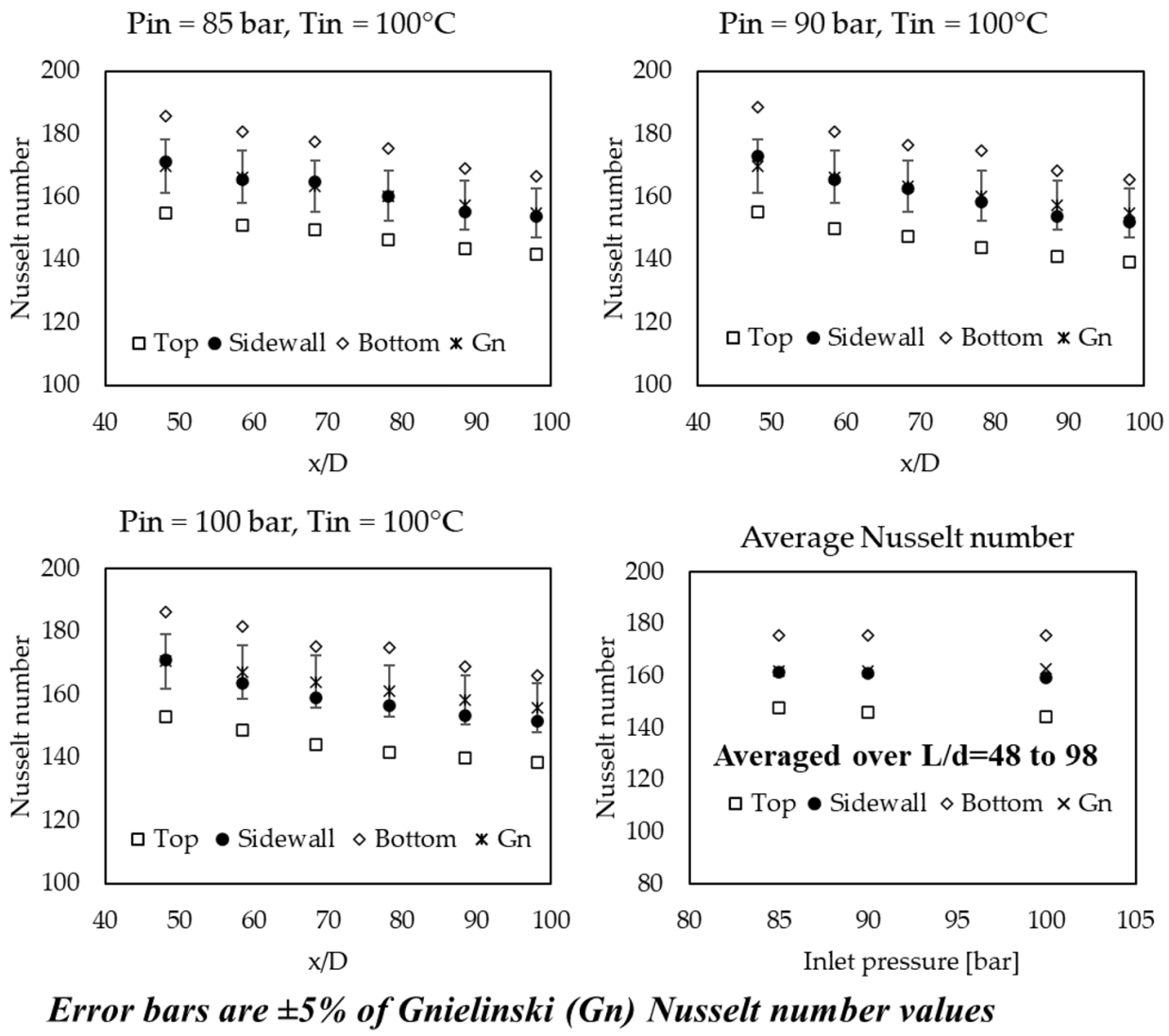

Figure 92: Axial Nusselt number plots to show effect of pressure on heat transfer: (a)P_{in} = 85bar, (b) P_{in} =90bar, (c) P_{in} = 100bar, (d) Average Nu plotted against pressure for for cases shown in (a), (b) and (c)

6.9 Effects of varying inlet temperature

To study effect of temperature on heat transfer away from critical point, experiments are performed at 85 bar inlet pressure at varying inlet temperature from 100ºC to 340ºC with the same

testing conditions. Mass flux of 180 kg/m^{2}s and heat flux of 47 kW/m^2 is kept constant for all cases to isolate effects of varying sCO_2 flow temperature. An additional CFD case with 400^{o}C inlet temperature is also presented here since the experiment could not be performed above 340^{o}C inlet temperature due to wall temperature increasing above the operating temperature limit of stainless steel (538^{o}C) at the fixed mass flux and heat flux. Figure 93 shows a plot of experimental Nusselt numbers for three different inlet temperature cases along with Nusselt numbers calculated using Gnielinski correlation (Gn) using bulk properties. Nusselt numbers shown in subfigures (a), (b) and (c) are calculated locally at top, bottom, and sidewall surface at each thermocouple station. Due to circumferential variation in surface temperature, the Nusselt number at a thermocouple station varies from top to bottom location. As expected for the heated horizontal tube with sCO2 flow, highest Nusselt numbers are obtained at the bottom surface, and the lowest Nusselt numbers are observed at the top surface. This is according to the theory of the formation of natural convection currents that flowing from bottom to top surface, resulting in the highest heat transfer at bottom surface.

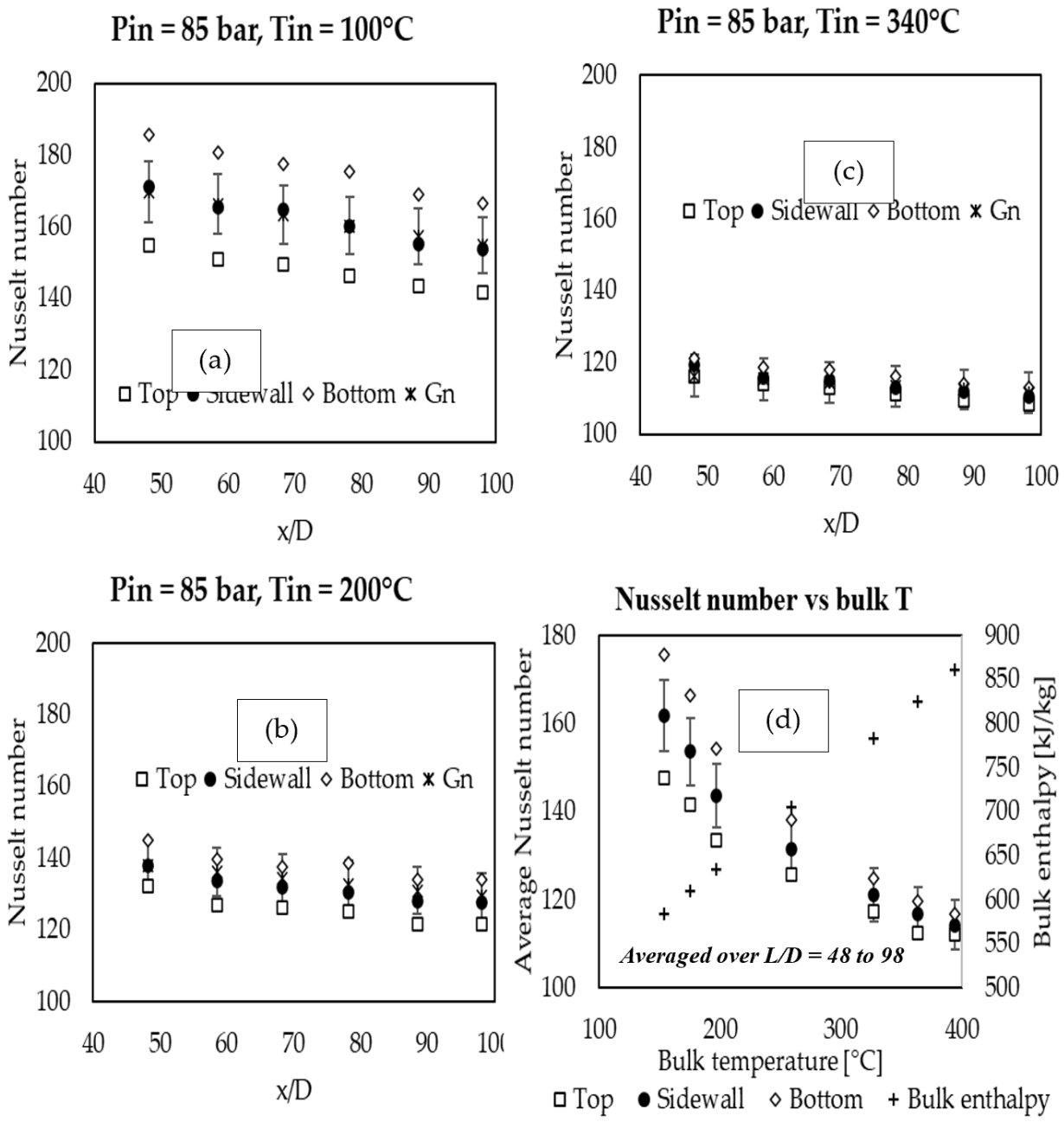

Figure 93: Experimental Nusselt number plotted against inlet bulk temperature showing diminishing effects of buoyancy effects on heat transfer (Error bars are ±10% of Nu_{Gn})

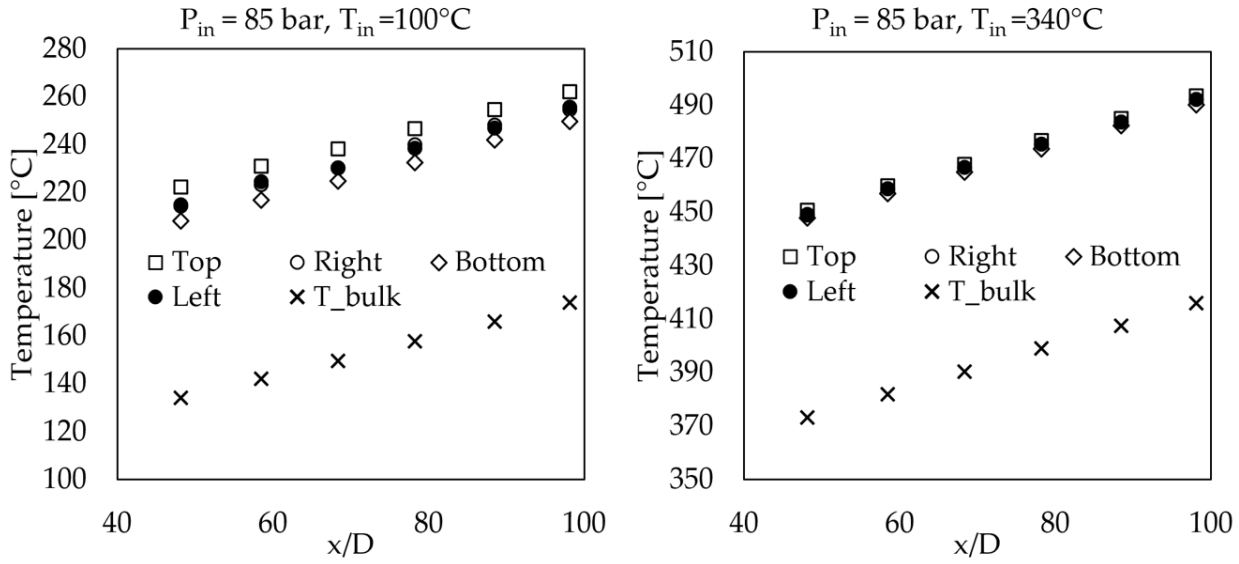

Figure 94: Experimentally measured external wall temperatures and calculated bulk flow temperature for lowest and highest inlet temperature cases

Interestingly for the temperature range studied, the experimental Nusselt number at sidewalls are the same as Gnielinski Nusselt numbers (maximum deviation of ±2.6%) and the same as the average of top and bottom Nusselt numbers too. Hence for the cases presented here, the following holds true:

$$Nu_{side} = \frac{Nu_{Top} + Nu_{Bottom}}{2} \approx Nu_{Gn}$$

As the inlet temperature increases, circumferential variation in temperature decreases. This can be seen from Figure 94, and its effect on Nusselt number can be seen in Figure 93 where the difference between top and bottom Nusselt number decrease. The difference between Nusselt number for top and bottom surface along with temperature difference is also listed in Table 21, showing diminishing effects of buoyancy formation. For 400ºC inlet temperature case results obtained from CFD at 85 bar inlet pressure, the formation of buoyancy forces is negligible as the

circumferential variation in temperature was obtained within 1.1°C. Hence it can be concluded, for the conditions presented here and at temperatures even higher than presented here, buoyancy forces formation will be absent, and the sCO_2 will have ideal gas-like behavior.

Table 21: Effects of temperature on sCO_2 heat transfer at constant pressure: Diminishing effects of buoyancy on heat transfer

T_{in} [°C]	$\frac{Nu_{Top} - Nu_{Bottom}}{Nu_{avg}}$	T_{top}-T_{bottom} [°C]
100	17%	13.6
120	16%	12.8
140	15%	12.0
200	10%	7.7
265	6%	4.8
300	6%	4.7
340	4%	3.1
400 (CFD)	1%	1.1

6.10 High Re cases at higher pressure and temperature

Experiments are performed to investigate the effects of buoyancy on heat transfer at a high Reynolds number at higher pressure and temperature. These conditions are based on the temperatures and pressures proposed for a sCO_2 primary heat exchanger designed for the DOE STEP Facility. However, the maximum temperature limit of 700°C proposed for the STEP heat exchanger is not tested for stainless steel and will be presented in the upcoming section for the Inconel tube. For ½" stainless steel tube, 2.04 kg/min mass flow rate is run at two different conditions as shown in Figure 95 to reach Reynolds numbers of 140,400 and 136,400. These tests serve as preliminary testing for heating/cooling requirements for experiments with 1/8" tube. Because the same mass flow rate is also required to reach 750,000 Reynolds number for 1/8" tube (Inconel 800H tube experiments). These two tests are performed to check if we have sufficient heating and cooling requirements for testing with 1/8" Inconel tube.

At higher Reynolds number, Nusselt numbers at every circumferential location falls within 7% of Gnielinski Nusselt number. Average deviation between top and bottom surface Nusselt numbers was also within 4%, indicating diminished effects due to gravity. This agrees with the fact that the effect of forced convection increases with increasing Reynolds number while the heat flux is constant.

6.11 Conjugate CFD study to complement experimental results

Experimental results are also compared with numerical results. A conjugate CFD setup is used modeling stainless steel solid domain as well as sCO_2 flow domain. Boundary conditions at inlet are the same as experimentally obtained inlet condition. Heat generation to the test section is same as experiments. Heat loss on the outer surface utilizes heat loss coefficient as obtained from heat loss test. This heat loss coefficient is given as an input function of temperature. Various Turbulence Models were initially explored. Results from all CFD models are shown in Figure 96. Results are highly sensitive to the class of turbulence model used. SST-kω model showed the best performance across the range of experimental conditions.

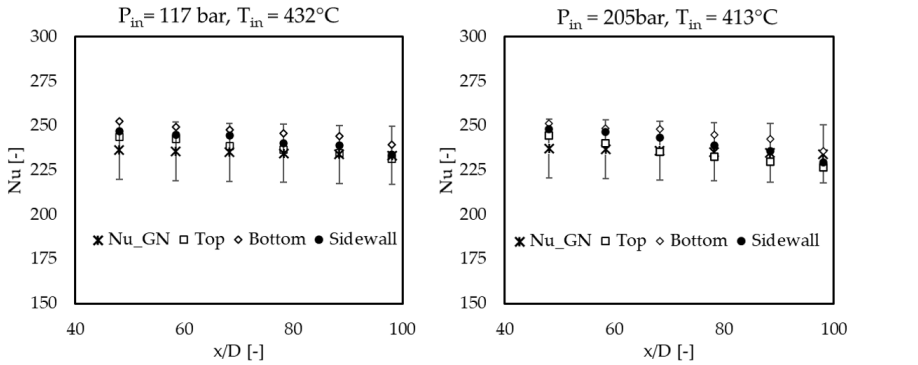

Mass flow rate = 2.04 kg/min
Heat flux = 4.6kW/m²
Inlet Re = 140,400
Maximum wall temperature reached = 505°C

Mass flow rate = 2.04 kg/min
Heat flux = 4.6kW/m²
Inlet Re = 136,400
Maximum wall temperature reached = 485°C

Figure 95: High Reynolds number cases at high temperatures

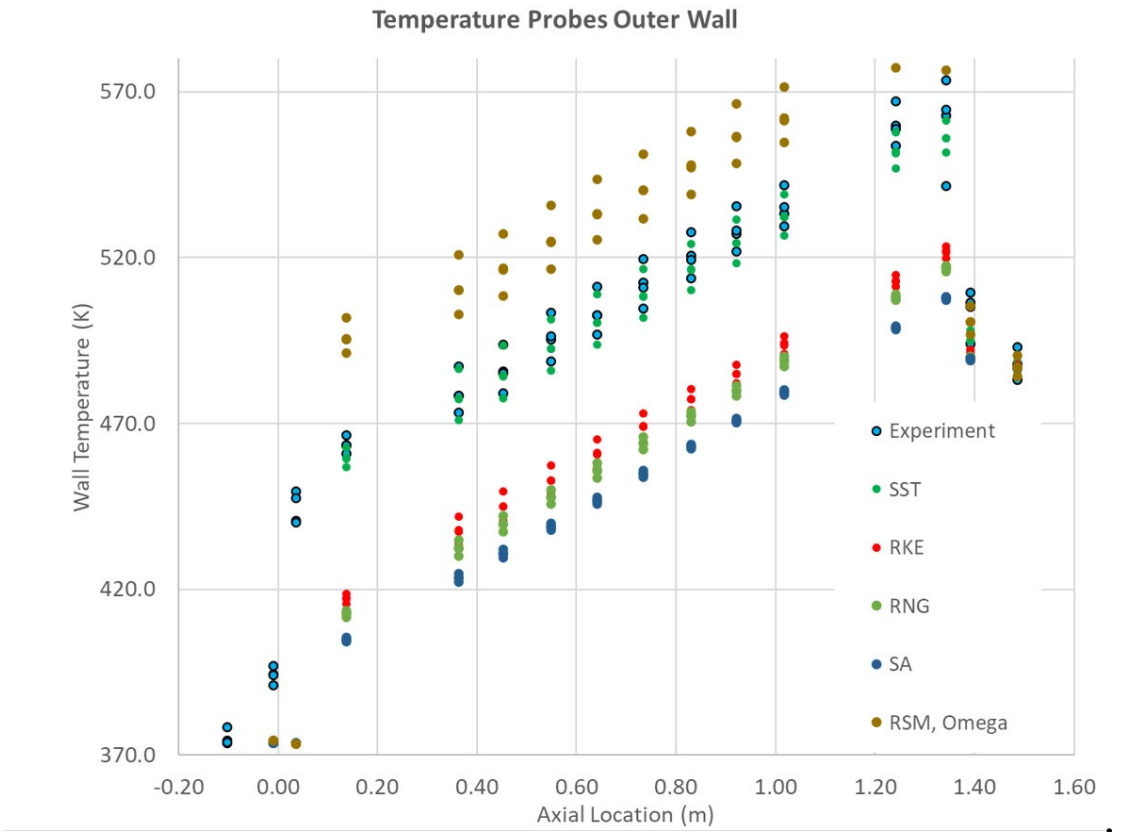

Figure 96: Turbulence models performance assessment: Comparison with experimental

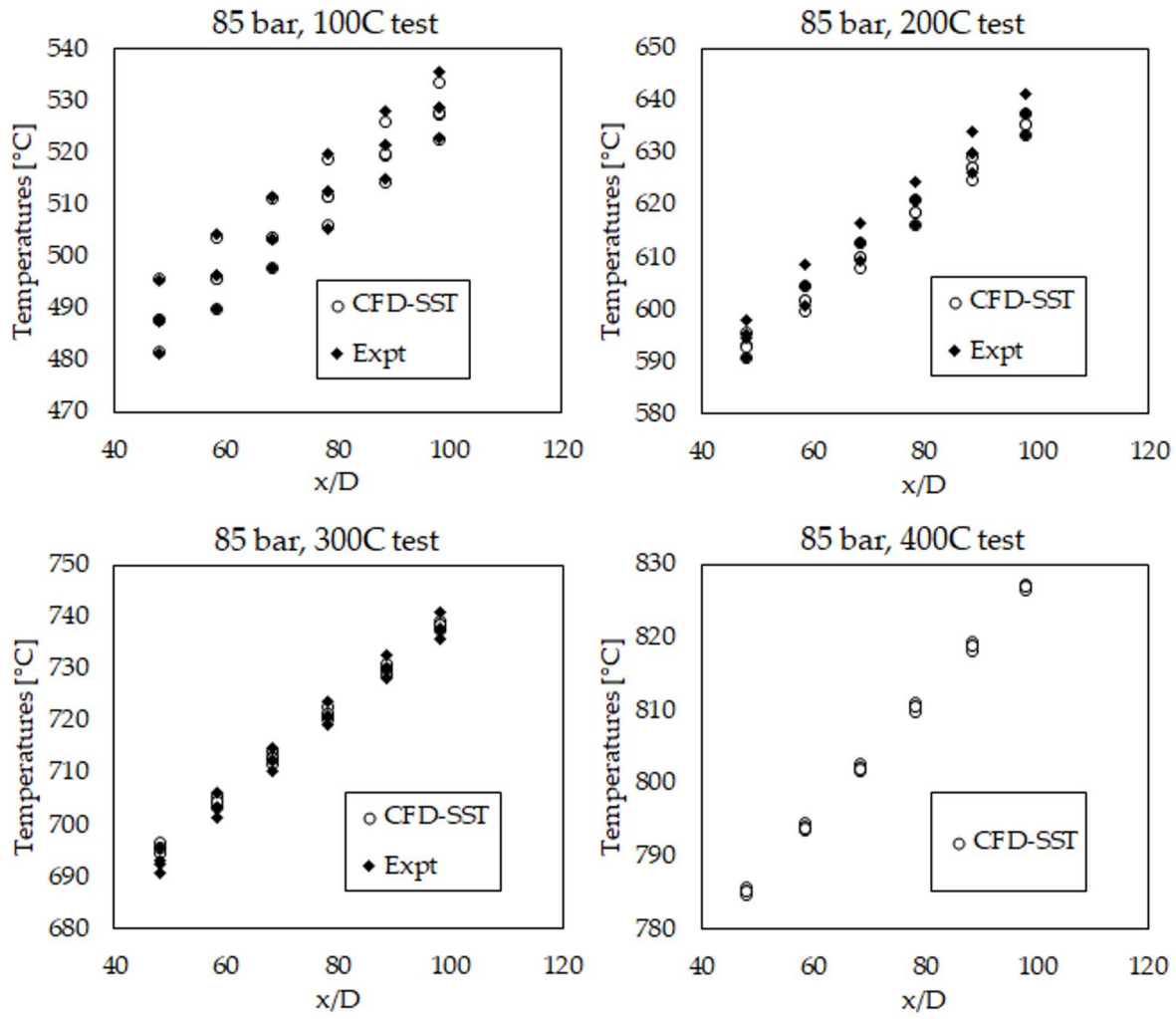

Figure 97: Surface Temperature Distributions: Measured vs CFD

Figure 97 shows plots of measured external surface temperatures vs values obtained from CFD. The SST model shows excellent agreement with experimentally measured temperatures. Diminishing effects of buoyancy can also be seen from these plots at elevated inlet temperatures. Temperature spreads at subsequent axial locations are seen to reduce due to an increase in bulk temperature and a decrease in bulk density. For the 400°C inlet case, all axial locations read temperatures within 1.1°C. Figures 98-101 show contour plots of temperature and density obtained from CFD. Temperature distribution at several axial locations along the heated length for 85 bar,

100ºC inlet case is shown in Figure 98, whereas Figure 99 shows density contours at same axial locations. These contours show variation in temperature and hence the variation in density due to the effects of buoyancy. Higher density can be seen near the bottom surface, and lower density can be seen at the top surface because of lower density fluid moving from bottom to top. However, along the heated surface, buoyancy effects seem to decrease due to an increase in bulk temperature and decrease in density, and a more uniform temperature distribution is obtained.

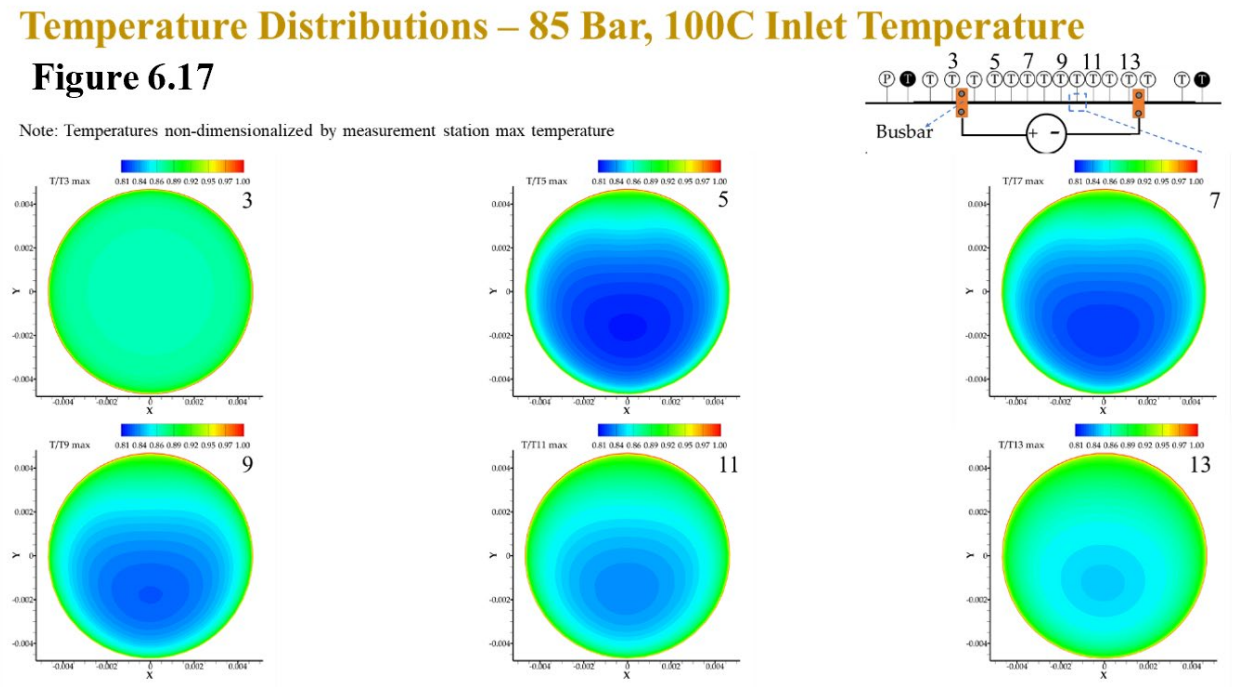

Figure 98: Temperature distributions – 85 bar, 100ºC Inlet Temperature

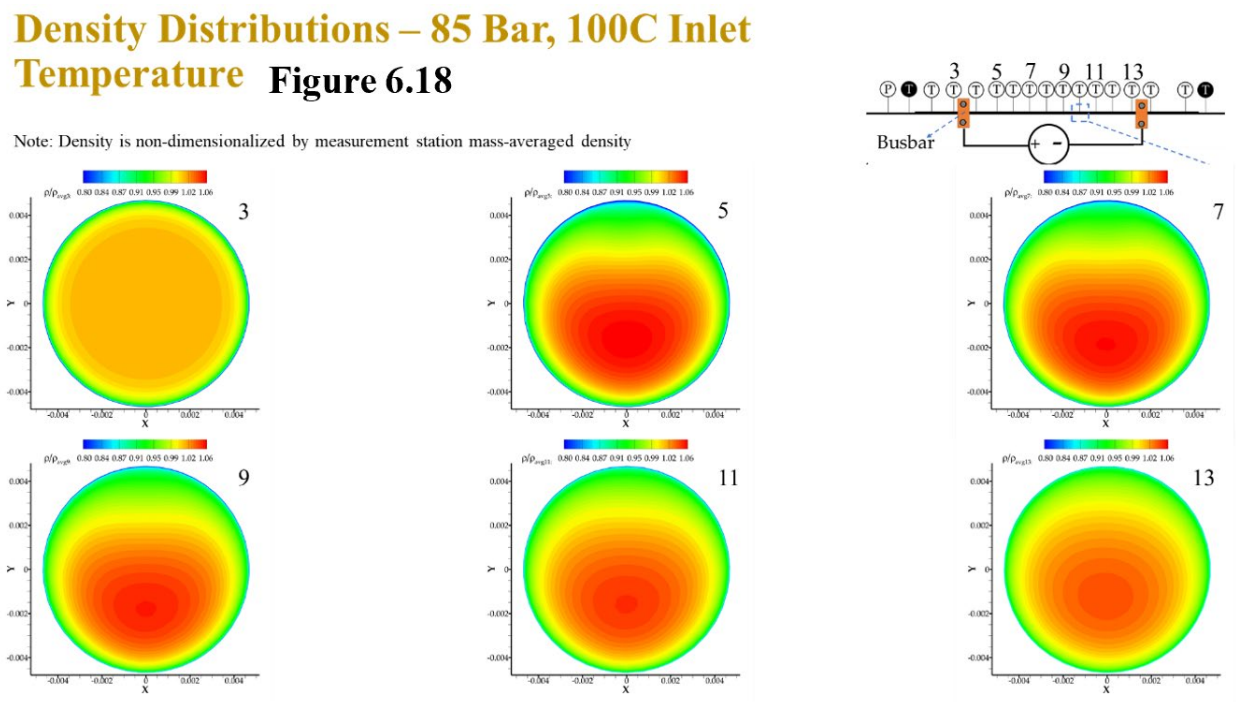

Figure 99: Density distributions – 85 bar, 100°C Inlet Temperature

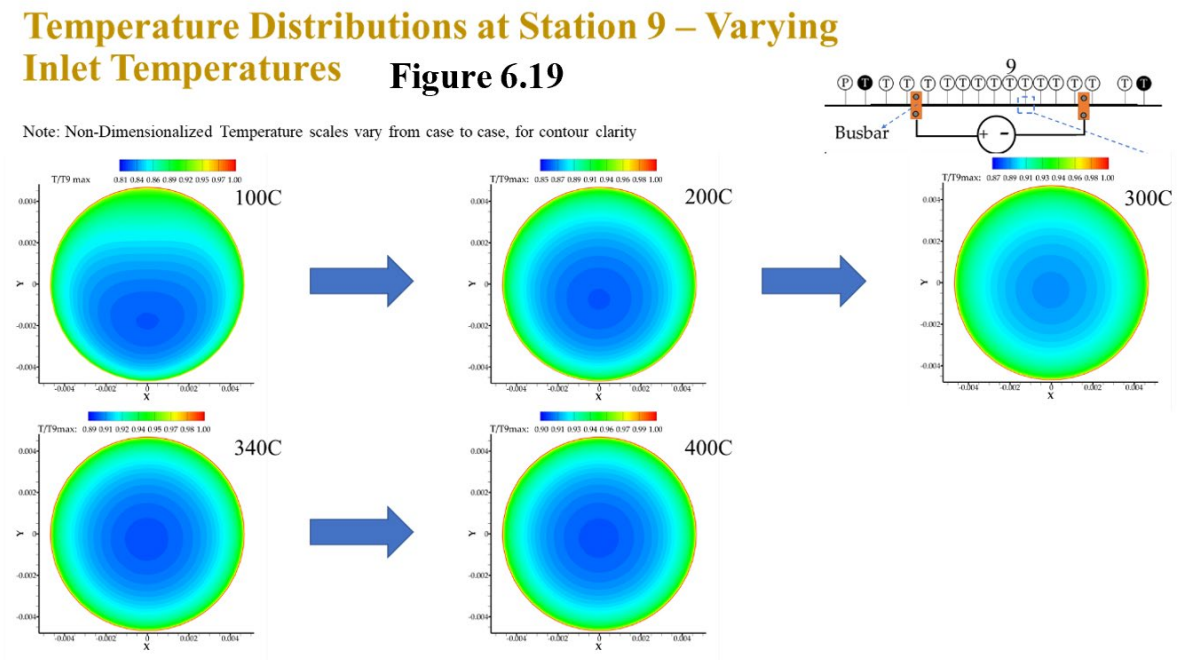

Figure 100: Temperature distributions at station 9 – Varying Inlet Temperature

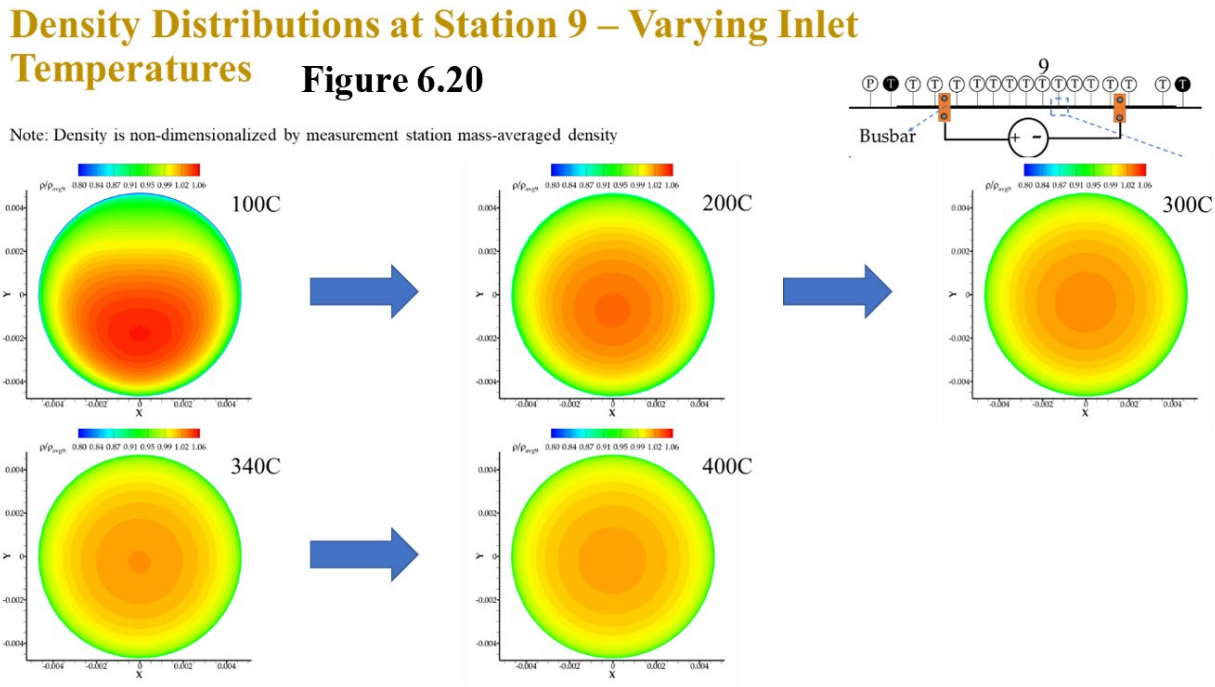

Figure 101: Density distributions at station 9 – Varying Inlet Temperature

Figures 100 and 101 show effects of varying inlet temperature cases at constant pressure, heat flux and mass flux. Contour plots are shown at section with L/D = 78. With increase in temperature distribution get more uniform. At 100°C inlet case, there is non-uniform temperature distribution. For 400°C inlet case, the contour looks almost uniform with no radial variation in temperature. This temperature distribution affects density distribution adversely where temperature is higher, density is lower and vice versa. That is why at 400°C, it can be concluded that buoyancy forces formation is almost absent. This matches very well with conclusions drawn from experimental results.

6.12 Results and Discussion: ½" Stainless steel test section inclined flow

In addition to testing horizontal tube, a separate experimental rig is fabricated to test heat transfer at various inclinations and directions. This inclined rig shares similar features as previously mentioned high temperature rig except the flow circulation pump used in this rig is a

gear pump from Micropump. Due to this pump's limitation, maximum pressure that can be tested in this rig is limited to 100 bar. Thermocouples used for surface measurements are T-type hence the temperature limit is 200°C. Thermocouples are instrumented in the same manner at 90° interval at top, bottom, and sidewalls. The schematic of the rig along with a photograph is shown in Figure 102.

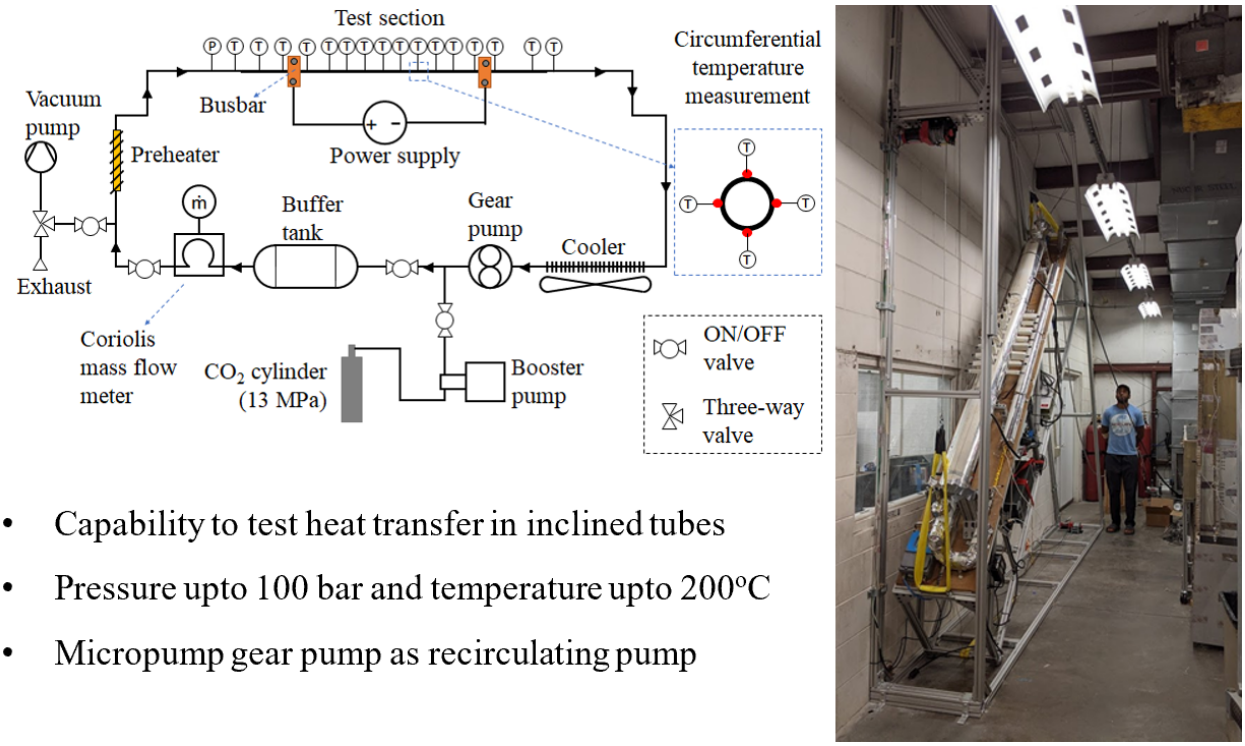

Figure 102: Schematic of inclined heat transfer rig (left) shown with photograph

Results of an experimental case are shown in Figure 103. Inlet pressure is maintained near 80 bar and inlet temperature is maintained near 39°C, which is very close to pseudocritical temperature of CO_2 at 80 bar. Horizontal and inclination of 45° with upward and downward direction is considered here. An increase in overall heat transfer as the flow direction changes from upward to downwards is observed which can be seen from values of Nusselt numbers. Higher heat transfer is expected in downward direction flow in the presence of buoyancy effects. Heat transfer at the wall is directly related to variation in the generation of wall shear stress. For upward direction

flow, buoyancy forces are opposing wall shear stress, decreasing turbulence hence in result decreasing heat transfer. On the other hand, buoyancy forces increase wall shear stress for downward direction flow, generating increased turbulence and hence increasing heat transfer at the wall.

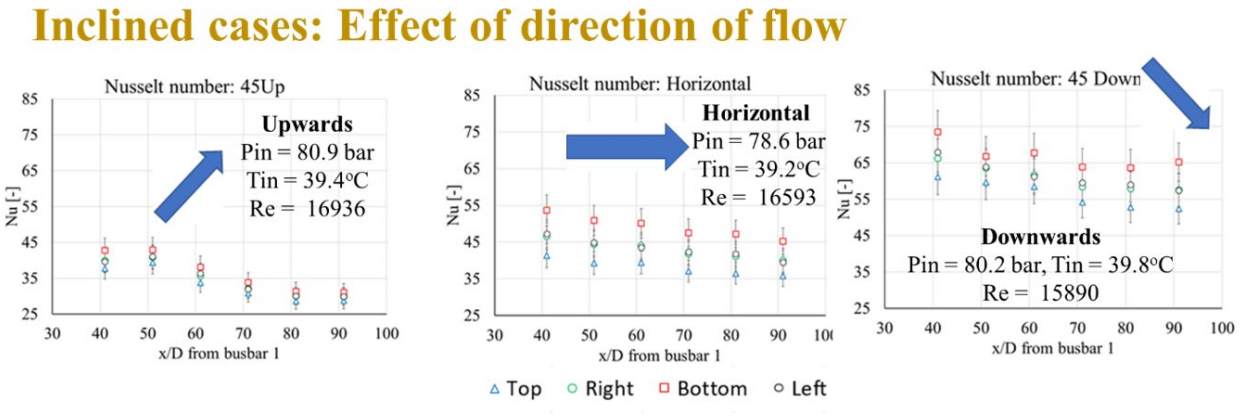

Figure 103: Effects of flow direction and inclination for 45° inclination case

6.13 Results and Discussion: 1/8" Inconel test section

The main high temperature and high pressure heat transfer loop are modified to test temperatures above 540°C (operating temperature of stainless steel) with 1/8" Inconel tube. An additional cooler is added downstream of the test section to bring the temperature down from 700°C o 540°C. On the test section, only top and bottom surface thermocouples are welded due to limited space on the outer surface of 1/8" tube. Weld quality is better than welding on Stainless steel tubing since both TCs and Inconel tubing has Nickel as major alloy component. The rest of the loop is the same as described previously. Air tests were performed to check the quality of welds and in-situ bias correction.

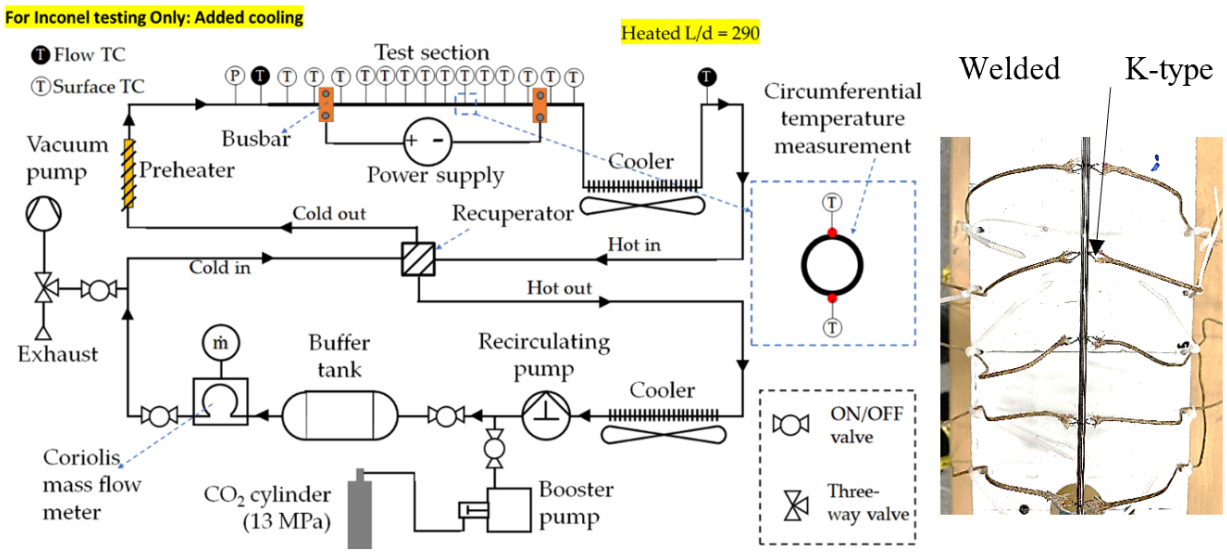

Figure 104: Schematic (left) of the experimental loop after implementing 1/8" Inconel tube (I.D. = 1.75 mm) to test temperatures higher than 540°C. Welded K-type thermocouples on

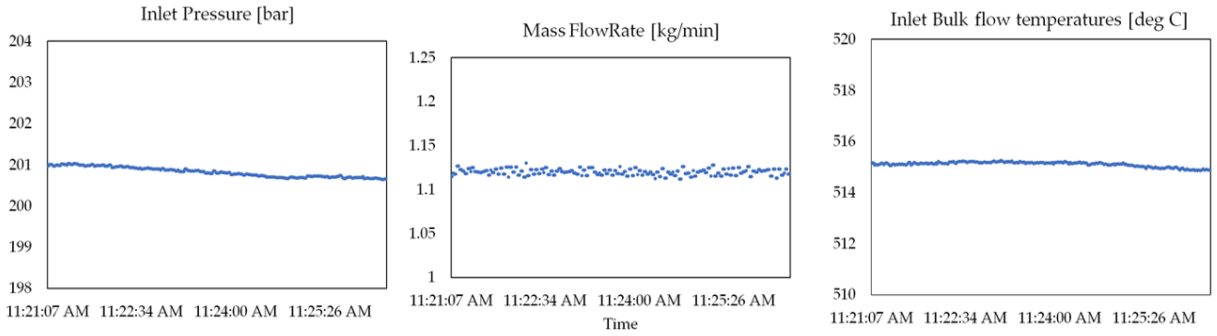

Figure 105: Steadiness of testing with 1/8" Inconel tube

The steadiness of testing is ensured for this test section too. Max Pressure fluctuations are observed within 0.2% of mean value, max temperature fluctuations are 0.39°C, and maximum mass flow rate fluctuations were 1.6% of the mean value. These are plotted against time in Figure 105.

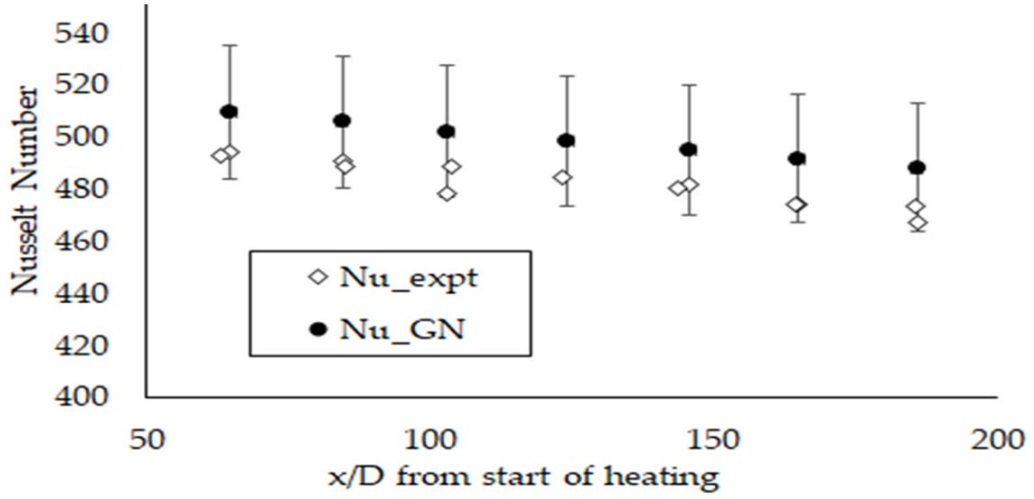

Figure 106: Nusselt number plot for 1/8”

Table 22: Experimental conditions for test with 1/8" Inconel tube (I.D. = 1.75 mm)

Parameter	**Conditions**
Inlet bulk T	515ºC
Inlet bulk P	201 bar
Inlet Re	371,850
Mass flux	7736 kg/m^{2}s
Heat flux	1235 kW/m^2
Max wall T	690ºC

The setup has been tested at high pressure (200+ bar) and high wall temperature (690ºC). Table 22 list conditions for the experiments performed. Nusselt numbers obtained from this experiment is plotted in Figure 107. sCO_2 at these conditions follows ideal gas behavior with minimal effects on buoyancy on heat transfer. Nusselt numbers also agree within 5% of Gnielinski Nusselt numbers. For such small diameter and such high Reynolds number, even with high values of heat fluxes, buoyancy effects are found negligible at high temperature.

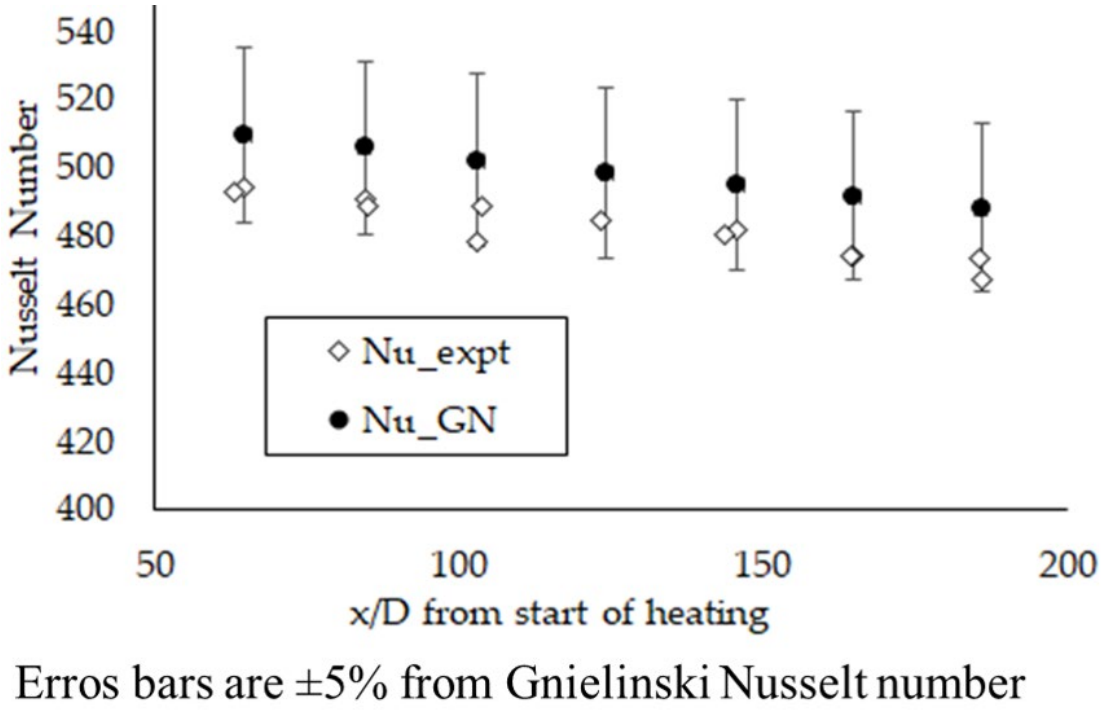

Figure 107: Nusselt number plot for 1/8" Inconel tube testing (I.D. = 1.75 mm)

Conclusions:

- A unique and versatile testing facility for study of sCO2 flow and heat transfer (*and leakage*) has been created.
- Comparisons with existing correlations performed over a large range of parameters – *a lot more being planned internally*.
- The rigs are being used or to be used for (1) turbine internal cooling (limited, with SwRI as Lead), (2) compressor cascade test with improved leading edge (from SETO), (3) topology-optimized, additively manufactured Rec Heat Exchanger (with Siemens Technology as lead, from ARPA-E, (4) high-accuracy PIV (for ONR).

- Unrelated to the Rig or this project: sCO2 cycle options (with corresponding PHX) for industry sector WHR (with Sandia Labs)
- (restricted) application to Hypersonic thermal management & harvesting

CHAPTER 7: TRANSPORT PROPERTIES FOR sCO_2 COMBUSTION USING MOLECULAR DYNAMIC SIMULATIONS

The goal of this task is to provide transport properties of real gas. Diffusion coefficients of alkanes under high pressure and temperature were performed by MD simulation. Since such properties are difficult to obtain by experiment, MD simulation provides valuable parameters to build up a real gas transport properties database.

7.1 Introduction

Computing species diffusivity D_k in a combustion, simulation is computationally expensive, especially if many species are involved [242]. Therefore, Lewis number is assumed unity ($Le = 1$) i.e. "the species diffuses at same rate as heat" in majority of the combustion models and simulations [247-250]. This assumption is proven to be valid under some cases [243]. However, studies show that this assumption is not substantial at supercritical conditions. A direct numerical simulation (DNS) of [251], as shown in Fig. 108 shows that the species-specific effective Le is much larger than unity in the shear layer and varies between -0.1 to 1.5. Also, the DNS work of [252] as shown in Fig. 109-B concludes that assuming $Le = 1$ for all species predicts temperatures up to 250 K higher than the physically realistic multi-component model.

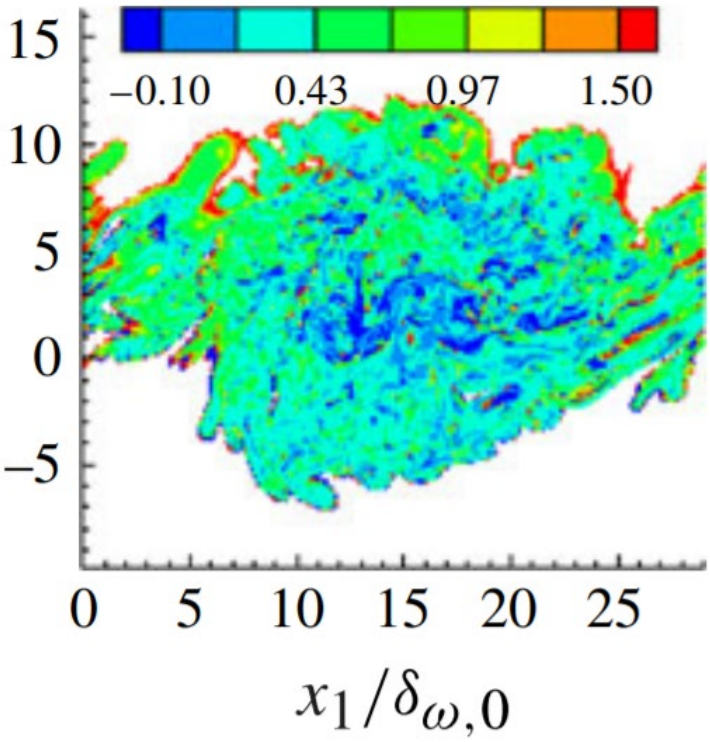

Figure 108: The Lewis number variation in the shear layer of supercritical combustion (DNS simulation of [251]).

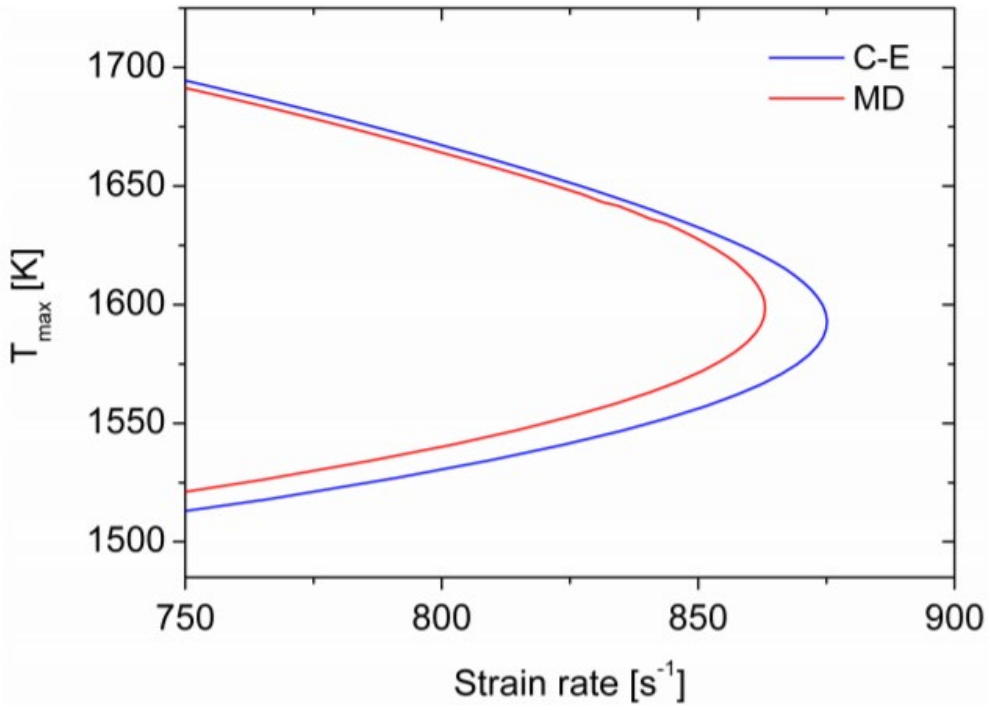

Figure 109-A: The figure shows a comparison between the results obtained with MD versus C-E theory, demonstrating a significant discrepancy between the two approaches when used in dodecane combustion [253].

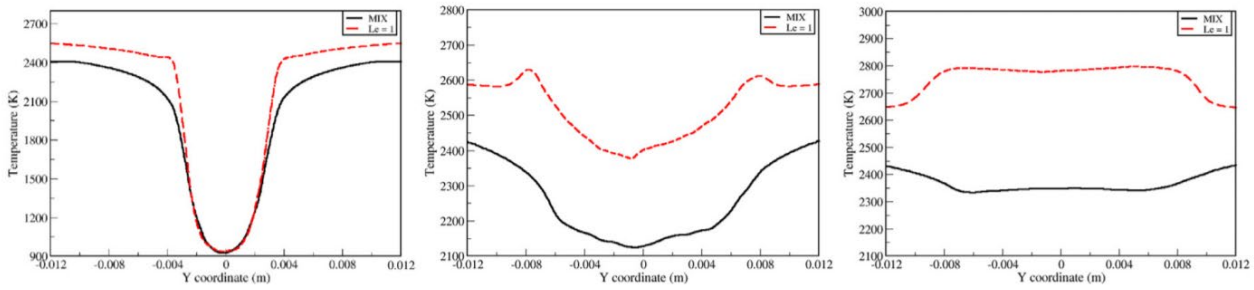

Figure 109-B: temperature profiles predicted by LESLIE with mixture-averaged diffusion and with constant Lewis number = 1 at different time instants (DNS work of Bruno, et al. [252])

Inspite of its complexity, a few high-fidelity simulations consider species diffusion models either through multi-component diffusion or mixture averaged diffusion models. However, these models are applicable under low pressure conditions only as these diffusion coefficient formulations are based on ideal gas kinetic theory [254]. For most of the combustion codes, the molecular properties of the species are provided as a transport database which contains the information of geometric configuration, Lennard-Jones (L-J) potential well depth ε/k_B, L-J diameter σ, dipole moment μ, polarizability α of the species. Hirschfelder et. al. [255] followed the Chapman–Enskog (C-E) approach, combined with the Lennard–Jones (L-J) intermolecular potential function, and suggested the Hirschfelder–Bird–Spotz (HBS) equation for mutual mass diffusion coefficients, and this method is extensively employed in combustion simulations [254]. However, its validity is limited to low-density gases with the assumption of spherical interactions between molecules. At supercritical conditions, the molecular structure and intermolecular

forces like ‘repulsion’, and ‘attraction’ due to molecular force field are prominent and molecular dynamic (MD) approaches account for them while computing transport properties. The work of [253] shows a significant difference in the estimation of flame strain and temperature profile when MD and C-E diffusion approaches are used. It is also quantified here that 10% differences in diffusion coefficients of dodecane flame can cause up to 50 K difference in ignition temperature as shown in Fig. 109-A.

Thus, it is vital to investigate the influence of the crucial molecular transport phenomena at supercritical CO_2 conditions. In this work, a canonical supercritical CO_2 flame will be simulated by using real gas thermal and transport properties, and the sensitivity of binary diffusion coefficients on the flame characteristics will be studied in detail. Further, the binary diffusion coefficients of important molecular systems under supercritical CO_2 conditions will be identified by high-fidelity molecular dynamic simulations using periodical boundary conditions and an all-atom force field known as the Transferable Potential for Phase Equilibria (TraPPE). Pure systems will be used to validate the force field parameters. The binary and multicomponent mixtures will be prepared by placing the molecules randomly inside periodic boxes, sampling the composition and density range of interest. After 200 ps of initial heating and equilibration, MD production runs of 10 ns in the NVT ensemble will be performed by coupling to an external bath through the Berendsen thermostat. The data obtained will be used to predict the self-diffusion coefficient, which is based on the mass current of a single target molecule and is calculated from the linear part of the mean-square displacement of the centers of mass of the molecules according to the Einstein and Smoluchowski relations.

7.2 Develop real gas binary diffusion coefficients data for supercritical CO_2 combustion modeling

Diffusion coefficients data of CH_4/CO_2 and C_2H_6/CO_2 system under 500 K to 2,000 K and 100 atm to 1,000 atm were obtained by MD simulation. United-atom force field Transferable Potential for Phase Equilibria (TraPPE) was applied in our simulation. Particles are randomly inserted by Packmol. 200 ps simulation run was performed for initial equilibration. 5 ns in the NVT ensemble (constant volume and temperature) was performed coupled by external bath through Nose-Hoover thermostat, followed by 5 ns in the NVE ensemble (constant volume and energy). All the analyses were done in the NVE ensemble. To validate our simulation results, CH_4/CO_2 system at lower temperature and pressure was performed to compare with experimental results at 14.7 MPa and 300 K to 340 K [1]. Mean-squared displacement (MSD) of the groups of atoms was evaluated. The slope of the MSD versus time is proportional to the diffusion coefficient of the diffusing atoms. Figure 110 shows the MD simulation results. Increased pressure depresses diffusion coefficient. The temperature increase will increase the diffusion coefficient. CH_4 and C_2H_6 have similar behavior at high temperatures.

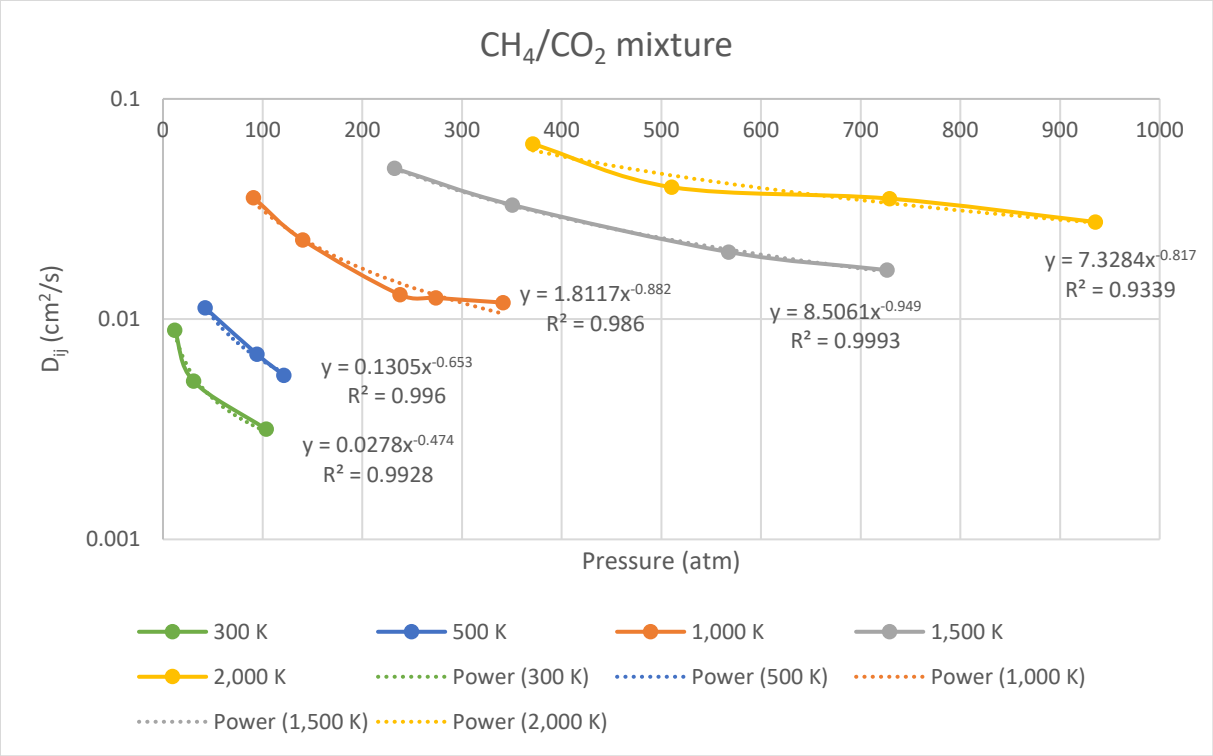

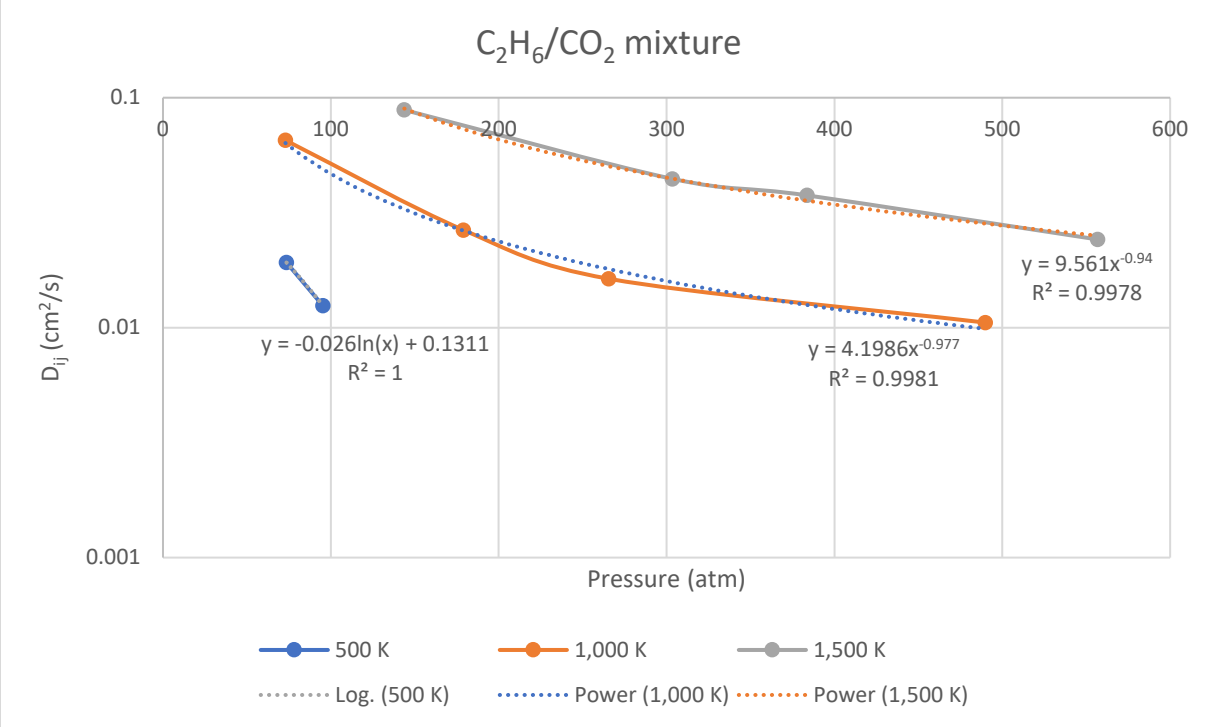

Figure 110: Diffusion coefficient of CH_4/CO_2 (above) and C_2H_6/CO_2 (below)

7.3 Influence of binary diffusion coefficients on counterflow flame

Figure 111 shows the comparison between binary diffusion coefficients computed by using MD simulations and by ideal gas kinetic theory for the CH_4-CO_2 system at various pressure and temperatures. The figure illustrates that there is a significant deviation between ideal gas kinetic theory and MD in terms of predicting the diffusion coefficients. Interestingly, the difference between ideal gas kinetic theory and the MD simulations is increasing with respect to temperature. At 2000 K and 420 bar, the difference is up to ~380%. Figure 112 shows the sensitivity of 300% change in diffusion coefficient on the supercritical CO2 counterflow flame [246, 256, 257] structure. The peak temperature is increased by ~150 K due to an increase in the diffusion coefficient. This difference is significant from the view of combustor design.

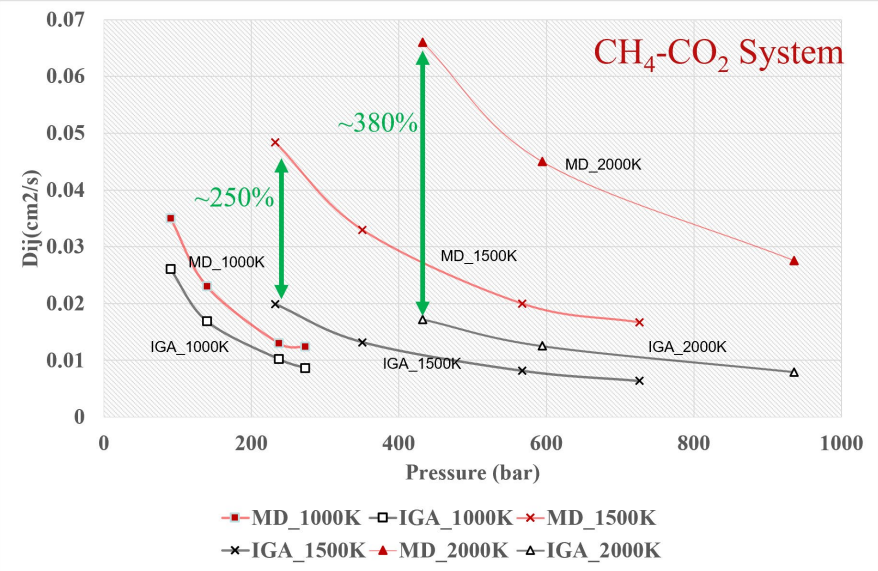

Figure 111: Comparison between binary diffusion coefficients computed by using MD simulations and by ideal gas kinetic theory for CH_4-CO_2 system at various pressure and temperatures.

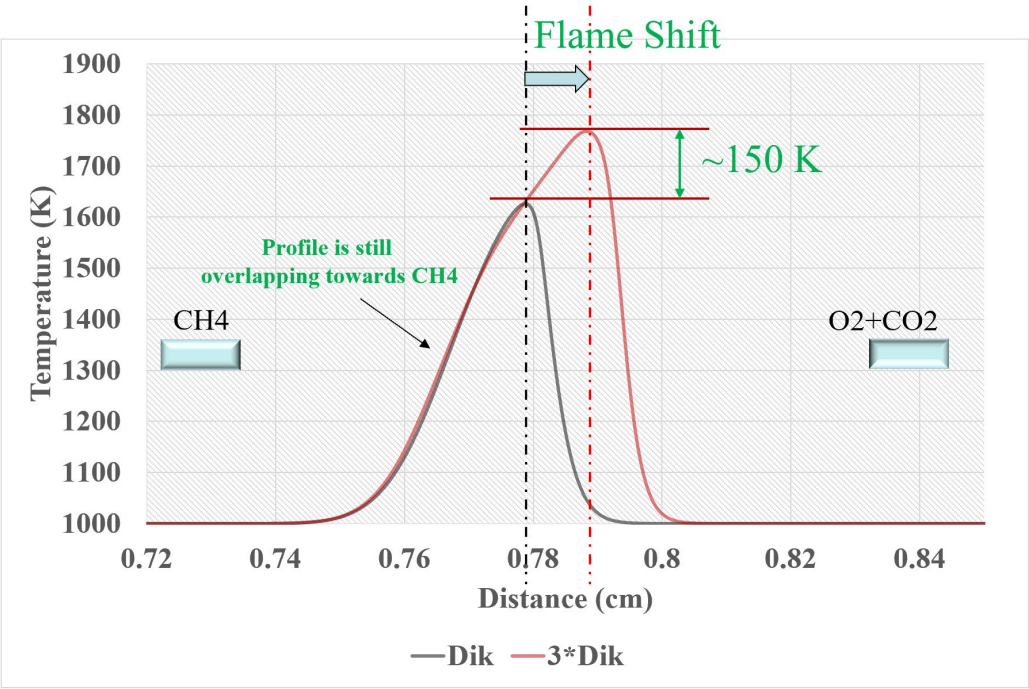

Figure 112: Sensitivity of diffusion coefficient on supercritical CO_2 counter-flow flame structure

7.4 Conclusions

It is observed that real gas effects are very prominent in diffusion characteristics of a gaseous mixture at supercritical conditions due to intermolecular attractive or repulsive forces. It is seen that binary diffusion coefficients of CH_4 and CO_2 estimated with molecular dynamic simulations are almost three times higher than the diffusion coefficients estimated with ideal gas kinetic theory. This order of difference has a huge impact (150K peak flame temperature difference) on a counterflow flame.

CHAPTER 8: STEADY-STATE JET FLOW MEASUREMENTS FOR CFD

In the present task, CH_4 was injected into supercritical CO_2. The tests covered pressures up to 200 bar. Achieving realistic initial thermodynamic conditions was difficult in the lab scale test. The focus was high pressure and above the supercritical temperature of CO_2 (31.10 C). Pressurized CO_2 was stationary, and a CH_4 jet was injected through an injector. Injecting jets of different species into the supercritical state of CO_2 will lead to an improved understanding of the fluids' behaviors at high pressure. The results from the experiments will provide validation for CFD transport models developed in task 7.0 and existing supercritical thermal property models by comparing velocity profiles, concentration profiles, temperature profiles, and jet characteristics. This task will utilize a static chamber as well as a shock tube to accumulate a range of pressures and temperatures. The following three types of measurements will be conducted:

8.1 Shadow imaging of supercritical methane jet in sCO_2 environment

The focus of this task is to observe the flow structures of the jets injected into sCO_2. A high-speed camera was implemented, which obtains the images. The schlieren image helped visualize the density gradients around the jet across the diagonal of optical access. At uniform fluid temperature condition, there will be light refraction, and shadow of the jet in the form of image is obtained due to the injection of lower dense CH_4 into the higher density CO_2. The actual density distribution was obtained, and the structure of the jet was analyzed by post-image processing. Jet diverging angle was estimated at a supercritical condition.

Industries are attracted towards gaining higher thermal efficiencies at high pressure in applications such as gas turbine, rocket engines [258]. Nevertheless, pressure values are reaching beyond the critical values for obtaining higher thermal efficiencies. The phenomena to obtain

higher thermal efficiencies can be better understood through knowledge of jet spreading [259]. Jet growth elucidates the mixing and development of jets [260]. However, it is challenging to understand the jet spreading by building such a high-pressure environment. The present study demonstrated and explicated jet structure and jet growth in such an environment at targeted pressures and temperatures. A constant volume chamber with two 3" diameter sapphire windows that can withstand up to 600 bar was used. A heating jacket surrounded the constant volume chamber to control initial temperature 0.105 m length and 0.0007 m diameter of injector was used. The injector length was decided by the length of the fully developed flow. A high-pressure solenoid valve was used to control the jet opening time. Schlieren image was used to capture CH_4 jet image with a high-speed camera (Phantom v12.1). The images were captured with a resolution of 512X512 at a rate of 5,000fps and 10,000 fps. LabVIEW controlled the high-speed camera and solenoid valve. A white LED with an iris was used as a pinned light source for the schlieren image setup. Three optics were used to generate a collimated beam and focus the collimated beam. A knife-edge was placed at the focal point. An air-driven gas booster (Maximator, DLE 15-1-2) was used to pressurize CO_2 and CH_4. Two pressure transducers were installed to measure chamber pressure and manifold pressure. Since one of the roles of the manifold is a storage of CH_4 to inject into the chamber, the manifold pressure is referred to as injector pressure.

Before introducing CO_2 in the chamber, the chamber was vacuumed at less than 0.1 psi. With the gas booster, CO_2 is pressurized up to 200 bar in the chamber. After stabilized CO_2 in the chamber, CO_2 in the manifold was exhausted and vacuumed less than 0.1 psi. After vacuuming the manifold, CH_4 was introduced in the manifold with the gas booster until desired pressure. It needed 5min to stabilize CH_4 in the manifold. After 5min, CH_4 was injected into the chamber. Figure 113 shows an image of the jet configuration along with time. Since there was the same pressure of CO_2 with

the chamber in the injector after the solenoid valve, CH_4 needed time to come out of the injector. However, it was hard to determine the timing when CH4 came out of the injector with the Schlieren image. To decide the time. 3.39um laser, which is absorbed in C-H, was used. Figure 114 shows 3.39 um laser history. Before CH_4 came out, the laser signal was constant, but when the CH_4 passed the laser path, the signal was dropped. The dropped signal could show the time of coming out of CH_4. To measure jet angle, image post-processing is needed. Post processing included removing the background, detecting jet edges, and calculating the angle using linear fit with detected jet edges. The post processing is shown in Figure 115. After the post processing, the jet angle was measured along with time.

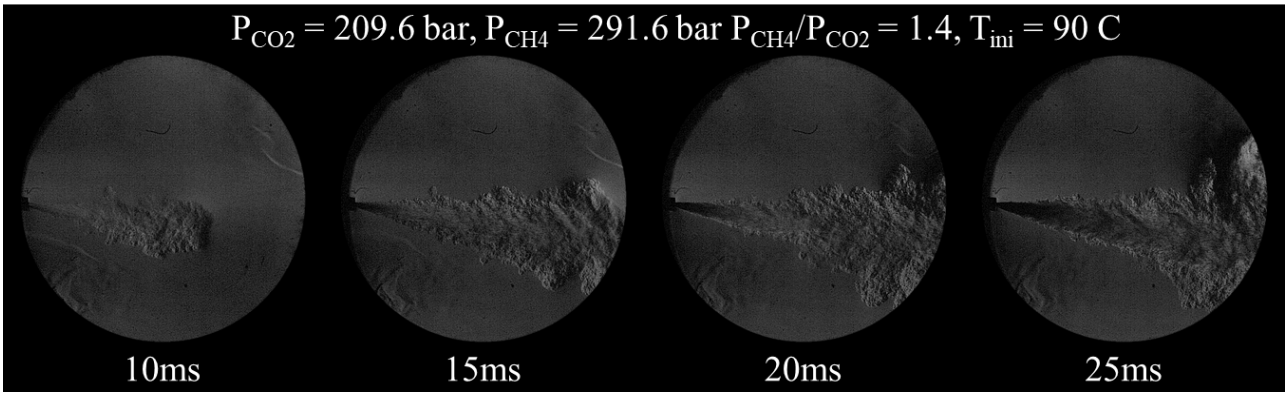

Figure 113: CH4 injection in to sCO_2 bar

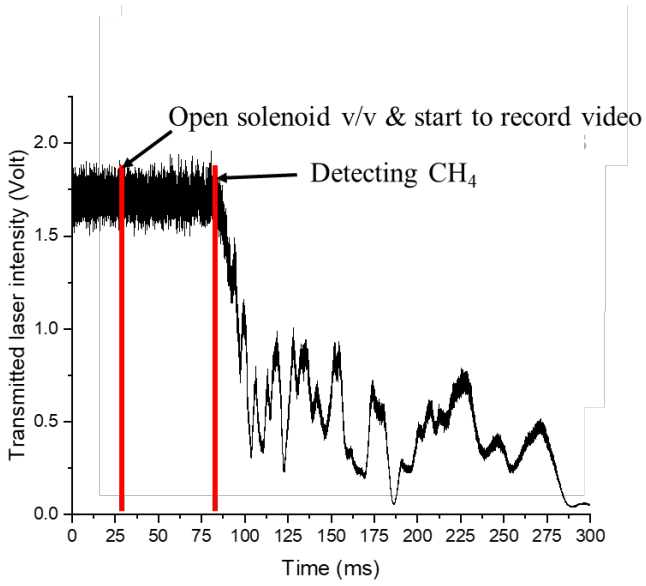

Figure 114: Detection of methane with 3.39 um laser

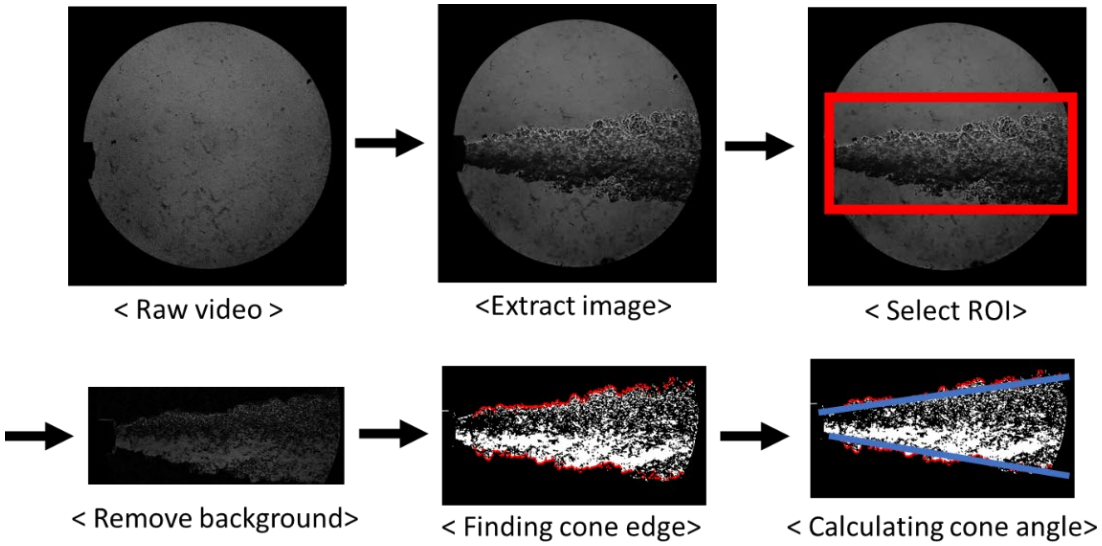

Figure 115: Post processing for jet analysis

Figure 117 [261] represents a variation of jet divergence for density ratios higher than 1. The experimental data (red squares) were graphed at pressure ranges 50 bar to 200 bar and temperature of 353 K. The result follows the trend explained by Abramovich's theory for turbulent jets [262].

The jet spreading increases as the density ratio increases which ultimately improves the jet mixing and entrainment of fluid.

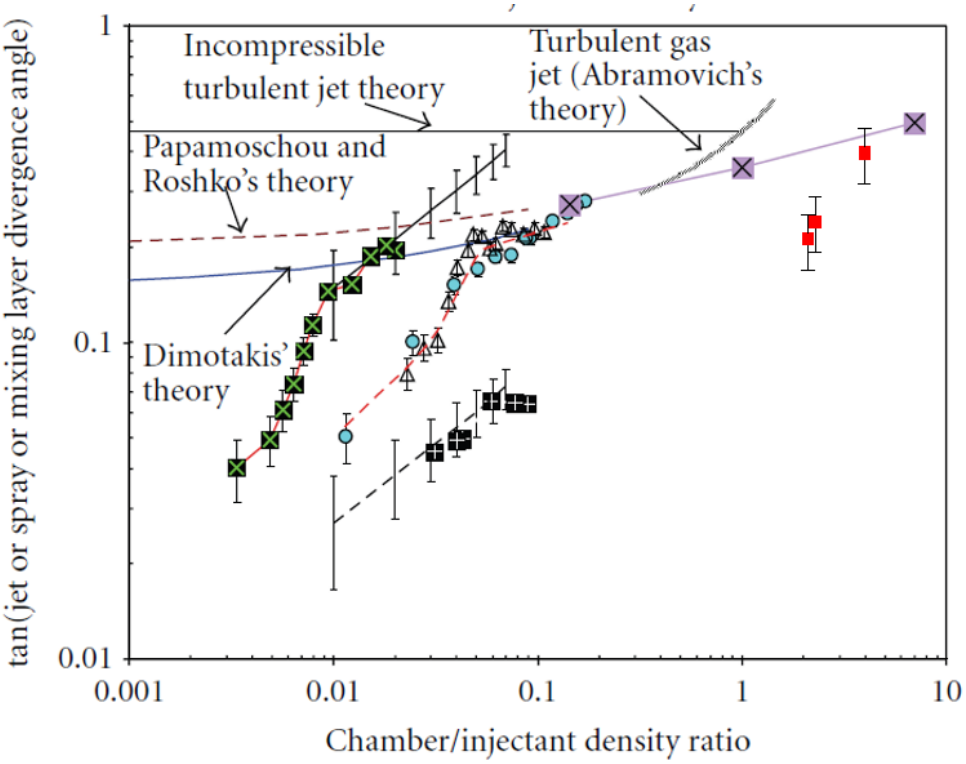

Figure 116: Variation of jet spreading for density ratios. Experimental data shown in Red square symbol

8.2 Planar laser-induced fluorescence measurements

Planar LED-induced fluorescence (P-LED-IF) measurements were completed in this task to obtain species information in a plane across a jet. Using species concentration measurements, differences in mixing characteristics between subcritical and supercritical jets were observed. Normalized distribution of concentrations on the laser plane is useful information to validate numerical models on molecular diffusion and turbulent mixing. CFD models will be validated by mixing jet concentration profiles obtained in this task. PLIF imaging is one of the

promising methods for visualization of flow field because PLIF is sensitive to species composition, temperature, number density, and velocity [263, 264]. Watson et al. [265] used a 390 nm laser to capture the carbon-hydrogen (C-H) bond in lifted jet diffusion methane-air flame at atmospheric conditions. DeSouza et al. [266] studied sub- and supercritical N_2 jet with 355nm laser.

For this task, a constant volume chamber is used. Since there is no information about the offset of the wavelength of a required wavelength of CH in high pressure, LED, which has a variety of wavelengths, was chosen. A LED is centered at 395nm ± 10 nm FWHM (Full Width at Half Maximum). In this setup, a planar LED was used to investigate jet configuration instead of the white LED. Since 390 nm excites only CH, 3.39 μm laser does not need to detect CH coming out the injector. Figure 118 shows the P-LED-IF of natural gas injection in a near sCO_2 environment. Natural gas consists of 92.9% of CH_4, 4.8% of C_2H_6, 1.5% of C_3H_8, and 0.8% of C_4H_{10}. As shown in Figure 112, before the injection, anything excited with the LED. After opening the injector, natural gas came out near sCO_2, and CH was excited by the LED and could capture emitted CH jet.

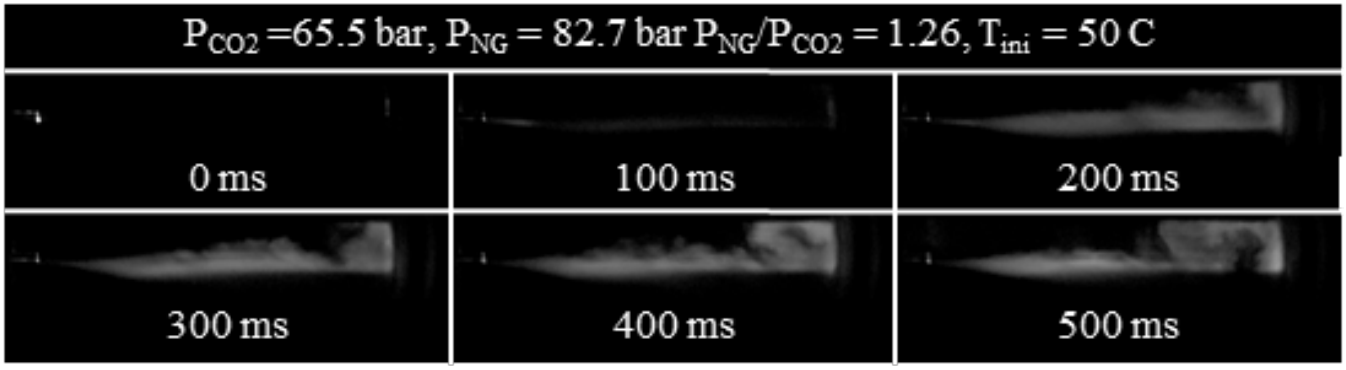

Figure 117: CH P-LED-IF through natural gas injection in CO_2

8.3 Laser absorption measurements

Measuring laser absorption of CH_4 in CO_2 at the pressure of above 100 bar was the goal of this task. Measuring absorption provided line-of-sight averaged concentration information at the laser probe beam. This subtask was conducted inside the constant volume chamber with two optical accesses.

The measured absorption cross-section can be used to determine the concentration of CH_4 in a high diluted CO_2 environment. Studies of absorption cross-section of CH_4 in low pressure are sufficient. Koroglu et al. [267] measured the CH_4 absorption cross-section in high diluted CO_2 at a high temperature but low pressure with a shock tube facility. Pyun et al. [268] measured CH_4 absorption cross-section up to 5.5 atm. There is no study about the absorption cross-section of CH4 in high pressure, especially in sCO_2 conditions. This task took the absorption cross-section of CH_4 from atmospheric to 100 bar with high diluted CO_2.

For Subtask 8.3, a constant volume chamber with two 2" diameter sapphire windows that can withstand up to 140 bar. The chamber was seated inside a furnace to create homogeneous mixtures. Two detectors, one is for reference signal, and the other one is for transmitted signal, and 3.39 um laser was used to measure absorbance cross-section. Figure 3 shows the absorbance cross-section of CH_4 with 3.39 μm laser and simulation with HITRAN. Vary concentrations of CH_4, 0.1% ~0.8% were used to measure absorbance cross-section. The measurement data is in good agreement with simulation data.

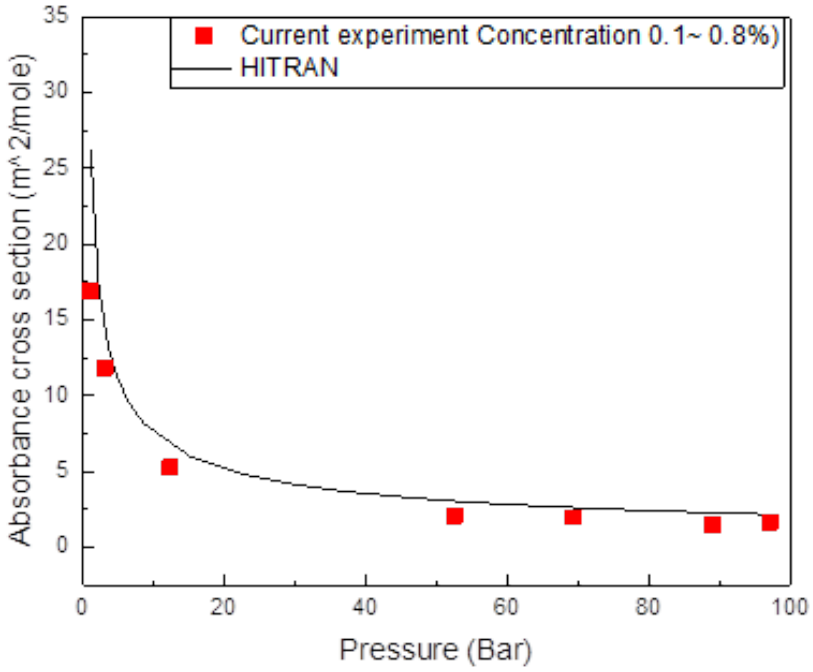

Figure 118: Absorbance cross-section of CH_4 in CO_2

8.4 Conclusions

Supercritical methane is injected into CO_2 environment at 70 - 200 bar, and jet flow is characterized by shadowgraphy and image processing. Also, LED-IF measurements are performed to investigate the mixing characteristics of methane jets. Further, laser absorption measurements are performed to experimentally verify the absorbance cross-section of CH_4.

APPENDIX 1 THERMAL AND TRANSPORT PROPERTIES FOR SCO_2

The direct-fired supercritical CO_2 (sCO_2) cycle is currently considered as a zero-emission power generation concept. It is of interest to know how to optimize various components of this cycle using computational tools, however, a comprehensive effort on this area is currently lacking. In this work, the behavior of thermal properties of sCO_2 combustion at various reaction stages has been investigated by coupling real gas CHEMKIN (CHEMKIN-RG) [1] with an in-house Premixed Conditional Moment Closure (PCMC) code [2] and the high-pressure Aramco-2.0 kinetic mechanism. Also, the necessary fundamental information for sCO_2 combustion modelling is reviewed.

The Soave-Redlich-Kwong equation of state (SRK EOS) is identified as the most accurate EOS to predict the thermal states at all turbulence levels. Also, a model for the compression factor Z is proposed for sCO_2 combustors, which is a function of mixture inlet conditions and the reaction progress variable. This empirical model is validated between the operating conditions 250-300 bar, inlet temperatures of 800-1200 K and within the current designed inlet mole fractions and the accuracy is estimated to be less than 0.5% different from the exact relation. For sCO_2 operating conditions the compression factor Z always decreases as the reaction progresses and this leads to the static pressure loss between inlet and exit of the sCO_2 combustor.

Further, the Lucas et al. and Stiel and Thodos methods are identified as best suitable models for predicting the viscosity and thermal conductivity of the sCO_2 combustion mixtures.

NOMENCLATURE

A^*	dimensionless form of 'a' for mixture
A1-A10	model constants for Z
B^*	dimensionless form of 'b' for mixture
BKW	Becker-Kistiakowsky-Wilson
CHEMKIN-RG	CHEMKIN for real gases [269]
CMC	Conditional Moment Closure
EOS	equation of state
LJ	Lennard-Jones model
NA	Nobel-Abel equation of state
N	turbulent dissipation rate
NIST	National Institute of Standards and Technology
P	pressure
Pc	critical pressure (dyne/cm^2)
PRS	Peng-Robinson Equation of state
PCMC	Premixed Conditional Moment Closure code [270]

R	universal gas constant (ergs/mole·K)
R_{mix}	gas constant of the mixture (kJ/Kg-K)
RPV	reaction progress variable
RK	Redlich-Kwong Equation of state
SRK	Soave-Redlich-Kwong Equation of state
T	temperature
a	mixture ‘a’ (dyne·cm4/mole2)
b	volume correction term in cubic equations of state (cm3/mole)
b_m	mixture ‘b’ (cm3/mole)
f_ω	function of ascentric factor
HP	high-pressure
LP	low pressure
n_s	process index
S_c	source term (1/s)
sCO2	supercritical CO_2
sO2	supercritical O_2
vdW	van der Waals Equation of state

u	a constant in the cubic equations of state
w	a constant in the cubic equations of state
ω	acentric factor of the species
X_i	mole fraction of species ‘i’
Y_i	mass fraction of species ‘i’
Z	compression factor
β_P	isobaric compressibility
β_T	isothermal compressibility
λ_i	thermal conductivity of species ‘i’
λ_{mix}	thermal conductivity of the mixture
μ_i	viscosity of the species ‘i’
μ_{mix}	viscosity of the mixture
$\bar{\rho}$	density
$N\|\zeta$	conditioned scalar dissipation
$\tilde{S}_c\|\zeta$	conditioned source term for RPV
$\dot{\tilde{\omega}}_i\|\zeta$	conditioned reaction rate

$\tilde{Q}_i$ conditioned mass fraction

INTRODUCTION

The fundamental research and technology development for direct-fired supercritical CO_2 (sCO_2) power plants is gaining the attention of researchers in academic institutions and industries, due to its remarkable theoretical promise of efficiency, compactness and eco-friendliness. The current state-of-the-art, optimized sCO_2 operating conditions (typical mixtures) are 200-300 atm. pressure, 800-1000 K inlet temperature and 1200-1500 K outlet temperature [271]. These unconventional and challenging operating conditions entail the need to review the fundamentals of all engineering fields involved in gas turbine power plant combustor technology. At these supercritical operating pressures, the mean free path between the molecules reaches to a distance where the intermolecular forces becomes prominent [272]. Though, there always exists an attraction or repulsion force between the molecules of any fluid, at sub-critical pressures the magnitudes of these forces are trivial [273] and do not impact the thermal properties of the fluid. In a supercritical combustion environment where there are hundreds of species and radicals, the influence of intermolecular forces depends on the proportion of the mixture constituents. Therefore, the rules or models of thermal properties which are developed to consider the combined effect of the mixture constituents is very important and needs to be identified before a simulation. The thermodynamic behavior of supercritical fluids has been well recorded by researchers for applications such as petroleum, food processing, pharmaceutical, textile, metallurgical and rockets. There is significant literature available on thermal properties, theoretical modelling and advanced numerical simulations [251,

274-279] of rocket combustion applications. However, for emerging sCO_2 combustion, the fundamental thermal quantities such as specific heats, speed of sound, enthalpy, entropy, compression factor etc., are not yet accurately quantified. Therefore, the main motivation of this work is to provide a quantification of the important thermal properties which are useful in calculations of combustion systems. The Equation of State (EOS) is most important in quantifying the thermal properties of a system because every thermal property is directly related to pressure, temperature and specific volume of that system and the EOS is the relation which connects these three parameters. The first and foremost aspect of any supercritical combustion simulation is, choosing a suitable the EOS. Therefore, a brief review of EOS's and the formulations of EOS for combustion mixtures are discussed in detail and then, a comprehensive analysis is carried out between most popular EOS such as Peng-Robinson (PRS) and Soave-Redlich-Kwong (SRK) at various turbulence levels to identify the best suitable EOS for sCO_2 combustion simulations.

In subsequent sections, the importance of compression factor (Z) in sCO_2 combustion modelling is discussed in detail along with a correlation to model Z in 1D combustor analysis is proposed. Later, important combustion parameters such as constant pressure specific heat (C_p), constant volume specific heat (C_v), ratio of specific heats (γ), compression factor (Z), isothermal compressibility (β_T), and process index (n_s) are quantified.

Finally, high-pressure viscosity and thermal conductivity models for mixtures and pure-components are reviewed from literature and the suitable models are identified for sCO_2 combustion simulations based on their accuracy and computational time.

Modelling

It is known that, under supercritical conditions the ideal gas assumption will not predict the system density correctly due to the existing repulsive or attractive forces between the molecules. These intermolecular forces completely alter the thermal and kinetic properties of combustion like enthalpy, entropy, reaction rates, etc., therefore, the kinetic tool which is being used for the simulation of sCO_2 combustion must have the capabilities to calculate the thermal and kinetic properties based on the EOS. The CHEMKIN-RG (extended version of CHEMKIN) is one such tool developed by Schmitt, R.G., et al., [269] in 1993 and this tool is coupled with an in-house Premixed-Conditional-Moment Closure code (PCMC) [280] for estimating the state related thermal properties of sCO2 combustion at different turbulence levels. The PCMC model as shown in Eq.1, is a premixed turbulent combustion model which conditions the species mass fractions on the reaction progress variable (RPV) and closes the chemical source terms in the enthalpy equation with conditioned reaction rates [270]. In other words, the PCMC can estimate all the species mass fractions involved in combustion as the reaction progresses from unburnt to fully-burnt conditions, at various turbulence levels by solving the second order PCMC ordinary differential equation for each species with a two-point boundary value problem solver.

A high-pressure methane kinetic mechanism, Aramco 2.0 [281], which is validated up to 260 atm. pressure in 67% argon dilution and up to 180 atm. in 55% N_2 dilution, is used. The mechanism is also validated with 90% CO_2 diluted, 110 atm., unpublished shock tube auto-ignition data. The *Aramco* mechanism is also compared with the GRI 3.0 [116] and USC [282] mechanisms up to 40 bar with equivalence ratios up to 3, and found to be better performing again available shock tube data [283]. This Aramco 2.0 mechanism, tailored for C1-C2 compounds has 73 species and 426 reactions.

The PCMC equation:

$$\langle \bar{\rho}\widetilde{N}|\zeta\rangle \tilde{Q}_i'' - \langle \bar{\rho}\tilde{S}_c|\zeta\rangle \, \tilde{Q}_i' + \langle \bar{\rho}\dot{\tilde{\omega}}_i|\zeta\rangle = 0 \qquad (1)$$

Here, $\bar{\rho}$ is the density, $\widetilde{N}|\zeta$ is the conditioned scalar dissipation (level of small scale turbulence), $\tilde{S}_c|\zeta$ is the conditioned source term for the RPV Eqn., $\dot{\tilde{\omega}}_i|\zeta$ is the conditioned reaction rate and $\tilde{Q}_i$ are the conditioned mass fractions and the derivatives are with respect to the RPV [2, 13].

The Equation of state

The Equation of state (EOS) is a correlation which describes the relation between pressure (P), temperature (T) and density (ρ) of a thermal system. Every fluid or mixture exists under a phase i.e., solid, liquid or gaseous vapor, based on the pressure and temperature acting on that system. At lower pressures and temperatures, the liquid phase of the system will have a different density than the gaseous phase. But, as the pressure and temperature increases, the difference between the phase densities decreases and at one combination of pressure and temperature, the density of both phases becomes the same and at this point the phase of the system cannot be distinguished based on the density. This combination of pressure and temperature is called the critical point and any pressure and temperature combination above the critical point is considered as supercritical state. A schematic diagram is shown in Fig. 1, to illustrate the critical point of CO_2

and the operating conditions of sCO_2 combustor in that state diagram. In these supercritical states, the molecules are pushed very close in such a way that the attractive or repulsive forces between the molecules becomes significant. A supercritical fluid has some liquid and some gas properties.

From molecular theory of collisions, the temperature is nothing but the average kinetic energy of the molecules in the system and the pressure is created when these moving molecules collide with the boundary of the system. Therefore, when there are significant intermolecular forces at the microscopic level the average kinetic energy of the molecules i.e., the temperature of the system may increase or decrease and similarly the specific volume of the system may be effected. Therefore, a correction factor is needed for temperature and pressure terms in the thermal equations. But any thermal property can be determined by two fundamental quantities from the pressure, temperature and density. The EOS is the relation which connects these three properties.

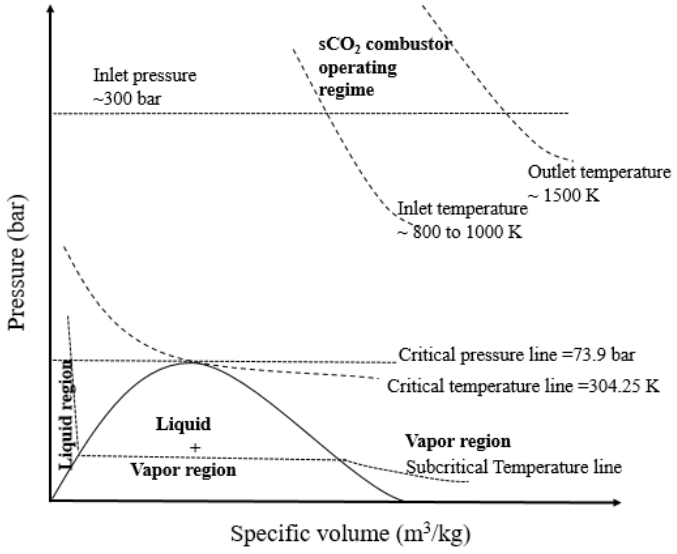

Figure 1: Schematic state diagram of a pure CO2.

For real gases, the thermodynamic state equation turns into the Eq. 2.

$$P = \rho Z R_{mix} T \qquad (2)$$

Here, P is pressure (Pa), ρ is density of mixture (kg/m^3), R_{mix} is gas constant of that mixture (kJ/Kg-K), T is temperature (K), Z is compression factor or compressibility factor. For ideal gases Z is unity and for real gases it can be either greater or less than one. A Z value less than one represents the attractive forces and Z greater than one represents the repulsive forces between the molecules. In general, the Z value is less than one after the critical point because as the molecules come closer due to pressure they initially experience attractive forces and after a certain combination of pressure and temperature it again becomes greater than one due to the strong repulsion of electron clouds over the molecules. Also, the behavior of Z varies from species to species and especially, in combustion it also depends on inter-species interactions. Therefore, the first interesting question to be asked is, whether sCO_2 operating conditions are in a zone where the molecules are repelling or attracting? This question is answered in the next sections.

In a combustion mixture, there exists polar molecules and non-polar molecules. The polar molecules are one which will have ionic-charges on their outer atoms (for example H_2O) and non-polar molecules will have neutral charges on the outer atoms (for example CO_2 and O_2). Therefore, to measure the repulsion or attraction forces accurately one may need to have finer molecular details.

Boyle was the first person to demonstrate the P-T-ρ relation for an ideal gas, but only the extensive work of Van der Waals in the late eighteenth century [284] delineated the first

approximation of EOS for real gases. The EOS can be broadly categorized into three types, they are the virial-type, molecular-based and van der Wall type EOS [233, 234]. The virial and molecular based EOS are highly accurate and complex in their formulations. Therefore, using such EOS types in CFD combustion applications is difficult because, the EOS must consider all the species involved in the mixture and solve for each cell in the computational domain at each time step. The NIST-REFPROP [285] is one such program where complex EOS of such type are used to calculate the thermal properties of the fluids and fluid mixtures. The computational expensiveness involved in using the NIST for CFD is reported in [286]. However, it must be noted that the NIST is considered as the most accurate EOS available. Therefore, it is usual in the literature to see the usage of NIST as a reference for EOS validations where experimental data is not available. The third category of EOS, i.e., the van der Waals type of EOS are empirical in nature and they are the main type used in combustion simulations.

Succeeding proposals after van der Waal have largely modified the basic van der Waals correlation for better accuracies. The improved van der Waals class equations like Redlich-Kwong (RK) [287], Soave-Redlich-Kwong (SRK) [236] and Peng-Robinson EOS (PRS) [235] are the most popular EOS for supercritical CFD simulations of Rocket combustion systems [237, 238] due to their simple formulation and modest computational cost.

The work of Patel [288] proposed a common cubic equation form for RK, SRK and PRS EOS as shown in Eq. 3.

$$P = \frac{RT}{(V-b)} - \frac{a(T)}{V(V+b)+c(V-b)} \qquad (3)$$

Here, R is the universal gas constant, a is a function of temperature and b and c are temperature corrections. The term a represents the temperature correction factor and b, c represent the corrective factors for volume terms in the equation. When $c = b$, Eq. 3 reduces to the Peng-Robinson equation and when c =0, it reduces to the Redlich-Kwong or Soave-Redlich-Kwong. Also, Eq. 3 can also be represented in a cubic form of Z as shown in Eq. 4. The following set of important equations are reproduced from the CHEMKIN-RG manual [269].

$$Z^3 - (1 + B^* - uB^*)\mathrm{Z}^2 + (A^* + wB^{*2} - uB^* - uB^{*2})Z - A^*B^* - wB^{*2} - wB^{*3} = 0 \qquad (4)$$

In Eq. 4, the Z can be solved analytically and it will have three solutions due to its cubic order. Only, when the mixture of interest is subcritical in both pressure and temperature, there are three real roots to this equation. Therefore, at subcritical conditions, the correct real Z must be identified by phase equilibrium procedure and for supercritical conditions the largest real root can be considered as the compressibility factor.

In Eq. 4, the term A^* is non-dimensional attraction term and is equal to $\frac{a_m P}{R^2 T^2}$, $B^*$is non-dimensional repulsive term and is equal to $\frac{b_m P}{RT}$. The mixing rules in Eq. 5 and 6 are used to find a_m and b_m.

$$a_m = \sum_{i=1}^{KK} \sum_{j=1}^{KK} X_i X_j (a_i a_j)^{1/2} - (1 - \overline{k_{ij}}) \quad (5)$$

and,

$$b_m = \sum_{i=1}^{KK} X_i b_i \qquad (6)$$

Here, the subscript i refers to a species index, X_i represent mole fractions, a_i and b_i are pure species properties, and k_{ij} are binary-interaction coefficients that are determined empirically. Although empirical in practice, this interaction coefficient is a measure of deviations from the ideal solution behavior for interactions between the i^{th} and j^{th} components [289]. Thus, its value is 1.0 when i equal j, i.e., for pure fluid interaction and it is nearly 1.0 for component pairs which form nearly ideal solutions. Its value differs considerably from 1.0 when the component pair forms highly non-ideal solutions. Thus, accurate values of k_{ij} are required when i or j is a light hydrocarbon or a nonhydrocarbon (for example methane with hydrocarbons heavier than n-butane, CO_2-hydrocarbon, H_2S-hydrocarbon and N2-hydrocarbon mixtures). More detailed information about k_{ij} can be found in [290-293]. Also, the coefficients u, w, a and b for Eq. 4 are presented in Table 1. The choice of these coefficients changes Eq. 4 to the EOS of interest.

The CHEMKIN-RG has the capabilities to model the EOS's by van der Waals (vdW), Redlich-Kwong (RK), Soave-Redlich-Kwong (SRK), Peng-Robinson (PRS), Becker-Kistiakowsky-Wilson (BKW) and Nobel-Abel (NA) EOS. In the current work, only the RK, SRK

and PRS EOS are used for comparison, because these are the most popular EOS which are being used in rocket combustion simulations.

TABLE 1: THE COEFFICIENTS FOR CUBIC EQUATION OF STATE

EOS	u	w	b	a
vdW	0	0	$\frac{RT_c}{8P_c}$	$\frac{27}{64}\frac{R^2T_c^2}{P_c}$
RK	1	0	$\frac{0.08664RT_c}{8P_c}$	$\frac{0.42748}{64}\frac{R^2T_c^{2.5}}{P_cT^{0.5}}$
SRK	1	0	$\frac{0.08664RT_c}{8P_c}$	$\frac{0.42748}{64}\frac{R^2T_c^{2.5}}{P_cT^{0.5}}\ l$
PRS	2	-1	$\frac{0.07780RT_c}{8P_c}$	$\frac{0.42748}{64}\frac{R^2T_c^{2.5}}{P_cT^{0.5}}\ l$

Here,

T_c −Critical Temperature of the species,

P_c − Critical pressure of the species,

ω −ascentric factor of the species,

$l = [1 + f_\omega(1 - T_r^{0.5})]^2$,

For SRK EOS, $f_\omega = 0.48 + 1.574\omega - 0.176\omega^2$ and

For PRS EOS, $f_\omega = 0.37464 + 1.54226\omega - 0.26992\omega^2$

It must be noted that, the critical properties like T_c , P_c and ω for all the species and radicals in a combustion phenomenon are not available in the literature. Therefore, it is the practice to assume the critical properties of the largest diluent in the simulation to the species or radicals for which the critical properties are not known.

Since these cubic-EOS are empirical by their origin, adopting them to an application requires a validation with data. For example, some investigations recommend SRK EOS for CH_4/LO_x and kerosene/LO_x mixtures [277, 294]. Whereas Poschner and Pfitzner [295] recommends PRS for H_2/O_2 mixtures. Nonetheless, the most used EOS are the SRK and PRS. The Figure 2 (a) and (b) shows the P-T-ρ correlations of CO_2 and O_2 with various EOS models. The Fig. 2 (a) illustrates a better accuracy for PRS EOS over SRK and RK EOS when compared with NIST and this accuracy increases as the temperature increases. Interestingly, the accuracy of SRK EOS also increases with temperature and beyond 1200 K, the SRK and PRS are not distinguishable. For sCO_2, the average deviations of PRS and SRK EOS with NIST are 0.04 and 1.87 percent respectively. Further, Fig. 2 (b) shows the better accuracy of SRK EOS over PRS and RK. For sO_2, the average deviations of PRS and SRK EOS with NIST are 1.47 and 0.25 percent respectively. The percentage deviations of EOS of sCO_2 and sO_2 illustrates that, the PRS EOS, which is accurate for sCO_2 is not as accurate as SRK EOS for sO_2. Therefore, the best EOS for combustion mixture depends on the proportions

of the CO2, O2 and other mixture constituents. It is known that the proportion of these species vary from unburnt to fully-burnt condition and at various turbulence levels.

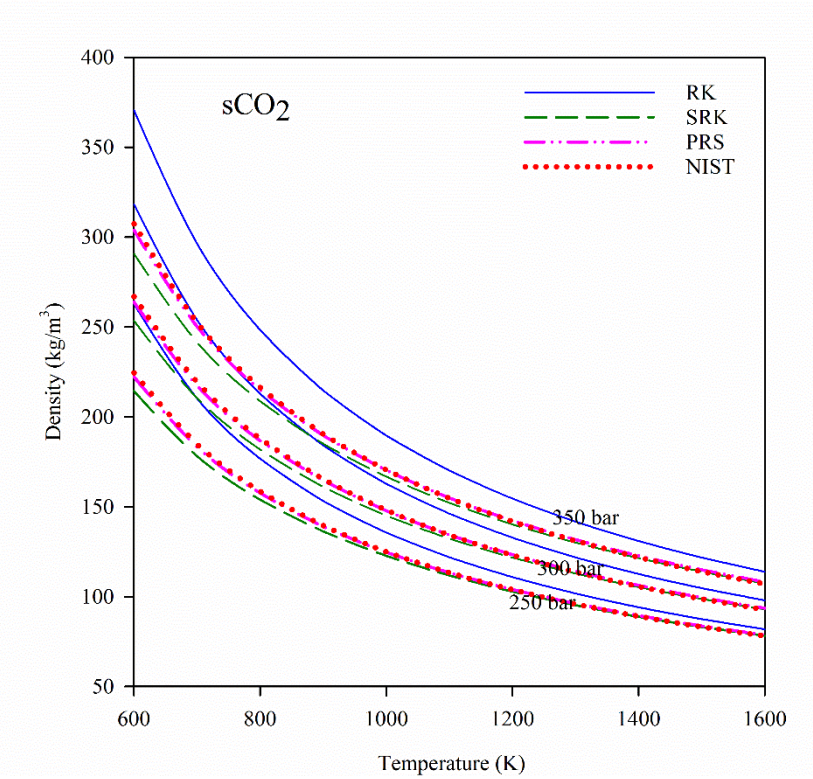

FIGURE 2 (a): P-T-ρ CORRELATION OF VARIOUS EOS MODELS FOR SCO2.

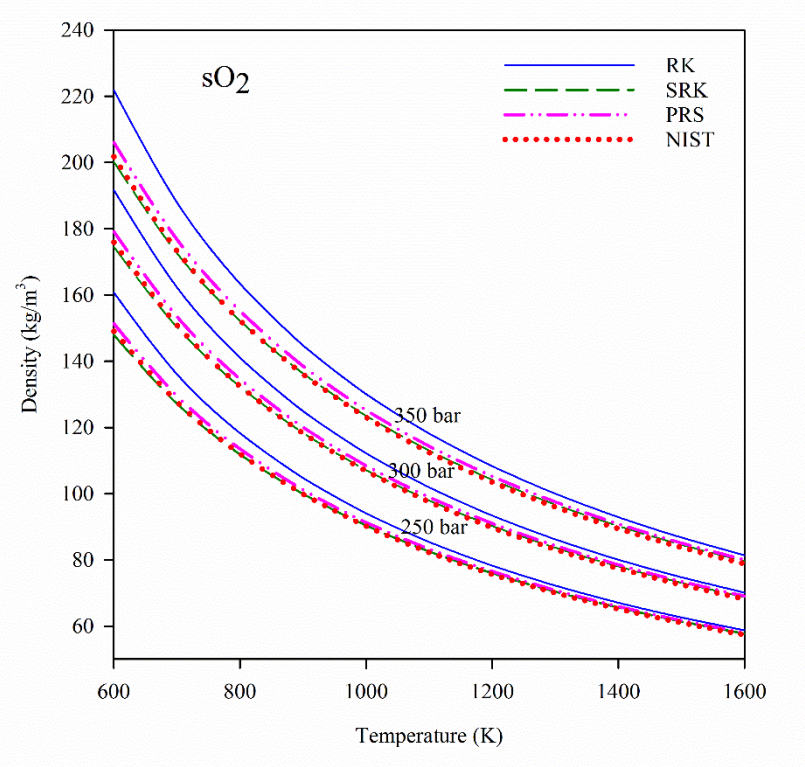

FIGURE 2 (b): P-T-ρ CORRELATION OF VARIOUS EOS MODELS FOR SO2

It is shown that, the chemical pathways are influenced by the small-scale turbulence (turbulent dissipation rates, N) [270]. The turbulent dissipation rate characterizes the magnitude of molecular mixing (small scale turbulence) in a combustion process, were the pockets of high strain change in the local chemical reactions which influence chemical kinetic pathways [296]. Therefore, the proportions of mixture constituents vary between the turbulent regimes of different dissipation rates [280]. Hence, this EOS validation is also carried between two turbulent dissipations values such as N=10,000 and N=1. Most of the EOS validation in previous literature is available only for

pure species. However, in the current investigation, the EOS validation is carried for combustion mixtures at various reaction progress variables (RPV).

For the comparison of EOS's, the determination of mass fractions at various RPV has been made with the PCMC code as described above and CHEMKIN-RG is used for thermal state prediction. The RPV determines the amount of enthalpy released out of reaction from the total available enthalpy of that mixture. When RPV is equal to zero, that is the mixture is still unburnt and when RPV is one, the mixture has released its complete enthalpy content, or in other word the combustion is complete.

Figure 3 is a schematic of the mixture compositions considered for EOS comparison and the reference inlet mixture is chosen as shown in Table 2. When RPV is zero, that is at the inlet unburnt mixture, the mole ratio of CH_4 to O_2 is fixed at 0.5 (stoichiometric) and the number of CO_2 moles is twenty-four. This combination of CH_4, O_2 and CO_2 gives the outlet temperature as ~1500 K. The PCMC first calculates the equilibrium solution of this inlet condition and then, it solves the PCMC equation (Eq. 1) between these inlet and equilibrium solutions for various turbulent dissipation values (N). Therefore, based on N value, the proportion of mixture constituents vary between RPV =0 to 1. The PCMC can calculate the mass fraction of all the species involved in the chemical mechanism i.e., Aramco 2.0 by a constant enthalpy and constant pressure process. But, NIST can only calculate the properties of the mixture having seven species such as CO_2, CH_4, O_2, H_2, H_2O, CO, and C_2H_6. Despite such limited number of species, the NIST can be still used for sCO_2 combustion EOS validation because, at any given RPV the sum of all these mole fractions are more than 99.99%. The operating condition one (OP1) as shown in Table. 2, is considered for the EOS comparison. This operating condition considers the approximate boundary conditions for

sCO_2 combustors, i.e., the inlet temperature as 1000 K, exit temperature as 1500 K and the inlet CH_4-O_2 ratio in stoichiometric proportions.

The difference in the mass fractions of the PCMC solution by SRK and PRS is observed to be negligible (less than 0.001%) for the major species like H_2O, O_2 and CO_2, but for CH_4 this difference is up to 2.1% and the temperatures differed by 0.12%. Therefore, an average mass fractions and corresponding temperatures of both SRK and PRS solutions has been taken to find the corresponding thermal properties from the NIST. In this comparison, the RK EOS is not considered due to its higher deviation from NIST.

Figure 4, shows the comparison of thermal state prediction of PRS and SRK EOS with NIST at a pressure of 300 atm. at two different turbulent dissipation rates. Due to the variation of species between the unburnt to completely burnt mixture at these turbulent dissipation values, a density difference of 2.5 % is observed. The primary vertical axis represents the mixture density, whereas the secondary vertical axis represents the difference of the EOS prediction with NIST.

The result shows that the SRK EOS has better accuracy for density prediction at both the turbulent dissipation values. The average deviation of SRK EOS is 0.71 %, whereas for PRS it is 1.78 % when N=1 and at N=10,000 the SRK EOS is 0.70 % and PRS has 1.71 %. These narrow deviations of SRK EOS with NIST shows that, SRK EOS is the most accurate EOS which can be used for sCO_2 combustors. Also, it is observed that, the computational time for these EOS is almost the same because both the EOS are derived from the same cubic equation of state.

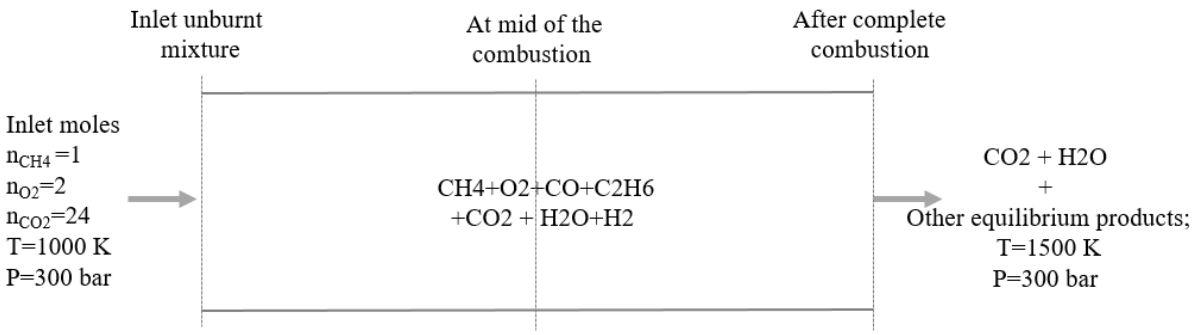

FIGURE 3: SCHEMATIC DIAGRAM TO ILLUSTRATE THE MIXTURE CONDITIONS CONSIDERED FOR COMPARING THE EOS

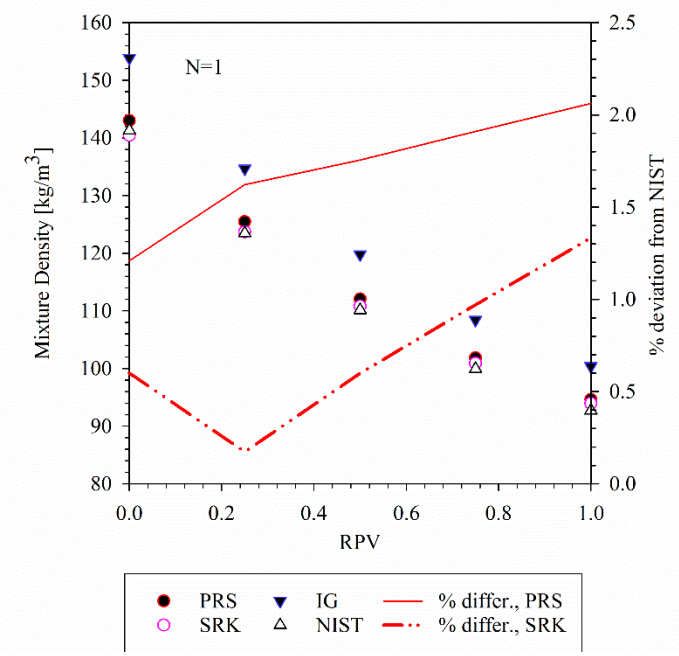

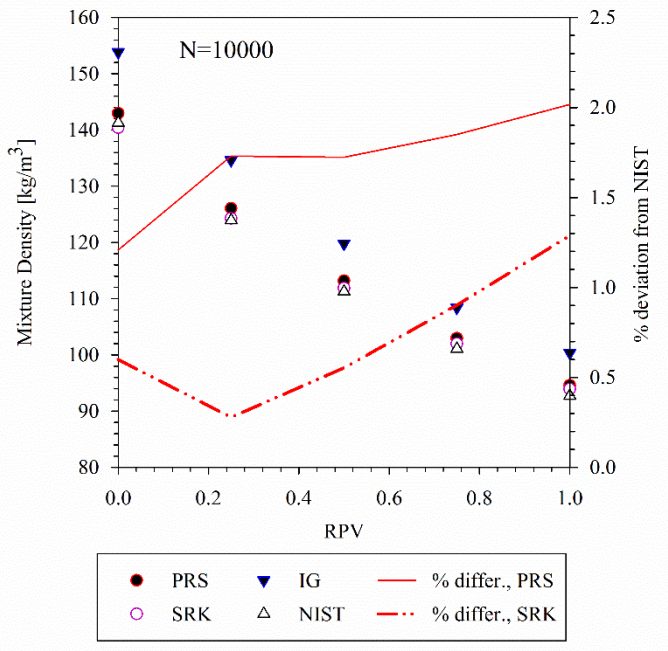

FIGURE 4: COMPARISON OF PRS AND SRK EOS WITH NIST FOR THE TURBULENT DISSIPATION RATES N=1 AND N=10000

THE COMPRESSION FACTOR (Z)

When the flow is incompressible, the thermodynamics can be separated from the fluid kinematics (the movement of the flow) and fluid dynamics (the forces in the flow) [297]; it is a simplified assumption for many of the non-reacting flows where the density of the system is almost constant and this incompressible assumption makes the flow much easier for analyzing. However, pressure gradients, temperature gradients, Mach number variations can cause the flow to be compressible. But in supercritical flows it also appears due to molecular attractive and repulsive forces which are represented by Z. Therefore, it is essential to understand the behavior of Z in sCO_2 combustion. In compressible flows, the density variation with in the working fluids transfers the energy from the fluid to the surroundings; in other words, the thermal energy in the system converts into mechanical energy (changes in velocity and momentum) or mechanical energy converts into thermal energy (increases the temperature and hence changes in density).

Figure 5 shows the variation of compressibility factor under various operating conditions as listed in Table 2. Here, the operating conditions represent various possibilities of sCO2 combustor operation. As explained in previous sections, OP1 is the reference case used in the current work, which considers the inlet and outlet boundary conditions for a sCO_2 combustor. The quantification of fundamental thermal properties in this literature are based on the OP1. The OP2 show what may happen to the Z when CO_2 mole fraction increases in the reference mixture, the OP3 shows what may happen to the Z when CH_4 and O_2 mole fractions in reference mixture increases, the OP4 shows what may happen when the inlet temperature in the reference mixture is decreased. In the

later part of this section an empirical correlation is proposed for the estimation of Z in the sCO2 combustor. The Operating condition OP5-OP8 are used as additional validating cases for this model.

Also, Fig. 5 answers the question which is being asked in the previous section, i.e., whether sCO2 operating conditions are in a zone where the molecules are repelling or attracting? The answer is, the sCO2 combustor exists in an operating zone where there exist repulsive forces among the molecules. The gradual decrement of Z with respect to the progress variable in Fig. 5 shows an important design aspect to the sCO_2 combustor designers. Because, from Eq. 2, the Z is a proportional to the pressure and as the reaction progresses (temperature of the mixture increases) the static pressure may reduce. It may result in the loss of turbine efficiency. In a conventional gas turbine combustor, the loss of static pressure may be due to flow obstacles or due to turbulent mixing, however in sCO_2 combustors the designers should deal with the depreciation of Z in the combustor due to the super critical nature of the flow. It is also interesting to note that, beyond the critical point, up to certain pressures the Z value increases with temperature and this phenomenon get reversed after a certain supercritical pressure. The sCO_2 combustor operating conditions are existing in a zone where the Z decreases with temperature.

Figure 5 also shows that, the slope of Z is larger for OP3, which indicates that, increasing the inlet CH_4 and O_2 would increase the static pressure loss, it is mainly due to the increase in temperature (the Z loss is 5% in this case). Whereas OP2 and OP4 show a minimum slope which indicates that, the static pressure loss can be minimized either by increasing the CO2 content in the initial mixture or by decreasing the inlet temperature. It is because, the addition of CO_2 absorbs the temperature released due to its high specific heat and the lower inlet temperature results in a lower final

temperature. The dilution of the combustion mixture with additional CO_2 after combustion would help in regaining the Z and hence the static pressure.

Table-2: Operating conditions considered for investigating the behavior of Z

Operating Condition	What it explains?	Initial molar mixture ($CH_4/O_2/CO_2$)	Initial Temperature (K) / Pressure (bar)
OP1	Reference Mixture	1/2/24	1000/300
OP2	When the inlet [CO_2] increases	1/2/40	1000/300
OP3	When the inlet [CH_4+O_2] increases	2/4/24	1000/300
OP4	When the inlet	1/2/24	800/300

	temperature decreases		
OP5	Validation case-1	2/4/24	800/300
OP6	Validation case-2	1/2/24	1000/250
OP7	Validation case-3	2/4/24	1000/250
OP8	Validation case-4	1/2/24	1200/300

In ideal gases, the pressure is nothing but the rate of change of momentum exchange per unit area of the combustor walls. In supercritical conditions, the repulsive forces between the molecules will be added to the overall momentum and hence pressure. Therefore, the pressure correction equation is modified for the Pressure Implicit Split Operation algorithm (PISO) and the suitable solution sequence is suggested by Park and Kim [298]. Basically, the Z factor is considered in the PISO algorithm from the real-gas EOS, instead of ideal gas EOS.

The calculation of Z is very important because the thermal properties in supercritical combustion are functions of Z. Some important isentropic flow relations are presented in Table 3, from the work of Baltadjiev [299]. Therefore, in this work an empirical model as shown in Eq. 7 is suggested. This equation is derived from the analysis of the operating conditions presented in Table

2. The density values can be computed from the ideal gas assumption and then corrected with the Z calculated from the Eq. 7, reducing computational time. This equation is validated for the inlet pressure 250-300 bar, inlet temperature 800 K – 1200 K, inlet stoichiometric CH_4 and O_2 mixture and CO_2 mole fraction up to 0.93. Here, $(n_{CO2})_{in}$is the inlet CO2 moles, $(n_{CH4})_{in}$ is the inlet methane moles, and T_{in} is the inlet temperature in K.

$$\mathrm{Z} = \left(\mathrm{A1} - \mathrm{A2} * \left(\frac{(n_{CH4})_{in}}{(n_{CH4})_{in} + (n_{O2})_{in} + (n_{CO2})_{in}}\right) - A3 * (300 - P_{in})\right)$$

$$-\left(1 - A4 * (300 - P_{in})\right) * A5 * \{(1 + A6 * (A7 - (n_{CO2})_{in}))$$

$$-\left(A8 * (1 - (n_{CH4})_{in})\right)$$

$$-(A9 * (A10 - T_{in}))\} * RPV \qquad (7)$$

The calibrated constants are as follows,

$\mathrm{A1} = 1.0965$, $\mathrm{A2} = 0.0217$, $\mathrm{A3} = 0.36e^{-3}$

$\mathrm{A4} = 0.38e^{-2}$, $\mathrm{A5} = 0.0272$, $\mathrm{A6} = 0.0237$,

$\mathrm{A7} = 24$, $\mathrm{A8} = 0.6581$, $\mathrm{A9} = 0.00136$ and $\mathrm{A10} = 1000$

Figure 6 shows the correlation plot between the modelled Z and calculated Z by the SRK EOS. This model is validated with all the operating conditions from OP1-OP8 in Table 2. Each symbol in the plot represents the Z value at an operating condition over a RPV values from 0 to 1. All these

data points in the plot are well inside the 0.5 % error lines, which indicates that the proposed model predicts the Z as accurate as 0.5%.

Table-3: Important fluid flow relations

Parameter	Real gas	Ideal gas
Isothermal compressibility (β_T)	$\frac{1}{P} - \frac{1}{Z}\left(\frac{\partial Z}{\partial P}\right)_T$	$\frac{1}{P}$
Isobaric compressibility (β_P)	$\frac{1}{T} + \frac{1}{Z}\left(\frac{\partial Z}{\partial T}\right)_P$	$\frac{1}{T}$
Isentropic pressure exponent (n_s)	$\frac{\gamma}{\beta_T P}$	γ
Isentropic temperature exponent (m_s)	$\frac{\gamma - 1}{\gamma}\frac{\beta_T P}{\beta_P T}$	$\frac{\gamma - 1}{\gamma}$
Speed of sound (a)	$\sqrt{n_s Z R T}$	$\sqrt{\gamma R T}$

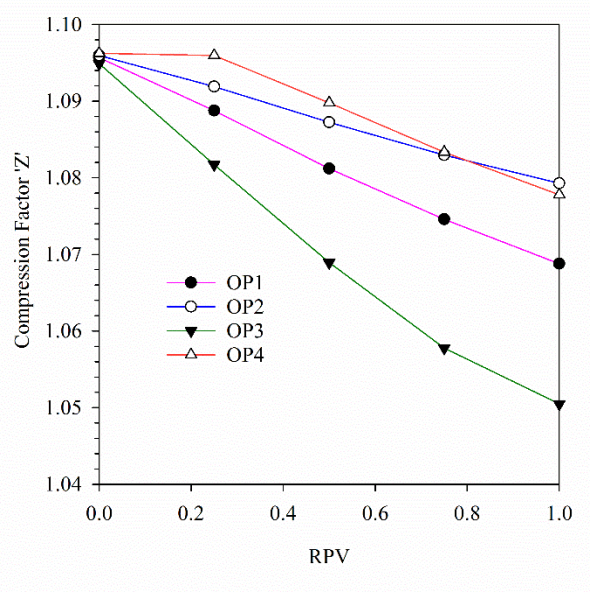

FIGURE 5: VARIATION OF Z WITH RESPECT TO RPV FOR VARIOUOS SCO2 OPERATING CONDITIONS

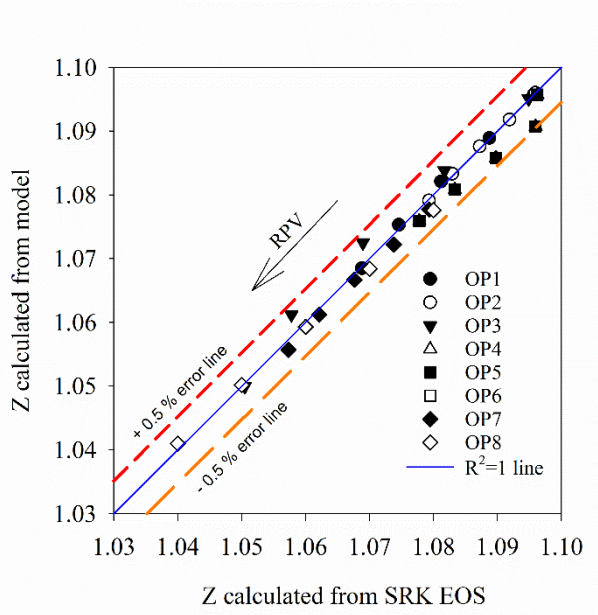

FIGURE 6: ERROR PLOT FOR THE Z FROM MODEL AND Z FROM SRK EOS

Specific heat capacities

The specific heat of a system indicates the resistance of the system to change its temperature when heat is added. Due to the high heat capacity of CO_2 compared to other species in a combustion mixture, the CO_2 in a sCO_2 combustor carries most the enthalpy with its flow rather than raising the temperature. However, for supercritical combustion, the Z factor also influences the specific heats. An attempt is made in this section to estimate its influence in sCO_2 combustors. Figure 7, shows the variation of c_p, c_v and γ (ratio of specific heats) for combustion mixtures with real gases and ideal gases. The figure illustrates that specific heat capacities calculated for sCO_2 combustion mixtures are always greater than the values calculated by ideal gas assumption because the Z value is always greater than unity. The general formula for specific heat is given by the expression.

$$c = \left(\frac{de}{dT}\right)_{p\ or\ v}$$

$$\Rrightarrow c = \left(\frac{d\left(\frac{E}{m}\right)}{dT}\right)_{p\ or\ v}$$

$$\Rrightarrow c = \left(\frac{d\left(\frac{E}{\frac{\rho_i}{Z}V}\right)}{dT}\right)_{p\ or\ v} \qquad (8)$$

From equation (8), for the same energy content (E) of the system, the specific heats in the sCO_2 combustion system is always higher than the ideal gas case. It must be noted that, as discussed in the earlier sections there are some operating conditions beyond the critical point, where the Z is less than unity and in this region, the specific heats are less than the ideal gas assumption. In other words, the specific energy in an sCO_2 combustion mixture is higher because of repulsive forces among the molecules. In fact, these repulsive forces when considered, increase all the specific properties such as entropy, Gibbs energy, etc.

Figure 8, shows the enthalpy-entropy relation for ideal and real gas assumptions. Here, the enthalpy and entropy are normalized with respect to its initial values at RPV equal to zero. These two curves deviate as they progress in combustion. It explains that there is a higher irreversibility associated in the combustion process due to the influence of Z and this irreversibility increases at higher temperatures. Also, the enthalpy released is approximately 1.6% more and entropy increased by 0.03% more than the ideal case at the end of the combustion.

The c_p of the mixture starts at a value 1.331 and by the end of combustion it reaches 1.381 kJ/kgK, whereas the c_v value starts at 1.111 and reaches 1.187 kJ/kgK. However, it must be noted that the c_p and c_v values are functions of Z and these values change when the operating conditions change Z. Also, the value of γ is about 1.2 for the inlet mixture and 1.164 for the fully burnt products. Another interesting trend can be seen from Fig. 7, that from c_p and c_v of ideal gas and real gases converges as the reaction progresses, it is because the repulsive forces decreases with increase in temperatures.

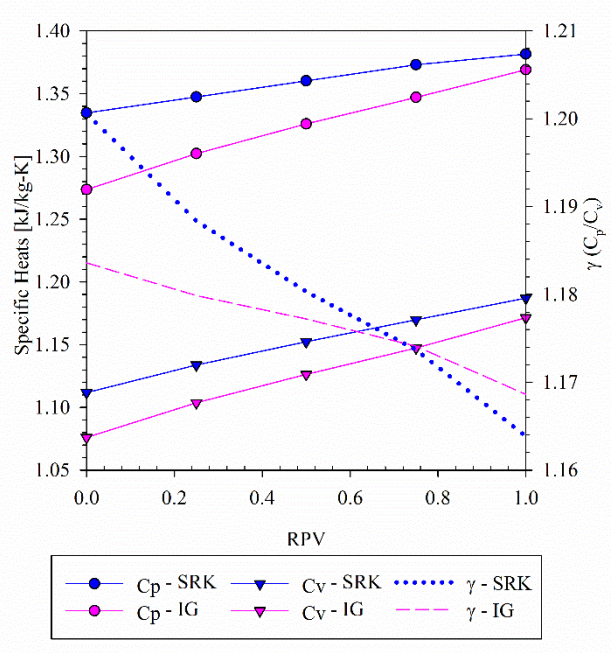

FIGURE 7: SPECIFIC HEATS FOR SCO2 COMBUSTOR

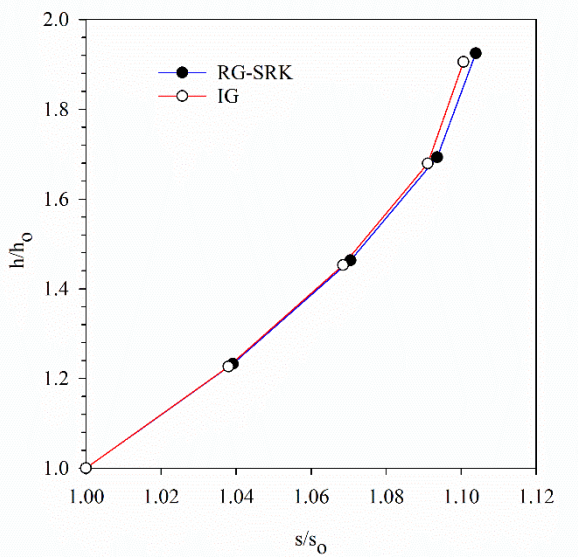

FIGURE 8: ENTHALPY-ENTROPY DIAGRAM FOR SCO2 COMBUSTOR

Pressure exponent

As shown in Table 3, the isentropic processes for real gases in the $p-v$ coordinate system is described as $pv^{n_s} = pv^{\frac{\gamma}{\beta_T P}} = c$ [299]. It is a crucial parameter which determines the path functions such as work and heat involved in a process.

Therefore, in this section the variation of n_s with respect to the reaction progress is discussed. The Fig. 9, shows that the value of pressure exponent n_s is 1.32 at the entry of the combustor and it gradually reduces to 1.245 by the end of combustion. It is because, the β_T which is constant for ideal gases is increasing as the combustion progresses and it results in a reduction of n_s. In general, for hand calculations, it is very common to assume the process index to be constant, but in sCO_2 applications this assumption may result in huge errors because the change of n_s is upto seven percent between the unburnt and fully-burnt mixture.

The isothermal compressibility β_T is the reciprocal of bulk modulus (K) of the combustion mixture. At first the β_T in the combustion mixture is less than its ideal gas value because the existing repulsive forces between the molecules resists the bulk compression. Secondly, it increases with respect to the RPV because the repulsive forces decrease as seen in Fig. 5 and hence the combustion mixture becomes relatively more compressible but still resistive to bulk compression compared to the ideal gas assumption. Therefore, the Isothermal compressibility will be overestimated up to seven percent when real gas assumption is not used.

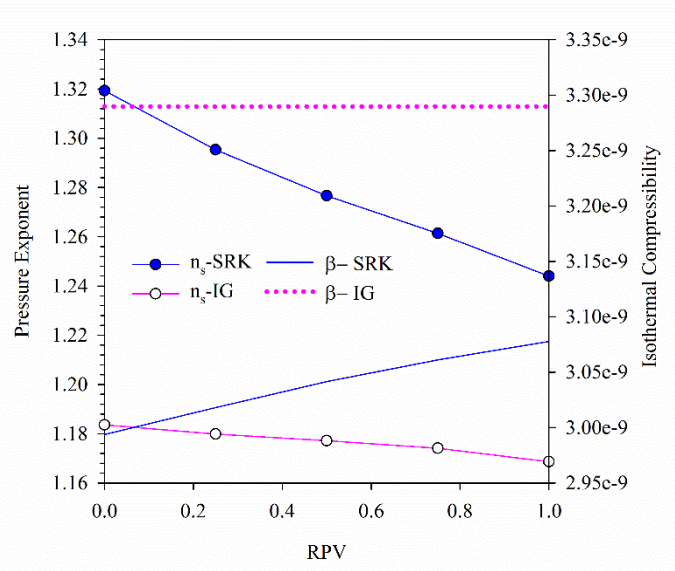

FIGURE 9: PRESSURE EXPONENT AND ISOTHERMAL COMPRESSIBILITY IN SCO2 COMBUSTOR

Speed of sound:

The speed of sound determines how fast a disturbance travels in a flow or in other words how fast information of an obstacle spreads in the flow. After a certain ratio of the flow speed and sound speed, the molecules will tend to compression or rarefaction and result in significant density changes in the flow. Therefore, an attempt is made in this section to estimate the speed of sound in the sCO_2 combustor. As shown in Table 3, the speed of sound is a function of n_s, Z and T. Therefore n_s and Z determines the speed of sound in the sCO_2 combustor. From the previous discussions, the values of these three parameters are larger when calculated with the ideal gas assumption.

Therefore, the speed of sound must be higher. Figure 10 shows the comparison of sound speed between the real gas assumption and ideal gas assumption. Also, the existing relation between speed of sound and density fluctuations in a flow has been modified for real gases.

The law of conservation of momentum is given as,

$$\rho V\, dV = -dP \qquad (9)$$

For Isentropic flow of real gases,

$$\frac{dP}{P} = n_s \frac{d\rho}{\rho} \qquad (10)$$

Substituting P= ρZRT in Eq. (10)

Therefore, $dP = n_s ZRT * d\rho$ (11)

From Table 3, $a^2 = n_s ZRT \Rightarrow dP = a^2 * d\rho$

Therefore, from Eq. (9)

$$\Rightarrow \rho V\, dV = a^2 * d\rho$$

$$\frac{-V^2}{a^2}\frac{dV}{V} = \frac{d\rho}{\rho} \qquad (12)$$

The term a^2 in Eq. (12) is higher for a sCO_2 combustor than the ideal gas value ($a^2 = \gamma RT$ in ideal gas assumption). Therefore, for a velocity change the change in corresponding density is lower for sCO_2 combustion by a factor $\left(\frac{\gamma}{n_s Z}\right)$ which is equal to ~13%.

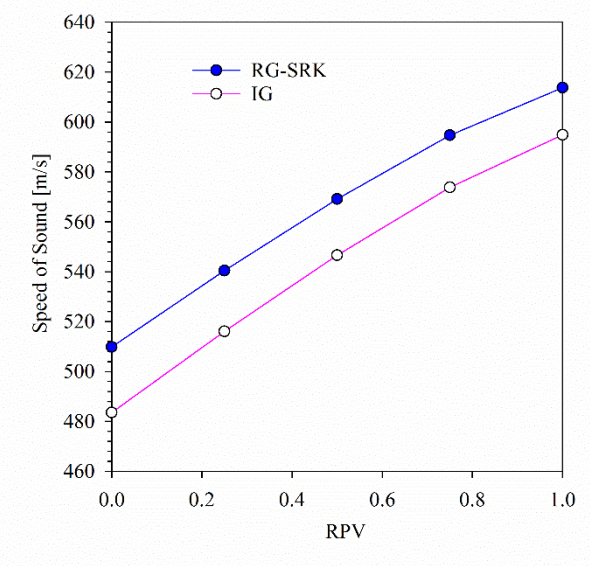

FIGURE 10: THE SPEED OF SOUND IN SCO2 COMBUSTOR

Viscosity

Modelling of viscosity is an important aspect in the simulation of any fluid flow where the shear stresses are prominent. Though the viscosity of sCO_2 has huge variation near to critical point, in the operating regime of sCO_2-combustor, as the temperature increases, the viscosity follows the

linear trend like ideal gas and the viscosity of sCO_2 is higher compared to viscosity of CO_2 at atmospheric pressures. This section gives an overall view of various viscous models which are being used in current supercritical mixture viscosity formulations and the best fits for 1D and CFD combustion modelling.

Figure 11 shows the flow chart of various methodologies which are being used currently to calculate viscosity in supercritical CFD simulations. There are basically two approaches, shown as two columns of Fig. 11, to estimate the viscosity of supercritical mixture. One is to calculate the individual species viscosity at required pressure and temperature and use mixing rules to calculate the resultant mixture viscosity [251]. It is represented in left column of Fig. 11. To calculate the individual species viscosity in the mixture, there are the Lucas method [300] which needs the temperature and pressure as input variable; Chung method [301] which needs the temperature and density as inputs. Out of these two methods, one can use either the Lucas method [300] or the Chung method [301] method for the viscosity calculation of the species involved in the sCO_2 combustion mixture and then use these species viscosities in the mixing rules to find the mixture viscosity. Though, the Wilkes mixing method defined for calculating the viscosity of low pressure mixtures, it has been used for the supercritical simulations because, it is a subset of Wassiljewa–Mason–Saxena (WMS) method [251]. The WSM is a thermal conductivity modeling method. Both the Wilkes method and WMS method have a common variable, and using both together provides consistency. The other column of Fig. 11 shows the one fluid approach. In this approach the mixture is assumed as one fluid and all the critical properties of the species are combined to find the effective critical properties and the viscosity is calculated based on these effective critical properties of the fluid. Chung and Lucas methods are two popular one fluid mixture viscosity methods for supercritical applications[228].

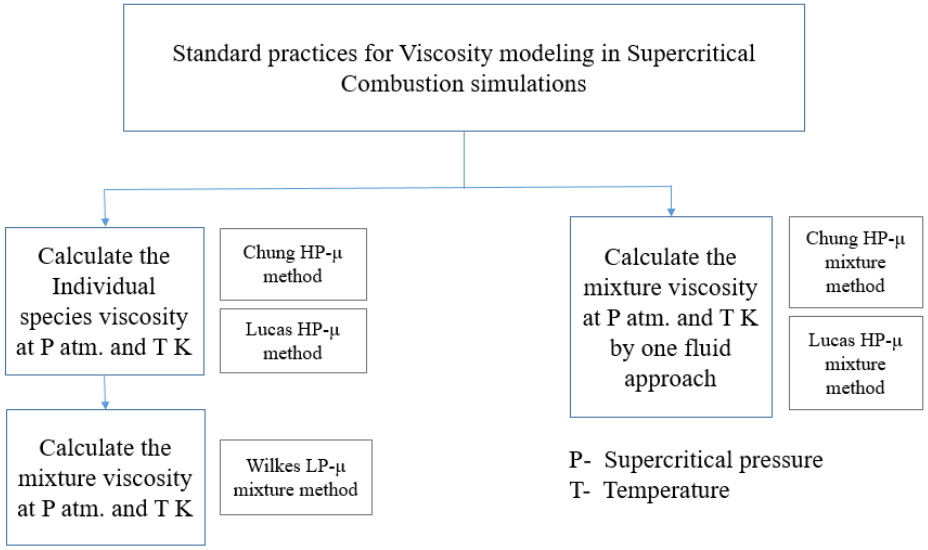

FIGURE 11: STANDARD PRACTICES FOR VISCOSITY MODELING IN SUPERCRITICAL COMBUSTION SIMULATIONS

A systematic investigation is presented in the following sections to estimate the suitable viscosity model for sCO_2 applications. Initially, the viscosities of prominent species are compared between Chung, Lucas and NIST methods. Further, the mixture viscosity methods are compared at various combustion progress variable values. Since, there is no reference mixture viscosity to compare the models, the suitable mixture models for sCO_2 combustion are judged based on the computational time, complexity and performance of the mixture models when applied to individual species. This plot has viscosities of CO_2, H_2O, CH_4, O_2 and CO at 300 bar pressure. Here, the viscosities of CO_2, H_2O and O_2 are shown between the temperature limits 600 -1600 K and for CH_4 and CO the temperature is shown only up to 600 K and 500 K, respectively. It is because, the NIST data for these species is available only to these temperatures.

Figure 12 shows the prominent species viscosity modelled with Lucas and Chung methods and the comparison of those models with NIST. The CO_2 viscosity plot has an additional viscosity model called Heidaryan et al., [302]. This model is validated between the pressures 75 bar and 1014 bar and between the temperatures 310 to 900 K. It is a simple empirical correlation which only needs pressure and temperature as an input. The plots show that, for CO_2 and O_2, the Chung et al., model is closer to NIST than the Lucas et al., model. The Heidaryan et al. is closer to NIST up to 900 K and deviates later. However, for H_2O, the Lucas et al., model is closer to NIST. Further, within the available NIST data limits, Lucas et al., is closer to NIST for CH_4 and Chung et al., is closer to NIST for CO. Therefore, Fig 12 shows that the a best individual species viscosity model vary from species to species. To identify more suitable species viscosity model for sCO_2 combustion applications, the typical weightage of these species distribution is considered and deviation from NIST is calculated based on this weighted deviation. Table 4 shows the comparison of these models and their weighted deviation from NIST. The distribution of these species is estimated by using the CMC method as discussed earlier. The average of weighted deviation of Lucas et al. is 0.66 percent, whereas for Chung et al. it is 4.56 percent. It shows that, the Lucas et al. method is more suitable for sCO_2 applications to calculate individual species viscosity.

As shown in Fig 11, the Wilkes method is a low-pressure mixture viscosity method. However, it is also used in supercritical CFD simulations [251] to calculate the mixture viscosity. More complete information about these models can be obtained from the references provided [228]. There is a simpler model suggested by Brokaw [303] for non-polar gaseous mixture where the inputs are just the gas composition, viscosities and the molecular weights of the constituents. It is a derivative of molecular based Chapman-Enskog theory. This method claims it's applicability for high-pressures beyond the critical point where there is no large concentration of free radicals. Also,

the largest error reported with this mixing rule is less than 4%. Since the major content (more than 90%) of the sCO_2 combustion mixture has non-polar molecules like CO_2, CH_4 and O_2, and the expectable radical concentration is comparatively low due to high specific heat of CO_2, this particular model [303] would be an accurate alternative fit for sCO_2 combustion applications, but needs more investigation because the combustion products contain H_2O which is a polar molecule.

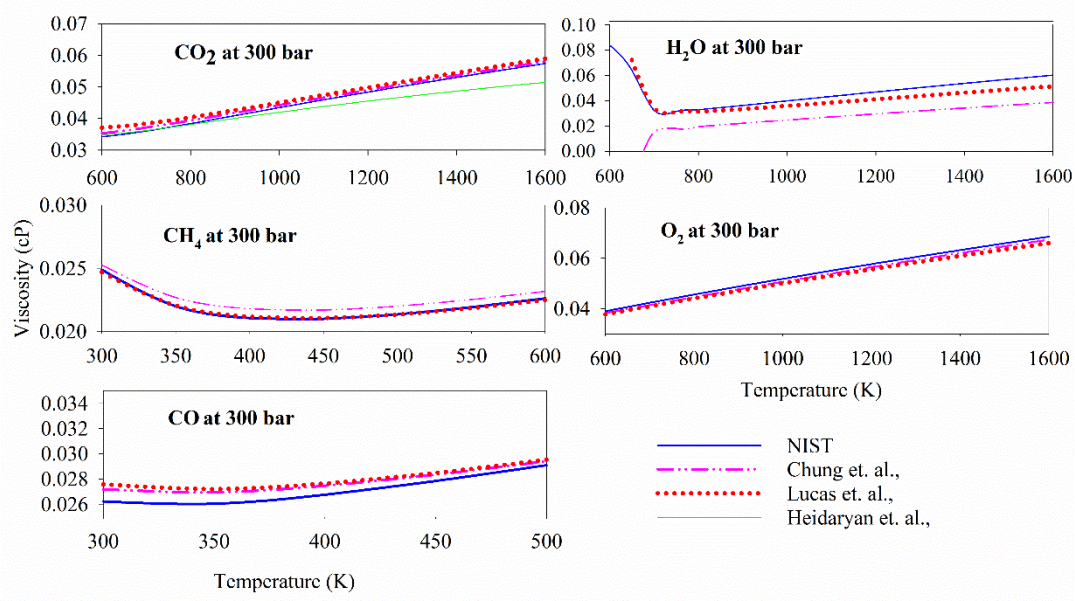

FIGURE 12: THE COMPARISON OF MODELLED INDIVIDUAL SPECIES VISCOSITY WITH NIST

Table-4: WEIGHTED DEVIATION OF MODELLED VISCOSITIES WITH NIST

Species	Weigthed deviation based on typical sCO2 mixture constituents at 1250 K (CO2-90%, H2O-1.8%, CH4-3.7%, O2-4.2%, CO-0.003%)	
	Chung et. al.,	Stiel and Thodos
CO2	12.69	1.72
H2O	0.70	0.26
CH4	-	-
O2	0.28	0.02
CO	-	-
Average	**4.56**	**0.66**

The formulations for the Brokaw mixing method are given as follows.

$$\mu_{mix} = \sum_{i=1}^{k} \frac{x_i \sqrt{\mu_i}}{\frac{x_i}{\sqrt{\mu_i}} + \sum_{j=1 \; and \; j \neq i}^{k} \frac{S_{ij} A_{ij}}{\sqrt{\mu_j}} x_j} \qquad (13)$$

Where,

$S_{ij} = 1$ for non $-$ polar gases, $M_i$and $M_j are$ molecular weights of the species i and j,

x_i and x_j are the molefractions of the species i and j,

μ_i is the viscosity of the species i,

$$A_{ij} = m_{ij} \left(\frac{M_j}{M_i}\right)^{0.5} \left[1 + \frac{\frac{M_i}{M_j} - \frac{M_i}{M_j}^{0.45}}{2\left(1 + \frac{M_i}{M_j}\right) + \frac{1 + \left(\frac{M_i}{M_j}\right)^{0.45}}{1 + m_{ij}} m_{ij}}\right] \qquad (14)$$

$$m_{ij} = \left[4M_iM_j/\left(M_i + M_j\right)^2\right]^{1/4}$$

In the current section the mixture viscosity models are analyzed. As discussed, the Chung et al. and Lucas et al. are two prominent mixture viscosity methods which are currently being used in supercritical combustion literature. One basic difference between these two mixture models is the method of calculating the combined critical properties. The detailed formulations of these models can be found in [228]. Unlike the Lucas et al. model, the Chung et al. model considers the interaction of one species with another species while calculating the combined critical properties. Therefore, in the Chung et al. method, if we have 'k' number of species in combustion mechanism, there will be a k by k matrix for calculating each combined thermal property of the system. Hence, computationally the Chung et al. is expensive. Also, the Chung et al. method needs the binary interaction parameter called 'k_{ij}'. As discussed in the equation of state section, the binery interaction parameter describes whether an interaction between two species is ideal or non-ideal. This parameter is empirical and there are many models as described earlier which calculates this parameter. However, these models are not evaluated with experiments for all the species involved in combustion. Therefore, it is usual practice to assume the unknown k_{ij} as unity. In the current section the Chung et al. mixture viscosity method is evaluated by considering both k_{ij} as unity and by choosing appropriate values for it.

Figure 13 compares the viscosity of a sCO_2 combustion mixture calculated by using various mixture models at three different temperatures, 1000, 1250 and 1500 K. These three temperatures are corresponding to unburnt, half-burnt and fully burnt conditions of the sCO_2 mixture. Again, the species distribution is solved by using the PCMC code at a dissipation rate of unity. Figure 13

also shows the viscosity calculated with Wilkes model and a weighted average. These two models require the individual species viscosities and they are calculated using the Lucas method of individual species viscosity. At all the temperatures, Lucas et al. has the highest calculated mixture viscosity and Chung et al. has the lowest. The Chung et al. when k_{ij} is unity predicts slightly higher viscosity than Chung et. al. At 1000 K, a ten percent deviation line is drawn below the highest viscosity model, i.e., the Lucas et al. to estimate the deviation of other models. This deviation shows that all the models used here are predicting the mixture viscosity within a ten percent deviation. Here, it must be noted that there is no reference data to compare these models to predict the best suitable viscosity mixture model. However, in the previous sections it is seen that the Lucas et al. is predicting the species viscosity more accurately than other models. Therefore, though there is no standard reference to identify the superiority of one model with other the Lucas et al. model can be considered as accurate due to its performance in calculating individual species viscosity. The dynamic viscosity may not be a influencing parameter in a pure turbulent regime, however when it comes to CFD the viscosity term in the diffusing term is important. Also, the viscosity is more important in simulating the internal flows, viscous sublayer, Prandtl and Schmidt numbers. How, this ten percent deviation in viscosity due to models is effecting the above-mentioned aspects is a point of interest at this moment and it requires the attention of researchers.

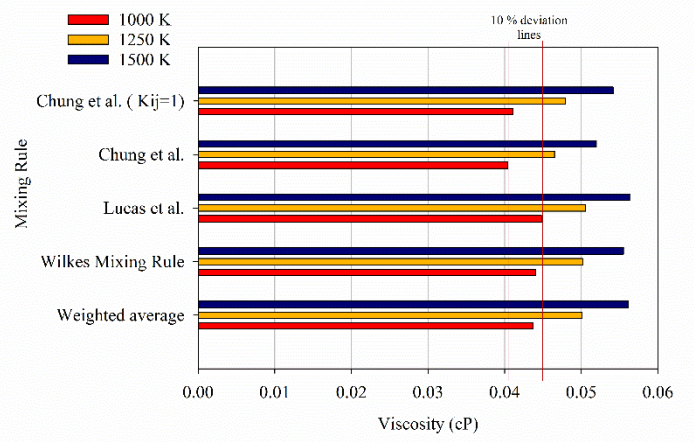

FIGURE 13: VISCOSITY OF SCO2 COMBUSTION MIXTURE USING VARIOUS MODELS

Figure 14 compares the computational time involved in calculating viscosity by these models. These models are simulated in MATLAB and the time is multiplied with a factor of ten thousand. It is to show the computational time if there are ten thousand cells in the computational domain. The plot shows that; Lucas et al. is least expensive in terms of computation and Chung et al. is more expensive. It is because the Chung et al. model accounts for the interaction of species and it adds many two-dimensional matrices in the computation. The Chung et al. is much more expensive for LES, DNS and detailed kinetic simulations. The Wilkes mixing rule and weighted averaging is more expensive than Lucas et al. because they need the input of individual species viscosities. Therefore, Lucas et al. is recommended for sCO_2 simulations due to its lower computational time and performance in calculating the individual species viscosity.

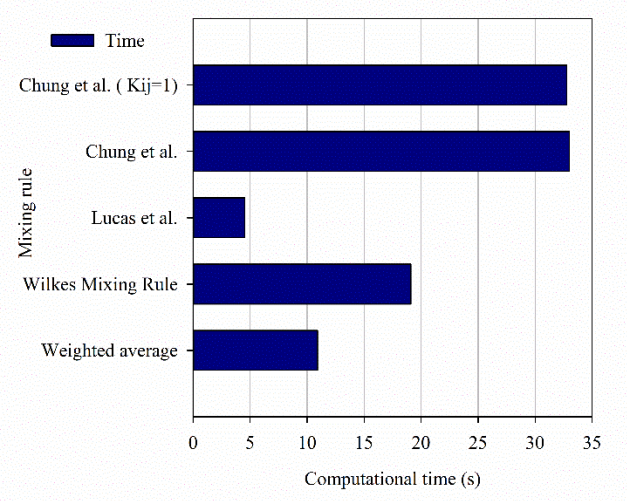

FIGURE 14: VISCOSITY OF SCO2 COMBUSTION MIXTURE USING VARIOUS MODELS

THERMAL CONDUCTIVITY

Thermal conductivity is the capacity of a system to transfer the heat energy from it. The thermal conductivity of the system increases as the pressure increases due to the increase in the density. However, it is important to note that, as the temperature increases, at low pressure the thermal conductivity tends to increase, but beyond the critical pressure and up to certain pressure limit the thermal conductivity reduces with temperature [228] and after this pressure limit the thermal conductivity increases again with temperature.

The Fig. 15 shows the current standard practices for calculating thermal conductivities in supercritical combustion simulations. The Chung et al. model for calculating thermal conductivity is the most widely used model. The Chung et al. high-pressure thermal conductivity model needs the low-pressure mixture viscosity as an input to estimate the high-pressure thermal conductivity. The first two columns in Fig. 15 illustrates the calculation of thermal conductivity by Chug et al. high-pressure model. The first column shows that, the mixture viscosity at one atmosphere is estimated by Wilkes methods and the input of individual species viscosities for Wilkes method are calculated either by the low pressure Chung et al. or Lucas et al. methods. The second column in Fig. 15 also shows the estimated thermal conductivity by the high-pressure Chung et al. method. However, here the low-pressure mixture viscosity is estimated by one fluid approach, i.e. either by the Chung et al. method or the Lucas et al. method. The third column shows the proposed method, the estimation of supercritical thermal conductivity by the Stiel and Thodos method. The Stiel and Thodos [228, 229] is a simple, generalized correlation for a high-pressure gas thermal conductivity of a mixture. It says that the excess thermal conductivity (excess from low pressure thermal conductivity) associated with a gas or mixture is a function of its critical properties, density and

molecular weight. This correlation has been validated against 20 data sets of non-polar gases including CO_2. This formulation is used for calculating the thermal conductivity of species involved in supercritical mixing studies [251]. One input to this Stiel and Thodos model is the low-pressure thermal conductivity of the mixture. The low-pressure thermal conductivity of the mixture can be estimated by the Wassiljewa model (as shown in Eq. 15). Also, this method is used by [251] for supercritical multi-component mixing simulation due to its simple formulation, though this model doesn't take any supercritical condition into account.

$$\lambda_{mix} = \sum_{i=1}^{k} \frac{x_i \lambda_i}{\sum_{j=1 \; and \; j \neq i}^{k} x_j B_{ij}} \qquad (15)$$

Where,

x_i and x_j are the molefractions of the species i and j,

λ_i is the thermal conductivity of the species i,

Here, the term B_{ij} is suggested by Mason and Saxena as,

$$B_{ij} = \varepsilon \left[\frac{\left(1 + \left(\frac{\lambda_{tri}}{\lambda_{trj}} \right)^{0.5} \left(\frac{M_i}{M_j} \right)^{1/4} \right)^2}{\left(8 \left(1 + \frac{M_i}{M_j} \right) \right)^{0.5}} \right] \qquad (16)$$

Here, the term $\left(\frac{\lambda_{tri}}{\lambda_{trj}}\right) = \left(\frac{\mu_i}{\mu_j}\right)\left(\frac{M_j}{M_i}\right)$;

The bracketed term in B_{ij}, also appear in Wilke's method for mixture viscosity correlation. The ε value is suggested as 1.065, later its value is modified by Tandon and Saxena to 0.85 [228].

It must be noted that, the Masi, et al. [251] used Wassiljeva method for calculating the high-pressure thermal conductivity, though it is defined for low-pressure thermal conductivities and the required individual species viscosities for this model are calculated by the high-pressure Lucas et al. model. However, in the proposed approach, the individual species viscosities are estimated by the low-pressure Lucas et al. model over a wide range of temperatures at one atmosphere pressure and tabulated. Later, the tabulated data is called into the Wassiljeva thermal conductivity model to estimate the low-pressure mixture thermal conductivity of the required mixture. Further, the Stiel and Thodos method is used for calculating the supercritical mixture thermal conductivity.

There is no reference mixture thermal conductivity data to identify the superiority of the Stiel and Thodos method over the Chung et al. method. However, when these models are used to identify individual species viscosities, the Stiel and Thodos method shows a better accurate match with NIST data. Figure 16 shows the comparison of individual species viscosities between Chung et al., Stiel and Thodos and NIST. The Amooey et al. is an emperical thermal conductivity model for CO_2 [304]. Therefore, the Amooey et al. model is also shown in CO_2 thermal conductivity plot of Fig. 16. It shows that, the Amooey et al. is accurate only up to 900 K and deviates significantly after that. The Stiel and Thodos method predicts the CO_2 and O_2 thermal conductivities very accurately. For H_2O, it is more accurate than the Chung et al. The CH_4 and CO are better with Chung et al. than Stiel and Thodos.

Table 5 shows the weighted deviation of the thermal conductivities calculated by the models from the NIST data at 1250 K. The weighted average deviation for Stiel and Thodos is 0.91 percent, whereas for Chung et al. it is 9.15 percent. It shows that Stiel and Thodos thermal conductivity model is more accurate for sCO_2 combustion simulations.

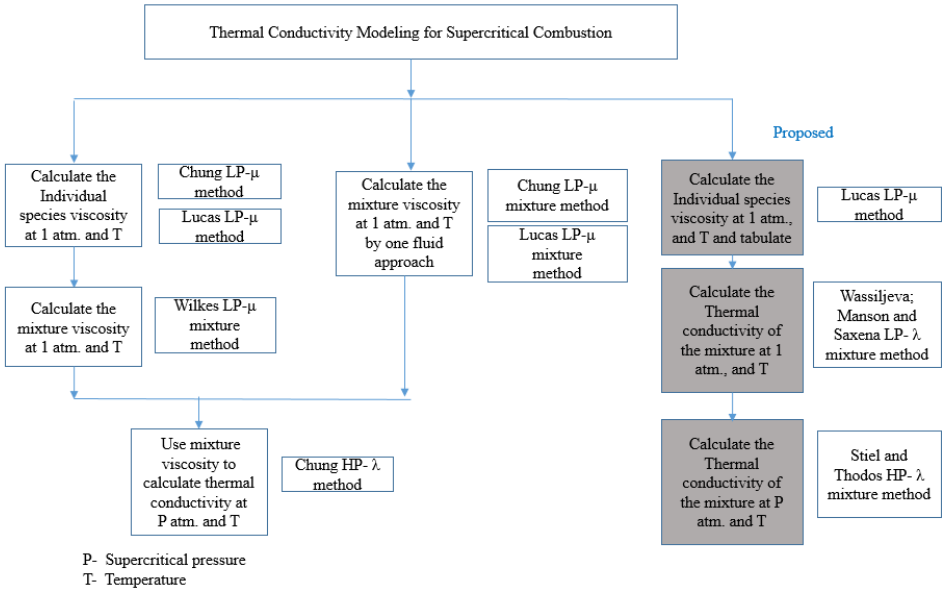

FIGURE 15: STANDARD PRACTICES FOR THERMAL CONDUCTIVITY MODELING IN SUPERCRITICAL COMBUSTION APPLICATIONS

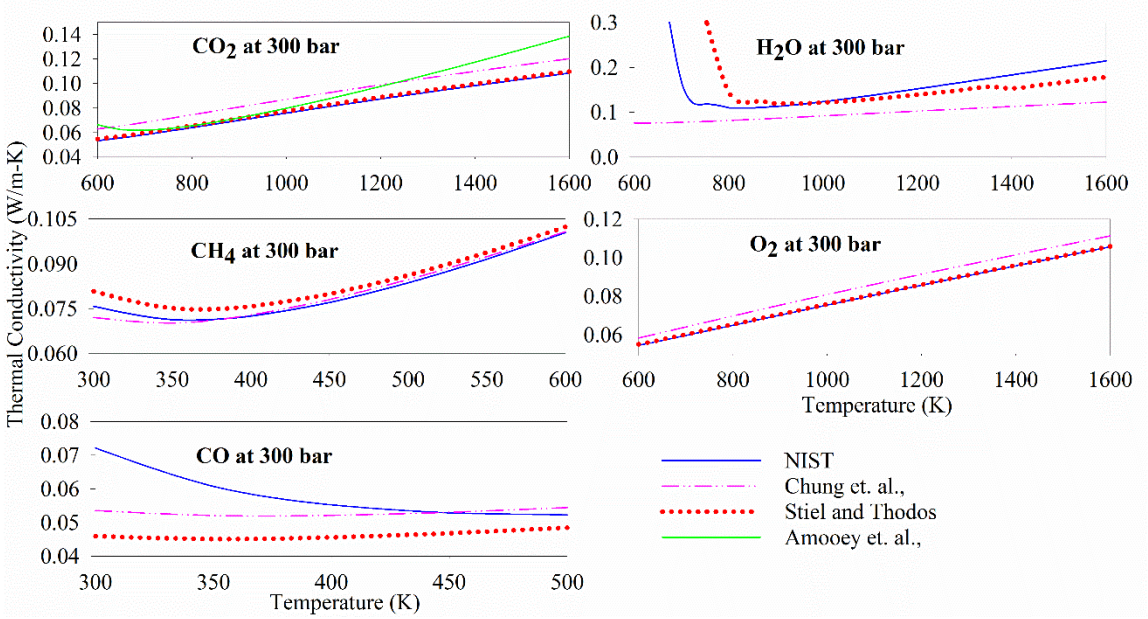

FIGURE 16: THE COMPARISON OF MODELLED INDIVIDUAL SPECIES THERMAL CONDUCTIVITIES WITH NIST.

Figure 17 shows the comparison of mixture thermal conductivity calculated by Chung et al. and Stiel and Thodos methods. The Chung et al. thermal conductivity model used here is corresponding to the second column of the Fig. 15. Both these methods show the increase in thermal conductivity with temperature. Also, the Chung et al. predicts the thermal conductivity better than the Stiel and Thodos method by fifteen percent. The fifteen percent difference in thermal conductivity may affect the heat energy transfer significantly. Besides the better performance of Stiel and Thodos for individual species thermal conductivities, it is also proven to be computationally modest. Figure 18 shows the computational time comparison between both these methods. The Stiel and Thodos method is shows the least computational time because all the necessary individual species viscosities are tabulated over the required temperature range.

The thermal conductivity simulations are carried out in MATLAB and the necessary species distribution with respect to temperature is identified by the PCMC code. Here, the computational times are multiplied with ten thousand. The difference between both the approaches will be significant for LES, DNS and simulations with a large number of species in the chemistry.

Table-5: WEIGHTED DEVIATION OF MODELLED THERMAL CONDUCTIVITIES WITH NIST

Species	Weigthed deviation based on typical sCO2 mixture constituents at 1250 K (CO2-90%, H2O-1.8%, CH4-3.7%, O2-4.2%, CO-0.003%)	
	Chung et. al.,	Stiel and Thodos
CO2	12.69	1.72
H2O	0.70	0.26
CH4	-	-
O2	0.28	0.02
CO	-	-
Average	**4.56**	**0.66**

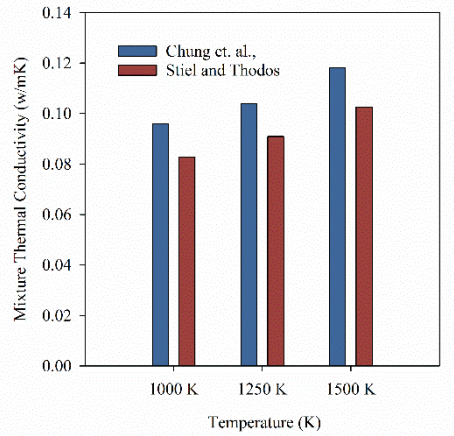

FIGURE 17: THE COMPARISON OF MODELLED MIXTURE THERMAL CONDUCTIVITIES

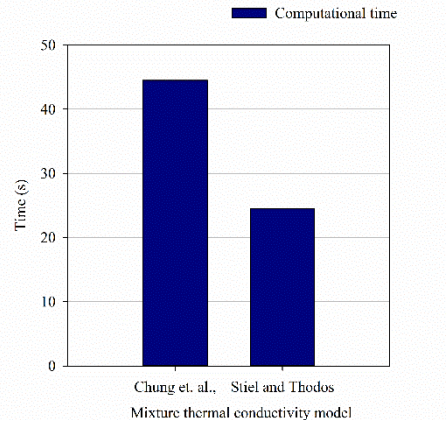

FIGURE 18: THE COMPARISON OF COMPUTATIONAL TIME BETWEEN THE MODELLED MIXTURE THERMAL CONDUCTIVITIES

Conclusions:

Here the available relations for EOS's and other thermal properties needed to model super critical CO_2 combustion were reviewed and recommendations given.

The cubic EOS must be validated for each application due to their empirical nature. The PRS EOS better predicts the thermal state of pure CO_2 compared to SRK and RK. However, over 1,000 K the PRS and SRK are indistinguishable and none of the cubic EOS predict the O_2 behavior. But, for sCO2 combustion mixtures, in all the turbulent regimes, the SRK and PRS EOS predict the densities by 0.7 and 1.71% when compared with NIST; which concludes that the SRK is the most appropriate EOS for sCO_2 mixtures.

The projected sCO_2 operating conditions for a supercritical regime where there always exist the repulsive forces (which are quantified by compression factor Z) between the molecules and these repulsive forces decreases as the combustion reaction progresses from unburnt to the fully burnt condition. The sCO_2 combustors are expected to observe a new kind of static pressure loss due to the reduction of Z. This reduction is more when there is more inlet CH_4 and O_2 mixture, and it can be reduced by decreasing the inlet temperature or increasing the inlet CO_2 moles. The fact that the compressibility factor Z is always greater than unity, signifies that the repulsive forces between the molecules always exists and there exists an energy transfer from the working fluid to the system boundaries.

Also, a new empirical model for Z is proposed for predicting its value at any stage of reaction progress. This model has been validated with Z calculated with SRK EOS over a wide range of sCO_2 combustor operating conditions. This model can be used with 1D sCO_2 combustion system simulations or in CFD.

Unlike the ideal gases, in real gases the pressure exponent n_s differs from the ratio of specific heats γ. The value of γ is about 1.2 for the inlet mixture and 1.164 for the fully burnt products. The resistivity of the sCO_2 mixture to change its temperature is higher due to the existing

intermolecular repulsive forces. In fact, all the specific thermal properties are expected to be higher due to the decrease in density. For example, the enthalpy increases by ~1% and entropy by 0.5%. The pressure exponent changes from 1.32 to 1.24 between the unburnt and fully burnt mixture. Further, the sCO_2 combustion mixture also becomes resistive to the compression by 6.5-9% when compared to the ideal gas assumption. The speed of sound is higher in sCO2 combustion by a factor $\left(\frac{\gamma}{n_s Z}\right)^{1/2}$. The combustion mixture is more resistant to density fluctuation induced due to changes in the velocity field by a factor of $\left(\frac{\gamma}{n_s Z}\right)$.

The popular viscosity and thermal conductivity models are evaluated based on their accuracy and computational cost. The results show that, the Lucas et al. mixture methods is more suitable for viscosity modeling and Stiel and Thodos method is suitable for thermal conductivity modeling of sCO2 mixture.

APPENDIX 2 REDUCED ARAMCO 3.0 MECHANISM FOR SCO2

The predicted growth in energy demand and the use of fossil fuels, alarms the world for possible global warming and irreversible climatic change. Therefore, the main attention of energy researchers is focused on efficient, economic and environmental friendly power production technologies [305-307]. The supercritical CO_2 (sCO_2) power cycle is one such concept which is theoretically promising high efficiency, complete CO_2 capture and compact foot print [33, 56]. The sCO_2 power cycle concept is adoptable in nuclear, solar-thermal, geo-thermal and natural gas based power producing technologies. This cycle uses supercritical CO_2 as the working fluid[308], therefore the CO_2 produced by the direct-fired, oxy-methane combustion power cycle can be recirculated within the same cycle loop and the excess supercritical CO_2 from the cycle can be used for other commercial purposes [10]. However, the current state-of-art peak operating pressures for sCO_2 combustion is approximately 300 atm and the level of CO_2 dilution in the combustor is more than ninety five percent by mass. At these extreme pressure conditions, experimentation is expensive, time consuming and dangerous. Thus, the simulation tools play a major role in the initial design aspects of the sCO_2 combustor development. One of the main tools for all combustion simulation is an accurate chemical kinetic mechanism and there are well established methane kinetic mechanisms in the literature, for example, GRI 3.0 [116] and Aramco 2.0 mechanisms [117, 118]. It is known that the Arrhenius constants defined in these mechanisms, i.e., pre-exponential factor, temperature exponent and activation energy, are derived from fundamental experiments or detailed theoretical based calculations [107, 108]. Under the absence of such studies (calculations or experiments), the rate constants are typically estimated based on similarity with other known reactions [109]. Also, these constants are valid only within the operating conditions in which they are defined. Therefore, the rate constants and the collision

efficiencies in these mechanisms need to be validated and if needed, updated to suit the sCO_2 combustion applications. In this process, a base mechanism which closely predicts the sCO_2 combustion behavior (including supercritical solvent effects) must be identified and then necessary modifications need to be implemented in that mechanism to derive a new sCO_2 combustion mechanism. The theoretical investigations related to these modifications are currently under progress [112-115] using quantum chemistry and molecular dynamic approaches, but the complete information required for deriving a new mechanism for sCO_2 combustion is not yet available. Therefore, there is an immediate need for identifying a mechanism which closely matches the currently available sCO_2 combustion experiments so that designers are able to conduct preliminary design and analysis of sCO_2 combustors.

The research from [120, 309, 310] provided methane shock tube experiments which are carried at the high pressures and at high CO_2 dilution levels. They found that the ignition delay times (IDT) predictions of the detailed Aramco 2.0 mechanism are close to the experimental data. Here, it should be noted that, these IDTs are estimated by ideal gas assumption. Also, the effect of real gas assumption in sCO_2, constant volume reactor simulations to approximate the IDTs is not available in literature. Therefore, in the current work, a real gas version of CHEMKIN, i.e., CHEMKIN-RG [311] is used to simulate the adiabatic constant volume reactor, Perfectly-Stirred-Reactor (PSR) and to solve the turbulence chemistry interactions by premixed conditional closure (PCMC) method. The CHEMKIN-RG is equipped with EOSs like Ideal gas assumption (IGA), van-der-Waals (VDW), Redlich-Kwong (RK), Soave-Redlich-Kwong (SRK) and Peng-Robinson (PR).

It is known that detailed chemical kinetic mechanisms explicitly account for the reaction pathways by considering many intermediate species and radicals, however, wide use of these

detailed mechanisms is not practical in CFD simulations. It is because every species in the mechanism adds an additional conservation equation to be solved along with mass, momentum and energy equations. Hence, using detailed mechanism in numerous combustion simulations to develop a combustor is not possible with the existing computational resources. Therefore, combustion CFD community prefers an equally performing reduced mechanism. There are several approached to reducing a detailed mechanism which include techniques of Directed Relation Graph (DRG) [312], Rate-Controlled Constrained-Equilibrium (RCCE) [313], detailed sensitivity analysis [314], optimization [315], etc. Detailed reviews on these techniques can be found in Tomlin et al. [316], Lu and Law [312], and Beretta et al. [317].

Here, SEVEN REDUCED MECHANISMS ARE DERIVED FROM THE SUITABLE DETAILED MECHANISM BY USING THE PATH FLUX ANALYSIS METHOD [121], which is an extension of the DRG technique. the most SUITABLE REDUCED MECHANISM IS IDENTIFIED FROM THESE SEVEN REDUCED MECHANISMS BY COMPARING AGAINST PREDICTIONS OF THE DETAILED one. ALSO, THE REDUCED AND DETAILED MECHANISMS ARE FURTHER COMPARED FOR PREDICTIONS OF PERFECTLY-STIRRED-REACTOR (PSR) AND PREMIXED CONDITIONAL MOMENT CLOSURE (PCMC) SOLUTION and ignition delay times of constant volume combustor. The PCMC procedure considers the interaction of the turbulent dissipation with the reaction progress [270]. In the literature [318], PCMC has shown that reduced mechanisms cannot capture the reaction pathways which are prominent at different turbulence scales. Therefore, in this work the reduced and detailed mechanisms are compared at various turbulent dissipation values as well.

THE EFFECT OF EQUATION OF STATE ON IGNITION DELAY TIMES:

As discussed in the introductory section, at supercritical pressures the ideal gas assumption is no longer valid to predict the state of a system, because at these pressures the intermolecular forces are significant and they must be accounted while calculating the chemical, thermodynamic properties and the state of the system. Therefore, choosing an appropriate EOS is very important.

The extensive work of van der Waals in the late eighteenth century [284] described the first approximation of EOS for real gases. The EOS can be broadly categorized into three types, they are the 1) virial-type, 2) molecular-based and 3) van der Waal type EOSs [233, 234]. In the current work, only the van der Waal type of EOSs are used due to their simplicity. Since, these EOSs are empirical by their origin, adopting them to an application requires validation with data. For example, some investigations recommend SRK EOS for sCO_2, CH_4/LO_x and kerosene/LO_x mixtures [39, 277, 294]. Whereas Poschner and Pfitzner [295] recommends PR for H_2/O_2 mixtures. However, the most used EOS are the SRK and PR. More detailed formulations of EOS and associated real gas mixture formulations can be found in [39, 228, 311]. Comparing the chemical kinetic mechanism with IDTs of shock tube data is one standard practice to validate a chemical kinetic mechanism. However, an unanswered question in the literature is "which EOS needs to be used to simulate the IDTs of supercritical combustion?". In the current section, the IDTs are calculated by van der Waals type of EOSs by using both the Aramco 2.0 and GRI 3.0 mechanisms. Further, the calculated IDTs are compared to understand the effect of EOS on IDTs. Figure 1 shows the absolute deviation of simulated IDTs with respect to experiments [120]. Here, the constant volume reactor is simulated with CHEMKIN-RG by using various real gas EOS. In Fig. 1, the left column of the plot consists of the IDTs calculated by the Aramco 2.0 mechanism while the right plot is by the GRI 3.0 mechanism. The vertical axis of each plot represents the absolute deviation of the simulated IDTs with respect to experiments. It should also be noted that, each subplot has

five absolute deviation values (for five EOSs considered) and also five mean values of those absolute deviations. Each row in this plot corresponds to a particular molar ratio of fuel and oxidizer used in the shock tube experiments.

The subplots (1,1) and (1,2) in Fig. 1 corresponds to stoichiometric hydrogen mixture (mixture-1, see also Table 3) diluted with CO_2. Here, it must be noted that the Aramco 2.0 has better performance then GRI 3.0. For the GRI 3.0 mechanism all simulation data points are clearly beyond the uncertainty of experiments, which is reported to be 15% [120]. However, for the subplot (1,1) some of the EOSs are within the uncertainty limits except SRK EOS. Also, from both subplots (1,1) and (1,2) it can be observed that, the estimation of each IDT is significantly different from each other.

The subplots (2,1) and (2,2) in Fig. 1 represent a lean methane mixture (mixture-2) diluted with CO_2. Here, both the IDTs of Aramco 2.0 and GRI 3.0 are predicting the experimental IDTs reasonably good. Also, the selection of EOS is not impacting the IDTs significantly as in the case of H_2 and O_2 mixture (mixture-1). Further, the subplots (3,1) and (3,2) in Fig. 1 represents the stoichiometric methane mixture (mixture-3) heavily diluted with CO_2. It can be seen that the GRI 3.0 is poorly predicting the IDTs (compared to Aramco 2.0) and all IDTs predicted by the Aramco 2.0 mechanism are within the experimental uncertainties. Also, interestingly the IDTs are not much impacted by the selection of EOS. The maximum difference among the EOS is less than 10%, which is less than the experimental uncertainty.

The EOS has significant impact on mixture-1, but not on mixtures-2 and 3. The main combustion product of mixture-1 is H_2O and for mixture-2 and 3 it is both CO_2 and H_2O. The critical pressure of H_2O (~220 atm) is approximately three times higher than the CO_2 (~74 atm). Hence, the higher amount of H_2O in the products of mixture-1 increases the resultant mixture critical point. It is

known that, the van der Waal's type EOSs deviate among them largely near to critical point. However, in the case of mixtures-2 and 3, the formation of CO_2 further reduces the overall critical point. Hence, the EOSs has smaller deviation. Also, another reason could be (for mixture-2 and 3) that the compressibility factor in real gas equation is closer to unity at higher temperatures, even at supercritical pressures [39]. Consequently, at higher temperatures and very high pressures (far above from critical point) real gases also behave like an ideal gas. Now, the practice to estimate the IDTs from shock tube experiments, to interpolate a tangential line to OH time history profile and the intersection of this line with abscissa is identified as an IDT. In general, this tangent pass through a series of high temperature points and due to this the real gas EOSs predictions for mixture-2 and 3 are not significantly deviating from IGA.

Therefore, as far as the constant volume reactor IDTs are concerned (for mixture-2 and 3), the equation of state does not have a notable effect, because the deviation of real gas IDTs are within 15% from the IGA IDTs. Over all, in this section it is re-confirmed that the performance of the Aramco 2.0 mechanism is better (compared to GRI 3.0) for estimating the supercritical CO_2 shock tube experiments. Therefore, in this work, reduced mechanisms are derived from the Aramco 2.0 mechanism for use in sCO_2-CFD simulations.

REDUCED MECHANISMS

As discussed in the introductory section, the usage of detailed mechanisms in CFD simulations is not practical due to associated expensive computational power. Therefore, a reduced accurate mechanism is of much interest to the combustion CFD community. An automated computer program called CHEM-RC from the work of [121, 122] is used in order to reduce the mechanism to a small number of species. This computer model uses the Multi-Generation Path Flux Analysis

(PFA) method to identify the important species to the targeted species. The PFA method is an extension of Direct Relation Graph (DRG) method and Direct Relation Graph with Error Propagation (DRGEP) methods [123] and proven to capture better flux . The previous section confirms that Aramco 2.0 mechanism is better suitable for sCO_2 simulations compared to GRI 3.0. Therefore, the Aramco 2.0 mechanism is used as a source for further reduction process. The full Aramco 2.0 mechanism consists of 493 species and 2714 reactions for fuels up to C6. A total of five reduced mechanisms are generated from this detailed mechanism by using CHEM-RC by varying the threshold values (a parameter used in PFA to choose the reaction paths). The higher the threshold value the smaller will be the reduced mechanism. The detailed information on the threshold value can be found in [121]. Also, various mixtures from lean to rich and moderate to highly CO_2 diluted conditions have been given to CHEM-RC as inputs (conditions shown in Table 1). The smaller the number of species, the lower will be the computational time for CFD simulations. Therefore, initially the reduction process started with a 15-species mechanism and the threshold values in CHEM-RC were reduced gradually to obtain all the necessary species which are needed to validate the targeted mixture conditions. Here, the performance of a reduced mechanism is compared with respect to the detailed Aramco 2.0. In the current work, the performance of the seven reduced mechanisms, namely, 15-species, 16-species, 19-species, 21-species, two 22-species and 23-species is discussed.

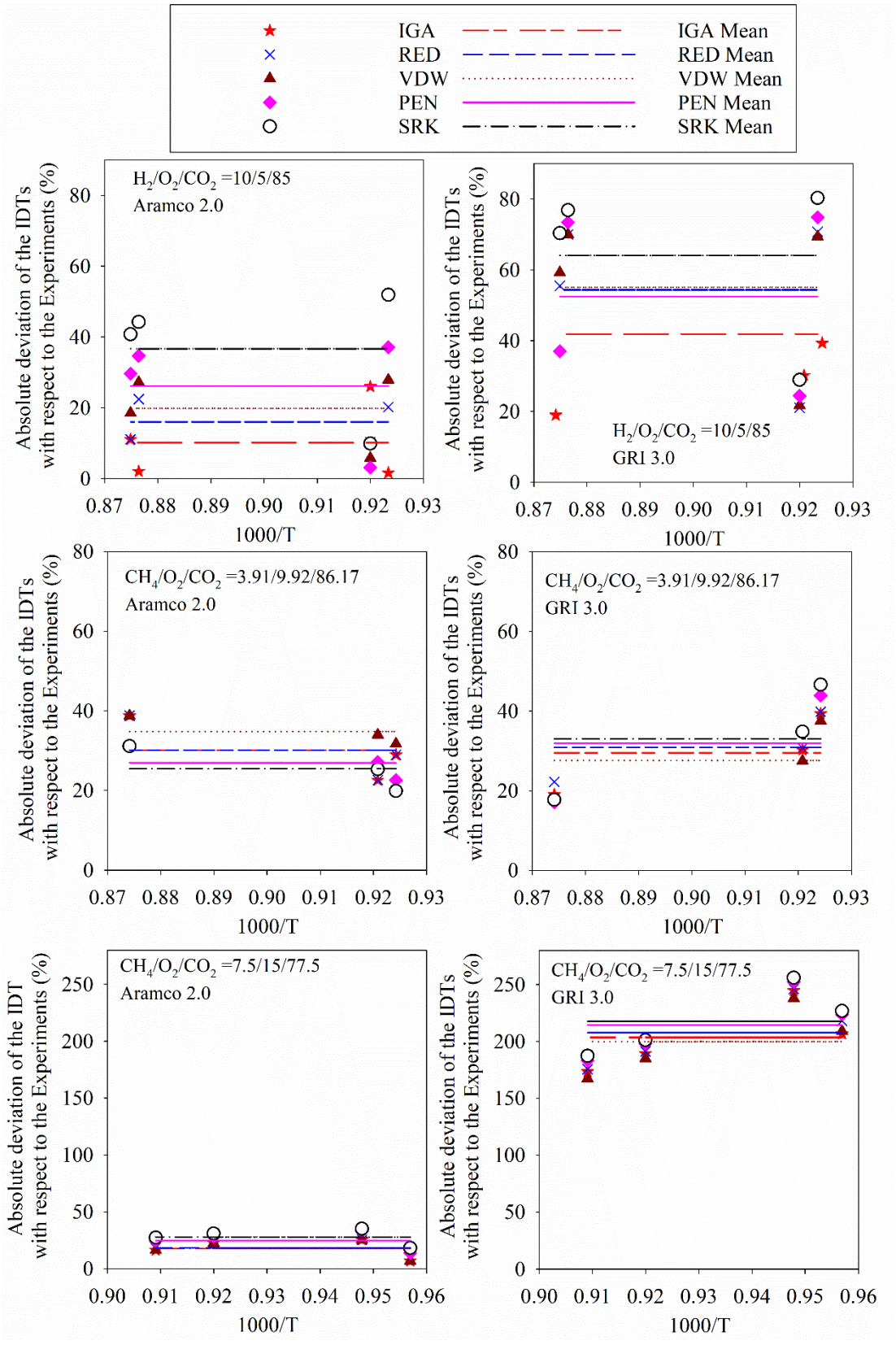
IGA
RED
VDW
PEN
SRK
IGA Mean
RED Mean
VDW Mean
PEN Mean
SRK Mean
H2/O2/CO2 =10/5/85
Aramco 2.0
H2/O2/CO2 =10/5/85
GRI 3.0
CH4/O2/CO2 =3.91/9.92/86.17
Aramco 2.0
CH4/O2/CO2 =3.91/9.92/86.17
GRI 3.0
CH4/O2/CO2 =7.5/15/77.5
Aramco 2.0
CH4/O2/CO2 =7.5/15/77.5
GRI 3.0
Absolute deviation of the IDTs with respect to the Experiments (%)
Absolute deviation of the IDT with respect to the Experiments (%)
1000/T

Figure 1: Comparison of sCO_2 shock tube ignition delay times [120] with the Aramco 2.0 and GRI 3.0 by various EOSs

The species in these mechanisms are tabulated in Table 2. Here, it should be noted that, the two 22 species mechanisms as mentioned in the table are derived from the 23-species mechanism by removing C_2H_3 and CH_3OH respectively. Basically, this test has been performed to understand the importance of these species in estimating the IDTs at lean conditions.

Figure 2 shows the comparison of IDT estimation of reduced mechanisms against those of the detailed mechanism for mixture-3 (stoichiometric mixture). It should be mentioned that the IDTs are estimated based on IGA EOS. Here, IGA EOS is used because, as discussed in the previous section, significant effect of real gas EOSs is not observed for mixture-2 and 3. It should be noted that the vertical axis is shown in logarithmic scale because the IDTs of the 15-species mechanism are deviating largely from the detailed mechanism predictions. Every other mechanism is performing very close to the detailed mechanism. The 16-species and 15-species mechanisms differ only by the species hydrogen peroxide (H_2O_2) and its associated reactions. Interestingly, this one species has changed the prediction of IDTs by as much as 50 times. The main reason is that for auto ignition of hydrocarbon and oxygenated fuels, the hydrogen atom (H) abstraction by hydroperoxyl radical HO_2 (forming H_2O_2) is an important reaction class in the autoignition of fuels, particularly at low-to-intermediate temperatures in the range 600-1300 K [124]. The role of the hydroperoxide radical, HO_2, in high-pressure ignition phenomena is well established as is the role of hydrogen peroxide decomposition [125].

A rate of production (ROP) and sensitivity analysis at stoichiometric, low temperature conditions is shown in Fig. 3. It illustrates that the reaction R1 is the second prominent reaction for CH_4 consumption:

$CH_4+HO_2 \Leftrightarrow CH_3+H_2O_2$ ……(R1)

Figure 4 corresponds to mixture-2, 16-species mechanism and for the case where the initial temperature is 1100 K and pressure is 285.5 atm. The calculated IDT for this case is around 320 μs. However, Fig.4 shows that, the H_2O_2 is formed in the constant volume reactor even before auto-ignition starts and interacts with CH_4 through R1. Therefore, the omission of H_2O_2 in the 15-species mechanism has significantly delayed the interaction of CH_4 and HO_2 and delayed the methane consumuption and formation of CH_3, hence the IDTs are delayed. Also, it must be noted that the accumulated H_2O_2 reacts with "+M" to produce two OH radicals and it is responsible for the bulk of heat release at high-pressure and high-temperatures. The detailed description of this phenomenon can be obtained in [125].

$H_2O_2(+M) \Leftrightarrow OH+OH\ (+M)$ ……(R2)

Therefore, the 16-species as shown in Table 2 are the minimum required in a reduced mechanism to estimate the IDTs of a highly CO_2 diluted, stoichimetric methane mixture. Also, there could be possibilities of reducing the species number further by other mechanism reduction methods than PFA (e.g., [126, 127]). But, it must be remembered that the PFA method in this analysis is

considered to capture the maximum path flux during the reduction process. Hence, other methods are not explored.

Further, the 15-species mechanism is not considered during IDTs comparison of lean mixture (mixture-2) and hydrogen mixture (mixture-1).

Figure 5 compares the lean mixture (mixture-2) IDTs estimated by 16, 19, 21, two 22-species and 23-species mechanism with those of the detailed mechanism. It is interesting to note that none of the reduced mechanisms below or equal to 21 species are able to predict the lean mixture IDTs. The 16 and 19-species mechanisms estimate almost similar IDTs. Further, the addition of two more species C_2H_5 and CH_2OH species to 19-species mechanism has slightly delayed the IDTs. However, this 21-species mechanism is still far from the detailed mechanism predictions and shows faster ignition. At the same time, the 23-species mechanism is predicting the IDTs of mixture-2 almost same as the detailed Aramco 2.0 mechanism. The two additional species in the 23-species mechanism compared to 21-species mechanism are CH_3OH and C_2H_3. These two species significantly delayed auto-ignition under lean conditions and matches the 23-species mechanism prediction with the detailed Aramco 2.0 (when compared to the predictions from the 21-species mechanism).

Table 1: The parameters chosen used in CHEM-RC to reduce the mechanism

CHEM-RC parameters	Value chosen
Mixture conditions	CH4/O2/CO2

	7. 1/2/35 (stoichiometric- high CO_2 dilution) 8. 1/2/16.5 (stoichiometric- low CO_2 dilution) 9. 1/2.5/40 (lean- high CO_2 dilution) 10. 1/2.5/20 (lean- low CO_2 dilution) 11. 1/0.84/20 (rich-high CO_2 dilution) 12. 1/0.84/10 (rich-low CO_2 dilution)
Threshold values	0.50 to 0.95
Initial temperature	800 K to 1500 K
Pressure	250 atm. to 350 atm.

Table 2: The list of species in the reduced mechanisms

Species. No	23 species	22 species (with CH3OH)	22 species (with C2H3)	21 species	19 species	16 species	15 species
1	H2	H2	H2	H2	H2	-	-
2	H	H	H	H	H	H	H
3	O2	O2	O2	O2	O2	O2	O2
4	O	O	O	O	O	O	O
5	H2O	H2O	H2O	H2O	H2O	H2O	H2O
6	OH	OH	OH	OH	OH	OH	OH

7	H2O2	H2O2	H2O2	H2O2	H2O2	H2O2	-
8	HO2	HO2	HO2	HO2	HO2	HO2	HO2
9	CO	CO	CO	CO	CO	CO	CO
10	CO2	CO2	CO2	CO2	CO2	CO2	CO2
11	CH4	CH4	CH4	CH4	CH4	CH4	CH4
12	CH3	CH3	CH3	CH3	CH3	CH3	CH3
13	CH3O2H	CH3O2H	CH3O2H	CH3O2H	CH3O2H	CH3O2H	CH3O2H
14	CH3O2	CH3O2	CH3O2	CH3O2	CH3O2	CH3O2	CH3O2
15	CH3OH	CH3OH	-	-	-	-	-
16	CH3O	CH3O	CH3O	CH3O	CH3O	CH3O	CH3O
17	CH2OH	CH2OH	CH2OH	CH2OH	-	-	-
18	CH2O	CH2O	CH2O	CH2O	CH2O	CH2O	CH2O
19	HCO	HCO	HCO	HCO	HCO	HCO	HCO
20	C2H6	C2H6	C2H6	C2H6	C2H6	-	-
21	C2H5	C2H5	C2H5	C2H5	-	-	-
22	C2H4	C2H4	C2H4	C2H4	C2H4	-	-
23	C2H3	-	C2H3	-	-	-	-

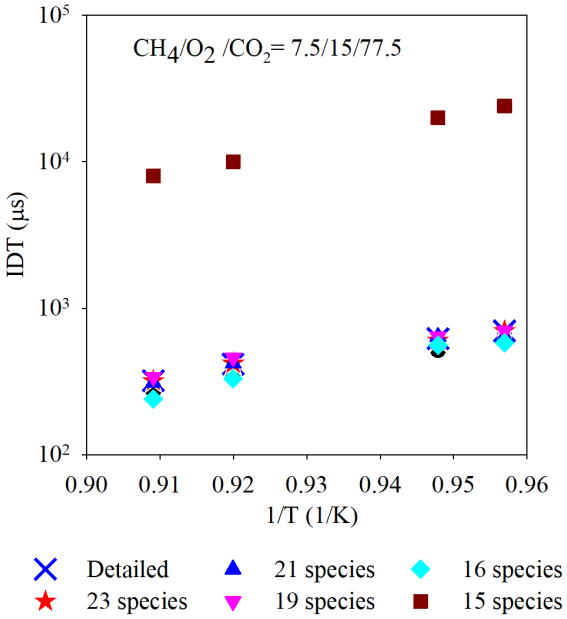

Figure 2: Comparison of IDTs (stoichiometric mixture) of the detailed Aramco 2.0 and reduced species mechanisms

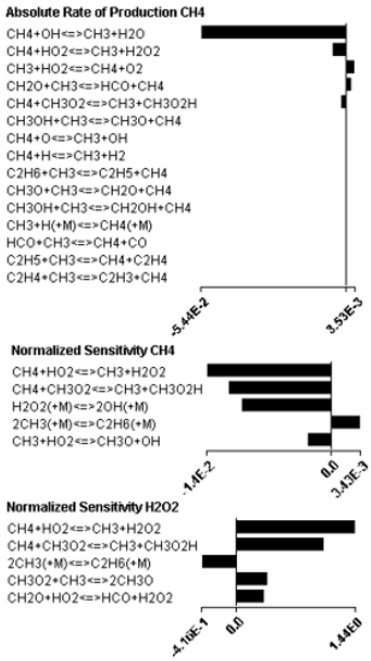

Figure 3: The absolute rate of production of CH_4 and sensitivity of CH_4 and H_2O_2 at T_{inl}=1100 K, P_{inl}=285.5 atm and 50% consumption

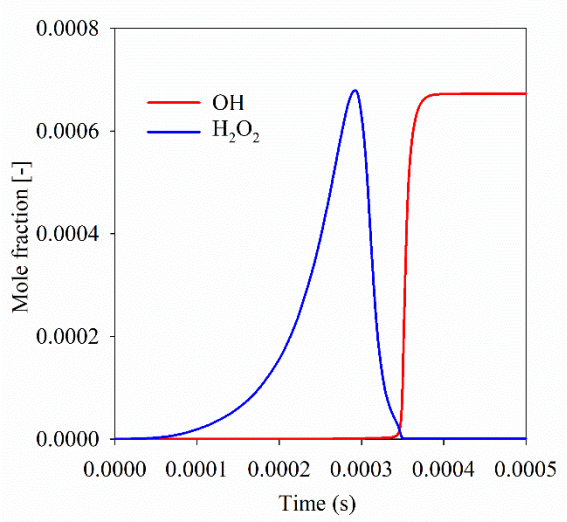

Figure 4: Production of OH and H_2O_2 during stoichiometric constant volume combustion for mixture-2 at T_{inl}=1100 K, P_{inl}=285.5 atm.

It is interesting to understand how these two species (CH_3OH and C_2H_3) are causing mixtures to ignite later. Therefore, each species is removed from the 23-species one at a time to make two new mechanisms (2-species as listed in Table 2). The IDTs predicted by these two 22-species mechanisms are also shown in Fig. 5. It can be observed that, the contribution of C_2H_3 in delaying the ignition is much more than the CH_3OH. But, as it can be observed from Fig. 5, the 22-species mechanism with C_2H_3 alone is not sufficient to predict IDTs within the 15% uncertainty. Therefore, it can be concluded that these two species are very important for lean sCO_2 mixtures.

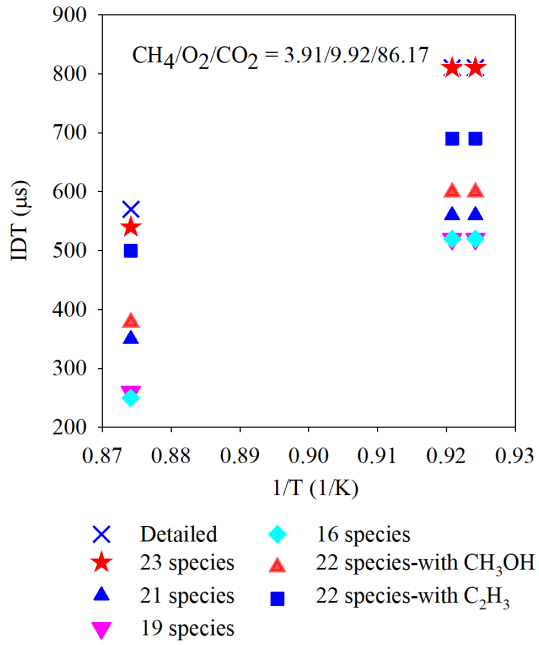

Figure 5: Comparison of lean mixture IDTs of the detailed Aramco 2.0 and reduced species mechanisms

Figure 6 compares IDTs of the stoichiometric H_2 mixtures with those of the detailed Aramco 2.0 predictions. The 19-species mechanism can capture IDTs on par with the detailed one. Thus the 19-species mechanism is sufficient for the H_2 mixtures selected in the current study.

From this analysis, it can be concluded that, minimum 16 species are required for predicting the stoichiometric CH_4 and high CO_2 diluted mixtures. Further, 19 species are required for supercritical H_2 mixtures and 23 species are required for lean CH_4 mixtures with high CO_2 dilution. The 23-species mechanism has better IDT prediction capabilities compared to all other reduced mechanisms discussed in this work. The average deviation of the IDTs calculated by 23-species mechanism with respect to those of the Aramco 2.0 mechanism is less than one percent.

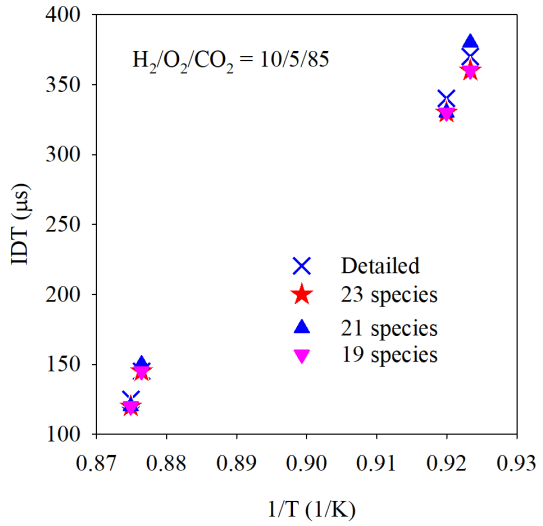

Figure 6: Comparison of stoichiometric H_2 mixture IDTs of the detailed Aramco 2.0 and reduced species mechanisms

PERFECTLY STIRRED REACTOR SIMULATION

From the previous analysis the 23-species mechanism is identified as the appropriate reduced mechanism for sCO_2 combustion simulations. In this section, the performance of the 23-species mechanism is compared with the detailed Aramco 2.0 mechanism while simulating a perfectly-stirred-reactor (PSR). The PSR simulation is a zero-dimensional simulation which is used as a tool for gas-turbine combustor development since the 1950s. The primary zone of the combustor can be simulated with the PSR [128]. In this section, various possible CO_2 dilution levels and methane-oxygen equivalence ratios in the primary zone are simulated by using a PSR model in CHEMKIN-II. The SRK EOS [39] is considered in the simulation by using CHEMKIN-RG. The inlet temperature of the reactor is 1000 K, pressure is 300 atm.

Figures 7 and 8 show a comparison of the detailed and 23-species mechanisms when they are applied to a PSR. The horizontal axis of the Fig. 7 represents the residence time in the PSR and the vertical axis represents the exit temperature of the PSR. Here, stoichiometric CH_4 and O_2 at

1000 K are diluted by 60 to 90 percent CO_2 by mass. The results show that, at all dilution levels, the predictions by both detailed and reduced mechanisms yield the same PSR exit temperature (the average deviation between the reduced and the detailed mechanisms are less than 0.5 percent).

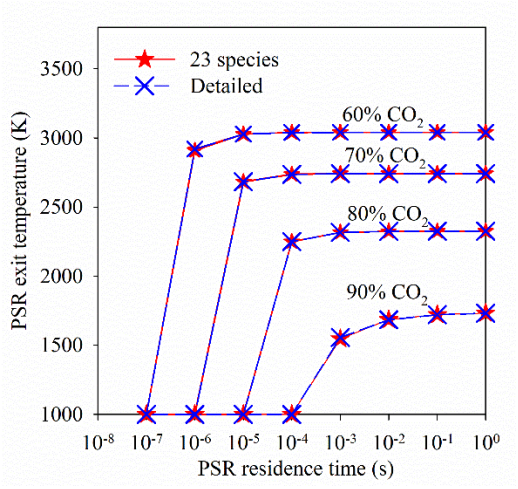

Figure 7: PSR exit temperature comparison of detailed Aramco 2.0 mechanism with the 23-species one at stoichiometric CH_4/O_2 ratio and at various CO_2 dilution levels.

Figure 8 shows the PSR simulation comparison at various equivalence ratios (ϕ). Here, at each equivalence ratio the percentage of CO_2 dilution is kept constant at 90 percent and the residence time as one millisecond. The results show that, the accuracy of 23-species mechanism is a little less in lean conditions compared to stoichiometric and rich conditions. However, the maximum deviation is observed at ϕ=0.8 and is 2.1 percent which is not considered as significant.

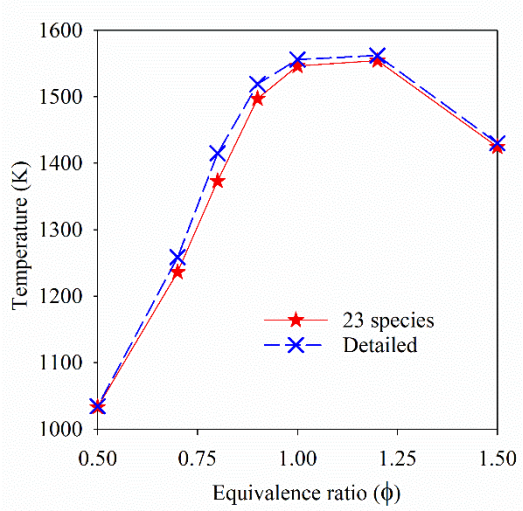

Figure 8: Comparison of detailed Aramco 2.0 mechanism with the reduced 23-species mechanism at various equivalence ratios of CH_4/O_2 at ninety percent CO_2 dilution level at one millisecond residence time.

EFFECT ON TURBULENCE INTERACTION

The Conditional Moment Closure (CMC) turbulent combustion model was developed by [319] for non-premixed flames. Later, it was extended by to premixed flames as PCMC [270]. The PCMC models the effects of all turbulence scales on the reaction rates. The detailed information of the PCMC can be found in the above-mentioned literature. It is shown that; the smaller turbulent scales significantly alter the reaction pathways. The turbulence effects on the combustion phenomenon will be significantly discarded if the reduced mechanism does not account the influential pathways at smaller turbulent dissipation values[318].

The 0D, PCMC model as shown in Eq.1, is a premixed turbulent combustion model which conditions the species mass fractions on the reaction progress variable (RPV) and closes the chemical source terms in the enthalpy equation with conditioned reaction rates [270]. In other words, the PCMC can estimate all the species mass fractions involved in combustion as the reaction progresses from unburnt to fully-burnt conditions, at various turbulence levels by solving

a second order, non-linear ordinary differential equation for each species with a two-point boundary value problem solver. Here the PCMC is solved with the real gas assumption. The SRK EOS is considered for the simulation. The unburnt mixture in this simulation consists of stoichiometric methane and oxygen, 90% of the mixture is CO_2 by mass. Also, the initial temperature and pressure are 1000 K and 300 atm.

The PCMC equation is:

$$\langle \bar{\rho}\widetilde{N}|\zeta\rangle \tilde{Q}_i'' - \langle \bar{\rho}\tilde{S}_c|\zeta\rangle \, \tilde{Q}_i' + \langle \bar{\rho}\dot{\tilde{\omega}}_i|\zeta\rangle = 0 \qquad (1)$$

Here, $\bar{\rho}$ is the density, $\widetilde{N}|\zeta$ is the conditioned scalar dissipation (level of small scale turbulence), $\tilde{S}_c|\zeta$ is the conditioned source term for the RPV Eqn., $\dot{\tilde{\omega}}_i|\zeta$ is the conditioned reaction rate and $\tilde{Q}_i$ are the conditioned mass fractions and the derivatives are with respect to the RPV [15].

Figure 9 shows the comparison of the PCMC solution with both detailed and reduced Aramco 2.0 mechanisms. The horizontal axis of each subplot in Fig. 9 corresponds to the RPV. The scale represents unburnt condition when RPV is zero and fully burnt condition when RPV is one. The vertical axis of each subplot represents mass fraction of a species. Here, the mass fractions of five species, CH_4, CO, CH_2O, C_2H_6 and OH has been shown with respect to the RPV. Each column in Fig. 9 corresponding a species and each row correspond to a turbulent dissipation value. Here, three turbulent dissipation values (N 1/s), 10000, 100 and 0.1 are presented. For larger N, for CH_4, the PCMC solution is just a straight line. It represents that, the reaction is following a single step pathway at higher N. However, as N decreases, the CH_4 profile is curved more implying that the CH_4 disintegration follows more complex reaction paths. Here, it must be noted that the

CH_4 disintegration is very well predicted by the 23-species mechanism on par with the detailed mechanism. Also, the intermediates and radicals, CO, CH_2O, C_2H_6 and OH mass fraction are increasing as the N value deceases. These variations are also predicted well by the 23-species mechanism. Though, it appears there is a deviation in the mass fractions at N=0.1, the difference is not significant. Note the difference in the y-axis scales for the different N values.

Figure 10 shows a comparison of the source term (S_c) between the detailed Aramco 2.0 mechanism and the reduced 23-species mechanism at various turbulent dissipation values. In the PCMC, the source term represents the non-dimensional reaction energy release per second. At N value 10000, the peak of the source term is towards the right side of the plot and it represents the maximum rate of energy releases towards the end of the reaction. However, at lower N the peak value moves towards the left. This trend is very well predicted by the 23-species mechanism.

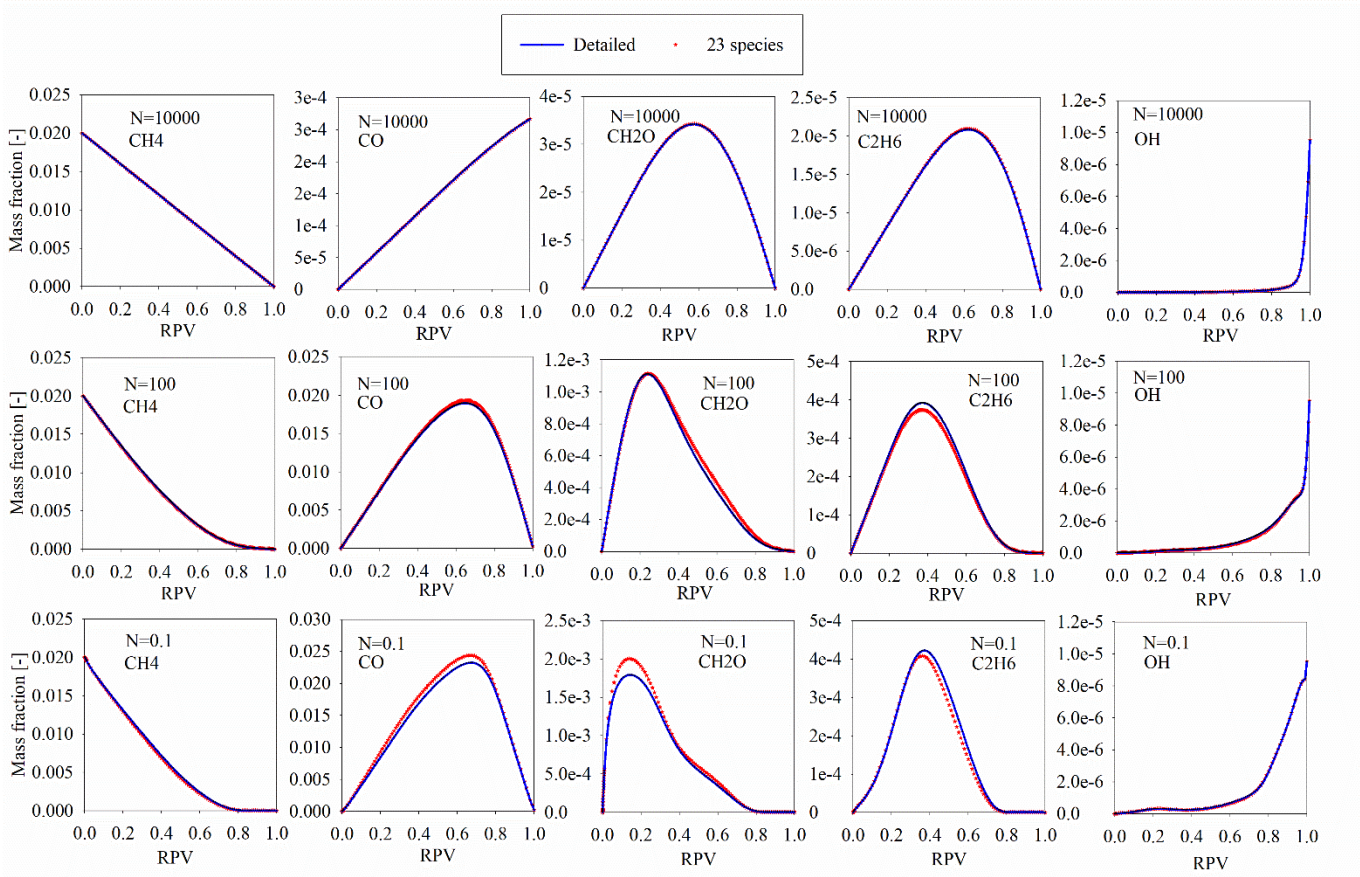

Figure 9: Comparison of detailed and reduced (23-species) Aramco 2.0 mechanisms at various turbulent dissipation values.

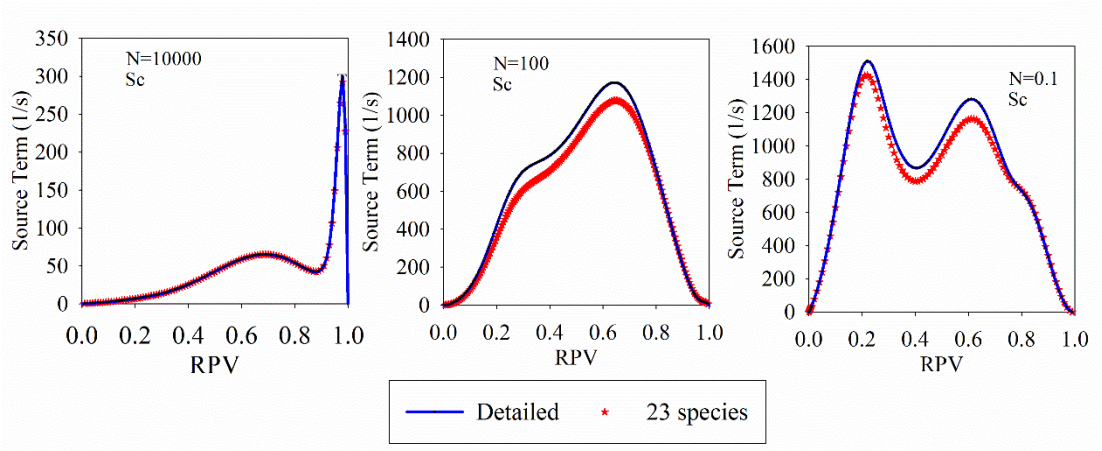

Figure 10: The comparison source term (S_c) estimated by detailed and reduced (23-species) Aramco 2.0 mechanisms at various turbulent dissipation values.

CONSTANT VOLUME SIMULATIONS

In this section, the 23-species and detailed Aramco 2.0 mechanisms are compared by using IDTs in constant volume reactor. Here, four mixture conditions (In addition to Mixture-1,2 and 3) are considered for comparison and each mixture has five initial temperature conditions varying from 1000 K to 1500 K. The temperature range chosen here corresponds to the approximate inlet and outlet temperatures of the sCO_2 combustion chamber. Also, these mixture conditions consist of two stoichiometric ratios, one lean and rich equivalence ratios.

The IDTs are shown in Fig. 11, which shows that, both the detailed Aramco 2.0 and 23-species mechanisms are predicting approximately the same IDTs. The maximum difference observed between both the predictions is less than 2%.

Table 3: Mixtures considered for comparing IDTs in constant volume combustion chamber

Initial Mixture	Mole ratios of fuel/O_2/CO_2
Mixture 1-H_2/O_2/CO_2	10/5/85
Mixture 2- CH_4/O_2/CO_2	3.91/9.92/86.17
Mixture 3- CH_4/O_2/CO_2	7.5/15/77.5
Mixture 4- CH_4/O_2/CO_2	1/2/26.7
Mixture 5- CH_4/O_2/CO_2	1/2/9
Mixture 6- CH_4/O_2/CO_2	1/4/15
Mixture 7- CH_4/O_2/CO_2	1/1.33/9

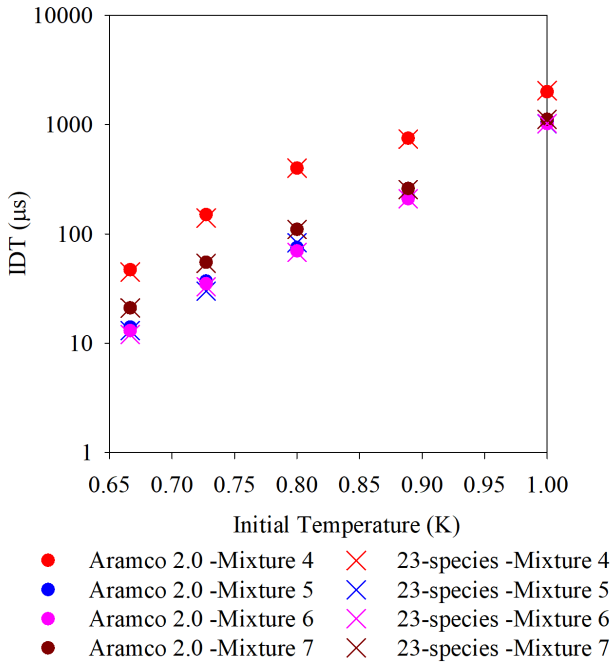

Figure 11: Comparison of the Aramco 2.0 and 23-species mechanism in terms of ignition delay times estimation in a constant volume combustion chamber.

CONCLUSIONS

The conceptual sCO_2 power cycle technology development has been gaining the attention of research and development due to its promise for high efficiency and CO_2 capture with compact foot-print. The extreme high pressure operating conditions of the direct-fired sCO_2 combustor makes the experimentation costlier, dangerous and time consuming and simulation tools play a major role. In the current work, a comparison is made between the Aramco 2.0 and GRI 3.0 mechanism by using various van der Waal's type of equations to predict the ignition delay times of a shock tube. From this analysis, the Aramco 2.0 mechanism is confirmed to be a better accurate mechanism available for sCO2 combustion applications. After that, a 23-species reduced mechanism has been developed from Aramco 2.0 mechanism by using the path-flux-analysis method (PFA) by employing the CHEM-RC tool. The conclusions of this research are as follows.

7) The equation of state is found to have no impact on estimating ignition delay times of supercritical $CH_4/O_2/CO_2$ mixtures unlike supercritical $H_2/O_2/CO_2$ mixture considered in this work. It may be because, in $H_2/O_2/CO_2$ mixture, the main product of combustion, i.e., H_2O is shifting the critical point of the mixture towards the testing pressure.
8) The $CH_4+HO_2 \Leftrightarrow CH_3+H_2O_2$ is very crucial in the prediction of auto ignition under sCO_2 conditions, because methane decomposes into CH_3 and H_2O_2 by this reaction even before the actual ignition starts.
9) The species C_2H_3 and CH_3OH and their associated reactions are very important in predicting the lean auto ignition.
10) The 16-species mechanism identified in this work is sufficient to recognize the ignition delay times of the stoichiometric conditions. However, for identifying lean conditions at least a 23-species mechanism is required. Also, the 19-species mechanism is needed in predicting the ignition delay times of stoichiometric sCO_2 hydrogen mixtures.
11) The 23-species mechanism presented in this work is performing on par with the detailed Aramco 2.0 mechanism in-terms of ignition delay times, perfectly stirred reactor estimation under various CO_2 dilutions and equivalence ratios, and prediction of turbulence chemistry interactions.

Current work provides the crucial reduced kinetic mechanism needed for the design and analysis of sCO_2 combustors using computational fluid dynamic codes. Future work will include incorporating the reaction kinetics data obtained from theoretical calculations at supercritical combustion conditions as well as testing the performance of reduced mechanisms against experimental data as they become available.

NOMENCLATURE

CHEMKIN-RG	CHEMKIN for real gases [269]
CMC	Conditional Moment Closure
EOS	equation of state
IDT	ignition delay time
N	turbulent dissipation rate
PCMC	Premixed Conditional Moment Closure code [270]
PFR	plug flow reactor
PSR	perfectly stirred reactor
RPV	reaction progress variable
RK	Redlich-Kwong Equation of state
SRK	Soave-Redlich-Kwong Equation of state
sCO2	supercritical CO_2
sO2	supercritical O_2
vdW	van der Waals Equation of state
$\bar{\rho}$	density
$N\|\zeta$	conditioned scalar dissipation
$\tilde{S}_c\|\zeta$	conditioned source term for RPV
$\dot{\tilde{\omega}}_i\|\zeta$	conditioned reaction rate
$\widetilde{\boldsymbol{Q}}_{\boldsymbol{i}}$	conditioned mass fraction
$\boldsymbol{\phi}$	equivalence ratio

APPENDIX 3 A Strategy of Reactant Mixing in Methane Direct-Fired sCO2 Combustors

The supercritical CO_2 (sCO_2) power cycle is an emerging technology which could address both environmental concerns and energy demands. The four prominent features of this power cycle are: 1) the high expected cycle efficiency compared to corresponding HE, AR and steam cycles, 2) compactness of the overall power plant, 3) complete capture of CO_2 and 4) the wide applicability over all power producing applications [10]. Conceptually, the sCO_2 power turbine is approximately 50 times smaller in size compared to conventional power turbines for the same power output [56]. However, there are many challenges involved in practical development of such turbines and power plant components at full scale.

This cycle uses supercritical CO_2 as the working fluid, therefore, CO_2 produced by the direct-fired, oxy-methane combustion power cycle can be recirculated within the same cycle loop and the excess supercritical CO_2 from the cycle can be used for other commercial purposes [10]. However, current state-of-art peak operating pressures for sCO_2 combustor is approximately 300 atm. [10] and the level of CO_2 dilution in the combustor is more than 95% percent by mass. At these extreme pressure and dilution conditions, experiments and testing is expensive, time consuming, and dangerous. Also, the traditional natural gas turbine combustor uses air as the oxidizer, whereas the sCO_2 combustor uses pure oxygen as the oxidizer [10]. Here, the presence of sCO_2 at 300 atm. shows a different dilution effect on combustion phenomenon than N_2 due to significant differences in their thermo-chemical properties. Therefore, the mixing strategies, ignition and blowout conditions are expected to be considerably different. Therefore, accurate simulation tools play a major role in the initial design aspects of the sCO_2 combustor development. As per the available literature, guidelines for designing and modeling sCO_2 combustors are

minimal [320-323] and still there is a need for testing a large number of combinations of initial operating conditions and design strategies before successfully constructing an efficient methane-sCO_2 combustor.

During the initial development of a combustor, even finalizing the design based on 3-D simulations is a tedious task because a wide range of operating conditions or strategies needs to be tested. Therefore, initial domain of operating conditions or strategies can be minimized by accurate 0-D and 1-D simulations. Further, the detailed 3-D simulations and experiments can be carried based on the directions of the 0-D and 1-D analysis.

The current paper investigates the suitable reactant mixing strategies for sCO_2 combustors by 0-D and 1-D analysis. It should be noted that, in this paper the "mixing strategy" refers to the reactant mixing composition and temperature. For the primary zone, a total of 35 stoichiometric mixing strategies are considered in this work as discussed in the modeling section and a suitable strategy is identified among them. Further, the equivalence ratio is varied between stoichiometric to lean to identify the most efficient mixing strategy for sCO_2 combustor primary zone. Here, a total of six design criteria have been chosen to eliminate the incompatible strategies as follows: 1) The primary zone blowout residence time, 2) primary zone reactor residence time, 3) primary zone reactor exit temperature, 4) primary zone aspect ratio, 5) primary zone scalability with respect to an equal power combustor, and 6) the rate of CO, O_2 and CH_4 consumption in the dilution zone. Though, the sixth criterion is a phenomenon which is observed in the dilution zone, it is relevant and depends on the percentage of CO_2 dilution in the primary zone. All of the above mentioned criteria is discussed in the following sections.

Perfectly-stirred reactor (PSR) modeling was extensively used in the 1950s to guide the development of gas turbine combustors and ramjets [128, 324, 325]. Also, complete gas turbine

combustor performance analysis was carried out by coupling plug-flow reactor (PFR) and PSR models [326-328]. It should be noted that, though the actual combustion chamber can be simulated by multiple PSR and PFR combinations [326], here only a single PSR and PFR combination is used because the main objective of this paper is not to simulate a particular combustor but to reduce the initial domain of operating strategies. Therefore, the results shown in this paper are qualitative in nature.

In the current work, the real gas version of CHEMKIN, i.e., CHEMKIN-RG [311] is coupled with existing FORTRAN PSR and PFR codes [329, 330]. The CHEMKIN-RG is equipped with equations of state (EOSs) such as van-der-Waals (VDW), Redlich-Kwong (RK), Soave-Redlich-Kwong (SRK) and Peng-Robinson (PR). These EOSs are empirical in nature and adopting them to an application needs validation. The work of [321] illustrated that the SRK EOS is a more accurate EOS for constant pressure sCO_2 combustion applications. Therefore, the SRK EOS is used in this work to simulate along with the detailed Aramco 2.0 mechanism.

This work is organized as follows: First, a better reactant mixing strategy is identified for the primary zone i.e. a combination of suitable primary CO_2 dilution level and temperature for a stoichiometric CH_4 and O_2 stream. The readers should note that important conclusions about the scalability of the combustor are drawn during this analysis. Further, the products of the primary zone (calculated based on the better primary mixing strategy) are allowed to react in three chosen dilution chamber configurations. It is known that the better dilution configuration must promote the consumption of CO, O_2 and CH_4. Therefore, based on the rates of CO, O_2 and CH_4 consumption over a given length of the dilution zone, a suitable dilution configuration is identified. In this analysis it is seen that, the exit CO levels from the dilution zone are relatively high. Therefore, the effect of lean combustion is studied further to identify the minimum amount of leanness that can

be used in sCO_2 combustor in order to consume CO completely. It is known that; the lean combustion adds additional O_2 separation cost in the sCO_2-plant maintenance hence in a companion paper (GT2018-75557) strategies are discussed to use the additional O_2 effectively in the sCO_2 combustor.

MODELING

A conventional gas turbine consists of air compressor, combustor and turbine in series. Incoming air is compressed by the compressor before supplying to combustor where it is mixed with fuel. Also, only the required amount of air is mixed with fuel in the primary zone (PZ) of the combustor for effective combustion and the remaining air is used to dilute the hot gases in the dilution zone (DZ) before entering the turbine (see Fig. 1). However, in the direct-fired sCO_2 plant compressor pressurizes CO_2, and fuel (methane) and oxidizer (oxygen) are injected directly into the combustor. One of the questions is how much CO_2 needs to be mixed with the reactants in the primary zone and at what temperature, i.e. the mixing strategy of the sCO_2 combustor? An attempt is made in this work to provide initial directions to designers and modelers from a combustion chemical kinetics point of view. As discussed in the introductory section, the 0-D PSR and 1-D PFR models are used to model the sCO_2 combustor. A schematic diagram is shown in Fig. 1 to explain the modeling of the sCO_2 combustor by coupling PSR and PFR. Here, the primary zone (PZ) or the recirculation zone is modelled as a PSR reactor and the dilution zone (DZ) is modeled as a PFR reactor.

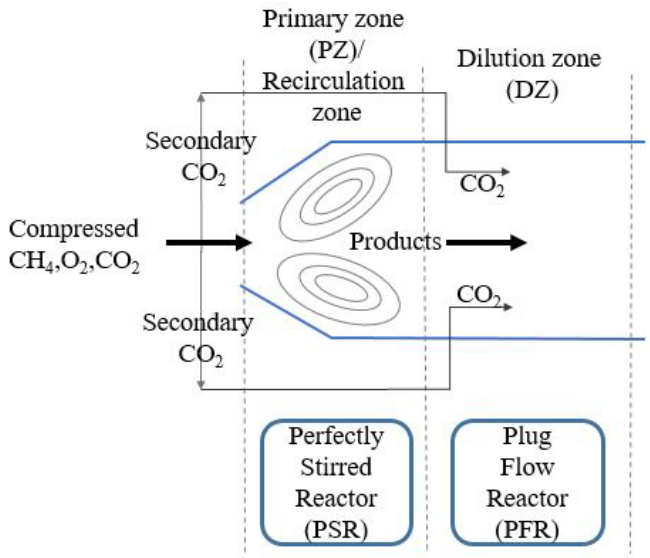

Figure 1: Modeling of sCO_2 combustor by PSR and PFR.

The PSR modeling assumes that reactants form products instantaneously, which is not the case in a real case where there are three time scales: The time for reactant gross mixing, the time for auto ignition, and the time associated with the molecules to enter and exit the reactor. The PSR modeling account only for the last one (called the residence time of the reactor), while the first two are assumed to take place at infinite time scales. It should be noted that, in-spite of not considering the former two time scales, the PSR and PFR coupling can be considered as a powerful tool to simulate real gas turbine combustors [326]. A highly turbulent recirculation zone reduces the first two time scales. In this study, it is assumed that the primary zone of the modelled sCO_2 combustor is highly turbulent, having strong recirculation so that the product formation is almost instantaneous. Detailed information of PSR and PFR formulations and programming can be found in refs. [327, 329, 330].

As mentioned earlier, one important characteristic of the sCO_2 power cycle concept is its compactness. The size of the sCO_2 turbine is almost 50 times smaller than the conventional turbine

for the same power output [331]. The approximate scalability of sCO_2 combustors is not reported in the literature until this work. For this purpose, a standard industrial combustor GE LM2500 is considered as a reference. The specifications of this reference combustor model is shown in Fig. 2.

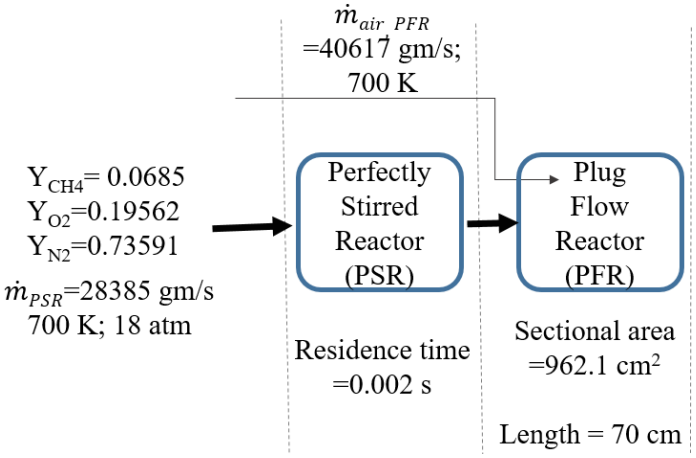

Figure 2: PSR and PFR model specifications for GELM2500 [327]

To design a sCO_2 combustor of 25 MW power, first the fuel flow rate entering the combustor must be defined for the sCO_2 combustor. In the current study, methane (with corresponding O_2 added stoichiometric) flow rate is defined in such a way that the efficiency of the entire plant is 60%. Also, methane and oxygen constitute only 5% of the total mass flow rates (remaining is CO_2). Only a portion of CO_2 is mixed in the PSR and the remaining is used to dilute the products (from PSR output). Further, the area of cross section of the sCO_2 combustor is chosen based on the corresponding Mach number of the GE LM2500 at the inlet. The Mach number is the important criteria for primary zone of a combustor and any change in its value (in the primary zone) significantly affects the combustor pressure losses. In general, the Mach number at the inlet of the primary zone is 0.02 to 0.05, however, based on the available data, the Mach number at the primary zone of GE LM2500 inlet is calculated to be 0.064 (the cross-sectional area of the sCO_2 combustor

is calculated based on this Mach number). Another constraint used in this study is the PSR fuel consumption efficiency. The PSR fuel consumption efficiency is defined as the ratio of fuel flow rate at the exit to the fuel flow rate into the PSR. It is found that for the GE LM2500 combustor, this efficiency is 99.99 percent and in this work the residence times in PSR are varied to achieve this efficiency.

$$PSR\ fuel\ consumption\ efficiency\ \left(\eta_{PSR,FUEL}\right) = 1 - \frac{(\dot{m}_{CH4})_{PSR\ exit}}{(\dot{m}_{CH4})_{PSR\ inlet}} \quad (1)$$

The solution from PSR is used as the input to PFR for simulating the dilution zone. In an actual combustor, the dilution zone has multiple holes around the circumference and length to dilute the hot gases before reaching the turbine. Therefore, the actual dilution zone must be simulated by considering a series of PFRs. However, since the main objective of this paper is qualitative design directions for detailed CFD and experiments, only a single PFR is considered (two PFRs are used in the section where the dilution zone configurations are investigated).

One of the main tools for any combustion simulation is an accurate chemical kinetic mechanism. Recent research from [37, 120, 309] provided methane shock tube experiments which are carried at the high pressures and at high CO_2 dilution levels. They found that the ignition delay times (IDT) predictions of the detailed Aramco 2.0 mechanism are close to the experimental data. The detailed Aramco 2.0 mechanism used in this study is tailored for C1-C2 compounds (73 species and 426 reactions).

Another important aspect which needs attention while simulating supercritical combustion is an accurate equation of state. It is understood that at 300 atm. pressure using the ideal gas assumption would lead to a significant deviation of approximately 7.5% in calculating density

[321]. Therefore, usage of ideal gas assumption at supercritical pressures is not valid to predict the state of a system, because at these pressures the intermolecular forces are significant and they must be accounted for while calculating the chemical and thermodynamic properties, and state of the system. The work of [4] illustrated that the SRK EOS is a more accurate EOS for constant pressure sCO_2 combustion applications and was chosen here as well. As discussed in the introductory section, the CHEMKIN-RG is coupled with the CHEMKIN-II PSR and PFR codes to consider the real gas effects in the simulation.

As shown in Fig. 3, five levels of CO_2 dilution are considered in the primary zone or the PSR. The total CO_2 in the cycle is 95% percent by mass. So, the rest of the CO_2 mass is directed into the dilution zone or PFR. Also, each PSR dilution level is considered at seven inlet temperatures ranging from 700 K to 1000 K (at 300 atm.). Hence, in total 35 possible sCO_2 operating conditions are tested in the current study.

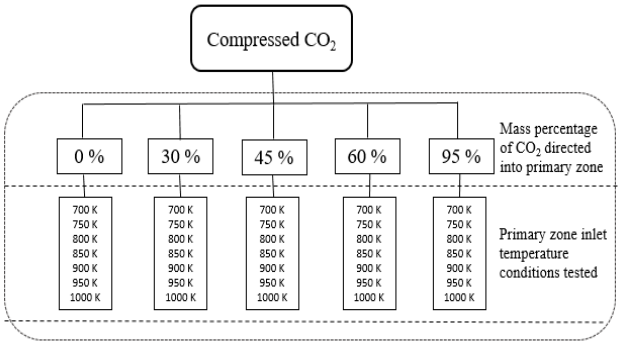

Figure 3: The tree diagram which shows inlet operating conditions tested for the sCO_2 combustor design.

RESULTS AND DISCUSSION

THE REACTANT MIXING STRATEGY IN PRIMARY ZONE:

In this section, unsuitable operating conditions for sCO_2 combustors are eliminated from 35 conditions shown in Fig. 3 by the six criteria listed in the introductory section of this paper. The first criterion is the blowout residence time. The blowout characteristics are the important and provides preliminary guidelines for the design of continuous flow combustion systems. Blowout generally refers the minimum residence time or the maximum flow rate beyond which the flame cannot sustain. The flow rate and the residence time are inter-related by the formula shown in Eq. 2. In the current work, the analysis is carried out for a fixed power output i.e. 25 MW and total cycle efficiency is sixty percent (assumed) [10]. Hence, the total flow rate is a fixed quantity, however based on the level of CO_2 mixing in the primary zone the flow rate into the PSR will vary.

$$PSR\ residence\ time = \frac{volume\ of\ the\ reactor}{volume\ flow\ rate} \quad (2)$$

Figure 4 shows the PSR blowout limits for various primary zone inlet CO_2 dilution levels and temperatures. Here, 5 levels of dilutions are shown between 0 to 95% of CO_2 by mass. The vertical axis in Fig. 4 is representing the PSR blowout residence times on a logarithmic scale. Figure 4 illustrates that at zero percent dilution level, the order of residence times are 10^{-8} seconds and the volume requirement of the reactor is in the order of 10^{-3} cm^3 (volumes are not shown in the figure). The order of the time scale and the volume shows that the operation of combustor at zero percent CO_2 dilution level is hazardous from the safety point of view i.e. any leakage would lead to rapid ignition. Also, at the zero percent CO_2 dilution level the order of temperature yield is approximately around 3500 K, which is very large for material specifications (maintaining this temperature in the combustor is not practical). Therefore, all the operating conditions at 0% CO_2

dilution level can be eliminated as not suitable for sCO_2 combustor design. In general, the order of total residence time in the combustor (PSR and PFR together) is in the order of 3-8 milliseconds. However, in Fig. 4, only 30% and 40% dilution levels have this order of blowout residence time. The blowout residence times for 60% and 90% dilution levels are very high and they are almost 10-100 times more than the total residence times inside a conventional combustor. In general, a factor of safety is considered for the blowout residence time while designing the combustor, hence, it is obvious to expect huge volume of the combustion chamber at higher PSR dilution levels (like 60% and 90%).

Figure 5 displays the relation between the volume of the PSR to its $\eta_{PSR,FUEL}$ (the PSR fuel consumption efficiency is defined in Eq. 1). Each curve represents a temperature as mentioned in the color legend. The solid lines correspond to 95% CO_2 while the dashed ones are for 60% CO_2 dilutions. The lower most point of each curve in this plot provides the $\eta_{PSR,FUEL}$ at the blowout volume. It is clear that the $\eta_{PSR,FUEL}$ is very poor at the blowout volume. This implies that volume needs to be increased to achieve this efficiency equal to that of the GE LM2500 combustor. As mentioned in the modeling section, the $\eta_{PSR,FUEL}$ for GE LM2500 is 99.99%. In Fig. 5, it can be seen that, the amount of PSR volume required for 95% and 60% CO_2 dilution levels to achieve the 99.99% $\eta_{PSR,FUEL}$ is very large. The 80% of fuel can be burnt within a relatively smaller volume, however, achieving the efficiency beyond this value needs a very large volume (the curve beyond 80% has a very small slope).

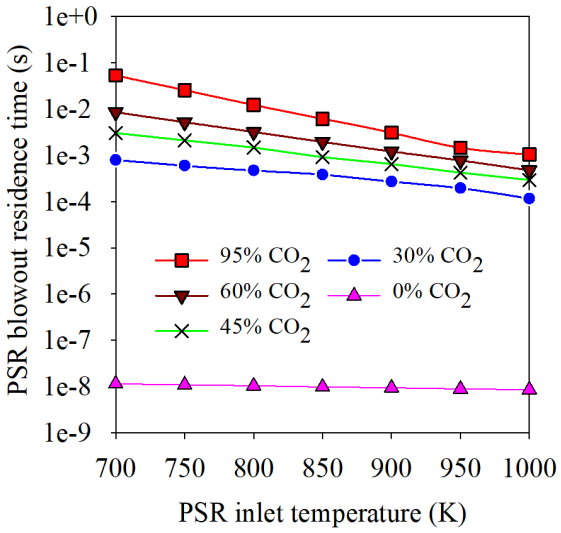

Figure 4: The PSR blowout limits under various inlet operating conditions.

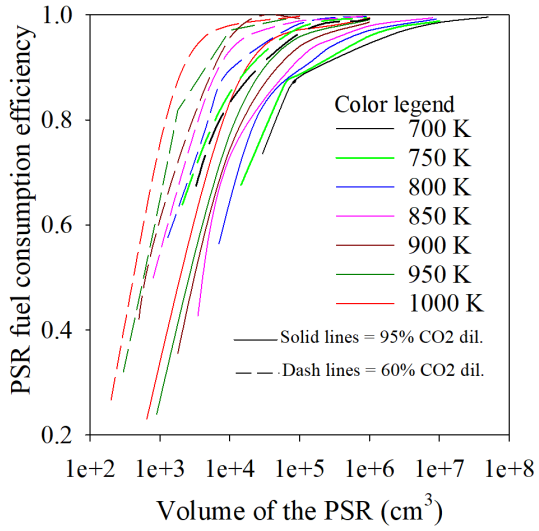

Figure 5: The relation between volume and PSR fuel consumption efficiency for PSR.

In the previous two paragraphs, it is seen that all temperature conditions under zero percent primary CO_2 dilution are unsuitable for the sCO_2 combustor design. In further analysis PSR residence time, PSR temperature, primary zone aspect ratio and scalability are taken into account for identifying satisfactory operating conditions.

The sCO_2 turbines are conceptually 50 times smaller than conventional turbines for the same power output due to the fact that at 300 atm pressure the working fluid will have a density almost 50 times higher. But, the possible scale down of the sCO_2 combustor is not discussed in the available literature. Since the Mach number is fixed for the primary zone, the area of cross section is also fixed under each operating condition. From the constraint to obtain 99.99% $\eta_{PSR,FUEL}$, the minimum volume required can be derived (thereafter, the aspect ratio of PSR or primary zone can be estimated from volume and cross-sectional area).

Figure 6 plots residence time, exit temperature, aspect ratio and the possible scalability for ninety-five, sixty, forty-five and thirty percent CO_2 dilutions in the primary zones under various PSR inlet temperature conditions. All subplots in Fig. 6 are calculated at a volume (PSR) which yields the 99.99% $\eta_{PSR,FUEL}$. The subplot (1,1) in Fig. 6 shows the residence time with respect to the inlet temperature (the vertical axis is in logarithmic scale). For ninety-five percent CO_2 dilution at all temperatures the residence time required is very high. Residence times at this dilution levels are varying between 74 s (at 700 K) to 0.8 s (at 1000 K). Also, for sixty percent CO_2 dilution, the residence times are varying between 1 s to 0.05 s. It appears that, for these two dilution levels the residence times at higher temperatures are achievable, the required PSR aspect ratios in subplot (2,1) are not practical. Two red lines are drawn in the subplot (2,1) which represent upper and lower possible aspect ratios. In general, the diameter to the length ratio of the primary zone is approximately between 0.5 and 5. Therefore, all operating conditions from sixty and ninety percent dilution levels can be eliminated from the sCO_2 combustor design considerations. Also, the inlet temperature conditions from 700 K to 900 K in forty-five percent dilution level are eliminated. The subplot (2,2) in Fig. 6 shows all possible scale downs of the cross-sectional area in comparison to the GE LM2500 combustor. For thirty percent CO_2 dilution, the achievable cross sectional area

scale down is between 19 times to 15 times lower than those of the GE LM2500 combustor. Also, for two temperature conditions mentioned above in forty-five percent dilution level has the scalability 13 and 11 times, respectively (the scalability is higher at lower inlet temperatures because the density is higher). Also, the residence times and aspect ratios are lower at higher temperatures as evident from the subplot (1,2) in Fig. 6.

Figure 7 plots the effect of PSR dilution and inlet temperature on the PFR emissions (only nine cases are considered for analysis because all other cases are so far eliminated). The products from PSR are diluted with the secondary CO_2. The density and temperature at the inlet of PFR are calculated based on adiabatic mixing method which conserves both mass and enthalpy. The horizontal axis of each subplot represents the length of PFR (note that the length of GE LM2500 combustor is 70 cm, however in the current plot a length is considered up to 210 cm). The solid and dashed lines in each subplot of Fig. 7 represent 35% and 45% dilution levels, respectively. Here, the subplot (1,1) indicates the CO level in PFR. At thirty percent dilution level as the inlet temperature increases CO emissions at the inlet of the PFR (exit of PSR) increase. Also, CO levels decrease as they pass through PFR. Interestingly, CO emissions at the inlet of the PFR, in forty-five percent dilution levels is less than the corresponding values at thirty percent dilution cases across the length of the PFR. Also, it must be seen that, the higher the inlet temperature, the lower will be the CO emissions at the exit. Also, the higher CO_2 dilution and a high temperature cases are consuming methane at higher rate as is evident from the subplot (1,2) of Fig. 7. Further, these high CO_2 dilution level cases also show the better performance in O_2 consumption (seen in subplot (2,1) of Fig. 7). The main reason for the better performance of forty-five percent dilution case is due to the fact that, it has less secondary CO_2 which is used as a diluent in the PFR. Therefore, due to the lower secondary mass flow rate, the resultant temperature in the PFR inlet is initially higher

than the corresponding thirty percent CO_2 dilution case as seen in subplot (2,2) in Fig. 7. This higher temperature at the PFR inlet enhances the consumption of CO.

To summarize this section, the higher temperatures and forty-five percent CO_2 dilution are recommended for the PSR inlet in order to reduce CO, CH_4, and O_2 at the PFR exit. Note that the ppm level of CO at the exit of the PFR is tremendously high. The strategies to reduce these levels in the products would be of interest for the sCO_2 combustor and cycle designers. It must be noted that the levels shown in the Fig. 7 can be taken as qualitative because they are the results from the exit of single PFR. In an actual combustor there are multiple holes along the circumference and length of the combustor.

THE STRATEGY OF MIXING IN sCO_2 DILUTION ZONE:

The main aim of this section is to identify the suitable dilution zone design configuration for sCO_2 combustor. The best operating condition identified so far (from previous sections, the forty-five percent dilution and 1000 K case) is considered for analysis. The products from PSR for this case are further passed through three different PFR configurations as shown in Fig. 8. The Case-1 configuration has only a single PFR and all the secondary CO_2 mix with the products (from PSR) and flow for 70 cm of combustor length. Also, in Case-2, the secondary CO_2 is equally distributed to two PFRs which are 35 cm distance apart. In Case-3, only twenty percent of secondary CO_2 is allowed through the first (PFR) and remaining eighty percent of the secondary flow through the secondary PFR. Here the PFR location can be considered as the diluent holes on the real combustor. In Case-2 all the holes are of equal size, whereas in Case-3 the size of holes is sequentially

increasing. The results of these strategies are shown in Fig. 9 (the horizontal axis depicts the length of PFR).

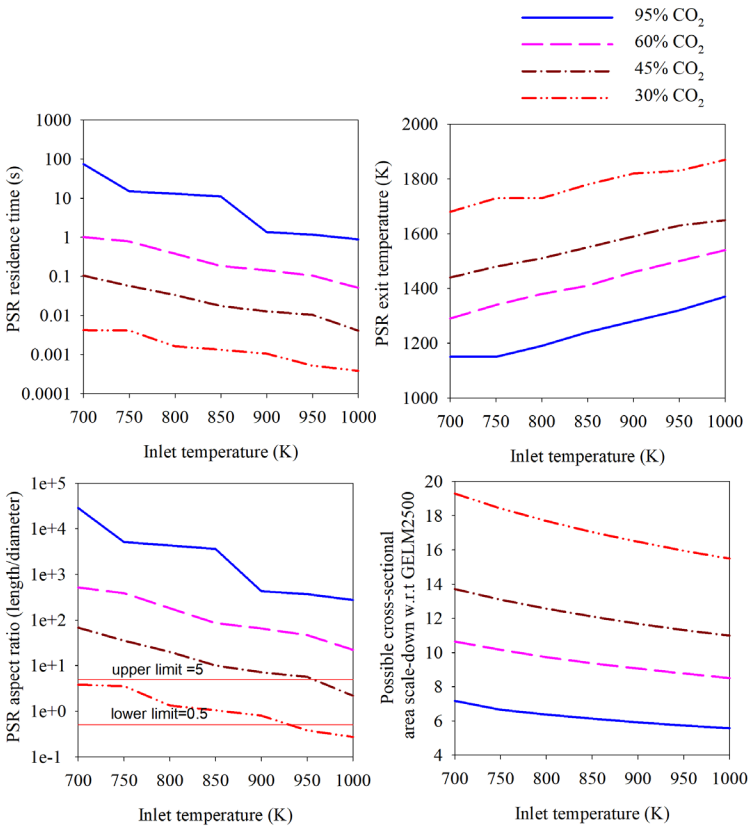

Figure 6: Requirements of PSR design under various CO_2 dilution and inlet temperature conditions

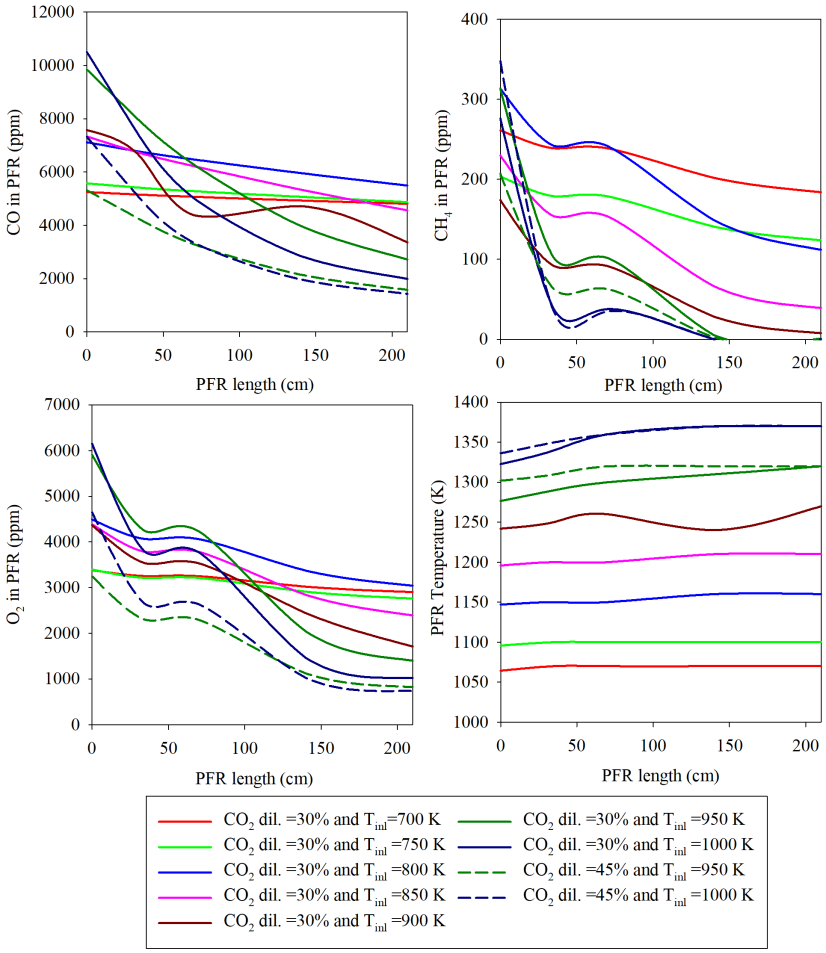

Figure 7: The effect of PSR dilution and inlet temperature in PFR emission.

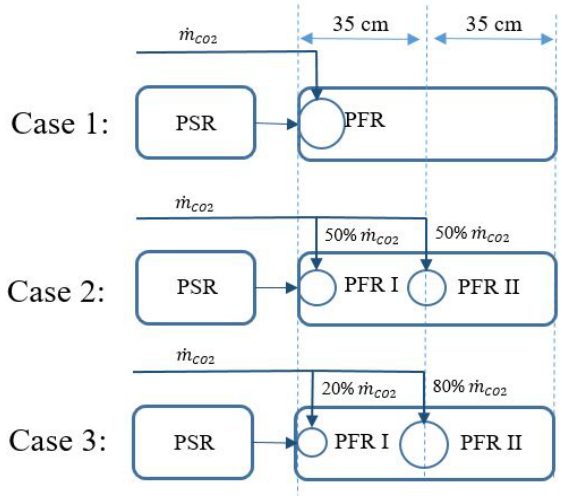

Figure 8: PFR configurations used to identify the best dilution strategy in sCO_2 combustor

Subplot (1,1) of Fig. 9 shows the variation of CO emissions across the PFR. The initial CO appears to be different for all three cases because these are the resultant CO after adiabatic mixing of PSR and secondary CO_2 streams. For Case-1, all secondary CO_2 is mixed with the PSR stream, therefore, the ppm level of CO is less. A rapid depreciation of CO can be observed in Case-3. The rate of consumption of CO in Case 2 lies between those of Case-3 and Case-1. For Case-3, only twenty percent of secondary CO_2 is mixed with the CO_2 stream before PFR I. Therefore, for Case-1, the flow in the PFR I has a higher temperature than other two cases. The temperature plots can be seen in the subplot (2,2) of Fig. 9. Here the end temperature is the same because the net amount of reactants in all three cases are equal. However, the initial temperatures are determined by the strategy of mixing in the PFR. The difference in the level of CO between Case-3 and Case-1 is around 1200 ppm, which is very large from the combustion point of view. Therefore, the strategy as shown in Case-3 is recommended for the design of the dilution zone in the sCO_2 combustor for reducing CO levels at the exit. However, the absolute end value of CO in Case-3 is 720 ppm, which is still higher than the allowed limits. A strategy of lean burn is discussed in the next section in

order to further reduce CO emissions. Also, Fig. 9 shows that the strategy as shown in Case-3 could reduce the O_2 and CH_4 faster.

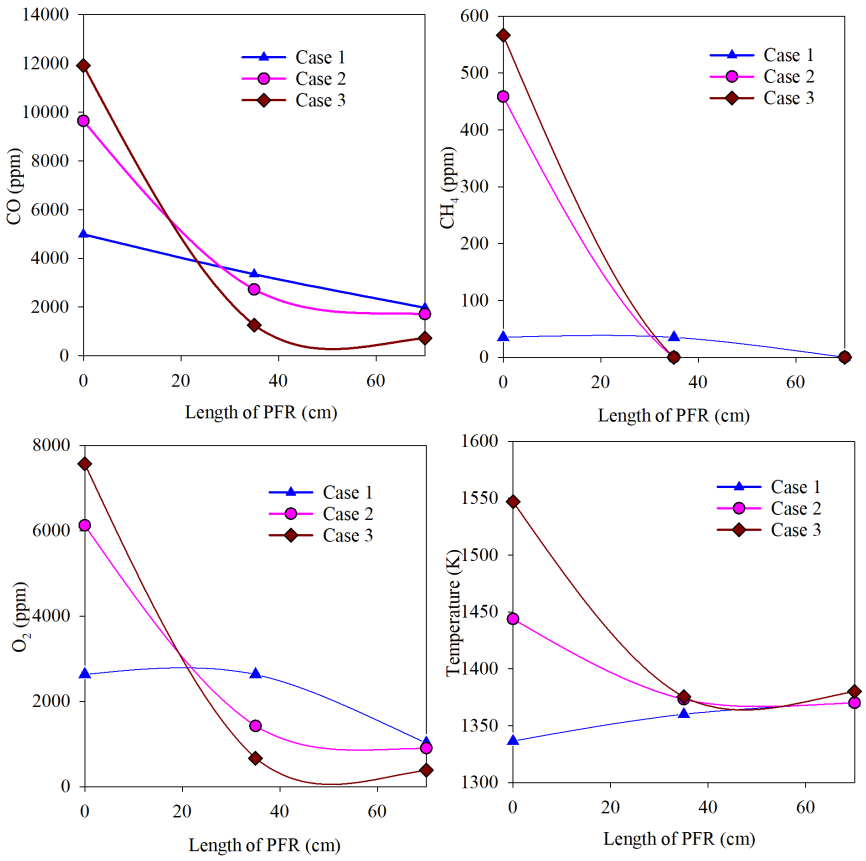

Figure 9: Effect of mixing strategy on PFR emissions

LEAN sCO_2 COMBUSTION:

Since the sCO_2 cycle is a closed loop cycle, another important requirement is to reduce the amount of major pollutants (CO and unburnt hydrocarbons) as much as possible so that an expensive exhaust cleanup system is not required. Therefore, in this section a popularly known CO reduction technique called “lean burn” is tested for the suitability in sCO_2 combustor. The

main disadvantage of lean burn condition in sCO_2 cycle application is the supply of O_2. The results in earlier sections (e.g., Fig. 9) shows the presence of traces of O_2 even though CH_4 is completely consumed. Therefore, supplying additional O_2 may hurt the cycle operation cost since O_2 is separated from atmospheric air by using auxiliary separation unit in the sCO_2 cycle. But it should be noted that oxidizing CO to CO_2 would increase the overall cycle efficiency. The lean burn operating conditions of sCO_2 may reduce the CO emission level, however, the best bet is to identify the trade-off between the CO level and excess O_2 supply. Therefore, in the current section four equivalence ratios (ϕ) =1, 0.9, 0.8, and 0.7 are analyzed. The percentage of inlet CO_2 mass is maintained as 95%, however the flow rates are adjusted for achieving 25 MW power with sixty percent over all plant efficiency. For all cases in this section, the 45% of CO_2 is mixed in the primary zone and the inlet temperature to the primary zone is1000 K.

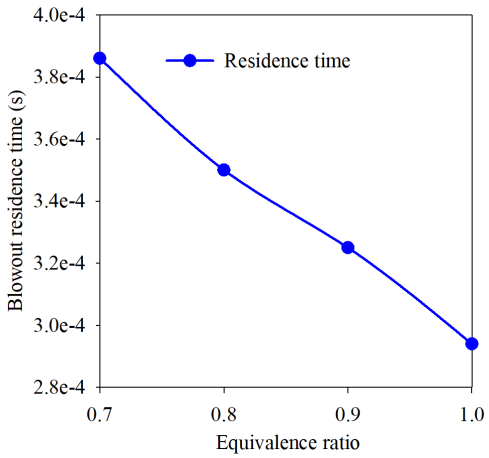

Figure 10: Blowout residence time under various ϕ values.

Figure 10 shows the blowout residence time requirement for sCO_2 combustor under various ϕ values, where it is seen that longer residence time is needed for lean burn conditions (than stoichiometric conditions). Longer residence time implies the molecules spend more time inside the combustor in order to sustain combustion. Figure 11 displays the various design possibilities

and PSR emissions under lean operating conditions. It should be noted that all subplots in Fig. 11 are made for PSR which gives 99.99% of $\eta_{PSR,FUEL}$. The subplot (1,1) shows the residence time requirement to achieve the 99.99% $\eta_{PSR,FUEL}$ under various lean operating conditions.

Here, it appears that for ϕ values 1, 0.9 and 0.8 the residence time requirement is not significantly different. However, at ϕ = 0.7 has significant difference with other cases. Also, subplot (1,2) shows the possible scale-down in terms of area of cross section compared to the GE LM2500 combustor. It must be noted that the area of cross section is determined based on Mach number=0.064. The result in this subplot shows that scalability for lean operating conditions is less compared to stoichiometric conditions. Also, the aspect ratio in the subplot (1,3) of Fig.11 indicates the practical possibility of designing the PSR zone in lean burn conditions, because the aspect ratio is just varying around 2 for the all cases considered. Further, the subplots (2,1) and (2,2) of Fig. 11 show the drop in the CO level from ϕ=1 to ϕ= 0.9 is drastic compared to other ϕ values. In conventional combustors, the level of CO after primary zone is 4000 ppm and it will be reduced to desired levels in subsequent dilution zones. However, the subplot (2,1) shows that, at ϕ=1 the CO level is almost 10,000 ppm and is in between 5000 to 3000 ppm for other lean conditions. There is a drop of approximately 5000 ppm CO due to lean equivalence ratio, ϕ (mainly because of the availability of O_2). Therefore, lean operation is necessary for sCO_2 combustor to reduce the CO emissions. The subplot (2,3) indicates more than 120 K difference between ϕ=1 and ϕ=0.7 for PSR exit temperature. This temperature drop warns us regarding the usage of lean conditions in sCO_2 combustion, because it would reduce the enthalpy associated with the system, which will affect the performance of the turbine. However, it should be noted that there is a rise in the total flow rate under lean conditions. Hence, loss in turbine power by temperature loss will be partially compensated by the rise in the flow rate as detailed next.

The best lean operating condition cannot be identified by doing PSR analysis alone. Therefore, a Case-3 PFR (as in previous section) strategy is used downstream of the PSR of all the lean conditions shown in Fig. 11. Figure 12 provides the emissions in PFR under various lean burn condition. Here, the subplot (1,1) shows that, all of CO is burnt to zero level at ϕ=0. 9, and interestingly, it is achieved at 35 cm length. Therefore, lean burn less than 0.9 may not be necessary in sCO_2 combustors because further lean burn may add operating cost of a larger oxygen separation unit. Also, it can be seen from subplot (2,1) that methane is completely consumed at 35 cm of PFR length. Therefore, the current analysis yields the possibility of scaling down the dilution zone of sCO_2 combustor to 50%. However, it must be noted that the "possible scale-down" mentioned in this investigation is only from the combustion point of view. The rate of diffusion mixing of reactants inside the sCO_2 combustor play another major role in determining the possible scale-down of the combustor. The subplot (2,2) in Fig. 12 illustrates that the PFR outlet temperature at 70 cm is dropped because of lean burn. The exit temperature difference between ϕ=1 and ϕ=0.9 is around 2.17 percent, however, the rise in mass flow rate is 8.76 percent. Therefore, the net turbine power increases because of lean operation of the combustor at ϕ=0.9. A companion paper will explore the effect of lean sCO_2 combustion on the overall plant performance.

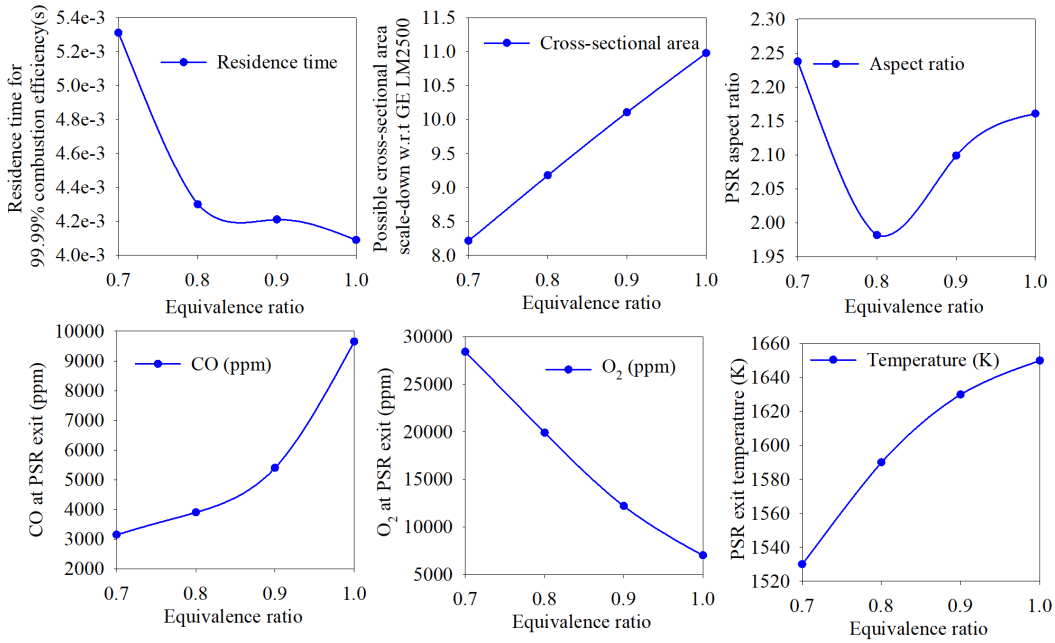

Figure 11: Effect of lean operation on PSR design and emissions (at 99.99% $\eta_{PSR,FUEL}$)

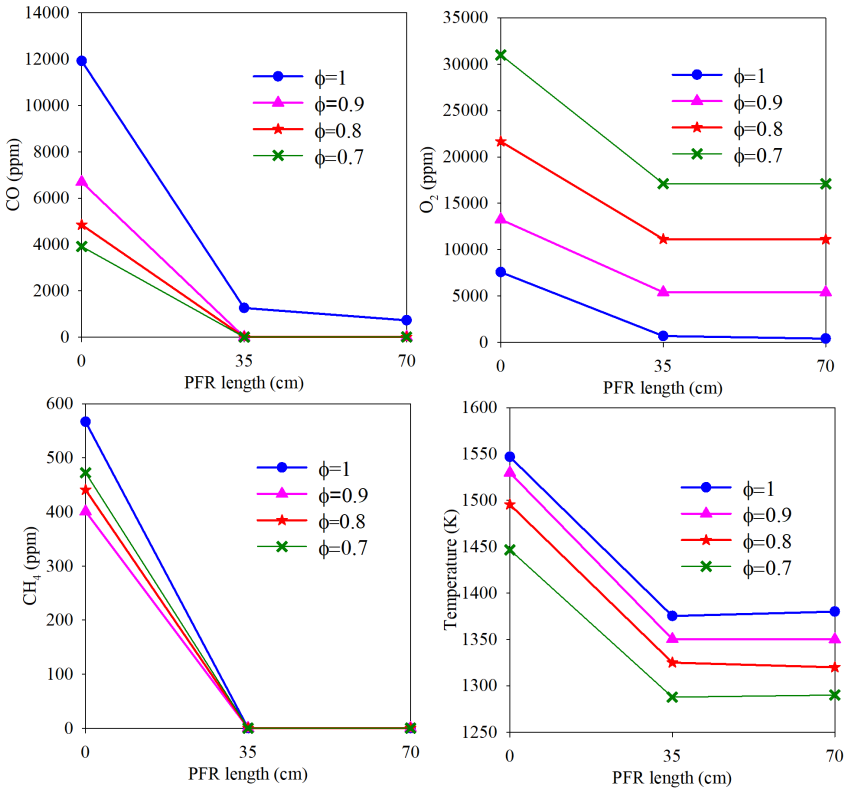

Figure 12: The emissions from the PFR under various lean burn conditions

CONCLUSIONS

The current work provides some strategies and best operating conditions for direct-fired sCO_2 combustors based on the zero-dimensional reactor modeling analysis. Here, the sCO_2 combustor is modelled by coupling perfectly stirred rector (PSR) and plug flow reactor (PFR) models. The real gas effects are considered using the Soave-Redlich-Kwong (SRK) equation of state. Also, the detailed Aramco 2.0 mechanism is used for accurate representation of the combustion kinetics. The scalability of the combustor is investigated with respect to the conventional 25 MW industrial combustor GE LM2500.

The total CO_2 in the cycle is 95% and the primary zone is diluted with a series of CO_2 dilution levels 0%, 30%, 45%, 60% and 95%. Under each primary dilution level seven inlet operating

conditions were analyzed between 700 K and 1000 K at 300 atm. The conclusions of the analysis are as follows:

1) Operating the combustor with no CO_2 dilution in the primary zone is very dangerous, because the blowout residence times are of the order of 10^{-8} s.
2) When the primary zone CO_2 dilution level is 95%, the amount of residence time required to achieve 99.99% PSR fuel consumption efficiency is very large and not practical at the relevant temperature conditions.
3) When the primary zone CO_2 dilution level is 60%, the PSR residence time required for achieving 99.99% PSR fuel consumption efficiency are of the order of 1 s. Also, the length to diameter aspect ratio is between 500 and 20. The design of the primary zone with these aspect ratios are not possible, therefore, all of the 60% dilution cases considered in this work are not suitable for sCO_2 combustor design.
4) The high temperature conditions (950 K and 1000 K) under 45% CO_2 dilution level, and all temperature conditions under 30% CO_2 dilution level are practically possible for sCO_2 combustor design.
5) The area of the cross section of sCO_2 combustor can be scaled-down between 10 to 20 times with respect to the conventional combustor (for the same power output).
6) The high temperature conditions under 45% CO_2 dilution level were observed to yield less emissions of CO and CH_4 at the exit of the combustor. Therefore, this study recommends the 45% CO_2 dilution in the primary zone at inlet temperatures of 950 K and 1000 K.
7) The holes with gradually increasing diameter on the combustor dilution zone are recommended. Because, the ascending diameter holes maintain the initial dilution zone

temperature relatively higher, which supports the drastic consumption of CO, O_2 and CH_4 in the dilution zone.

8) The sCO_2 combustor can be operated at a lean burning condition of ϕ=0.9 to completely consume CO from the combustor. The length of the PFR can be scaled-down to half of the conventional combustor.
9) It is observed that, the exit temperature difference between ϕ=1 and ϕ=0.9 is around 2.17 percent, however, the rise in mass flow rate is 8.76 percent. Therefore, the net turbine power increases because of lean operation of the combustor at ϕ=0.9.

Future work will involve providing design guidelines for syngas (mixture of CO and H_2 mix) and natural gas (mixture of methane, ethane, butane) under sCO2 operating conditions.

APPENDIX 4 A Strategy of Mixture preparation for Methane Direct-Fired sCO2 Combustors

NOMENCLATURE

ASU	air separation unit
CHEMKIN-II	a chemical kinetic solver in Fortran
CHEMKIN-RG	an extended version of CHEMKIN-II for real gases
DZ	dilution zone
EOS	equation of state
IDT	ignition delay time
LOx	liquid oxygen
PSR	perfectly-stirred-reactor
PFR	plug-flow-reactor
PZ	primary zone
PR	Peng-Robionson equation of state
RK	Redlich-Kwong equation of state
SRK	Soave-Redlich-Kwong equation of state
VDW	van-der-Waals equation of state
sCO2	supercritical CO2
τ_R	primary zone residence time

INTRODUCTION

The supercritical CO_2 (sCO_2) power cycle is considered an emerging conceptual power production technology which could address both environmental concerns and energy demands. This cycle uses supercritical carbon dioxide as the working fluid. The high density supercritical operating conditions allow it to operate the compressor with a lower power, hence increase the net power. Also, the turbine can be scaled down approximately fifty times for the same power output [56]. The prominent features of this power cycle are: 1) the high expected cycle efficiency compared to the corresponding Helium, Argon and steam cycles, 2) compactness of the overall power plant, 3) complete capture of CO_2 and 4) the wide applicability over most power producing applications.

The layout of the direct-fired oxy-methane sCO_2 power cycle is shown in the Figure 1. The layout shows that, the oxygen is separated from air by using an air separation unit (ASU) and the methane and oxygen are ignited in the combustion chamber in the presence of sCO_2.

The CO_2 by mass is ninety-five percent and methane and oxygen compose the remaining five percent. The products of the combustion are mainly CO_2 and H_2O. The H_2O is separated in the water separation unit and the CO_2 is recirculated into the combustion chamber through high pressure compressor and heat exchanger. Since, the cycle operates in a closed loop, the combustion products which are not separated in post combustion units may re-enter the combustion chamber along with the CO_2 stream and may greatly influence the combustor chamber performance. Therefore, the impurities in the recycled CO_2 stream must be considered in the design of the sCO_2 combustor. The influence of these impurities may be favorable or unfavorable to the performance of the combustion chamber. The effect of these impurities in the recycled CO_2 stream on the combustion chamber performance is not reported in the available literature. Therefore, in the

current research an attempt is made to understand the possible major constituents in the product mixture and possible techniques to utilize theses major products to improve the design of the sCO_2 combustion chamber.

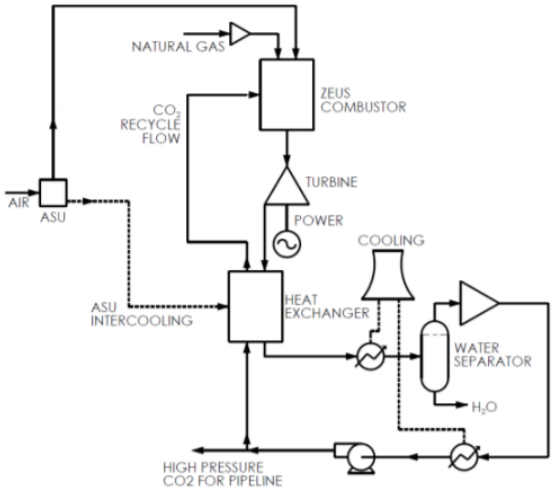

Figure 1: Layout of oxy-methane sCO_2 cycle (Allam cycle; reproduced from [10])

The current state-of-art peak operating pressures for sCO_2 combustor is approximately 300 atm. At these extreme pressure conditions, experiments are expensive, time consuming and dangerous. Therefore, simulation tools play a major role in the initial design of the sCO_2 combustor development. In the current work, an investigation has been carried out using zero dimensional perfectly-stirred-reactors (PSR) and one-dimensional plug-flow-reactors (PFR). The PSR and PFR modeling was extensively used in the 1950s as a guide to the development of gas turbine combustors and ramjets [128, 324, 325]. Also, complete gas turbine combustor performance analysis was carried out by coupling the PFR model with the PSR model [326-328].

The current work uses, the real gas version of CHEMKIN, i.e., CHEMKIN-RG [311] and it is coupled with PSR and PFR codes from CHEMKIN-II [329, 330]. The CHEMKIN-RG is equipped with equations of state (EOSs) such as Van-der-Waals (VDW), Redlich-Kwong (RK), Soave-Redlich-Kwong (SRK) and Peng-Robinson (PR). These EOSs are empirical in nature and adopting

them to an application needs the validation. The work of [321] illustrates that the SRK EOS is the more accurate EOS for constant pressure sCO_2 combustion applications. Therefore, the SRK EOS is used in this work to simulate the reactors.

In the results and discussion section of this paper, first, the primary zone design challenges of the sCO_2 combustor are compared to a conventional air-dilution combustor. Here, the results compare the difference between the two combustors in terms of primary zone exit combustion products. Also, these results show that, the required residence time to burn 99.99% of the fuel in the primary zone of a sCO_2 combustor, is more than that of the conventional air-dilution combustor. The residence times generally used for blow-out -the reactor residence time- also refers to the minimum time required for the flow to be in the PSR reactor, to consume 99.99% of the fuel. Additionally, CO_2 and O_2 levels at the exit of both these combustors are qualitatively compared. In short, the above mentioned sCO_2 and air-dilution comparison section shows the necessity of the reactant preparation strategy. That implies that any strategy of reactant preparation must reduce the reactor residence time requirement. If the composition, temperature and pressure of reactants are fixed, then the residence time can be minimized by making use of exhaust products because the sCO_2 cycle operates on a closed loop. Also, it must be noted that the purification of exhaust impurities may have an additional cost on the plant operation. A companion paper (GT2018-75547) concludes that, a high level of CO can be expected from sCO_2 combustors because of the unavailability of enough CO consuming species in the dilution zone. Hence this paper addresses an important challenge “how to make use of the exhaust impurities effectively and reduce the reactor residence time requirement?” In this paper, following two options for exhaust re-circulations are discussed: 1) re-circulate excess CO back to the combustion chamber along with the CO_2 bulk flow, and 2) completely burn CO before the exit by lean operation (excess O_2) and

re-circulate the excess O_2 along with the CO_2 bulk flow. It is seen (in GT2018-75547) that, even at stoichiometric operation of the combustor there is a large amount of un-consumed O_2 at the exit though the CH_4 is completely consumed. Therefore option-2 may further increase the exhaust O_2. Hence "the strategy of mixture preparation" in the title of this paper refers to the way by which we can make use of excess CO in option-1 and O_2 in option-2 to reduce the large reactor residence times.

Two novel strategies are tested in this work along with one established strategy which is widely used. The known common strategy is to send pure CO_2 stream to the combustion chamber. However, this routine strategy is seen to have higher required residence times and additional cost of purifying the exhaust product stream for pure CO_2. In the direct-fired sCO_2 cycle, the CO_2 stream is optimized to be at a higher temperature (~1000 K). This temperature is sufficient to initiate few reactions if minimum adequate quantities of fuel and oxidizer are together for enough time. This is the fundamental idea behind the following two novel strategies analyzed. First, if CO impurity is recirculated along with CO_2 as in option-1, then before the entry of the combustor some small amount of O_2 can be mixed with the bulk stream. These small amounts of CO and O_2 may react, if allowed for sufficient time and help in increasing the bulk CO_2 stream temperature. Further, this higher temperature stream reduces the required residence time in the combustor. Secondly, if O_2 impurity is recirculated along with CO_2 as in option-2, then before the entry of the combustor some small amount of CH_4 can be mixed with bulk stream and it may also increase the temperature and release few radical species. The above mentioned three strategies are shown in Fig. 2.

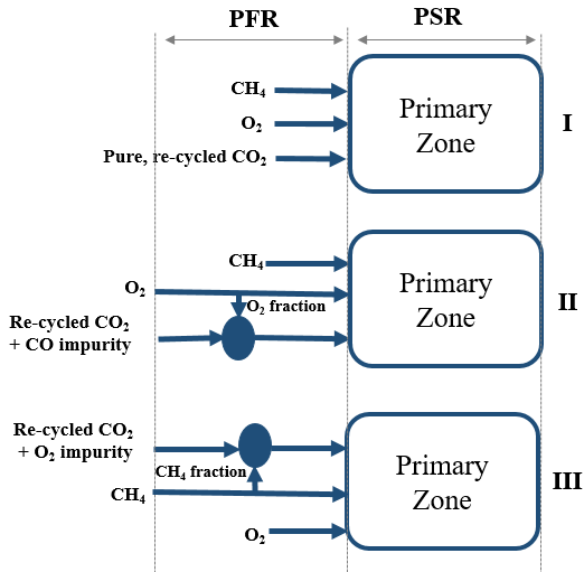

Figure 2: Mixture preparation strategies investigated in the current work

MODELING

A conventional gas turbine consists of an air compressor, combustor and turbine in series. The air is compressed in the compressor before supplying it to the combustor where the fuel is injected in to the combustor. Here, only the required amount of air is mixed with the fuel in the primary zone (PZ) of the combustor for effective combustion and the remaining air is used to dilute the hot gases in the dilution zone (DZ) before entering the turbine.

As discussed in the introductory section, the PSR and PFR are used to model the sCO_2 combustor. A schematic diagram is shown in Fig. 3 to explain the modeling of the gas turbine combustor by PSR and PFR coupling. Here, the primary zone (PZ) or the recirculation zone is modelled as a PSR reactor and the dilution zone (DZ) is modeled as a PFR reactor. The literature [326] has simulated a real combustor with multiple PSR and PFR. However, only a simple series arrangement of PSR and PFR is considered because of the qualitative nature of the objective of this work.

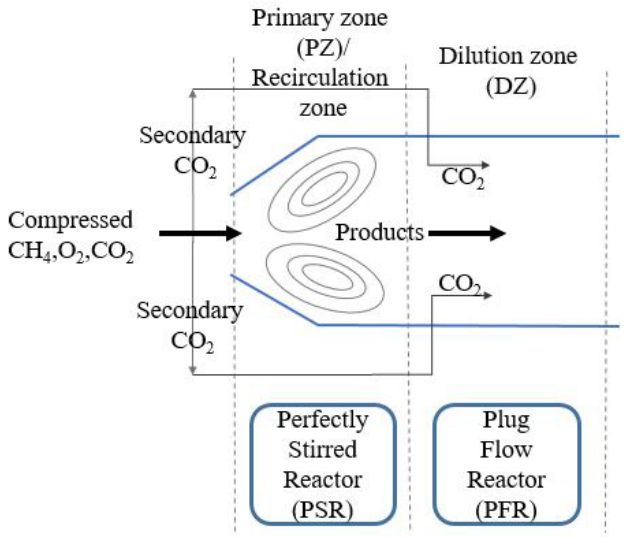

Figure 3: Modeling of sCO_2 combustor by PSR and PFR.

The PSR modeling assumes that the reactants form the products instantaneously, which is not the case in a real combustor. In the real case, there are three time scales. They are, the time for reactant gross mixing, time for auto ignition and the time associated with the molecules to enter and exit the reactor. The PSR modeling accounts for only the third-time scale. This third-time scale is generally referred as the residence time of the reactor. A highly turbulent, well designed recirculation zone reduces the first two time scales. Therefore, in this study it is assumed that the primary zone of the modelled sCO_2 combustor is highly turbulent, having strong recirculation so that the product formation is almost instantaneous. It should be noted that, in-spite of not considering the former two time scales. Detailed information of the PSR and PFR formulation and programming can be found in [327, 329, 330].

The novel mixture preparation strategies before combustor (II and III in Fig. 2) are modeled by a PFR reactor. It is assumed that the mixing process is instantaneous and adiabatic, hence the enthalpy and mass conservation is accounted for.

Also, one of the main tools for any combustion simulation is an accurate chemical kinetic mechanism. Recent research from [120, 309, 310] provided methane shock tube experiments which are carried at the high pressures and high CO_2 dilution levels. They found that the ignition delay times (IDT) predictions of the detailed Aramco 2.0 mechanism are close to the experimental data. Therefore, Aramco 2.0 mechanism is used in this current work. Another important aspect which needs attention while simulating supercritical flow is the equation of state. It is understood that at 300 atm. pressure using the ideal gas assumption would lead to a deviation of approximately seven percent in calculating density [321]. Therefore, usage of the ideal gas assumption at supercritical pressures is not valid to predict the state of a system, because at these pressures the intermolecular forces are significant and they must be accounted for while calculating the chemical and thermodynamic properties, and state of the system. The EOS can be broadly categorized into three types, they are 1) the virial-type, 2) molecular-based and 3) van der Waal type EOSs [233, 234]. However, van der Waal type equations are popular due to their simplicity. Since, these EOSs are empirical by their origin, adopting them to an application requires validation with data. For example, some investigations recommend SRK EOS for sCO2, CH_4/LOx and kerosene/LOx mixtures [277, 294, 321]. Whereas Poschner and Pfitzner [295] recommend PR for H2/O2 mixtures. More detailed formulations of EOS and associated real gas mixture formulations can be found in [228, 311, 321]. The CHEMKIN-RG is coupled with the CHEMKIN-II PSR and PFR codes to consider the real gas effects in the simulation.

The analysis carried out in this work corresponds to a 25 MW power plant. For the air-diluted combustor and sCO_2 combustor discussed in this work, the flow rates are calculated based on cycle efficiencies of 44.4% and 60%, respectively and the corresponding pressures are 18 atm. and 300 atm., respectively.

RESULTS AND DISCUSSION

THE PRIMARY ZONE RESIDENCE TIME

The blowout residence time and the primary zone required residence time are important parameters to design a combustion chamber. The blowout refers to minimum residence time or the maximum flow rate beyond which the flame cannot be sustained. In other words, blowout occurs when the residence time is less than the chemical time needed to react. Therefore, the primary zone in the combustion chamber should be designed in such a way that the total primary flow stays above the blowout residence time, so that the reactions initiate within the mixture. In general, the primary zone is designed so that the 99.99% of the fuel is burnt before entering the dilution zone. An important parameter "PSR fuel consumption efficiency" is defined as shown in Eq. 1 to the measure the fuel consumption in the primary zone. It is defined as the ratio of the rate of Methane consumed in the primary zone to the rate of methane inflow to the primary zone.

$$PSR\ fuel\ consumption\ efficiency = 1 - \frac{(\dot{m}_{CH4})_{PSR\ exit}}{(\dot{m}_{CH4})_{PSR\ inlet}} \qquad (1)$$

The comparison of CO_2 dilution in sCO_2 combustor and air-diluted conventional combustor are discussed in this section. As discussed in the modeling section, the flowrates for the sCO_2 combustor and air-diluted combustor are chosen to achieve 25 MW power and more details are shown in Table 1. It should be noted that, here, practical over all efficiencies are chosen to calculate the flow rates. For the sCO_2 combustor the total flow (primary and dilution) molar ratios are chosen so that the CO_2 is ninety-five percent by mass and CH_4 and O_2 constitute the remain five percent

in a stoichiometric proportion. In both the cases, fifty percent of total flow is used as diluent in the dilution zone.

The flow rate and the required residence time are inter-related by the formula shown in Eq. 2.

$$PSR\ residence\ time = \frac{volume\ of\ the\ reactor}{volume\ flow\ rate} \quad (2)$$

Figure 4 shows the blowout PSR residence time between both the CO_2 dilution and air-dilution cases. Here, the horizontal axis represents the PSR inlet temperature and the vertical axis shows the blowout residence time in logarithmic scale. The result shows that, at lower inlet temperatures the residence times are high and they reduce with an increase in inlet temperature. Also, the blowout residence times of CO_2 diluted combustion are a couple of orders higher than air-diluted combustion. It is mainly because, the specific heat of the CO_2 is much higher than the N_2. The sCO_2 mixture absorbs more enthalpy before it raises its temperature. Therefore, the chemical time scales are higher for sCO_2 mixtures and hence the blowout residence times are higher.

Table 1: The operating conditions chosen for calculating PSR residence time

	Air-diluted combustor	sCO_2 combustor
Power (MW)	25	25
Pressure (atm.)	18	300
Moles in primary zone	$CH_4/O_2/N_2$ =1/2/7.52	$CH_4/O_2/CO_2$ =1/2/16.39
Overall cycle efficiency (%)	44.8	60

Primary flow rate (kg/s)	20.2	41.7
Secondary dilution	air	sCO_2
Secondary flow rate (kg/s)	20.2	41.7

Figure 5 shows the PSR residence time required to burn 99.99% of the total fuel. It shows that, the consumption of fuel takes a longer time in the sCO_2 combustor. Again, the reason is due to the high specific heat and lower temperature of the sCO_2 mixture. However, this data shows the challenges associated in the development of an sCO_2 combustor. A higher required residence time makes it difficult to design the combustion chamber. The required residence time for a sCO_2 combustor primary zone at 1000 K is much more than the air-diluted combustor. In general, for a conventional combustor the residence time in the primary zone is about two milliseconds [327]. However, for sCO_2 combustor at 1000 K the residence time is approximately ten milliseconds. Here, it should be noted that the factor of safety is not considered yet. If the factor of safety is considered for the sCO_2 combustor residence times, the design of combustor becomes more challenging. Therefore, it is very important to identify techniques to reduce the resonance time requirement in the primary zone of an sCO_2 combustor.

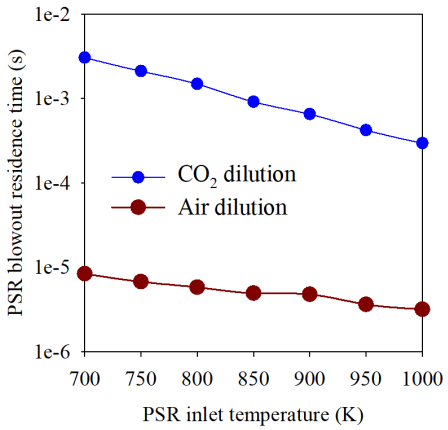

Figure 4: The PSR blowout residence times for sCO_2 combustor and air-diluted combustor at various inlet temperatures

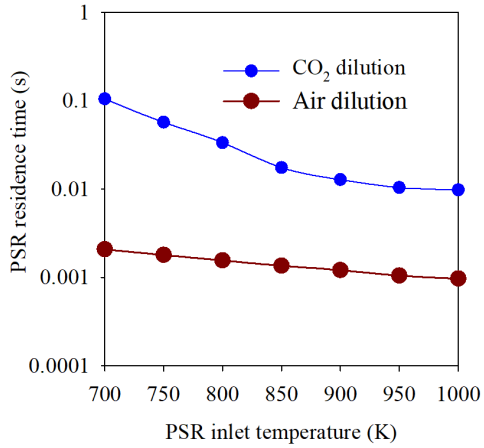

Figure 5: The PSR residence time for achieving 99.99% of PSR fuel consumption efficiency

CO AND O_2 IN THE PRIMARY ZONE

As discussed in the modeling section, it obvious that the CO and O_2 are the two major components in the combustor exhaust besides CO_2 and H_2O. Therefore, it is very important to understand the variation of these two species after the primary zone and dilution zone of the sCO_2 combustor. The "mixture preparation strategies" discussed in this paper are better appreciated, when the basic

difference between the sCO_2 combustor and air-diluted combustor are compared in terms of consumption of CH_4, O_2 and CO in the primary zone (PSR) and dilution zones (PFR).

Figure 6 shows the variation of CH_4, CO and O_2 in the sCO_2 and air-diluted combustors primary zone exit with respect to inlet temperature, under various reactor conditions. Here, each subplot has inlet temperature of the PSR in the horizontal axis. All the subplots in the first three columns in Fig. 6 represent the levels of CH_4, CO and O_2 in parts-per-million and they are shown in the vertical axis of each subplot in the first three columns. The fourth column corresponds to the PSR exit temperature. Further, each row in Fig. 6 corresponds to a particular reactor condition. All the subplots in first and second rows correspond to a primary zone reactor volume equal to 2000 cm^3 and 10,000 cm^3, respectively. The third row corresponds to a reactor residence time of 2 milliseconds and the fourth row corresponds to the equilibrium condition i.e. an infinite residence time. In each subplot, the comparison is made between sCO_2 diluted combustion and air-diluted combustion.

Subplot (1,1) in Fig. 6 corresponds to CH_4 variation at the PSR exit with 2000 cm^3 PSR volume (primary zone volume). At the same reactor volume, since the inlet flow rate of the sCO_2 and air-diluted combustion are different, the residence times are different. As, shown in subplot (1,1) the CH_4 at low temperature for sCO_2 diluted combustion is very high. It is mainly because the reactivity is very poor due to the low temperature. The corresponding PSR exit temperature profiles can be seen in subplot (1,4) of Fig. 6. The CH_4 level becomes zero within the 2000 cm^3 volume for air-diluted combustion at all the inlet temperatures. The subplot (1,1) also shows that, at least 1000 K inlet temperature is needed to consume most of the CH_4 in the primary zone. The subplot (2,1) shows the variation of PSR exit CH_4 at 10,000 cm^3 volume. The trend of CH_4 in subplot (1,1) and (2,1) are similar, however, with the increase in volume the level of CH_4 decreases

because the reaction continues for more time i.e. the residence time increases as the volume increases. The subplot (3,1) corresponds to a reactor residence time of 2 ms. It should be noted that, at the same residence time, the sCO_2 and air-diluted combustion will have different reactor volumes due to the difference in their flow rates (refer Eq. 2). The primary zone of sCO_2 combustor has higher CH_4 traces at the end of 2 milliseconds reactor residence time.

The trend of CO in subplot (1,2) is interesting, because with the rise in the inlet temperature, the CO level is increasing for air-diluted combustion at the PSR exit, whereas, the level of CO is decreasing for the sCO_2 diluted combustion case. In general, the CO can be formed as an intermediate of CH_4 and CO_2 or by the dissociation of CO_2, therefore the exact reasons for reduction in CO level needs a detailed kinetic analysis. However, expected dissociation of CO_2 in sCO_2 combustor is very low due to the low temperature combustion. Therefore, the CO levels in sCO2 dilution could be mainly due to its intermediate formation. As the exit CH_4 level is decreasing with an increase in PSR inlet temperature, the intermediate CO also reduces in this case. The same trend of CO can be observed in both the 2000 cm^3 and 10,000 cm^3 cases ((1,2) and (2,2)). However, the CO levels in 10,000 cm3 case are lower than the 2000 cm3 case because the increase in volume increases the respective residence times and hence the CH_4 consumption increases and the CO is lower. Further, in subplot (3,2) shows the CO level comparison at 2 milliseconds residence time. For sCO_2 combustion at 700 K inlet temperature of PSR, the CO appears to be zero because the chosen residence time in this case is less than the blowout limit at 700 K for sCO_2 combustion. Further, as the inlet temperature increases the level of CO decreases and at 1000 K the values of both sCO_2 and air-diluted combustion are almost equal. Subplot (4,2) shows the CO comparison at the equilibrium condition i.e. at an infinite residence time or at an

infinite volume. Interestingly, at equilibrium the CO is almost zero for sCO2 diluted combustion and very high for air-diluted combustion.

.

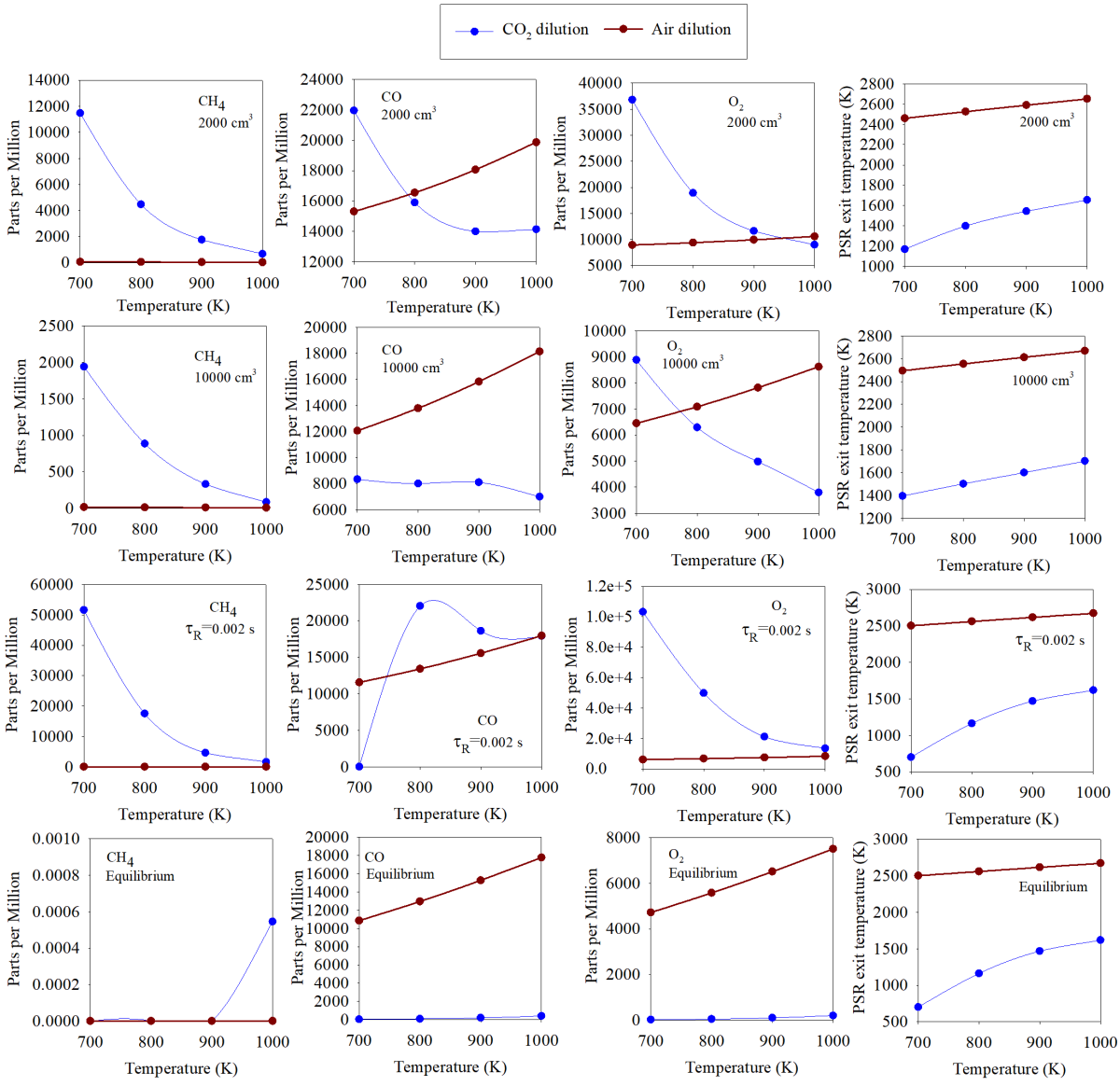

Figure 6: The variation of CH_4, CO and O_2 in the sCO_2 and air-diluted combustor primary zone exit with respect to inlet temperature under various reactor conditions.

The subplots (1,3), (2,3), (3,3) and (4,3) of Fig. 6 show the O_2 at the PSR exit for the reactor conditions, 2000 cm^3, 10,000 cm^3, 2 millisecond residence time and equilibrium conditions respectively. The variation of O_2 is also similar to CO for both sCO_2 and air-diluted combustions. For air-diluted combustion, the O_2 level increases with an increase in PSR inlet temperature, whereas decreases for sCO_2 diluted combustion. At 10,000 cm^3, the level of O_2 is much less than the level of $_{O2}$ at 2000 cm^3. When the residence time is 2 milliseconds and at 1000 K, the O_2 levels are almost the same for both the combustion phenomenon. Also, at equilibrium significant O_2 remains at the exit of air-diluted combustion compared to sCO_2 diluted combustion.

Overall, if the sCO_2 combustor is operated at higher inlet temperatures i.e. around 1000 K, the CO and O_2 at the primary zone exit of the sCO_2 combustor are less then or in some cases equal to CO and O_2 levels of the primary zone exit of same power air-diluted combustor. In the next section the products of the primary zone are also expanded in the dilution zone by using a PFR reactor mode.

THE CO AND O_2 IN THE DILUTION ZONE

The products of the combustion from the primary zone are expanded in the dilution zone for a time of one millisecond. In this section, the comparison is made only with a PSR inlet temperature 1000 K. The products from the PSR are adiabatically mixed with the secondary dilution. Here, the residence time in the primary zone is chosen in such a way that 99.99% of the CH_4 is burnt in the primary zone itself. Therefore, it should be noted that the residence times in the PSR are different for both the sCO_2 and air-diluted combustion. The secondary dilution temperature is also taken as 1000 K. A schematic diagram is shown in Fig. 7 to illustrate the coupling of the PSR and PFR. The

actual combustor consists of multiple PFR zones. However, in the current section only one PFR is considered to qualitatively judge the combustor output CO and O_2.

Figure 8 shows the variation of CO and O_2 in the dilution zone for both sCO_2 and air-diluted combustors. Here, the horizontal axis is corresponding to the residence time in the PFR. It is very interesting to see that, the level of CO is drastically reduced for air-diluted combustion, whereas, it is very gradual for the sCO_2 diluted combustion. In other words, the CO changed only a little by the end of one millisecond. In fact, the similar gradual change is observed even after four milliseconds (not shown in the figure). This is mainly because, the presence of O_2 in air-diluted combustion reacts with the CO. However, the reactivity is very poor in sCO_2 combustor dilution zone due to presence of CO_2 at lower temperatures and lack of O_2.

Therefore, the results in this section shows that the CO levels at the exit of the sCO_2 diluted combustor are much more than the air-diluted combustor. At the same time, the O_2 levels are much lower than the air-diluted combustor. The actual levels of CO and O_2 may vary based on actual design of the combustion chamber.

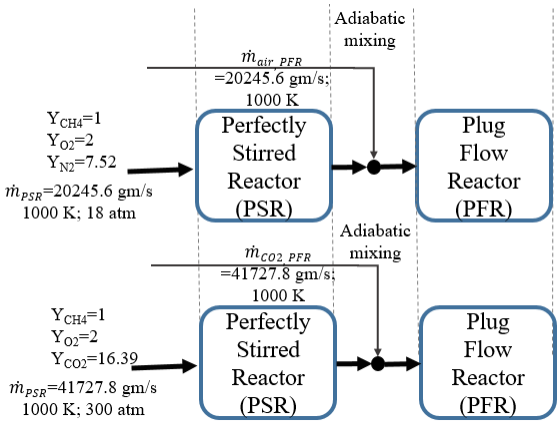

Figure 7: The coupling of PSR and PFR for the analysis of CO and O_2 variation in dilution zone.

A STRATEGY TO REDUCE THE RESIDENCE TIME

In the previous section it was shown that the exit CO levels are higher for a sCO_2 combustor and the consumption of CH_4 and O_2 are poorer compared to an air-diluted combustor. This difference must be considered while designing the sCO_2 combustor. The CO itself acts as a fuel, therefore after combustion, instead of filtering the CO from the products, the CO in the re-cycled CO_2 stream can be mixed with the primary oxidizer stream before entering the primary zone. This strategy produces some heat and radicals which may help to reduce the blowout residence time in the primary zone. Also, the enthalpy lost during the combustion in the form of CO can be re-used in the cycle. This strategy is elaborately discussed in the introductory section of this paper (in Fig. 2) this strategy is shown as strategy-II.

Our companion paper (GT2018-75547) discusses the lean operation of sCO2 combustors and some of its advantages in terms of consuming the entire CO and increasing the net turbine power. The lean operation increases net turbine power because the flow rate must be increased in order to keep the mass fraction of CO_2 above 95% and the temperature loss due to lean operation is four times lower than the increase in the flow rate. However, the O_2 levels are much higher in the exhaust stream if the combustor is operated under lean conditions. In sCO_2 combustor the usage of excess O_2 is not economical because it is supplied by the air separation unit (ASU) as shown in Fig. 1. Therefore, under lean operating conditions, the exhaust O_2 can be retained with the re-cycled CO_2 stream and the primary CH_4 stream is mixed with this oxygenated CO_2 stream before the primary zone. This strategy may also help to reduce the blowout and required residence time in the primary zone. In the introductory section, in Fig. 2, this strategy is shown as strategy-III.

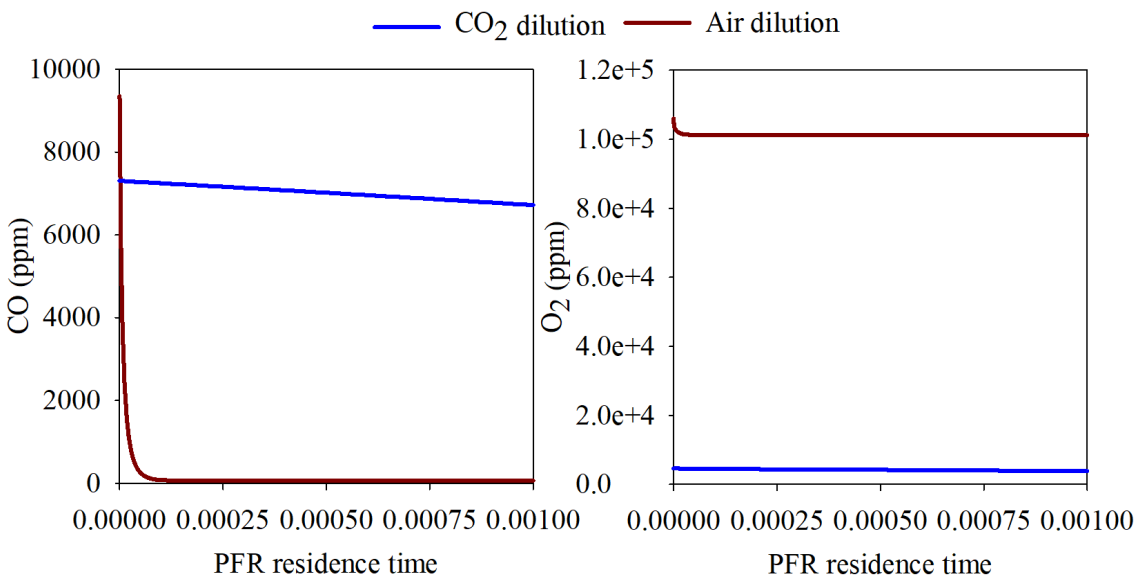

Figure 8: The comparison of levels of CO and O_2 in the PFR with respect to residence time (PSR inlet temperature is 1000 K)

Figure 9 shows the possible operation range of strategies II and III. The minimum amount of residence time (in the pre-mixing chamber) and ppm level of CO and O_2 impurities are needed to make the proposed strategies feasible. Here, the term "mixing chamber" is used, but it is assumed as instantaneous and adiabatic mixing. Therefore, the mixing phenomenon is not simulated. The strategies proposed in this paper are qualitative in nature and they are the guidelines to be considered for further detailed design simulations and experiments. The reactivity within the mixture is modeled as a PFR. Therefore, in reality, the required residence times needed would be more than what is calculated in this work.

The first and second rows in Fig. 9 corresponds to strategies II and III, respectively, as shown in Fig.2. The horizontal axis in each subplot in Fig. 9 corresponds to the residence time (shown up to 8 ms) in the mixing chamber. The vertical axis of each subplot corresponds to the level of the

impurity in ppm. Here, the impurities are chosen from 500 to 15000 ppm. Further, the total mass flow rate is kept constant in each case and the mixture temperature is held at 1000 K.

Here, the subplot (1,1) in Fig. 9 shows the CO mass fraction with respect to both CO level and residence time in the mixing chamber. It is corresponding to strategy-II. Interestingly, the CO mass fraction remains constant with respect to residence time. Also, there is no temperature rise in the mixing chamber irrespective of the CO level and residence time in the mixing chamber. Therefore, the overall results show that strategy-II is not productive to reduce the blowout and residence times in the primary zone of the sCO_2 combustion chamber.

The subplot (2,1) in Fig. 9 shows the CH_4 mass fraction variation with respect to both O_2 level and residence time in the mixing chamber. This plot shows that, approximately up to 6000 ppm of O_2 impurity level, the mass fraction of CH_4 remains constant irrespective of the residence time. Also, approximately up to four milliseconds of residence of time, the mass fraction of CH_4 remains constant irrespective of the O2 level in the re-cycled CO_2 stream. The subplot (2,2) in Fig. 9 shows that a temperature rise of 70 K can be achieved by using the strategy-III.

Overall, the results show that strategy-II is not productive to reduce the blowout and residence times in the primary zone of the sCO_2 combustion chamber. However, strategy-III could reduce PSR residence time required. Also, the disadvantage of strategy-III could be possible flash back. The investigations for calculating flash back for sCO_2 mixture are currently under progress.

.

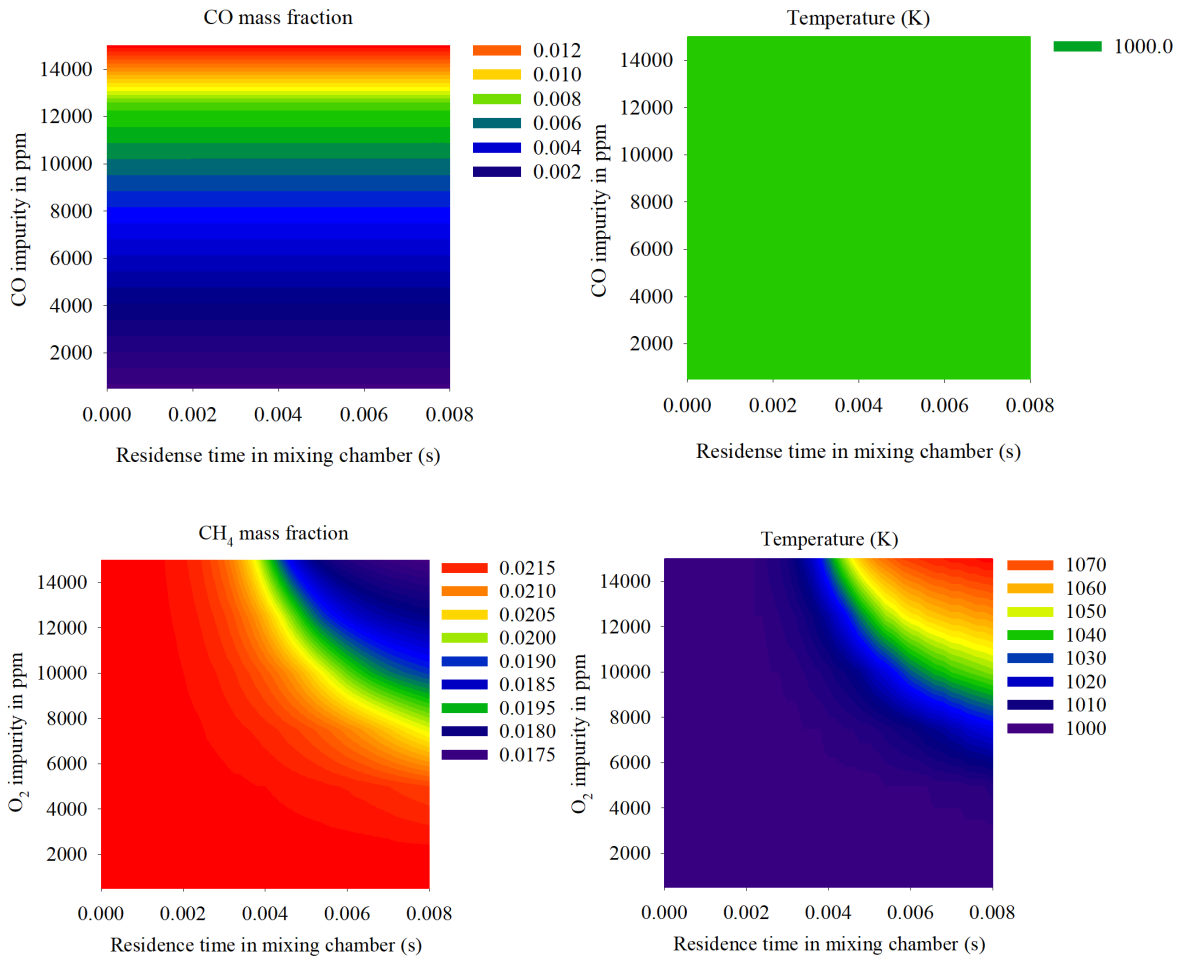

Figure 9: The effect of O_2 and CO impurities in the re-cycled sCO_2 stream when reacted in the mixing chamber (at 1000 K)

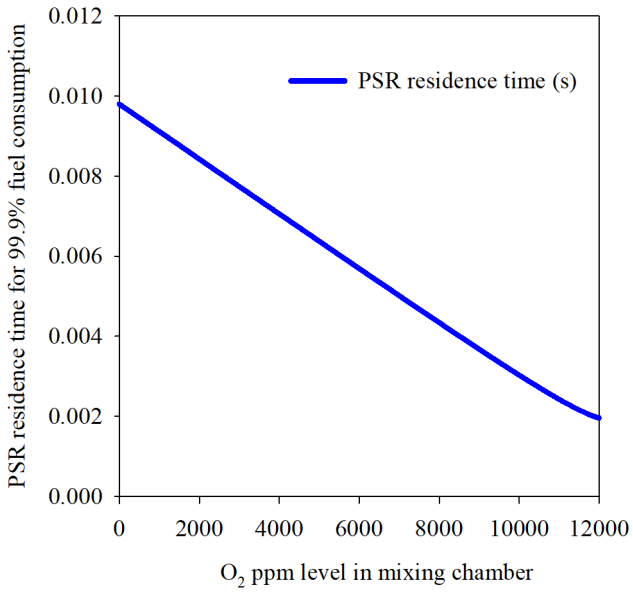

Figure 10: The reduction in PSR residence time requirement with respect to the O_2 level in mixing chamber.

THE ADVANTAGES OF STRATEGY-III

Figure 10 shows the reduction in PSR residence time requirement (the time required to consume 99.99% fuel in the primary zone) with respect to the O_2 level in mixing chamber. The results show that the PSR residence time required in the primary zone will reduce linearly with respect to the O_2 level in the mixing chamber.

Also, it is noticed that the resultant exit temperature of the sCO_2 combustor increases with strategy-III. This rise in temperature increases the turbine power for the same mass flow rate. Further, strategy-III could create a more uniform temperature profile near the injector.

Overall, strategy-III seems a very useful technique in sCO_2 combustor design to reduce the PSR residence time requirement and to utilize the excess oxygen in the re-cycled CO_2 stream. However, further investigations are required for estimating the flashback.

Some of the recently developed sCO_2 combustor designs have a combined stream of primary CO_2 and primary O_2 entering the combustion chamber. In that case, the strategy-III can be moved a step backwards, before the primary O_2 mixes with bulk CO_2 stream as shown in Fig. 11.

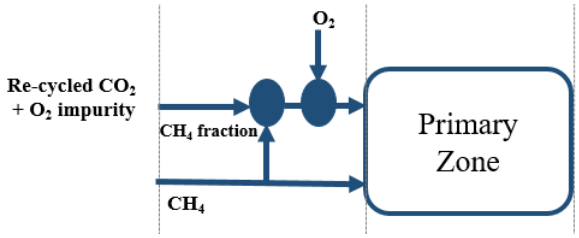

Figure 11: The reactant preparation strategy for some new designs of sCO_2 combustors.

CONCLUSIONS

The sCO_2 power cycle concept is identified as a possible efficient, economical, and pollutant free power generation technique for future power generation. Simulation tools play a major role in the development of this technology, because any experiments at supercritical pressures are expensive, time consuming and dangerous. The current work proposes lean combustion so that the excess O_2 in the exhaust stream can be used to reduce the chemical time of the sCO_2 mixture in the primary zone. Here, the sCO_2 combustor is modelled by coupling perfectly stirred rector (PSR) and plug flow reactor (PFR) models. The real gas effects are considered by using the Soave-Redlich-Kwong (SRK) equation of state. The detailed Aramco 2.0 mechanism is used for the combustion kinetics. Some important conclusions from the analysis are as follows.

1) The blowout and residence time required for a sCO_2 combustor are very high compared to an equal power air-breathing combustor. It is mainly due to the high specific heat of CO_2 which is leading to the low temperature combustion. Therefore, reduction of the required residence time is very crucial in sCO_2 combustion.

2) The CO level at the exit of the sCO_2 combustor primary zone is lower or in some cases equal to the CO level at the exit of the air-diluted combustor.
3) It is observed that, for air-diluted combustion, the CO production increases with an increase in the primary zone inlet temperature. However, in the case of a sCO_2 combustor, CO reduces. It is mainly because in sCO_2 combustion CO forming via the dissociation of CO_2 is very low. Here, CO is formed mainly as an intermediate product of CH_4 and CO_2. Therefore, for an sCO_2 combustor, as the inlet temperature increases the CH_4 mass fraction at the primary zone exit decreases and hence the CO is reduced.
4) O_2 follows the same trend as CO in the sCO_2 combustor primary zone with respect to the inlet temperature.
5) The combustion phenomenon in the dilution zone of sCO_2 combustor is much different from those of an air-dilution combustor. It is because air in the dilution zone contains O_2 which helps to drastically reduce the primary zone CO. Whereas, in a sCO_2 combustor dilution zone, a significant change to primary zone CO is not possible due to low temperature and due to the lack of reactive species. Therefore, a very high CO level can be expected at the exit of the sCO_2 combustor.
6) The lean operation of sCO_2 combustor is recommended in this work to reduce the CO emission levels in the combustor. Also, the excess O_2 in the re-cycled CO_2 stream can be mixed with CH_4 ahead of the primary zone. This mixing strategy reduces the residence time requirement of the sCO_2 combustor.
7) The mixing strategy mentioned above needs at least 5000 ppm of O_2 in the re-cycled CO_2 stream and the mixing residence time must be more than four milliseconds. It is also noticed that, this mixing strategy increases the exit temperature from the combustor.

APPENDIX 5 EFFECT OF IMPURITIES IN THE RE-CYCLED CO2 STREAM ON A SUPERCRITICAL CO2 COMBUSTOR

This work provides a short review of sCO_2 combustor design considerations and provides more insights into the effect of impurities in the re-cycled CO_2 stream of the sCO_2 combustor. Two main impurities studied here are, O_2 and H_2O. Incomplete combustion and inefficiency of water separation unit in the Allam cycle [15] may increase the probability of these impurities to re-enter into the combustion chamber.

In this work, Large-Eddy Simulations (LES) are also performed on a sCO_2 combustor by using Converge® CFD tool. Here, realgas corrections are accounted for with the Soave-Redlich-Kwong equation-of-state (SRK EOS) and kinetics are accounted for by an Aramco 2.0 derived 23-species mechanism. The results show that, when the O_2 and H_2O impurities are up to 5000 ppm, the near burner radial reaction zone increases in width. Further, the CO production/oxidation in the primary zone is significantly influenced by these impurities. Also, the CO distribution is observed to be higher at the core of the swirl in the primary zone due to impurities. Under the studied conditions, the H_2O impurity is delaying the CO oxidation. Hence, higher CO levels can be expected at the end of combustor if H_2O impurities are higher in the re-cycled CO_2 stream. However, O_2 impurities support the complete oxidation of CO hence a better thermal efficiency can be achieved.

INTRODUCTION

The supercritical CO_2 (sCO_2) power cycle is an emerging technology which has the potential to address both environmental concerns and energy demands. The well-known features of this power cycle are: 1) the high expected cycle efficiency compared to corresponding HE, AR and steam cycles, 2) compactness of the overall power plant, 3) complete capture of CO_2 and 4) the wide applicability over all power producing applications. This is a closed cycle and uses sCO_2 as

the working fluid, therefore, CO_2 produced by the direct-fired, oxy-methane combustion can be recirculated within the same cycle loop and the excess supercritical CO_2 from the cycle can be used for other commercial purposes [10]. However, current state-of-art peak operating pressures for sCO_2 combustion is approximately 300 atm [10] and the level of CO_2 dilution in the combustor is more than 95% percent by mass. Here, the presence of sCO_2 at 300 atm shows a different dilution effect on combustion phenomenon than N_2 (air-diluted combustion) due to significant differences in their thermo-chemical properties. Therefore, the mixing and reaction phenomenon, ignition and blowout phenomenon are expected to be considerably different in sCO_2 combustion than an air-diluted combustor. At these extreme pressure and dilution conditions, experiments and testing are expensive, time consuming, and dangerous. Also, during the initial development of a combustor, even finalizing the design based on 3-D simulations is a tedious task because a wide range of operating conditions or strategies needs to be tested. Therefore, initial domain of operating conditions or strategies can be minimized by accurate 0-D and 1-D simulations. Further, the detailed 3-D simulations and experiments can be carried based on the directions of the 0-D and 1-D analysis. As per the available literature, guidelines for designing and modeling sCO_2 combustors are minimal [24, 39, 320, 322, 323, 332-336] and still there is a need for testing a large number of combinations of initial operating conditions and design strategies before successfully constructing an efficient sCO_2 combustor.

The perfectly-stirred reactor (PSR) modeling was extensively used in the 1950s to guide the development of gas turbine combustors and ramjets [128, 324, 325]. Also, complete gas turbine combustor performance analysis was carried out by coupling plug-flow reactor (PFR) and PSR models [326-328]. This method is used in [239, 337] to provide crucial design considerations for sCO_2 combustor development. In these works, only a single PSR and PFR combination is used as

shown in Fig.1, because the main objective of those works is not to simulate a particular combustor but to reduce the initial domain of operating strategies. Therefore, the results shown in those papers are qualitative in nature. These works use the real gas version of CHEMKIN, i.e., CHEMKIN-RG [311] and coupled with CHEMKIN PSR and PFR codes [329, 330].

Also, some important requirements for sCO_2 combustors are as follows: 1) lower residence time/ smaller volume, 2) protection from impurities developed in the closed loop of the cycle, and 3) complete burning of fuel within the combustion chamber.

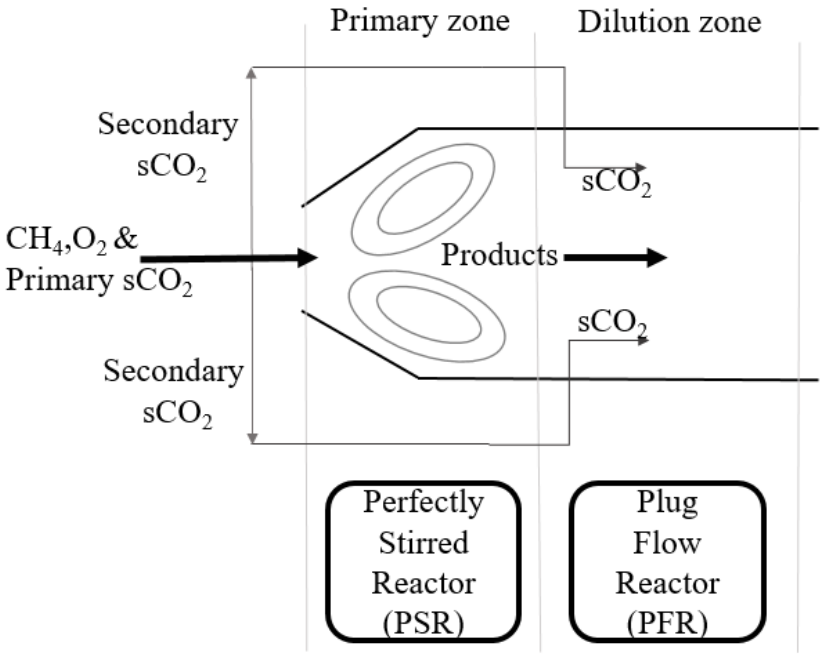

Figure 1: Modeling of sCO_2 combustor by PSR and PFR [239, 337]

The first requirement as mentioned earlier is essential from the design point of view because, the previous studies show that the sCO_2 turbine is fifty-times smaller than an equal power steam turbine, hence the combustor volume should be scaled down to an optimal level for proper alignment with the turbine. A combustion chamber primary zone volume can be reduced by having only pure oxy-methane combustion in the primary zone and by purging recycled CO_2 into the dilution zone. However, the study [239] shows that, operating the combustor without any CO_2

dilution in the primary zone is very dangerous at 300 bar pressure. On the other extreme, supplying 100% of re-cycled CO_2 into the primary zone is also not feasible because the amount of residence time required to oxidize 99.99% of the fuel is very large. Hence, the size requirement of the combustor will be large. An optimum CO_2 split between primary and dilution zones in sCO_2 combustors is 50-50% for reasonable size of the combustor and complete oxidation of CO.

The earlier works [239, 337] qualitatively show the possibility of high CO and O_2 traces for a smaller residence time combustor and recommends a novel idea of incorporating a pre-reaction chamber ahead of the combustion chamber in the sCO_2 Allam cycle as shown in the Fig. 2. This pre-reaction chamber is shown to reduce the sCO_2 combustion chamber required residence time for complete burning of fuel, however it should be noted that, a detailed cycle analysis is further needed for understanding the feasibility of using a pre-reaction chamber in Allam cycle.

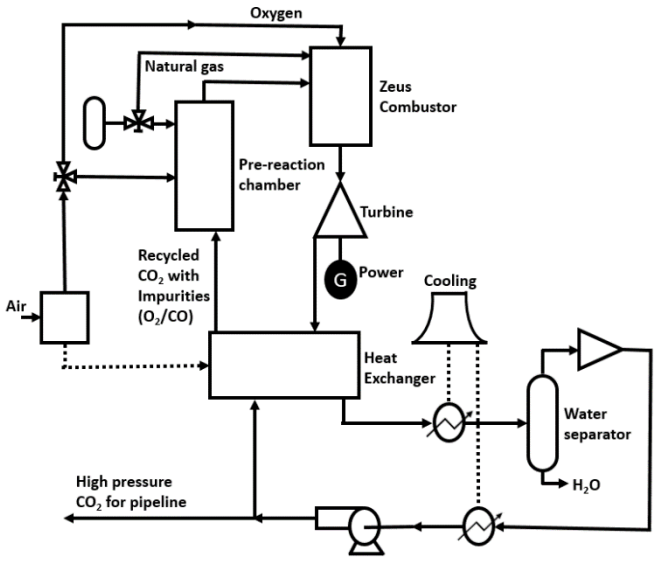

Figure 2: Allam cycle with pre-reaction chamber [337]

Also, another challenge in the sCO_2 combustor design is that the traces of CO, O_2 and H_2O may buildup over a period of closed loop operation and it may influence the combustion performance. The work of [26] showed that, impurities could significantly influence sCO_2 cycle performance. Hence, in this current work the effect of O_2 and H_2O in re-cycled CO_2 stream of Allam cycle on combustor performance is studied by using Large-eddy-simulations (LES). The LES simulations are performed by a commercial CFD tool called Converge®

MODELING

A recent sCO_2 combustor model [338] of Southwest Research Institute (SwRI), which is under development is used in these simulations as shown Fig.3 with a slight change in the dilution zone geometry. The inlet flow conditions to the combustor are reproduced from [339] and shown in Fig. 4. A detailed description of this combustor can be found in the work of [339].

Here, the oxidizer jet consists of O_2 and CO_2 and it mixes with pure a CH_4 jet inside a swirl injector in a crossflow configuration. The swirl angle of the injector is 40^o and the reacting jet which is coming out of the swirl injector mixes with fifty-percent of purging CO_2 in the primary zone. The remaining 50% of the CO_2 is distributed across the inlets of the dilution zone. Here, it should be noted that the design of the dilution zone shown in this work is different from the work of [339].

The detailed simulation parameters are listed in Table 1. Here, Large-eddy simulations are performed with the Viscous-One equation model which is developed by [340]. The Converge® CFD uses adaptive mesh refining (AMR) strategy hence the base cell size and AMR are used in order to have approximately six million cells in the combustor. Also, Soave-Redlich-Kwong equation of state is used in these simulations. Here, an Aramco 2.0 derived 23-species mechanism

[230] is used and all the species transport equations are solved by using SAGE detailed chemistry in which all species conservation equations are solved. Further, the viscosity and thermal conductivity are modeled by assuming that the working fluid is pure CO_2 and these transport property profiles are obtained from NIST-REFPROP. An important point to be noted here is that, the reactor residence time for this combustor is large i.e., approximately thirty milliseconds, hence the simulation is continued until six flow-through times (180 milliseconds). A statistically stationary solution is observed after 90 milliseconds, but the data presented in this work are obtained at a sufficiently large simulation time (after 140 milliseconds) for better confidence.

Three cases as shown in Table 2 are simulated to investigate the effect of impurity in the re-cycled sCO_2 stream on the combustor performance. It must be noted that, the influence of CO impurity is not studied in this work because as a design requirement the CO must be burnt within the combustion chamber, hence no CO is considered in the re-cycled CO_2 stream. It should also be noted that the total flow rate is kept constant in each case.

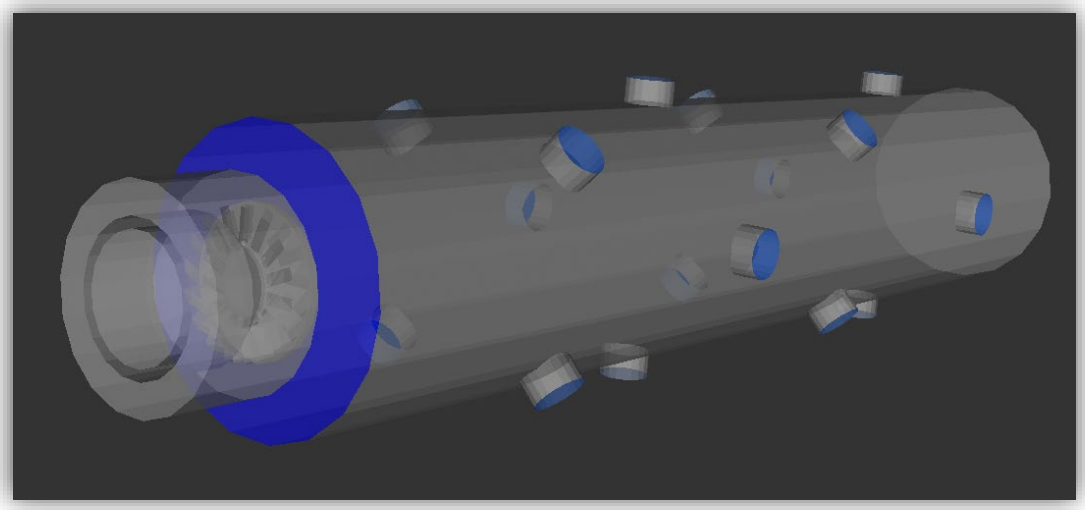

Figure 3: A three-dimensional view of recent SwRI sCO_2 combustor [338, 339]. (blue colored boundaries indicate the inlets of re-cycled CO_2 stream for dilution)

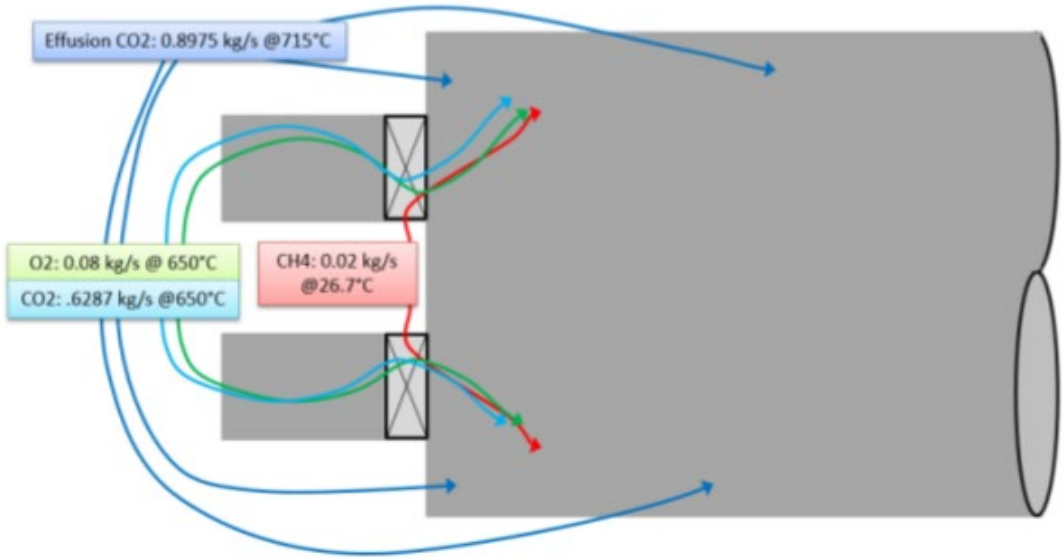

Figure 4: Inlet flow conditions to the combustion chamber; reproduced from [339]

Table 1: Simulation parameters used in this study

S. No	Modeling	Parameter /model chosen
1)	Turbulence modeling	Large-eddy simulation → Viscous One Equation. This model uses sub-grid kinetic energy in modeling the turbulent viscosity [340].
2)	Wall heat transfer modeling	O'Rourke and Amsden [341]
3)	Combustion modeling	SAGE detailed chemistry (all species transport equations are solved).
4)	Number of cells	Approximately six million cells (Adaptive mesh refinement is used)

5)	Equation of state	Soave-Redlich-Kwong equation of state based on [39]
6)	Viscosity and Thermal conductivity	Pure CO_2 properties between 800 -1600 K from REFPROP [342] are used.
7)	Chemical kinetic mechanism	A 23-species mechanism derived from Aramco 2.0 [230]
8)	Simulation time	6 follow-through times

RESULTS AND DISCUSSION

As discussed in the introduction purifying the exhaust products of the combustion to obtain 100% pure re-cycled CO_2 stream is expensive. In fact, the separation of the final traces of impurities would be costlier. Therefore, the operation cost of exhaust separation can be reduced if the combustor is designed to perform under some optimum levels of impurities. The major impurities in the exhaust stream could be CO, O_2 and H_2O. In the Allam cycle, H_2O can be separated by condensing the exhaust products, but the separation of CO and O_2 from the products is difficult. Therefore, it is recommended to design the combustion chamber in order to have either CO or O_2 [337] at the exit. As observed from the work [239], for smaller reactor residence time combustors, most of the fuel can remain in the form of unburnt CO. Also, CO does not react in the

dilution zone due to the unavailability of O_2 (If re-cycled CO_2 is pure). Therefore, an optimal lean operation is necessary for sCO_2 the combustor to burn all of the CO. Now, in such cases of lean operation the major exhaust products would be CO_2, O_2 and H_2O. Therefore, three cases as shown in Table 2 are considered in the current work to understand the influence of impurities. Also, as mentioned in the modeling section, the total flow rate of the re-cycled stream is kept constant in all three cases. Here, Case-1 contains pure re-cycled CO_2 without any impurities, Case-2 has 5000 ppm of O_2 and Case-3 has 5000 ppm of H_2O in the re-cycled CO_2 stream.

Table 3 shows a comparison of time averaged temperature profiles from the LES simulation for the three cases considered. Here, there is a difference in the near burner temperature distribution in the radial direction. Radial width of temperature is smaller for Case-1 compared to Cases-2 and 3. This change is basically due to changes in the reaction zone. In Cases-2 and 3, the O_2 and H_2O present in CO_2 stream is reacting with the combustion products and increases in the reaction zone are observed.

Further, Table 4 shows the time averaged mass fraction of CO for the three cases considered. Here, it is evident that the CO in the primary zone is higher in Cases 2 and 3 compared to Case-1. Also, a high CO concentration region can be observed symmetrical to the axis in all the cases. These high CO concentration zones are formed just after the first set of radial dilution holes as seen in Fig. 5. Here, the low temperature CO_2 which is coming from the dilution holes is quenching the reaction zone products temperature and delaying the CO oxidation. It should be noted that, CO concentration just after first set of dilution holes is higher in Case-3 of Table 4 and lower for Case-2. It is because H_2O present in the CO2 is retarding the CO oxidation in Case-3 and accelerating CO oxidation in Case-2.

Table 2: Various cases considered in this study

Cases investigated in this study	What does the case represent?
Case-1	The recycled stream consists of pure CO_2.
Case-2	The recycled CO_2 stream consists of O_2 impurity by 5000 ppm
Case-3	The recycled CO_2 stream consists of H_2O impurity by 5000 ppm

Table 5 shows the spatial mean values of CO, O_2, CH_4 and temperature at the exit of the combustor. Here, the inlet CH_4 flow rate is the same for all three cases and we can see that all three cases show that the CH_4 is fully oxidized before the exit. However, the CO levels are significantly different. The CO is highest for Case-3 and lowest for Case-2. Which signifies the need of better CO oxidation strategies when we cannot separate H_2O in the water separation unit of the Allam cycle. Also, it is interesting to note that the exit temperature of Case-3 is increased slightly even though there is a plenty of CO remains at the exit. Further Case-2 shows that almost 2000 ppm of O_2 is left at the combustor exit when there is O_2 impurity in the re-cycled CO_2 stream and this case has the least CO and highest temperature. Therefore, these show that the lean operation is the best strategy to achieve a better thermal efficiency. As per current state-of-art, operating air-separation units is costlier in the Allam cycle and hence the lean operation is less acceptable. Therefore, further cycle analysis is required in this direction.

Table 3: The comparison of combustor mid-section temperature contours

Case	Contours of Temperature
1	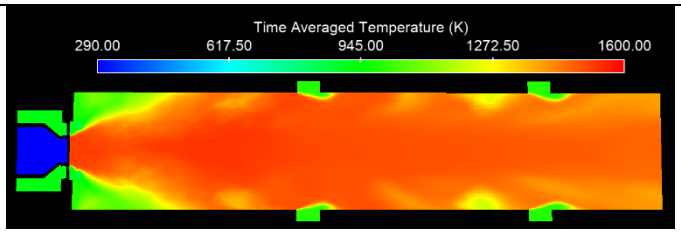
2	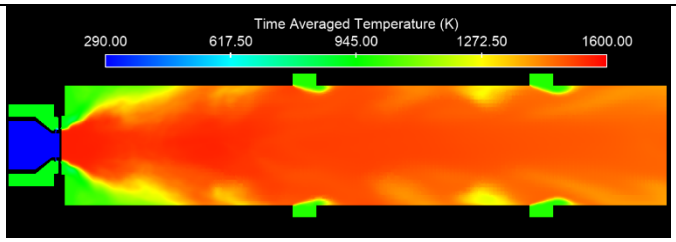
3	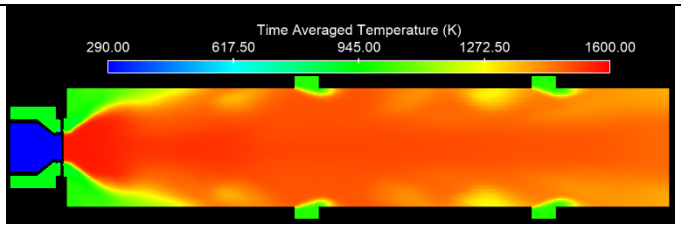

. Table 4: The comparison of combustor mid-section CO contours

Case	Contours of CO Mass Fraction
1	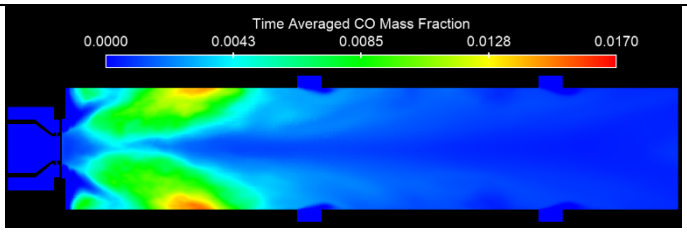

2	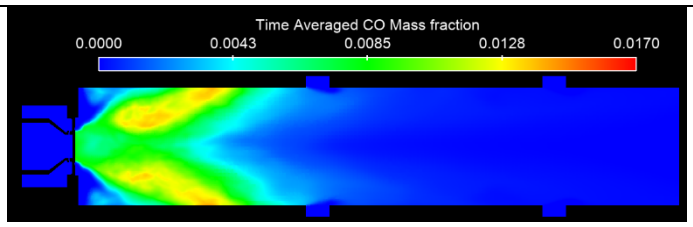
3	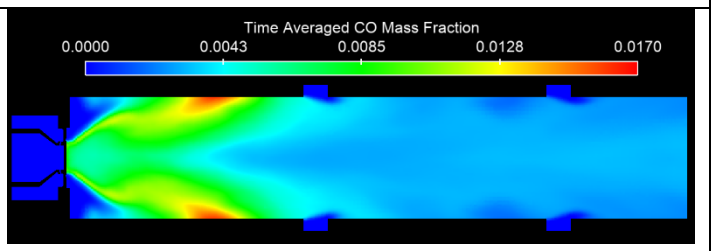

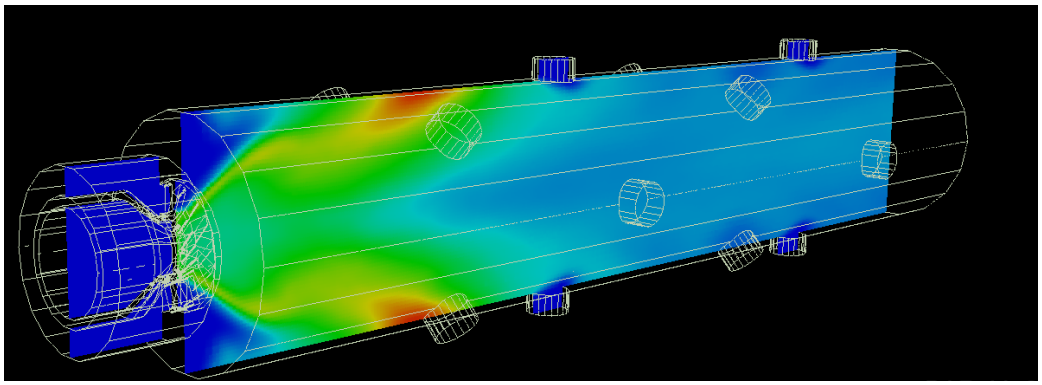

Figure 5: A 3D view of CO mass fraction distribution on the cross-section plane.

Table 5: The spatial, time averaged mean values CO, O_2, CH_4 and temperature at the exit plane of the combustor

	CO (ppm)	O2 (ppm)	CH4 (ppm)	Temperature (K)
Case1	1194	351	0	1402.3
Case2	185	2000	0	1415.9
Case3	1782	248	0	1408.4

CONCLUSIONS

In the current work, recent zero and one-dimensional design investigations for sCO_2 combustion are reviewed and large-eddy simulations are performed using the Converge® CFD tool to investigate the effect of impurities such as O_2 and H_2O in the re-cycled CO_2 stream on the combustor performance. The conclusions are as follows:

1) Presence of H_2O in the re-cycled CO_2 stream retards CO oxidation, hence higher CO concentrations can be expected at the exit of the sCO_2 combustor.

2) Presence of O_2 in the re-cycled CO_2 stream improves CO oxidation, hence CO can be burnt completely within the combustion chamber.

3) O_2 impurities also improve the thermal efficiency in the sCO_2 combustor.

APPENDIX 6 The Effects of Pressure and Dilution on Turbulence-Chemistry Interaction inside sCO2 Combustor

The sCO_2 power cycle technology addresses the global concerns like growing energy demand and environmental pollution. The main features of this cycle are, high efficiency, compact foot print and carbon capture. Moreover, this concept of the sCO2 power cycle is applicable in almost all the existing power producing technologies. However, the significant research towards developing a supercritical gas-turbine power plant is started after the extensive study on supercritical CO_2 (sCO_2) power cycle concept by Dostal, et al. [1]. The direct-fired sCO_2 cycle is one such conceptual power producing technology where the maximum operating pressures are as high as 300 atm and CO_2 dilution level is as high as 95% by mass. This pressure is approximately four times higher than the critical pressure of CO_2. At these pressures, the experimentation is very expensive, dangerous and time consuming. Therefore, simulation play a major role in the initial development of sCO_2 combustors. Currently, very few research groups have directed their focus on the simulation of sCO_2 combustion phenomenon. Therefore, some fundamental investigations to understand the behavior of sCO_2 combustion would help in the analysis of the future simulation results. Thus, in the current literature the effect of pressure and dilution on the turbulence-chemistry interaction has been studied by using an inhouse premixed conditional moment closure (PCMC) code [2]. The earlier studies [3] have shown that at lower turbulent dissipation values the reaction chooses complex paths. However, the effect of pressure and dilution is not quantified, hence studied in the current work for a typical sCO_2 mixture condition. Here a comparison is made between atmospheric air combustion and a highly diluted supercritical N_2 (sN_2) and CO_2 (sCO_2) diluted, constant pressure combustion. The Soave-Redlich-Kwong (SRK) EOS which is considered as most accurate for sCO_2 combustion [4] is included in PCMC code through

CHEMKIN-Real gas [5]. It should be noted that, the chemical kinetic mechanism is critical for the accurate combustion simulations. The recent studies [6-8] have shown that the Aramco 2.0 mechanism [9] is better suitable for sCO_2 combustion simulations. Therefore, Aramco 2.0 mechanism is used in this study for accounting the chemistry.

MODELING

The PCMC model as shown in Eq.1, is a premixed turbulent combustion model which conditions the species mass fractions on the reaction progress variable (RPV) and closes the chemical source terms in the enthalpy equation with conditioned reaction rates. In other words, the PCMC can estimate all the species mass fractions involved in combustion as the reaction progresses from unburnt to fully-burnt conditions, at various turbulence levels by solving the second order PCMC ordinary differential equation for each species with a two-point boundary value problem solver.

The PCMC equation: $\langle \bar{\rho} N|\zeta\rangle \tilde{Q}_i'' - \langle \bar{\rho}\tilde{S}_c|\zeta\rangle \tilde{Q}_i' + \langle \bar{\rho}\dot{\tilde{\omega}}_i|\zeta\rangle = 0$ (Eq.1)

Here, $\bar{\rho}$ is the density, $N|\zeta$ is the conditioned scalar dissipation (level of small scale turbulence), $\tilde{S}_c|\zeta$ is the conditioned source term for the RPV Eqn., $\dot{\tilde{\omega}}_i|\zeta$ is the conditioned reaction rate and $\tilde{Q}_i$ are the conditioned mass fractions and the derivatives are with respect to the RPV.

Four different cases are considered in this section as shown in Table 1. The first case is the atmospheric combustion in air dilution. For the remaining cases, the molar ratios are chosen in such a way that the initial mass fractions of the CH_4, O_2 and the diluent are same. The case two has additional N_2 compared to case one. Also, the operating pressure of case three and four are 300 times more than the operating pressure of the case two. Further, in case four, the sN2 is replaced by sCO_2 in such a way that their corresponding mass fractions are same. The case three and four are solved by using Soave-Redlich-Kwong EOS.

S. No	Case	Operating conditions	EOS	Equilibrium Temperature (K)
1	Air dilution	Inlet $CH_4/O_2/N_2$ moles =1/2/7.52; Tin = 1000 K; Pin = 1 atm	Ideal Gas	2550
2	N_2 dilution	Inlet $CH_4/O_2/N_2$ moles =1/2/42; Tin = 1000 K; Pin = 1 atm	Ideal Gas	1511
3	sN_2 dilution	Inlet $CH_4/O_2/N_2$ moles =1/2/42; Tin = 1000 K; Pin = 300 atm	SRK	1531
4	sCO_2 dilution	Inlet $CH_4/O_2/CO_2$ moles =1/2/26; Tin = 1000 K; Pin = 300 atm	SRK	1500

RESULTS AND DISCUSSION

The work [2, 10] shows the need of considering the turbulence effects while reducing a detailed chemical mechanism. According to [2, 10], the reaction pathways at smaller turbulence levels are significantly different from the reaction pathways at larger turbulent levels, therefore these influences must be accounted while eliminating the species and reactions from larger chemical mechanisms. This section discusses the effect of turbulence level on the highly diluted, high pressure methane combustion. In the current section, two extreme turbulent dissipation values such as N=200,000 and 0.05 are chosen for each case of interest.

Figure 1 shows the mass fractions of species CO, OH, HCO, H, and CH_4 for the four cases of interest. The first four species are the important radicals in the prominent CO reactions as discussed in [11]. Each column in Fig. 1 is corresponding to a particular case as listed in Table 1. Also, each plot has corresponding mass fraction variation of a species at two extreme turbulent dissipation values. The case one, i.e. the air dilution case is having higher initial mass fractions of CH_4 and O_2 dilutions and lesser N_2 dilution compared to other cases. Therefore, the final temperatures after complete combustion is higher in the first case i.e. 2550 K. Though the initial mass fractions for remaining three cases are same, the third case which is having sCO_2 as a diluent is having the lowest equilibrium temperature i.e. 1500 K due to the higher specific heat of CO_2. Basically, the last three cases are representing a highly diluted, low-temperature combustion.

The subplot (1,1) in Fig. 1 shows the variation of the mass fraction of CO for case one and here the average percentage deviation of CO mass fraction between the two considered turbulent dissipation values is ~260 %. However, in the subplot (1,2) in Fig. 1, the corresponding average percentage deviation of CO mass fraction is about ~1150 %. Though the deviation in CO mass fraction is high by its percentage the absolute values of the CO mass fraction is small compared to other cases. A careful observation of all the plots in column two of Fig. 1 shows that the all the radicals produced in highly N_2 diluted combustion, at lower turbulent dissipation values are very small by magnitude and they do not have any impact on the CH_4 disintegration as it can be seen from subplot (4,2) in Fig. 1. Therefore, the turbulence effects are very small in highly diluted, atmospheric combustion. However, when it comes to the third case i.e. sN2 dilution at 300 atm the percentage deviation of CO mass fraction between the turbulent dissipation values is ~338500%. The similar magnitude of deviation can be observed in the fourth case (sCO_2 dilution) also. Though the absolute mass fractions of the radicals are smaller compared to air diluent combustion, these

mass fractions have a significant effect on the CH_4 consumption at lower turbulent dissipation values and it is evident from the subplots (4,3) and (4,4) of Fig. 1. It essentially shows the need of considering turbulence effects in reducing a mechanism for high-diluent, supercritical combustion applications. Another important observation from the sub plot (1,3) and subplot (1,2) of Fig. 1 is that the peak CO mass fraction is higher in the case of sN_2 dilution compared to N_2 dilution, which shows that the pressure is the main parameter which helps in radical production in highly diluted combustion. Also, the subplot (1,3) and (1,4) in Fig. 1 shows that there is no significant difference between sN_2 and sCO_2. Also, another interesting observation is that the mass fractions of CO in sCO_2 combustion are much lesser in atmospheric combustion, the main reasons is that the sCO_2 combustion is a low-temperature combustion, therefore the dissociation effect on CO_2 is lesser.

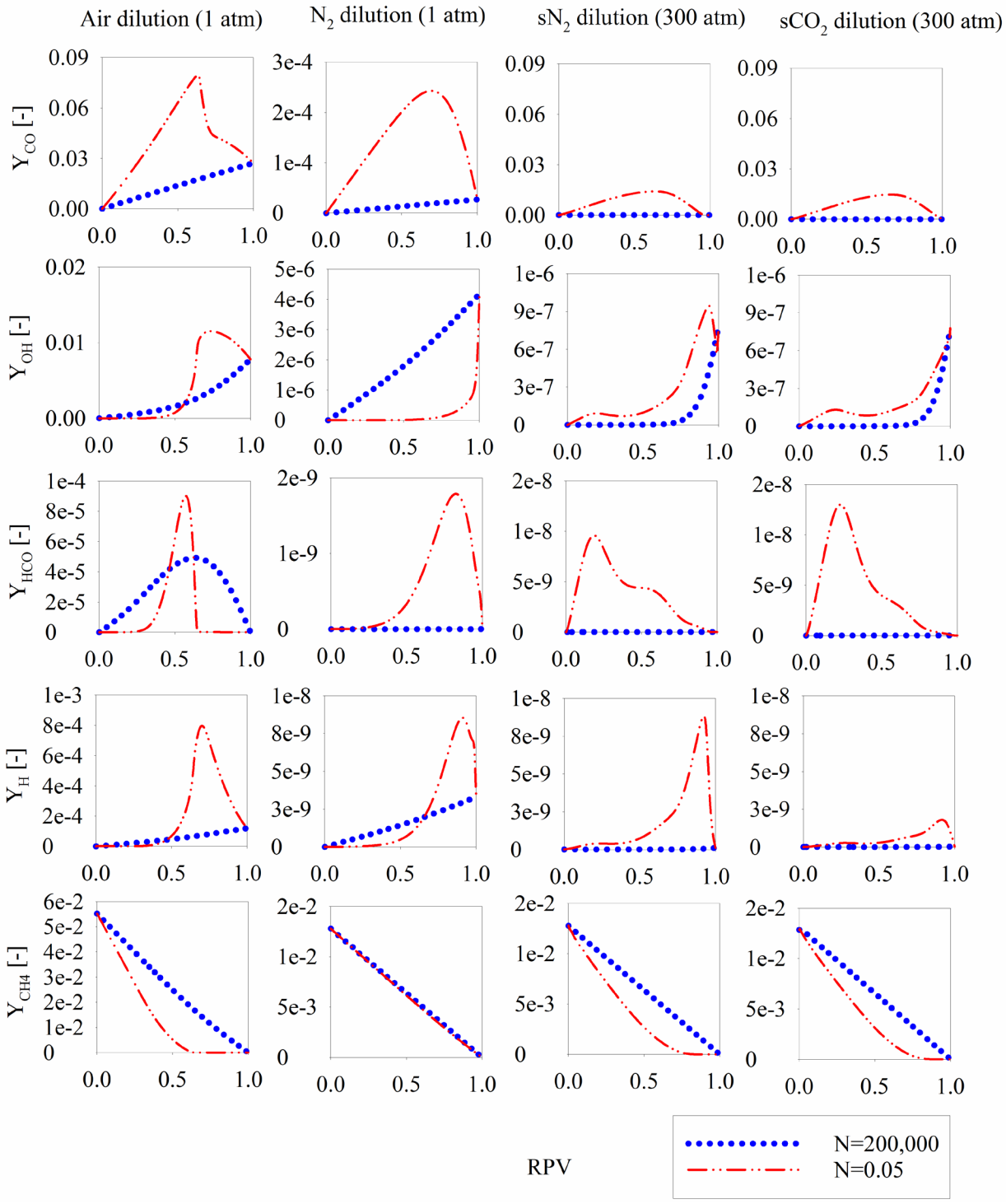

Figure 1: The effect of turbulence dissipation on the highly diluent, high-pressure combustion

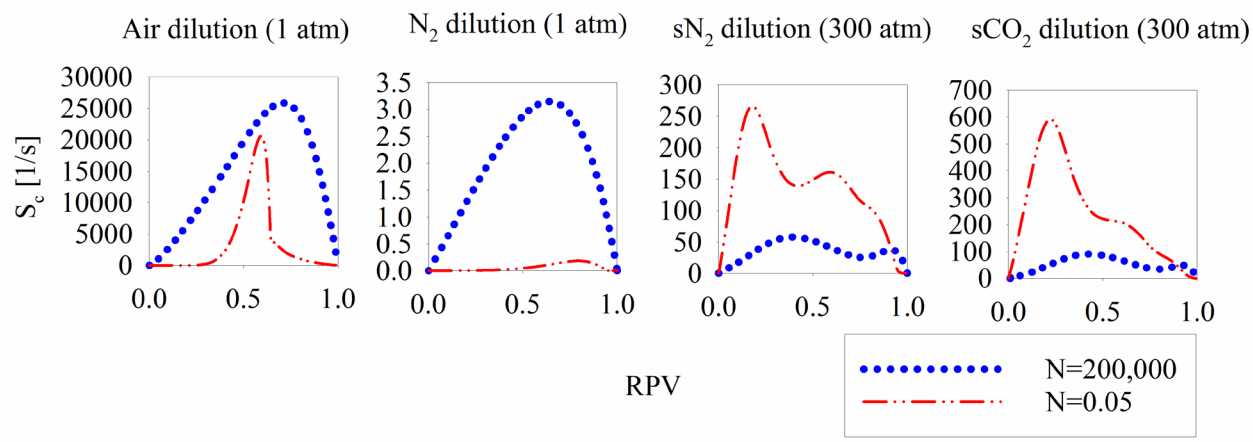

Figure 2: The source term (S_c) in highly diluent, high-pressure combustion

Figure 2 shows the variation of the conditional source term Sc in PCMC equation, in a highly diluent, high-pressure combustion. According to Martin, et al. [12], at atmospheric pressures, initially, the peak value of S_c increases with decrease in turbulent dissipation value and after a certain turbulent dissipation it decreases with further decrease in turbulent dissipation. Moreover, at very small turbulent dissipation values it remains constant. The subplot (1,1) and (1,2) of Fig. 2 shows the same phenomenon as observed in previous literature. However, for high pressure cases i.e. for subplots (1,3) and (1,4) of Fig. 2 shows that, up to N=0.05 the S_c is observed to be increasing. Also, the maximum S_c for atmospheric combustion is reported to occur after RPV is equal to 0.5 and the same observation can be re-confirmed from the subplots (1,1) and (1,2) of Fig. 2. However, interestingly, for supercritical combustion the peak is towards the left which signifies that the maximum energy release occurs before RPV value of 0.5.

CONCLUSIONS

A comparison is made between turbulence-chemistry interactions of atmospheric air diluted combustion with respect to highly diluted, supercritical N_2 and CO_2 diluted, constant pressure combustion by using an inhouse premixed conditional moment closure method. The important conclusions are listed as follows.

Lower turbulent dissipation has almost same influence as larger turbulent dissipation on CH_4 consumption for a high N_2 diluted, atmospheric combustion. However, at supercritical pressures both the levels of turbulent dissipation have a distinctive and significant effect on CH_4 consumption throughout the reaction progress. It is mainly due to the high intermediate CO which is formed because of supercritical pressure.

The influence of turbulent dissipation on methane consumption is almost same on sN_2 and sCO_2 diluted combustion phenomenon.

The rate of energy release in sCO_2 diluted combustion is twice as that of sN_2 diluted combustion.

Further, the source term (S_c) has small magnitudes in supercritical combustion. Hence, the energy release rate is very small compared to atmospheric air-combustion.

APPENDIX 7 GLOBAL MECHANISM FOR OXY-METHANE COMBUSTION IN A CO2 ENVIRONMENT

There has been some recent work on the global kinetic modeling of flames in oxy-fuel combustion for methane. The main challenge is that none of the mechanisms were developed to understand the time-scales of ignition. Here, a 3-step mechanism was developed for methane combustion in oxy-fuel environment. The mechanisms were simulated using a closed batch homogeneous batch reactor with constant pressure and compared to baseline simulations performed using a detailed mechanism. All simulations were performed for methane used a mixture of $X_{CH4} = 0.05$, $X_{O2} = 0.10$ and $X_{CO2} = 0.85$. Mechanisms were altered using the global mechanism equilibrium approach to ensure that the steady-state values matched the reference values and were further altered using an optimization scheme to match experimental data that was taken in a shock tube. Simulation results of methane, CO time-histories, and temperature profiles from the global mechanism were compared to those from the detailed mechanism. Ignition delay times were used to represent the time-scales of combustion. This was defined for current simulations as the time required for methane concentration to reach 5% of its initial value during combustion. Using this approach, the 3-step methane combustion mechanism showed excellent improvement in the ignition timing over a range of pressures (1 to 10 bar) and initial temperatures (1500 to 2000 K) for both lean and stoichiometric mixtures but fails to predict ignition delay times at 30 bar or the ignition delay times of fuel rich mixtures. Ongoing effort focuses on extending this new global mechanism to higher pressures and to syngas mixtures.

Nomenclature

CFD	Computational Fluid Dynamics

X_{CH4}	CH_4 mole fraction
T	Temperature
P	Pressure
ϕ	Equivalence Ratio

Introduction

Accurate mechanisms are crucial for the development of future combustor and turbine designs. New techniques in manufacturing and improvements in numerical techniques have opened the door for complex designs in the combustor. This leads to a feedback loop as more analysis and simulations are needed for design and verification of these designs. Computational time and costs increase with the size of the mechanism, and therefore a reduced mechanism is necessary for CFD simulations [39, 343]. This paper focuses on the development of a global mechanism that captures the most important species in oxy-fuel combustion that can be utilized in CFD simulations with complex geometries.

There are several mechanisms that exist in the literature for methane combustion that have been developed over the years. Jones and Lundstedt developed a four-step mechanism that included two fuel breakdown reactions and then included hydrogen oxidation and the water-gas shift reaction [344]. A second mechanism was created by Westbrook and Dryer that was most recently updated in 2007 combining fuel breakdown with the oxidation of carbon monoxide [345]. The problem was that as novel concepts to improve the efficiency and reduce the emissions are conceived, the two mechanisms start to leave the narrow range of conditions that the mechanisms were designed for. Neither mechanism could match the CO-CO_2 interactions that had been shown to be have important effects when CO_2 was used as the diluent compared to air [41, 93, 346-350].

In the last 10 years, these global mechanisms have been modified as oxy-fuel has become an increasingly important topic. Andersen et al. developed two mechanisms based on each of the mechanisms above and modified the reaction rates to predict oxy-fuel combustion in an isothermal plug flow reactor [351]. The mechanisms kept the initiation reactions from the original mixtures and modified the other steps to match the time-histories of major species. Improvements to the CO-CO_2 reaction subsets allowed for major improvements in the performance for oxy-fuel conditions. The problem is that the mechanisms were not able to match the combustion time-scales that are seen in larger detailed mechanisms.

The new mechanism developed in this paper examines matching ignition delay time measurements while maintaining the improvements that Andersen et al. showed with the modified Westbrook and Dryer mechanism for the key species time-histories. The mechanism was also compared to data taken from the literature to understand the extent of conditions that the modified mechanism can accurately model the oxy-fuel combustion.

Theory and Mechanism Development

Modifications to the 3-step mechanism from Andersen et al. were taken to improve the combustion time-scales while maintaining the emissions improvements found in the original version. The modifications were performed on all three reactions on the pre-exponential factor, the activation energy and the reaction orders using a closed-homogeneous reactor with constant-pressure. The time-scales were based on ignition delay times. The mechanism was compared to the Westbrook and Dryer mechanism, the modified mechanism from Andersen et al. and the detailed Aramco 2.0 mechanism which contains 493 species and 2716 reactions [345, 351, 352]. The simulations were compared to data taken from Pryor et al. [353]. The modifications to the 3-step mechanism are shown in Table 1.

Simulations were performed using Chemkin Pro [354] software. All ignition delay times for comparison were measured in UCF's shock tube. The shock tube was modeled using a constant-pressure reactor and the energy equation was solved. The initial temperature range for these simulations was 1000 – 2000 K. The mixture used for the development of the mechanism was kept constant at $X_{CH4} = 0.05$, $X_{O2} = 0.10$, $X_{CO2} = 0.85$. All five species (CH_4, O_2, CO, H_2O, CO_2) and temperature profiles were monitored during the simulations.

Typically, the ignition delay time is taken from an emissions profile for both experiments and the simulations. The ignition delay times for these simulations are taken from the methane time-histories of the experiments. Because the global mechanism does not include any radical species in the mechanism, a new definition for the ignition delay time has been created for this work. The ignition delay time was defined for all simulations as the time difference between the start of the simulation and the time when methane concentration reaches 5% of its initial value. Methane decay has been shown in Koroglu et al. to be a good approximation of the ignition delay times [355]. As a result, the methane profile was also included as a parameter for global mechanism improvements.

The original modified mechanism used by Andersen et al. employed an equilibrium approach to match the global mechanism constants to the stoichiometric constants. The mechanism created by Andersen et al. left the initiation reaction untouched from the values that were calculated from Westbrook and Dryer and focused on the CO-CO_2 subset. The problem is that ignition delay times

Table 23. Modifications to the Andersen et al. mechanism

	Reactions	A	β	E	Reaction Orders
1	$CH_4 + 1.5O_2 \Rightarrow CO + 2H_2O$	5.0×10^9	0.0	56.0×10^3	$[CH_4]^{0.4}\,[O_2]^{0.6}$
2	$CO + 0.5O_2 \Rightarrow CO_2$	4.0×10^8	0.0	10.0×10^3	$[CO]^{1.2}\,[O_2]^{0.25}\,[H_2O]^{0.5}\,[CO_2]^{-0.2}$
3	$CO_2 \Rightarrow CO + 0.5O_2$	6.0×10^8	-0.97	66.5×10^3	$[CO_2]^{0.8}\,[H_2O]^{0.5}\,[O2]^{-0.2}\,[CO]^{-0.3}$

are relatively insensitive to CO-CO_2 subset, being dominated by the first reaction. As such the initiation reaction was modified to more accurately model the system. The mechanism developed in this work was based on the methods outlined in Andersen et al. for developing a global mechanism for oxy-fuel conditions [351].

The accuracy of global mechanisms suffers as a result in the minimum number of species that are used in the model. This results in the breakdown in the fundamental thermodynamics that define the chemical kinetics field. This also allows for modifications to be made not only to the pre-exponential factor and the activation energy but also the reaction orders that are typically calculated internally in a detailed mechanism. The reaction orders were both reduced in order to ensure that the methane time profile matched the profile from the Aramco 2.0 mechanism which has been confirmed in the Koroglu et al. [355]. Figure 1 shows a comparison of the methane time-histories with the time-normalized to the ignition delay times for a temperature of 1500 K. Similar profiles are seen at other temperatures.

The issue that was created by altering the initiation reaction was that the peak CO level becomes much lower than the level compared to the detailed mechanism. The activation energies and the pre-exponential factors were altered as a result. The reaction orders were also edited to match the profile shapes of the major species time-histories. The addition of CO_2 and CO as negative reaction orders in the forward and reverse CO oxidation reaction allowed for a high peak CO level while maintaining the carbon monoxide steady-state level and matching the max temperature during the simulation.

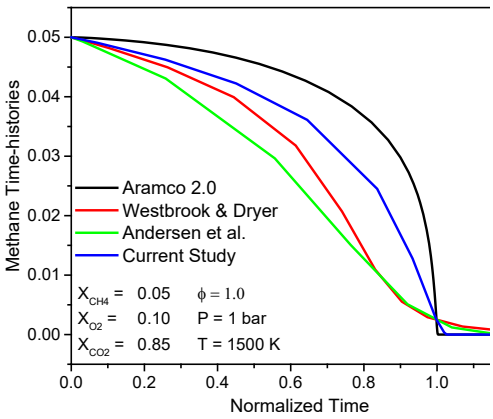

Figure 119. Comparison of the methane time-histories between different mechanisms at 1500 K. Time was normalized based on the ignition delay time for each mixture. The ignition delay times were defined as the time to reach 5% of the initial value of methane.

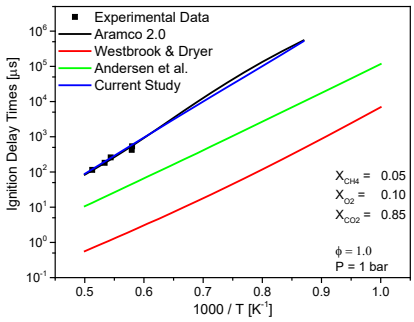

Figure 120. Ignition delay times for oxy-methane combustion using four different mechanisms. The experimental data was taken from Pryor et al [353]. Pressure for all simulations was kept at 1 bar. Mixture Composition: $X_{CH4} = 0.05$, $X_{O2} = 0.10$, $X_{CO2} = 0.85$.

Results and Discussion

Results from Mechanism Development

The mechanism was compared to experimental data that was taken from Pryor et al. [353].The ignition delay times are much better modeled with the improved oxy-methane global mechanism compared to the previous state-of-the-art. Figure 2 shows the ignition delay times using the modifications to the reactions compared to the original Westbrook and Dryer mechanism and the modifications undertaken by Andersen et al. The different mechanisms are also compared to data taken from Pryor et al. that shows the Aramco 2.0 mechanism does a good job predicting the

ignition delay times [353]. By editing the pre-exponential factor and the activation energy of Reaction 1, both the ignition delay times and the slope of the curve could be matched to the detailed mechanism and experimental data that has been taken for this mixture. The new mechanism is unable to match the curve that occurs at the low temperatures of the detailed mechanism but there is no data that has been taken in this area to verify that this curvature is real.

The CH_4, CO, H_2O time-histories as well as temperature profiles were all considered during the development of the new mechanism. Three different temperatures were considered during this system at 1200 and 1800 K to represent the full range simulations.

CO concentration was an important species to monitor during the mechanism development. CO is the only intermediate and is a regulated species for power generation. Both the peak CO concentration and the steady-state CO level after ignition were considered during the development. Figure 3 shows the CO concentrations during the simulations at the 1200 K (Left) and 1800 K (Right). The mechanism is not able to match the peak level of CO during the simulations compared to the Aramco 2.0 mechanism. By altering the first reaction and the ignition delay times, the peak CO remained at a lower level than is expected by the detailed mechanism. The trends that are present in the Aramco 2.0 mechanism are maintained by the mechanism and the CO steady-state value is modeled relatively well at all conditions. The Andersen et al. mechanism did an excellent job of matching the steady-state value and was an important parameter shown in the paper but some accuracy in the level was sacrificed in this paper to match the time-scales that are shown by the Aramco 2.0 mechanism.

The final two parameters that were considered during the simulations were the water time-histories and the temperature profiles. Both values were considered to ensure that there was little deviation from the desired trends in the Aramco 2.0 mechanism so that the mechanism could be as robust

and accurate as possible. The maximum water concentration was already well modeled by both the Andersen et al. and Westbrook and Dryer mechanisms. During the development of the mechanism in this study, the water concentration did not undergo major changes and is still accurate throughout the simulations performed. Temperature profiles are shown at two different temperatures in Figure 4. The temperature profiles new mechanism can accurately measure the temperatures during the simulations at the lower temperatures but slightly over predicts the max temperature compared to the Aramco 2.0 and Andersen et al. mechanisms. The temperature profile of a decrease in the rate of the temperature rising was unable to be accurately simulated by any of the global mechanisms.

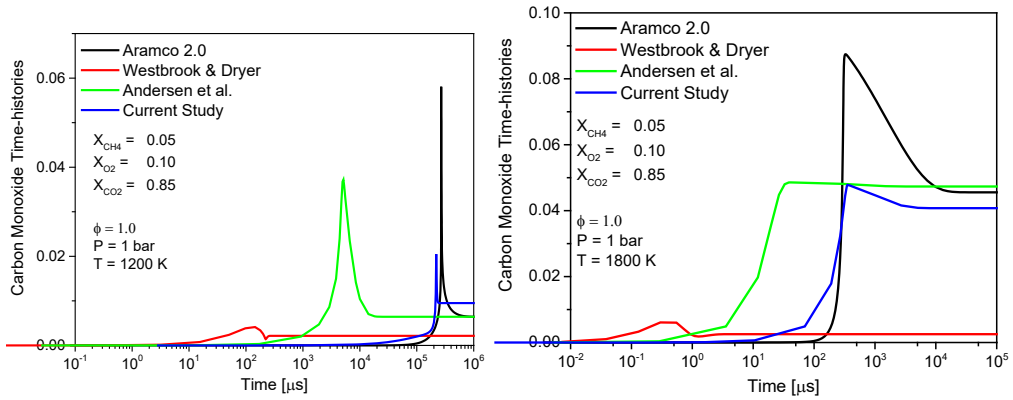

Figure 121. CO concentration time-histories. Left) temperature at 1200 K. Right) Temperatur
Pressure was 1 bar. Mixture Composition: $X_{CH4} = 0.05$, $X_{O2} = 0.10$, $X_{CO2} = 0.85$.

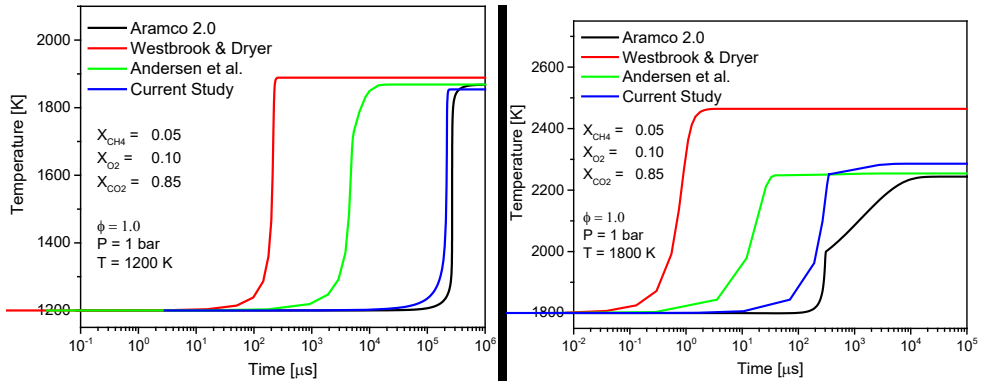

Figure 122. Comparison of temperature profiles between different mechanisms. Left) Temperature at 1200 K. Right) Temperature at 1800 K. Pressure was 1 bar. Mixture Composition: $X_{CH4} = 0.05$, $X_{O2} = 0.10$, $X_{CO2} = 0.85$.

Mechanism Validation and Comparison to Experiments

The global mechanism was compared to ignition delay times found in the literature to determine the full range of conditions that the mechanism could accurately predict. The mechanism was compared data taken from Koroglu et al. and Pryor et al. to understand the limits of the mechanism. The new updated mechanism does an excellent job at low pressures based on the data taken from Koroglu et al. and Pryor et al. [37, 355]. The mechanism can accurately predict the ignition delay times for one mixture and set of experiments but those were a limited number of experiments. The combination of these experiments includes various levels of carbon dioxide, different equivalence ratios, four different pressure ranges and several distinct levels of fuel loading.

The mechanism can accurately predict the ignition delay times for equivalence ratios between ϕ = 0.5 to 1.0, particularly at pressures close to 1 bar. Figure 5 (Left: Stoichiometric Mixture, ϕ = 1.0, Right: Lean Mixture, ϕ = 0.5) show the different mechanisms compared to experiments from Koroglu et al. [355]. The mechanism fails to predict the ignition delay times at rich mixtures. Using

the data for $\phi = 2.0$ from Koroglu et al., the updated mechanism does the worst performance of the three mechanisms. The Andersen et al. mechanism was originally under predicted the ignition delay times by an order of magnitude compared to the Aramco 2.0 mechanism and experimental data, but it does much better with higher equivalence ratios. The current study over predicts the ignition delay times by an order of magnitude while the Andersen et al. mechanism over predicts by 3 times the Aramco 2.0 mechanism.

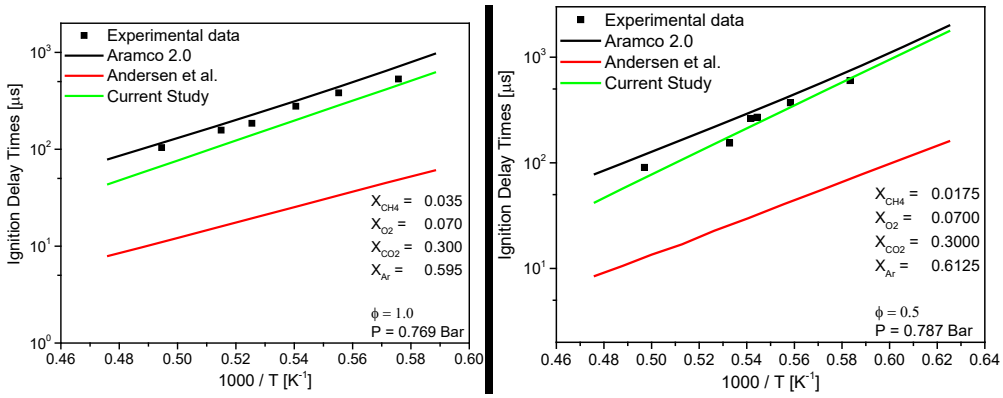

Figure 123. Ignition Delay time comparisons to data from Koroglu et al [355]. Left) Average pressure was 0.769 Bar. Mixture Composition: $X_{CH4} = 0.035$, $X_{O2} = 0.070$, $X_{CO2} = 0.300$, $X_{Ar} = 0.595$. Right) AVERAGE pressure was 0.787 Bar. Mixture Composition: $X_{CH4} = 0.0175$, $X_{O2} = 0.070$, $X_{CO2} = 0.300$, $X_{Ar} = 0.6125$.

The mechanism was also compared to data that was taken at elevated pressures. Experimental data existed in Koroglu et al. and Pryor et al. at pressures around 4 bar, 8 bar and 30 bar [36, 37, 355]. Two sets of experiments at different pressures are shown in Figure 6. The mechanism does not perform as well at these elevated pressures. The mechanism predicts the ignition delay times between equivalence ratios between 0.5 and 1.0 but still is unable to predict the ignition delay times for rich conditions. For the lean and stoichiometric mixtures, the ignition delay times are over predicted by approximately a factor of 2 – 2.5 but can predict the energy required for the

ignition delay times or the slope of the ignition delay time on the graph. For comparison, the Andersen et al. mechanism differed from the Aramco 2.0 mechanism by a factor of 7 – 10 and had much greater variance in the numbers so it failed to match the slope that the Aramco 2.0 mechanism predicts.

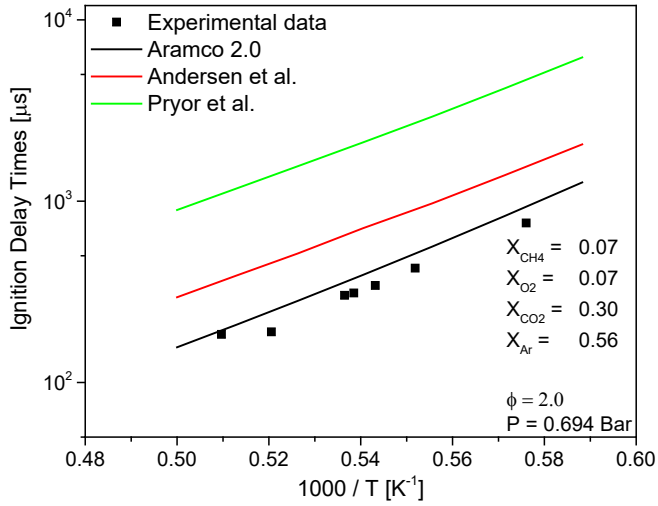

Figure 124. Ignition Delay time comparisons for fuel rich conditions. Data taken from Koroglu et al [355]. Average pressure was 0.694 Bar. Mixture Composition: $X_{CH4} = 0.07$, $X_{O2} = 0.07$, $X_{CO2} = 0.30$, $X_{Ar} = 0.56$.

The same trend was seen in the ignition delay times for the experiments around 8 atm. The ratio between the ignition delay times predicted by the new mechanism compared to the Aramco 2.0 mechanism was 3.3 for both levels of CO_2 dilution while the Andersen et al. mechanism was off by a factor between 10 and 12. The new mechanism over predicts the mechanism and the experimental data points but still improves upon the original mechanism that it was built upon.

The final experiments that the mechanism was compared to was experiments taken at an average pressure of 30 bar. The new mechanism over predicts the ignition delay times by approximately 9 times the Aramco 2.0 mechanism while the Andersen et al. mechanism under predicts the ignition delay times by a factor of 12. The Aramco 2.0 mechanism also slightly over predicts the ignition delay times compared to the experimental trace so both mechanisms tend to be off by one order of magnitude.

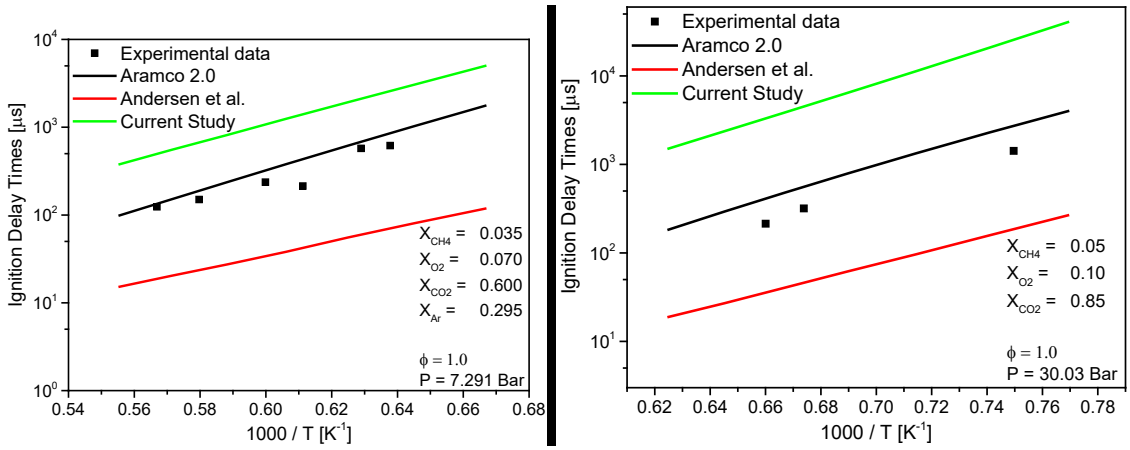

Figure 125. Ignition Delay time comparisons to data from Pryor et al [37]. LEFT) Average pressure was 7.291 Bar. Mixture Composition: X_{CH4} = 0.035, X_{O2} = 0.070, X_{CO2} = 0.600, X_{Ar} = 0.295. RIGHT) AVERAGE pressure was 30.03 Bar. Mixture Composition: X_{CH4} = 0.05, X_{O2} = 0.10, X_{CO2} = 0.300, X_{Ar} = 0.85.

Conclusions

A 3-step global mechanism has been developed for oxy-fuel combustion of methane in CO_2. The mechanism was compared to experimental results and a detailed mechanism was used as a baseline for the comparisons.

The methane mechanism which was developed from a previous mechanism designed for oxy-fuel can match the ignition delay times for a range of conditions. The mechanism showed good

agreement with the detailed mechanism for the methane and water time-histories. It also displayed agreement with the steady-state CO level but fails to simulate the peak CO concentration accurately. Temperature profile predicted was also shown to match those of the detailed mechanism. The mechanism was compared to ignition delay time experiments from the literature and it showed that the mechanism is valid for an equivalence ratio between 0.5 and 1.0 over a range of temperatures between 1500 and 2200 K. The mechanism failed to predict the rich conditions that were measured by Koroglu et al. The mechanism was also compared to elevated pressures up to 30 bar. The mechanism was able to simulate experiments up to 10 bar within a factor of 3 but shows improvement compared to the literature which was off by an order of magnitude for similar experiments. The mechanism failed to accurately predict the ignition delay times at 30 bar, over predicting the ignition delay times by an order of magnitude while the Andersen et al. mechanism under-predicted the ignition delay times by a similar amount. The current methane mechanism over-predicted ignition delay times by increasing amounts as the pressure increases and work is being undertaken to address the validation range of the global mechanism to higher pressures.

REFERENCES

1. Agency, U. S. E. P. "Overview of Greenhouse Gases." 2019, April 11.
2. Lindsey, R. "Climate Change: Atmospheric Carbon Dioxide." 2018, August 2018.
3. Brun, K., Friedman, P., and Dennis, R. *Fundamentals and applications of supercritical carbon dioxide (sCO2) based power cycles*: Woodhead publishing, 2017.
4. Dostal, V., Driscoll, M. J., and Hejzlar, P. "A supercritical carbon dioxide cycle for next generation nuclear reactors." Massachusetts Institute of Technology, Department of Nuclear Engineering, 2004.
5. Grant O Musgrove, D. S., Shaun Sullivan, Lalit Chordia, Mrac Portnoff. "Tutorial: Heat Exchangers for Supercritical CO2 Power Cycle Applications," *sCO2 symposium*. 2016.
6. Elson, A., Tidball, R., and Hampson, A. "Waste heat to power market assessment," *Oak Ridge National Laboratory*, 2015.
7. Wright, S., Davidson, C., and Scammell, W. "Thermo-economic analysis of four sCO2 waste heat recovery power systems," *Fifth International SCO2 Symposium, San Antonio, TX, Mar*. 2016, pp. 28-31.
8. Huck, P., Freund, S., Lehar, M., and Peter, M. "Performance comparison of supercritical CO2 versus steam bottoming cycles for gas turbine combined cycle applications," *5th International Supercritical CO2 Power Cycle Symposium*. 2016.
9. Bauer, M. L., Vijaykumar, R., Lausten, M., and Stekli, J. "Pathways to cost competitive concentrated solar power incorporating supercritical carbon dioxide power cycles," *Proceedings of the 5th International Symposium–Supercritical CO2 Power Cycles, San Antonio, TX, USA*. 2016, pp. 28-31.
10. Allam, R., Fetvedt, J., Forrest, B., and Freed, D. "The Oxy-Fuel, Supercritical CO2 Allam Cycle: New Cycle Developments to Produce Even Lower-Cost Electricity From Fossil Fuels Without Atmospheric Emissions," *ASME Turbo Expo 2014: Turbine Technical Conference and Exposition*. American Society of Mechanical Engineers, 2014, pp. V03BT36A016-V03BT36A016.
11. Ahn, Y., Bae, S. J., Kim, M., Cho, S. K., Baik, S., Lee, J. I., and Cha, J. E. "Review of supercritical CO2 power cycle technology and current status of research and development," *Nuclear Engineering and Technology* Vol. 47, No. 6, 2015, pp. 647-661.

doi: https://doi.org/10.1016/j.net.2015.06.009

12. NetPower. "Natural Gas, Syngas, or Oil Allam Cycle CCS Power Plant." 2018.
13. Darde, A., Prabhakar, R., Tranier, J.-P., and Perrin, N. "Air separation and flue gas compression and purification units for oxy-coal combustion systems," *Energy Procedia* Vol. 1, No. 1, 2009, pp. 527-534.
14. Tranier, J.-P., Dubettier, R., Darde, A., and Perrin, N. "Air Separation, flue gas compression and purification units for oxy-coal combustion systems," *Energy Procedia* Vol. 4, 2011, pp. 966-971.
15. Allam, R. J., Palmer, M. R., Brown Jr, G. W., Fetvedt, J., Freed, D., Nomoto, H., Itoh, M., Okita, N., and Jones Jr, C. "High efficiency and low cost of electricity generation from

fossil fuels while eliminating atmospheric emissions, including carbon dioxide," *Energy Procedia* Vol. 37, 2013, pp. 1135-1149.

16. Park, S., Parahovnik, A., Peles, Y., and Vasu, S. S. "Laser-induced fluorescence thermometry of supercritical CO2 flows inside a micro-channel," *Optics Letters* Vol. 46, No. 8, 2021, pp. 1924-1927.

doi: 10.1364/OL.422854

17. Rahman, R. K., Barak, S., Manikantachari, K. R. V., Ninnemann, E., Hosangadi, A., Zambon, A., and Vasu, S. S. "Probing the Effects of NOx and SOx Impurities on Oxy-Fuel Combustion in Supercritical CO2: Shock Tube Experiments and Chemical Kinetic Modeling," *Journal of Energy Resources Technology* Vol. 142, No. 12, 2020.

doi: 10.1115/1.4047314

18. Park, S., Urso, J., Manikantachari, K. R. V., Hosangadi, A., Zambon, A., and Vasu, S. S. "Measurements of Density and Sound Speed in Mixtures Relevant to Supercritical CO2 Cycles," *Journal of Energy Resources Technology* Vol. 142, No. 10, 2020.

doi: 10.1115/1.4047081

19. Park, S., Kim, G., Terracciano, A. C., and Vasu, S. "High-Pressure Ignition and Flame Propagation Measurements of CO2 Diluted Natural Gas/Oxidizer Mixtures for Advanced Rocket and Gas Turbine Combustors," *AIAA Scitech 2020 Forum*. 2020.

20. Laich, A. R., Baker, J., Ninnemann, E., Sigler, C., Naumann, C., Braun-Unkhoff, M., and Vasu, S. S. "Effects of High Fuel Loading and CO2 Dilution on Oxy-Methane Ignition Inside a Shock Tube at High Pressure," *Journal of Energy Resources Technology* Vol. 142, No. 10, 2020.

doi: 10.1115/1.4047023

21. Barak, S., Pryor, O., Ninnemann, E., Neupane, S., Vasu, S., Lu, X., and Forrest, B. "Ignition Delay Times of Oxy-Syngas and Oxy-Methane in Supercritical CO2 Mixtures for Direct-Fired Cycles," *Journal of Engineering for Gas Turbines and Power* Vol. 142, No. 2, 2020.

doi: 10.1115/1.4045743

22. Wait, E. E., Masunov, A. E., and Vasu, S. S. "Quantum chemical and master equation study of OH + CH2O → H2O + CHO reaction rates in supercritical CO2 environment," *International Journal of Chemical Kinetics* Vol. 51, No. 1, 2019, pp. 42-48.

doi: doi:10.1002/kin.21228

23. Park, S., Kim, G., Terracciano, A. C., Barak, S., and Vasu, S. S. "Experimental Ignition Studies of Supercritical CO2 Oxy-Fuel Mixtures," *The 44th International Technical Conference on Clean Energy: The Clearwater Clean Energy Conference* Vol. Jun 16-21, 2019, Clearwater, FL, paper# 68, 2019.

24. Manikantachari, K. R. V., Martin, S., Rahman, R. K., Velez, C., and Vasu, S. "A General Study of Counterflow Diffusion Flames for Supercritical CO2 Combustion," *Journal of Engineering for Gas Turbines and Power* Vol. 141, No. 12, 2019.

doi: 10.1115/1.4045195
25. Barak, S., Pryor, O., Ninnemann, E., Neupane, S., Lu, X., Forrest, B., and Vasu, S. "Ignition Delay Times of Syngas and Methane in sCO2 Diluted Mixtures for Direct-Fired Cycles," *ASME Turbo Expo 2019: Turbomachinery Technical Conference and Exposition*. Vol. Volume 9: Oil and Gas Applications; Supercritical CO2 Power Cycles; Wind Energy, 2019.
26. Vesely, L., Manikantachari, K. R. V., Vasu, S., Kapat, J., Dostal, V., and Martin, S. "Effect of Impurities on Compressor and Cooler in Supercritical CO2 Cycles," *Journal of Energy Resources Technology* Vol. 141, No. 1, 2018, pp. 012003-012003-8.

doi: 10.1115/1.4040581
27. Pryor, O. M., Vasu, S., Lu, X., Freed, D., and Forrest, B. "Development of a Global Mechanism for Oxy-Methane Combustion in a CO2 Environment," No. 51180, 2018, p. V009T38A004.

doi: 10.1115/GT2018-75169
28. Panteleev, S. V., Masunov, A. E., and Vasu, S. S. "Molecular Dynamics Study of Combustion Reactions in a Supercritical Environment. Part 2: Boxed MD Study of CO + OH → CO2 + H Reaction Kinetics," *The Journal of Physical Chemistry A*, 2018.

doi: 10.1021/acs.jpca.7b09774
29. Masunov, A. E., Wait, E. E., and Vasu, S. S. "Catalytic Effect of Carbon Dioxide on Reaction OH + CO → H + CO2 in Supercritical Environment: Master Equation Study," *The Journal of Physical Chemistry A* Vol. 122, No. 31, 2018, pp. 6355-6359.

doi: 10.1021/acs.jpca.8b04501
30. Manikantachari, K. R. V., Vesely, L., Martin, S., Bobren-Diaz, J. O., and Vasu, S. "Reduced Chemical Kinetic Mechanisms for Oxy/Methane Supercritical CO2 Combustor Simulations," *Journal of Energy Resources Technology* Vol. 140, No. 9, 2018, pp. 092202-092202-10.

doi: 10.1115/1.4039746
31. Manikantachari, K. R. V., Martin, S., Vesely, L., Bobren-Diaz, J. O., Vasu, S., and Kapat, J. "A Strategy of Reactant Mixing in Methane Direct-Fired sCO2 Combustors," No. 51180, 2018, p. V009T38A008.

doi: 10.1115/GT2018-75547
32. Koroglu, B., Neupane, S., Pryor, O., Peale, R. E., and Vasu, S. S. "High temperature infrared absorption cross sections of methane near 3.4 μm in Ar and CO2 mixtures," *Journal of Quantitative Spectroscopy and Radiative Transfer* Vol. 206, No. Supplement C, 2018, pp. 36-45.

doi: https://doi.org/10.1016/j.jqsrt.2017.11.003
33. Khadse, A., Blanchette, L., Kapat, J., Vasu, S., Hossain, J., and Donazzolo, A. "Optimization of Supercritical CO2 Brayton Cycle for Simple Cycle Gas Turbines Exhaust Heat Recovery Using Genetic Algorithm," *Journal of Energy Resources Technology* Vol. in press, No. doi:10.1115/1.4039446, 2018.

doi: 10.1115/1.4039446

34. Barak, S., Ninnemann, E., Neupane, S., Barnes, F., Kapat, J., and Vasu, S. "High-Pressure Oxy-Syngas Ignition Delay Times With CO2 Dilution: Shock Tube Measurements and Comparison of the Performance of Kinetic Mechanisms," *Journal of Engineering for Gas Turbines and Power* Vol. 141, No. 2, 2018, pp. 021011-021011-7.

doi: 10.1115/1.4040904

35. Pryor, O. M., Barak, S., Koroglu, B., Ninnemann, E., and Vasu, S. S. "Measurements and interpretation of shock tube ignition delay times in highly CO2 diluted mixtures using multiple diagnostics," *Combustion and Flame* Vol. 180, 2017, pp. 63-76.

doi: 10.1016/j.combustflame.2017.02.020

36. Pryor, O., Koroglu, B., Barak, S., Lopez, J., Ninnemann, E., Nash, L., and Vasu, S. "Ignition Delay Times of High Pressure Oxy-Methane Combustion With High Levels of CO2 Dilution," No. 50848, 2017, p. V04AT04A044.

doi: 10.1115/GT2017-63666

37. Pryor, O., Barak, S., Lopez, J., Ninnemann, E., Koroglu, B., Nash, L., and Vasu, S. "High Pressure Shock Tube Ignition Delay Time Measurements During Oxy-Methane Combustion With High Levels of CO2 Dilution," *Journal of Energy Resources Technology* Vol. 139, No. 4, 2017, pp. 042208-042208-6.

doi: 10.1115/1.4036254

38. Masunov, A. E., Wait, E., and Vasu, S. S. "Quantum Chemical Study of CH3 + O2 Combustion Reaction System: Catalytic Effects of Additional CO2 Molecule," *The Journal of Physical Chemistry A* Vol. 121, No. 30, 2017, pp. 5681-5689.

doi: 10.1021/acs.jpca.7b04897

39. Manikantachari, K. R. V., Martin, S., Bobren-Diaz, J. O., and Vasu, S. "Thermal and Transport Properties for the Simulation of Direct-Fired sCO2 Combustor," *Journal of Engineering for Gas Turbines and Power* Vol. 139, No. 12, 2017, pp. 121505-121505-14.

doi: 10.1115/1.4037579

40. Khadse, A., Blanchette, L., Kapat, J. S., S., V. S., and Ahmed, K. "Optimization of supercritical CO2 Brayton cycle for simple cycle gas turbines exhaust heat recovery using genetic algorithm," *Proc. ASME Turbo Expo* Vol. Paper No: GT2017-63696 2017.

41. Barak, S., Pryor, O., Lopez, J., Ninnemann, E., Vasu, S., and Koroglu, B. "High-Speed Imaging and Measurements of Ignition Delay Times in Oxy-Syngas Mixtures With High CO2 Dilution in a Shock Tube," *Journal of Engineering for Gas Turbines and Power* Vol. 139, No. 12, 2017, pp. 121503-121503-7.

doi: 10.1115/1.4037458

42. Vasu, S. S., Pryor, O. M., Kapat, J. S., Masunov, A., and Martin, S. M. "Developing a validated chemical kinetics model for sCO2 combustion and implementation in CFD," *Proc. of Supercritical CO2 Power Cycles Symposium, San Antonio, TX.* Vol. Paper#7, 2016.

43. Masunov, A. E., Wait, E., and Vasu, S. S. "Chemical Reaction CO+OH• → CO2+H• Autocatalyzed by Carbon Dioxide: Quantum Chemical Study of the Potential Energy Surfaces," *The Journal of Physical Chemistry A* Vol. 120, No. 30, 2016, pp. 6023-6028.

doi: 10.1021/acs.jpca.6b03242
44. Masunov, A. E., Atlanov, A. A., and Vasu, S. S. "Potential Energy Surfaces for the Reactions of HO2 Radical with CH2O and HO2 in CO2 Environment," *The Journal of Physical Chemistry A* Vol. 120, No. 39, 2016, pp. 7681-7688.

doi: 10.1021/acs.jpca.6b07257
45. Koroglu, B., Pryor, O., Lopez, J., Nash, L., and Vasu, S. S. "Shock tube ignition delay times and methane time-histories measurements during excess CO2 diluted oxy-methane combustion," *Combustion and flame* Vol. 164, 2016, pp. 152-163.

doi: http://dx.doi.org/10.1016/j.combustflame.2015.11.011
46. Shao, J., Choudhary, R., Davidson, D. F., Hanson, R. K., Barak, S., and Vasu, S. "Ignition delay times of methane and hydrogen highly diluted in carbon dioxide at high pressures up to 300 atm," *Proceedings of the Combustion Institute*, 2018.

doi: https://doi.org/10.1016/j.proci.2018.08.002
47. Shao, R., Choudhary, R., Davidson, D. F., Hanson, R. K., Barak, S., and Vasu, S. S. "Ignition Delay Times of Methane and Hydrogen Highly Diluted in Carbon Dioxide," *International Symposium on Shock WavesNagoya*, 2017.

48. Chiesa, P., Lozza, G., and Mazzocchi, L. "Using Hydrogen as Gas Turbine Fuel," *Journal of Engineering for Gas Turbines and Power* Vol. 127, No. 1, 2005, pp. 73-80.

doi: 10.1115/1.1787513
49. Kéromnès, A., Metcalfe, W. K., Heufer, K. A., Donohoe, N., Das, A. K., Sung, C.-J., Herzler, J., Naumann, C., Griebel, P., Mathieu, O., Krejci, M. C., Petersen, E. L., Pitz, W. J., and Curran, H. J. "An experimental and detailed chemical kinetic modeling study of hydrogen and syngas mixture oxidation at elevated pressures," *Combustion and Flame* Vol. 160, No. 6, 2013, pp. 995-1011.

doi: http://dx.doi.org/10.1016/j.combustflame.2013.01.001
50. Walton, S. M., He, X., Zigler, B. T., and Wooldridge, M. S. "An experimental investigation of the ignition properties of hydrogen and carbon monoxide mixtures for syngas turbine applications," *Proceedings of the Combustion Institute* Vol. 31, No. 2, 2007, pp. 3147-3154.

doi: 10.1016/j.proci.2006.08.059
51. Vasu, S. S., Davidson, D. F., and Hanson, R. K. "Shock Tube Study of Syngas Ignition in Rich CO2Mixtures and Determination of the Rate of H + O2+ CO2→ HO2+ CO2," *Energy & Fuels* Vol. 25, No. 3, 2011, pp. 990-997.

doi: 10.1021/ef1015928
52. Thi, L. D., Zhang, Y., and Huang, Z. "Shock tube study on ignition delay of multi-component syngas mixtures – Effect of equivalence ratio," *International Journal of Hydrogen Energy* Vol. 39, No. 11, 2014, pp. 6034-6043.

doi: 10.1016/j.ijhydene.2014.01.170
53. Petersen, E. L., Kalitan, D. M., Barrett, A. B., Reehal, S. C., Mertens, J. D., Beerer, D. J., Hack, R. L., and McDonell, V. G. "New syngas/air ignition data at lower temperature and elevated pressure and comparison to current kinetics models," *Combustion and Flame* Vol. 149, No. 1-2, 2007, pp. 244-247.

doi: 10.1016/j.combustflame.2006.12.007
54. Koroglu, B., Pryor, O. M., Lopez, J., Nash, L., and Vasu, S. S. "Shock tube ignition delay times and methane time-histories measurements during excess CO2 diluted oxy-methane combustion," *Combustion and Flame* Vol. 164, 2016, pp. 152-163.

doi: http://dx.doi.org/10.1016/j.combustflame.2015.11.011
55. Koroglu, B., Pryor, O., Lopez, J., Nash, L., and Vasu, S. S. "Methane Ignition Delay Times in CO2 Diluted Mixtures in a Shock Tube," *51st AIAA/SAE/ASEE Joint Propulsion Conference*. American Institute of Aeronautics and Astronautics AIAA 2015-4088, 2015.
56. Dostal, V., Driscoll, M. J., and Hejzlar, P. "A supercritical carbon dioxide cycle for next generation nuclear reactors." MIT-ANP-TR-100, 2004.
57. McClung, A. "Oxy-Combustion Integration for Direct Fired sCO2 Cycles," *The 5th Intl Symposium - Supercritical CO2 Power Cycles* San Antonio, TX, 2016.
58. Fetvedt, J. "8Rivers Development Of The sCO2 Allam Cycle 50MWth Demonstration Plant," *The 5th International Symposium - Supercritical CO2 Power Cycles*. San Antonio, TX, 2016.
59. Pryor, O., Barak, S., Ninnemann, E., and Vasu, S. "High Pressure Shock Tube Ignition Delay Time Measurements During Oxy-Methane Combustion With High Levels of CO2 Dilution," *Journal of Energy Resources Technology* Vol. 139, No. 4, 2017, pp. 042208-042208-6.

doi: 10.1115/1.4036254
60. Smith, G. P., Golden, D. M., Frenklach, M., Moriarty, N. W., Eiteneer, B., Goldenberg, M., Bowman, C. T., Hanson, R. K., Song, S., and Gardiner Jr, W. C. "GRI-Mech 3.0," *URL: http://www.me.berkeley.edu/gri_mech* Vol. 51, 1999, p. 55.

61. Gaydon, A. G. "The Carbon Monoxide Flame," *The Spectroscopy of Flames*. Springer Netherlands, Dordrecht, 1974, pp. 127-143.
62. Matthew, F., Thomas, A. K., John, H., and Frederick, S. "Study of the Experimental Performance of a Rotating Detonation Engine with Nozzled Exhaust Flow," *53rd AIAA Aerospace Sciences Meeting*. American Institute of Aeronautics and Astronautics, 2015.
63. Pryor, O. M., Barak, S., Koroglu, B., Ninnemann, E., and Vasu, S. "Measurements and interpretation of shock tube ignition delay times in highly CO2 diluted mixtures using multiple diagnostics," *Combustion and Flame* Vol. 180, 2017, pp. 67-76.

64. Liu, F., Guo, H., and Smallwood, G. J. "The chemical effect of CO2 replacement of N2 in air on the burning velocity of CH4 and H2 premixed flames," *Combustion and Flame* Vol. 133, No. 4, 2003, pp. 495-497.

doi: http://dx.doi.org/10.1016/S0010-2180(03)00019-1

65. Ninnemann, E., Pryor, O., Barak, S., Koroglu, B., Sosa, J., Ahmed, K., and Vasu, S. "High-Speed Imaging of the Dynamics of H2/O2 Ignition at Low to Moderate Temperatures in a Shock Tube," *55th AIAA Aerospace Sciences Meeting*. American Institute of Aeronautics and Astronautics AIAA 2017-1796, 2017.
66. Hargis, J. W., and Petersen, E. L. "Methane Ignition in a Shock Tube with High Levels of CO2 Dilution: Consideration of the Reflected-Shock Bifurcation," *Energy & Fuels* Vol. 29, No. 11, 2015, pp. 7712-7726.

doi: 10.1021/acs.energyfuels.5b01760
67. Ihme, M., Sun, Y., and Deiterding, R. "Detailed Simulations of Shock-Bifurcation and Ignition of an Argon-diluted Hydrogen/Oxygen Mixture in a Shock Tube," *51st AIAA Aerospace Sciences Meeting including the New Horizons Forum and Aerospace Exposition*. American Institute of Aeronautics and Astronautics, 2013.
68. Dryer, F. L., and Chaos, M. "Ignition of syngas/air and hydrogen/air mixtures at low temperatures and high pressures: Experimental data interpretation and kinetic modeling implications," *Combustion and Flame* Vol. 152, No. 1-2, 2008, pp. 293-299.

doi: 10.1016/j.combustflame.2007.08.005
69. Olm, C., Zsély, I. G., Varga, T., Curran, H. J., and Turányi, T. "Comparison of the performance of several recent syngas combustion mechanisms," *Combustion and Flame* Vol. 162, No. 5, 2015, pp. 1793-1812.

doi: http://dx.doi.org/10.1016/j.combustflame.2014.12.001
70. Atkinson, R., Perry, R. A., and Pitts Jr., J. N. "Absolute rate constants for the reaction of OH radicals with allene, 1,3-butadiene, and 3-methyl-1-butene over the temperature range 299–424 °K," *J. Chem. Phys.* Vol. 67, 1977, p. 3170.

71. Li, Y., Zhou, C.-W., Somers, K. P., Zhang, K., and Curran, H. J. "The oxidation of 2-butene: A high pressure ignition delay, kinetic modeling study and reactivity comparison with isobutene and 1-butene," *Proceedings of the Combustion Institute* Vol. 36, No. 1, 2017, pp. 403-411.

doi: http://dx.doi.org/10.1016/j.proci.2016.05.052
72. G.P. Smith, Y. T., and H. Wang. "Foundational Fuel Chemistry Model Version 1.0 (FFCM-1)." http://nanoenergy.stanford.edu/ffcm1, 2016.
73. Varga, T., Olm, C., Nagy, T., Zsély, I. G., Valkó, É., Pálvölgyi, R., Curran, H. J., and Turányi, T. "Development of a Joint Hydrogen and Syngas Combustion Mechanism Based on an Optimization Approach," *International Journal of Chemical Kinetics* Vol. 48, No. 8, 2016, pp. 407-422.

doi: 10.1002/kin.21006
74. Ranzi, E., Frassoldati, A., Grana, R., Cuoci, A., Faravelli, T., Kelley, A. P., and Law, C. K. "Hierarchical and comparative kinetic modeling of laminar flame speeds of hydrocarbon and oxygenated fuels," *Progress in Energy and Combustion Science* Vol. 38, No. 4, 2012, pp. 468-501.

doi: http://dx.doi.org/10.1016/j.pecs.2012.03.004

75. Davis, S. G., Joshi, A. V., Wang, H., and Egolfopoulos, F. "An optimized kinetic model of H2/CO combustion," *Proceedings of the Combustion Institute* Vol. 30, No. 1, 2005, pp. 1283-1292.

doi: http://dx.doi.org/10.1016/j.proci.2004.08.252

76. Li, J., Zhao, Z., Kazakov, A., Chaos, M., Dryer, F. L., and Scire, J. J. "A comprehensive kinetic mechanism for CO, CH2O, and CH3OH combustion," *International Journal of Chemical Kinetics* Vol. 39, No. 3, 2007, pp. 109-136.

doi: 10.1002/kin.20218

77. Li, X., You, X., Wu, F., and Law, C. K. "Uncertainty analysis of the kinetic model prediction for high-pressure H2/CO combustion," *Proceedings of the Combustion Institute* Vol. 35, No. 1, 2015, pp. 617-624.

doi: https://doi.org/10.1016/j.proci.2014.07.047

78. Healy, D., Kalitan, D. M., Aul, C. J., Petersen, E. L., Bourque, G., and Curran, H. J. "Oxidation of C1−C5 Alkane Quinternary Natural Gas Mixtures at High Pressures," *Energy & Fuels* Vol. 24, No. 3, 2010, pp. 1521-1528.

doi: 10.1021/ef9011005

79. "Combustion Research Group, Mechanical and Aerospace Engineering, San Diego Mechanism, version 2016-12-14 " *Chemical-Kinetic Mechanisms for Combustion Applications* University of California at San Diego: <http://combustion.ucsd.edu>.

80. Hai Wang, X. Y., Ameya V. Joshi, Scott G. Davis, Alexander Laskin, Fokion Egolfopoulos, & Chung K. Law. "USC Mech Version II. High-Temperature Combustion Reaction Model of H2/CO/C1-C4 Compounds.." http://ignis.usc.edu/USC_Mech_II.htm, May 2007, 2007.

81. Yang, S., Yang, X., Wu, F., Ju, Y., and Law, C. K. "Laminar flame speeds and kinetic modeling of H2/O2/diluent mixtures at sub-atmospheric and elevated pressures," *Proceedings of the Combustion Institute* Vol. 36, No. 1, 2017, pp. 491-498.

doi: https://doi.org/10.1016/j.proci.2016.06.122

82. Bates, R. W., Golden, D. M., Hanson, R. K., and Bowman, C. T. "Experimental study and modeling of the reaction H + O2 + M [rightward arrow] HO2 + M (M = Ar, N2 , H2O) at elevated pressures and temperatures between 1050 and 1250 K," *Physical Chemistry Chemical Physics* Vol. 3, No. 12, 2001, pp. 2337-2342.

doi: 10.1039/B010002L

83. Hong, Z., Davidson, D. F., Barbour, E. A., and Hanson, R. K. "A new shock tube study of the H + O2 → OH + O reaction rate using tunable diode laser absorption of H2O near 2.5 μm," *Proceedings of the Combustion Institute* Vol. 33, No. 1, 2011, pp. 309-316.

doi: http://dx.doi.org/10.1016/j.proci.2010.05.101

84. Rostrup-Nielsen, J. R. "Catalytic steam reforming," *Catalysis*. Springer, 1984, pp. 1-117.

85. Davidson, D. F., and Hanson, R. K. "Interpreting shock tube ignition data," *International Journal of Chemical Kinetics* Vol. 36, No. 9, 2004, pp. 510-523.

doi: 10.1002/kin.20024

86. Hall, J. M., Rickard, M. J. A., and Petersen, E. L. "Comparison of Characteristic Time Diagnostics for Igntion and Oxidation of Fuel/Oxidizer Mixtures Behind Reflected Shock Waves," *Combustion Science and Technology* Vol. 177, No. 3, 2005, pp. 455-483.

doi: 10.1080/00102200590909003

87. Hong, Z., Pang, G. A., Vasu, S. S., Davidson, D. F., and Hanson, R. K. "The use of driver inserts to reduce non-ideal pressure variations behind reflected shock waves," *Shock Waves* Vol. 19, 2009, pp. 113-123.

88. Barak, S., Ninnemann, E., Neupane, S., Barnes, F., Kapat, J., and Vasu, S. "High pressure oxy-syngas ignition delay times: Shock tube measurements and comparison of the performance of kinetic mechanisms," *Journal of Engineering for Gas Turbines and Power*, 2018.

doi: 10.1115/1.4040904

89. Zeng, W., Ma, H., Liang, Y., and Hu, E. "Experimental and modeling study on effects of N2 and CO2 on ignition characteristics of methane/air mixture," *Journal of Advanced Research* Vol. 6, No. 2, 2015, pp. 189-201.

doi: https://doi.org/10.1016/j.jare.2014.01.003

90. Liss, W., Thrasher, W., Steinmetz, G., Chowdiah, P., and Attari, A. "Variability of natural gas composition in select major metropolitan areas of the united states. final report, august 1990-february 1992." American Gas Association Labs., Cleveland, OH (United States), 1992.

91. Flores, R., McDonell, V., and Samuelsen, G. "Impact of ethane and propane variation in natural gas on the performance of a model gas turbine combustor," 2003.

92. Ly, H. "Effects of natural gas composition variations on the operation, performance and exhaust emissions of natural gas-powered vehicles," *IANGV, December*, 2002.

93. Almansour, B., Thompson, L., Lopez, J., Barari, G., and Vasu, S. S. "Laser Ignition and Flame Speed Measurements in Oxy-Methane Mixtures Diluted With CO2," *Journal of Energy Resources Technology* Vol. 138, No. 3, 2016, p. 032201.

94. Petersen, E. "A shock tube and diagnostics for chemistry measurements at elevated pressures with application to methane ignition," 1999.

95. Petersen, E. L., and Hanson, R. K. "Nonideal effects behind reflected shock waves in a high-pressure shock tube," *Shock Waves* Vol. 10, No. 6, 2001, p. 405.

96. Zhou, C.-W., Li, Y., Burke, U., Banyon, C., Somers, K. P., Ding, S., Khan, S., Hargis, J. W., Sikes, T., Mathieu, O., Petersen, E. L., AlAbbad, M., Farooq, A., Pan, Y., Zhang, Y., Huang, Z., Lopez, J., Loparo, Z., Vasu, S. S., and Curran, H. J. "An experimental and

chemical kinetic modeling study of 1,3-butadiene combustion: Ignition delay time and laminar flame speed measurements," *Combustion and Flame* Vol. 197, 2018, pp. 423-438.

doi: https://doi.org/10.1016/j.combustflame.2018.08.006

97. Glarborg, P., and Bentzen, L. L. B. "Chemical Effects of a High CO2 Concentration in Oxy-Fuel Combustion of Methane," *Energy & Fuels* Vol. 22, No. 1, 2008, pp. 291-296.

doi: 10.1021/ef7005854

98. "ANSYS Chemkin-Pro." http://www.ansys.com/products/fluids/ansys-chemkin-pro, San Diego, CA., 2018.

99. Jasper, A. W., and Miller, J. A. "Theoretical unimolecular kinetics for CH4+ M⇄ CH3+ H+ M in eight baths, M= He, Ne, Ar, Kr, H2, N2, CO, and CH4," *The Journal of Physical Chemistry A* Vol. 115, No. 24, 2011, pp. 6438-6455.

100. Koike, T., Kudo, M., Maeda, I., and Yamada, H. "Rate Constants of CH4+ M□ CH3+ H+ M and CH3OH+ M□ CH3+ OH+ M over 1400–2500 K," *International Journal of Chemical Kinetics* Vol. 32, No. 1, 2000, pp. 1-6.

101. Wu, Y., Tang, D., Verploegh, R. J., Xi, H., and Sholl, D. S. "Impacts of gas impurities from pipeline natural gas on methane storage in metal–organic frameworks during long-term cycling," *The Journal of Physical Chemistry C* Vol. 121, No. 29, 2017, pp. 15735-15745.

102. Mansfield, A. B., and Wooldridge, M. S. "The effect of impurities on syngas combustion," *Combustion and Flame* Vol. 162, No. 5, 2015, pp. 2286-2295.

doi: 10.1016/j.combustflame.2015.01.026

103. Mathieu, O., Hargis, J., Camou, A., Mulvihill, C., and Petersen, E. L. "Ignition delay time measurements behind reflected shock-waves for a representative coal-derived syngas with and without NH3 and H2S impurities," *Proceedings of the Combustion Institute* Vol. 35, No. 3, 2015, pp. 3143-3150.

doi: 10.1016/j.proci.2014.06.062

104. Mathieu, O., Kopp, M. M., and Petersen, E. L. "Shock-tube study of the ignition of multi-component syngas mixtures with and without ammonia impurities," *Proceedings of the Combustion Institute* Vol. 34, No. 2, 2013, pp. 3211-3218.

doi: 10.1016/j.proci.2012.05.008

105. Deng, F., Yang, F., Zhang, P., Pan, Y., Zhang, Y., and Huang, Z. "Ignition delay time and chemical kinetic study of methane and nitrous oxide mixtures at high temperatures," *Energy & Fuels* Vol. 30, No. 2, 2016, pp. 1415-1427.

106. Mathieu, O., Pemelton, J. M., Bourque, G., and Petersen, E. L. "Shock-induced ignition of methane sensitized by NO2 and N2O," *Combustion and Flame* Vol. 162, No. 8, 2015, pp. 3053-3070.

107. Gokulakrishnan, P., Lawrence, A. D., McLellan, P. J., and Grandmaison, E. W. "A functional-PCA approach for analyzing and reducing complex chemical mechanisms," *Computers & Chemical Engineering* Vol. 30, No. 6, 2006, pp. 1093-1101.

doi: https://doi.org/10.1016/j.compchemeng.2006.02.007

108. Gokulakrishnan, P., Kwon, S., Hamer, A. J., Klassen, M. S., and Roby, R. J. "Reduced Kinetic Mechanism for Reactive Flow Simulation of Syngas/Methane Combustion at Gas Turbine Conditions," No. 42363, 2006, pp. 513-521.

doi: 10.1115/GT2006-90573

109. Barari, G., Pryor, O., Koroglu, B., Lopez, J., Nash, L., Sarathy, S. M., and Vasu, S. S. "High Temperature Shock Tube Experiments and Kinetic Modeling Study of Diisopropyl Ketone Ignition and Pyrolysis," *Combustion and Flame* Vol. 177, 2017, pp. 207-218.

110. Curran, H. J. "Developing detailed chemical kinetic mechanisms for fuel combustion," *Proceedings of the Combustion Institute* Vol. 37, No. 1, 2019, pp. 57-81.

111. Jacob Delimont, A. M., Marc Portnoff, Lalit Chordia. "Direct Fired Oxy-Fuel Combustor for sCO2 Power Cycles," *UTSR meeting*. 2016.

112. Masunov, A. E., Atlanov, A. A., and Vasu, S. S. "Potential Energy Surfaces for the Reactions of HO2 Radical with CH2O and HO2 in CO2 Environment," *J. Phys. Chem. A* Vol. 120, No. 39, 2016, pp. 7681-7688.

113. Masunov, A. E., Atlanov, A. A., and Vasu, S. S. "Molecular Dynamics Study of Combustion Reactions in a Supercritical Environment. Part 1: Carbon Dioxide and Water Force Field Parameters Refitting and Critical Isotherms of Binary Mixtures," *Energy & Fuels* Vol. 30, No. 11, 2016, pp. 9622-9627.

doi: 10.1021/acs.energyfuels.6b01927

114. Masunov, A. E., Wait, E. E., Atlanov, A. A., and Vasu, S. S. "Quantum Chemical Study of Supercritical Carbon Dioxide Effects on Combustion Kinetics," *The Journal of Physical Chemistry A*, 2017.

115. Masunov, A. m. E., Wait, E., and Vasu, S. S. "Quantum Chemical Study of CH3+ O2 Combustion Reaction System: Catalytic Effects of Additional CO2 Molecule," *The Journal of Physical Chemistry A* Vol. 121, No. 30, 2017, pp. 5681-5689.

116. Smith, G. P., Golden, D. M., Frenklach, M., Moriarty, N. W., Eiteneer, B., Goldenberg, M., Bowman, C. T., Hanson, R. K., Song, S., and Gardiner Jr, W. C. "GRI 3.0 Mechanism," *Gas Research Institute (http://www. me. berkeley. edu/gri_mech)*, 1999.

117. Metcalfe, W. K., Burke, S. M., Ahmed, S. S., and Curran, H. J. "A hierarchical and comparative kinetic modeling study of C1− C2 hydrocarbon and oxygenated fuels," *International Journal of Chemical Kinetics* Vol. 45, No. 10, 2013, pp. 638-675.

118. Wang, H., You, X., Joshi, A. V., Davis, S. G., Laskin, A., Egolfopoulos, F., and Law, C. K. "USC mech version II," *High-temperature combustion reaction model of H* Vol. 2, 2007.

119. Shao, J., Choudhary, R., Davidson, D. F., Hanson, R. K., Barak, S., and Vasu, S. "Ignition delay times of methane and hydrogen highly diluted in carbon dioxide at high pressures up to 300 atm," *Proceedings of the Combustion Institute* Vol. 37, No. 4, 2019, pp. 4555-4562.

120. Jiankun Shao, R. C., David F. Davidson, Ronald K. Hanson, Samuel Barak, Subith Vasu. "Ignition Delay Times of Methane and Hydrogen Highly Diluted in Carbon Dioxide," *International Symposium on Shock Waves*. Nagoya, Japan, 2017.

121. Sun, W., Chen, Z., Gou, X., and Ju, Y. "A path flux analysis method for the reduction of detailed chemical kinetic mechanisms," *Combustion and Flame* Vol. 157, No. 7, 2010, pp. 1298-1307.

122. Gou, X., Sun, W., Chen, Z., and Ju, Y. "A dynamic multi-timescale method for combustion modeling with detailed and reduced chemical kinetic mechanisms," *Combustion and Flame* Vol. 157, No. 6, 2010, pp. 1111-1121.

123. Niemeyer, K. E., Sung, C.-J., and Raju, M. P. "Skeletal mechanism generation for surrogate fuels using directed relation graph with error propagation and sensitivity analysis," *Combustion and flame* Vol. 157, No. 9, 2010, pp. 1760-1770.

124. Aguilera-Iparraguirre, J., Curran, H. J., Klopper, W., and Simmie, J. M. "Accurate Benchmark Calculation of the Reaction Barrier Height for Hydrogen Abstraction by the Hydroperoxyl Radical from Methane. Implications for C n H2 n+ 2 where n= 2⟶ 4," *The Journal of Physical Chemistry A* Vol. 112, No. 30, 2008, pp. 7047-7054.

125. Lieuwen, T., Yang, V., and Yetter, R. *Synthesis gas combustion: fundamentals and applications*: CRC Press, 2009.

126. Pepiot-Desjardins, P., and Pitsch, H. "An efficient error-propagation-based reduction method for large chemical kinetic mechanisms," *Combustion and Flame* Vol. 154, No. 1, 2008, pp. 67-81.

doi: https://doi.org/10.1016/j.combustflame.2007.10.020

127. Lu, T., and Law, C. K. "A directed relation graph method for mechanism reduction," *Proceedings of the Combustion Institute* Vol. 30, No. 1, 2005, pp. 1333-1341.

doi: https://doi.org/10.1016/j.proci.2004.08.145

128. Swithenbank, J., Poll, I., Vincent, M., and Wright, D. "Combustion design fundamentals," *Fouteenth Symposium (International) on Combustion*. Vol. 14, Elsevier, 1973, pp. 627-638.

129. Kajimoto, O. "Solvation in Supercritical Fluids: Its Effects on Energy Transfer and Chemical Reactions," *Chemical Reviews* Vol. 99, 1999, pp. 355-389.

130. Tucker, S. C., and Maddox, M. W. "The Effect of Solvent Density Inhomogeneities on Solute Dynamics in Supercritical Fluids: A Theoretical Perspective," *Journal of Physical Chemistry B* Vol. 102, No. 14, 1998, pp. 2437-2453.

131. Truhlar, D. G., Garrett, B. C., and Klippenstein, S. J. "Current Status of Transition State Theory," *Journal of Physical Chemistry* Vol. 100, 1996, pp. 12771-12800.

132. Truhlar, D. G., and Garrett, B. C. "Variational Transition State Theory," *Annual Review of Physical Chemistry* Vol. 35, 1984, pp. 159-189.

133. Fernández-Ramos, A., Miller, J. A., Klippenstein, S. J., and Truhlar, D. G. "Modeling the Kinetics of Bimolecular Reactions," *Chemical Reviews* Vol. 106, 2006, pp. 4518-4584.

134. Klippenstein, S. J. "RRKM Theory and Its Implementation," *Comprehensive Chemical Kinetics* Vol. 39, 2003, pp. 55-103.

135. Garrett, B. C., and Truhlar, D. G. "Semiclassical tunneling calculations," *The Journal of Physical Chemistry* Vol. 83, No. 22, 1979, pp. 2921-2926.

136. Miller, J. A., and Klippenstein, S. J. "Master Equation Methods in Gas Phase Chemical Kinetics," *Journal of Physical Chemistry A* Vol. 110, No. 36, 2006, pp. 10528-10544.

137. Raghavachari, K., Trucks, G. W., Pople, J. A., and Head-Gordon, M. "A fifth-order perturbation comparison of electron correlation theories " *Chemical Physics Letters* Vol. 157, No. 6, 1989, pp. 479-483.

138. Robb, M. A., and Eade, R. H. A. "Direct minimization in MC SCF theory. The quasi-Newton method," *Chemical Physics Letters* Vol. 83, No. 2, 1981, pp. 362-368.

139. Hegarty, D., and Robb, M. A. "Application of unitary group methods to configuration interaction calculations," *Molecular Physics* Vol. 38, No. 6, 1979, pp. 1795-1812.

140. Roos, B. O., Linse, P., Siegbahn, P. E. M., and Blomberg, M. R. A. "A simple method for the evaluation of the second-order-perturbation energy from external double excitations with a CASSCF reference wavefunction," *Chemical Physics* Vol. 66, No. 1-2, 1982, pp. 197-207.

141. Anderson, K. "Different forms of the zeroth-order Hamiltonian in second-order perturbation theory with a complete active space self-consistent field reference function," *Theoretica Chimica Acta* Vol. 91, No. 1-2, 1995, pp. 31-46.

142. Klippenstein, S. J., Georgievskii, Y., and Harding, L. B. "Predictive theory for the combination kinetics of two alkyl radicals," *Physical Chemistry Chemical Physics* Vol. 8, 2006, pp. 1133-1147.

143. Houston, P. L., Nandi, A., and Bowman, J. M. "A Machine Learning Approach for Prediction of Rate Constants," *Journal of Physical Chemistry Letters* Vol. 10, No. 17, 2019, pp. 5250-5258.

144. Harding, L. B., Klippenstein, S. J., and Jasper, A. W. "Ab initio methods for reactive potential surfaces," *Physical Chemistry Chemical Physics* Vol. 9, No. 31, 2007, pp. 4055-4070.

145. Miller, J. A., Pilling, M. J., and Troe, J. "Unravelling combustion mechanisms through a quantitative understanding of elementary reactions," *Proceedings of the Combustion Institute* Vol. 30, No. 1, 2005, pp. 43-88.

146. Duchovic, R. J., and Pettigrew, J. D. "An Application of Conventional Transition State Theory To Compute High-Pressure Limit Thermal Rate Coefficients for the Reaction: H(D) + O2 ⇌ H(D)O2* ⇌ OH(D) + O," *Journal of Physical Chemistry* Vol. 98, No. 42, 1994, pp. 10794-10801.

147. Manion, J., Huie, R., Levin, R., Burgess Jr, D., Orkin, V., Tsang, W., McGivern, W., Hudgens, J., Knyazev, V., and Atkinson, D. "NIST chemical kinetics database, NIST standard reference database 17, version 7.0 (web version), release 1.6.8, data version 2017.07, National Institute of Standards and Technology, Gaithersburg, Maryland, 20899," *Web address: http://kinetics.nist.gov*, 2017.

148. Masunov, A. E., Wait, E. E., and Vasu, S. S. "Chemical Reaction CO+OH• → CO2+H• Autocatalyzed by Carbon Dioxide: Quantum Chemical Study of the Potential Energy Surfaces," *Journal of Physical Chemistry A* Vol. 120, No. 30, 2016, pp. 6023-6028.

doi: 10.1021/acs.jpca.6b03242

149. Masunov, A. E., Wait, E. E., Atlanov, A. A., and Vasu, S. S. "Quantum Chemical Study of Supercritical Carbon Dioxide Effects on Combustion Kinetics," *Journal of Physical Chemistry A* Vol. 121, No. 19, 2017, pp. 3728-3735.

doi: 10.1021/acs.jpca.7b02638

150. Masunov, A. E., Wait, E. E., and Vasu, S. S. "Catalytic Effect of Carbon Dioxide on Reaction OH + CO → H + CO2 in Supercritical Environment: Master Equation Study," *Journal of Physical Chemistry A* Vol. 122, No. 31, 2018, pp. 6355-6359.

151. Li, J., Zhao, Z. W., Kazakov, A., Chaos, M., Dryer, F. L., and Scire, J. J. "A comprehensive kinetic mechanism for CO, CH2O, and CH3OH combustion," *International Journal of Chemical Kinetics* Vol. 39, No. 3, 2007, pp. 109-136.

doi: 10.1002/kin.20218

152. Li, J., Chen, J., Zhang, D. H., and Guo, H. "Quantum and quasi-classical dynamics of the OH + CO → H + CO2 reaction on a new permutationally invariant neural network potential energy surface," *Journal of Chemical Physics* Vol. 140, 2014, p. 044327.

153. Zhu, R. S., Diau, E. G. W., Lin, M. C., and Mebel, A. M. "A computational study of the OH(OD) plus CO reactions: effects of pressure, temperature, and quantum-mechanical tunneling on product formation," *Journal of Physical Chemistry A* Vol. 105, No. 50, 2001, pp. 11249-11259.

doi: 10.1021/jp0104536

154. Chen, W.-C., and Marcus, R. "On the theory of the CO + OH reaction, including H and C kinetic isotope effects," *The Journal of chemical physics* Vol. 123, No. 9, 2005, pp. 094307-1-094307-16.

155. Medvedev, D. M., Gray, S. K., Goldfield, E. M., Lakin, M. J., Troya, D., and Schatz, G. C. "Quantum wave packet and quasiclassical trajectory studies of OH+CO: influence of the reactant channel well on thermal rate constants," *Journal of Chemical Physics* Vol. 120, No. 3, 2004, pp. 1231-1238.

doi: 10.1063/1.1632901

156. Masunov, A. E., Atlanov, A. A., and Vasu, S. S. "Potential Energy Surfaces for the Reactions of HO2 Radical with CH2O and HO2 in CO2 Environment," *Journal of Physical Chemistry A* Vol. 120, No. 39, 2016, pp. 7681-7688.

doi: 10.1021/acs.jpca.6b07257

157. Li, Q. S., Zhang, X., and Zhang, S. W. "Direct Dynamics Study on the Hydrogen Abstraction Reaction CH2O + HO2 → CHO + H2O2," *Journal of PHysical Chemistry A* Vol. 109, No. 51, 2005, pp. 12027-12035.

158. Christensen, M., Nilsson, E. J. K., and Konnov, A. A. "A Systematically Updated Detailed Kinetic Model for CH2O and CH3OH Combustion," *Energy & Fuels* Vol. 30, No. 8, 2016, pp. 6709-6726.

159. Eiteneer, B., Yu, C. L., Goldenberg, M., and Frenklach, M. "Determination of Rate Coefficient for Reactions of Formaldehyde Pyrolysis and Oxidation in the Gas Phase," *Journal of Physical Chemistry A* Vol. 102, No. 27, 1998, pp. 5196-5205.

160. Anglada, J. M., and Domingo, V. M. "Mechanism for the Gas-Phase Reaction between Formaldehyde and Hydroperoxyl Racical. A Theoretical Study," *Journal of Physical Chemistry A* Vol. 109, No. 47, 2005, pp. 10786-10794.

161. Kanno, N., Tonokura, K., and Koshi, M. "Equilibrium constant of the HO2-H2O complex formation and kinetics of HO2 + HO2-H2O: Implications for tropospheric chemistry," *Journal of Geophysical Research: Atmospheres* Vol. 111, 2006, p. D20312.

162. Stone, D., and Rowley, D. M. "Kinetics of the gas phase HO2 self-reaction: Effects of temperature, pressure, water and methanol vapours," *Physical Chemistry Chemical Physics* Vol. 7, No. 10, 2005, pp. 2156-2163.

163. Maricq, M. M., and Szente, J. J. "A kinetic study of the reaction between ethylperoxy radicals and HO2," *Journal of Physical Chemistry* Vol. 98, No. 8, 1994, pp. 2078-2082.

164. Anglada, J. M., Olivella, S., and Solé, A. "New Insight into the Gas-Phase Bimolecular Self-Reaction of the HOO Radical," *Journal of Physical Chemistry A* Vol. 111, No. 9, 2007, pp. 1695-1704.

165. Masunov, A. E., Wait, E. E., and Vasu, S. S. "Quantum Chemical Study of CH3 + O2 Combustion Reaction System: Catalytic Effects of Additional CO2 Molecule," *Journal of Physical Chemistry A* Vol. 121, No. 30, 2017, pp. 5681-5689.

doi: 10.1021/acs.jpca.7b04897

166. Vasudevan, V., Davidson, D. F., and Hanson, R. K. "Direct measurements of the reaction OH + CH2O → HCO + H2O at high temperatures," *International Journal of Chemical Kinetics* Vol. 37, No. 2, 2005, pp. 98-109.

167. Yetter, R. A., Rabitz, H., and Dryer, F. L. "Evaluation of the rate constant for the reaction OH+H2CO: Application of modeling and sensitivity analysis techniques for determination of the product branching ratio," *Journal of Chemical Physics* Vol. 91, No. 7, 1989, pp. 4088-4097.

168. Zhao, Y., Wang, B., Li, H., and Wang, L. "Theoretical studies on the reactions of formaldehyde with OH and OH-," *Journal of Molecular Structure-Theochem* Vol. 818, No. 1-3, 2007, pp. 155-161.

169. Li, J., Zhao, Z. W., Kazakov, A., and Dryer, F. L. "An updated comprehensive kinetic model of hydrogen combustion," *International Journal of Chemical Kinetics* Vol. 36, No. 10, 2004, pp. 566-575.

doi: 10.1002/kin.20026

170. Francisco, J. S. "An examination of substituent effects on the reaction of OH radicals with HXCO (where X=H, F, and Cl)," *Journal of Chemical Physics* Vol. 96, No. 10, 1992, pp. 7597-7602.

171. Xu, S., Zhu, R. S., and Lin, M. C. "Ab initio study of the OH + CH2O reaction: The effect of the OH..OCH2 complex on the H-abstraction kinetics," *International Journal of Chemical Kinetics* Vol. 38, No. 5, 2006, pp. 322-326.

172. Srinivasan, N. K., Su, M.-C., and Michael, J. V. "CH3 + O2 → H2CO + OH Revisited," *Journal of Physical Chemistry A* Vol. 111, No. 45, 2007, pp. 11589-11591.

173. Michael, J. V., Kumaran, S. S., and Su, M.-C. "Rate Constants for CH3 + O2 → CH3O + O at High Temperature and Evidence for H2CO + O2 → HCO + HO2," *Journal of Physical Chemistry A* Vol. 103, No. 30, 1999, pp. 5942-5948.

174. Hwang, S. M., Ryu, S.-O., De Witt, K. J., and Rabinowitz, M. J. "Rate coefficient measurements of the reaction CH3 + O2 = CH3O + O," *Journal of Physical Chemistry A* Vol. 103, No. 30, 1999, pp. 5949-5958.

doi: 10.1021/jp990998o

175. Yu, C.-L., Wang, C., and Frenklach, M. "Chemical Kinetics of Methyl Oxidation by Molecular Oxygen," *Journal of Physical Chemistry* Vol. 99, No. 39, 1995, pp. 14377-14387.

176. Ohmori, K., Yoshimura, M., Koshi, M., and Matsui, H. "A Flash Photolysis Study of CH4-O2 Mixtures behind Shock Waves: Examination of Reaction of CH3+O2," *Bulletin of the Chemical Society of Japan* Vol. 65, No. 5, 1992, pp. 1317-1322.

177. Srinivasan, N. K., Su, M.-C., Sutherland, J. W., and Michael, J. V. "Reflected Shock Tube Studies of High-Temperature Rate Constants for CH3 + O2, H2CO + O2, and OH + O2," *Journal of Physical Chemistry A* Vol. 109, No. 35, 2005, pp. 7902-7914.

178. Grela, M. A., Amorebieta, V. T., and Colussi, A. J. "High-temperature oxidation of methyl radicals in open systems," *Journal of Physical Chemistry* Vol. 96, No. 17, 1992, pp. 7013-7018.

179. Ing, W.-C., Sheng, C. Y., and Bozzelli, J. W. "Development of a detailed high-pressure reaction model for methane/methanol mixtures under pyrolytic and oxidative conditions and comparison with experimental data," *Fuel Processing Technology* Vol. 83, No. 1-3, 2003, pp. 111-145.

180. Zellner, R., and Ewig, F. "Computational Study of the CH3 + O2 Chain Branching Reaction," *Journal of Physical Chemistry* Vol. 92, No. 10, 1988, pp. 2971-2974.

181. Higgin, R. M. R., and Williams, A. "A shock-tube investigation of the ignition of lean methane and n-butane mixtures with oxygen," *Symposium (International) on Combustion* Vol. 12, No. 1, 1969, pp. 579-590.

182. Marcotte, F. B., and Noyes, W. A., Jr. "Hydrocarbon reactions. B. Oxidation reactions. The reactions of radicals from acetone with oxygen," *Discussions of the Faraday Society* Vol. 10, 1951, pp. 236-241.

183. Van Duin, A. C. T., Dasgupta, S., Lorant, F., and Goddard, W. A., III. "ReaxFF: A Reactive Force Field for Hydrocarbons," *Journal of Physical Chemistry A* Vol. 105, No. 41, 2001, pp. 9396-9409.

184. Lin, H., and Truhlar, D. G. "QM/MM: what have we learned, where are we, and where do we go from here?," *Theoretical Chemistry Accounts* Vol. 117, 2007, pp. 185-199.

185. Duster, A. W., Wang, C.-H., Garza, C. M., Miller, D. E., and Lin, H. "Adaptive quantum/molecular mechanics: what have we learned, where are we, and where do we go from here?," *WIREs Computational Molecular Science* Vol. 7, No. 5, 2017, p. e1310.

186. Field, M. J., Bash, P. A., and Karplus, M. "A Combined Quantum Mechanical and Molecular Mechanical Potential for Molecular Dynamics Simulations," *Journal of Computational Chemistry* Vol. 11, No. 6, 1990, pp. 700-733.

187. Dewar, M. J. S., and Thiel, W. "Ground states of molecules. 38. The MNDO method. Approximations and parameters," *Journal of the American Chemical Society* Vol. 99, No. 15, 1977, pp. 4899-4907.

188. Potoff, J. J., and Siepmann, J. I. "Vapor-liquid equilibria of mixtures containing alkanes, carbon dioxide, and nitrogen," *AIChE Journal* Vol. 47, No. 7, 2001, pp. 1676-1682.

doi: 10.1002/aic.690470719

189. Glowacki, D. R., Paci, E., and Shalashilin, D. V. "Boxed molecular dynamics: a simple and general technique for accelerating rare event kinetics and mapping free energy in large molecular systems," *Journal of Physical Chemistry B* Vol. 113, No. 52, 2009, pp. 16603-16611.

doi: 10.1021/jp9074898

190. Glowacki, D. R., Paci, E., and Shalashilin, D. V. "Boxed molecular dynamics: decorrelation time scales and the kinetic master equation," *Journal of Chemical Theory and Computation* Vol. 7, No. 5, 2011, pp. 1244-1252.

doi: 10.1021/ct200011e
191. Panteleev, S. V., Masunov, A. E., and Vasu, S. S. "Molecular Dynamics Study of Combustion Reactions in Supercritical Environment. Part 3: Boxed MD Study of CH3 + HO2 -> CH3O + OH Reaction Kinetics," *Journal of Physical Chemistry A* Vol. 122, 2018, pp. 3337-3345.

192. Panteleev, S. V., Masunov, A. E., and Vasu, S. S. "Molecular dynamics of combustion reactions in supercritical carbon dioxide. Part 4: boxed MD study of formyl radical dissociation and recombination," *Journal of Molecular Modeling* Vol. 25, 2019, p. 35.

193. Hong, Z. K., Davidson, D. F., Lam, K. Y., and Hanson, R. K. "A shock tube study of the rate constants of HO2 and CH3 reactions," *Combustion and Flame* Vol. 159, No. 10, 2012, pp. 3007-3013.

doi: 10.1016/j.combustflame.2012.04.009
194. Vasu, S. S., Davidson, D. F., and Hanson, R. K. "OH time-histories during oxidation of n-heptane and methylcyclohexane at high pressures and temperatures," *Combustion and Flame* Vol. 156, No. 4, 2009, pp. 736-749.

195. Jasper, A. W., Klippenstein, S. J., and Harding, L. B. "Theoretical rate coefficients for the reaction of methyl radical with hydroperoxyl radical and for methylhydroperoxide decomposition," *Proceedings of the Combustion Institute* Vol. 32, 2009, pp. 279-286.

doi: 10.1016/j.proci.2008.05.036
196. Krasnoperov, L. N., Chesnokov, E. N., Stark, H., and Ravishankara, A. R. "Unimolecular dissociation of formyl radical, HCO -> H plus CO, studied over 1-100 bar pressure range," *Journal of Physical Chemistry A* Vol. 108, No. 52, 2004, pp. 11526-11536.

doi: 10.1021/jp0403994
197. Krasnoperov, L. N., Chesnokov, E. N., Stark, H., and Ravishankara, A. R. "Elementary reactions of formyl (HCO) radical studied by laser photolysis - transient absorption spectroscopy," *Proceedings of the Combustion Institute* Vol. 30, 2005, pp. 935-943.

doi: 10.1016/j.proci.2004.08.223
198. Hippler, H., Krasteva, N., and Striebel, F. "The thermal unimolecular decomposition of HCO: effects of state specific rate constants on the thermal rate constant," *Physical Chemistry Chemical Physics* Vol. 6, No. 13, 2004, pp. 3383-3388.

doi: 10.1039/b402139h
199. Glowacki, D. R., Orr-Ewing, A. J., and Harvey, J. N. "Product energy deposition of CN + alkane H abstraction reactions in gas and solution phases," *Journal of Chemical Physics* Vol. 134, 2011, p. 214508.

200. Glowacki, D. R., Orr-Ewing, A. J., and Harvey, J. N. "Non-equilibrium reaction and relaxation dynamics in a strongly interacting explicit solvent: F + CD3CN treated with a

parallel multi-state EVB model," *Journal of Chemical Physics* Vol. 143, No. 4, 2015, p. 044120.

doi: 10.1063/1.4926996

201. Wang, C.-H., Panteleev, S. V., Masunov, A. E., Allison, T. C., Chung, S., Lim, C., Jin, Y., and Vasu, S. S. "Molecular Dynamics of Combustion Reactions in Supercritical Carbon Dioxide. Part 5: Computational Study of Ethane Dissociation and Recombination Reactions C2H6 ⇌ CH3 + CH3," *Journal of Physical Chemistry A* Vol. 123, No. 22, 2019, pp. 4776-4784.

doi: 10.1021/acs.jpca.9b02302

202. Wang, C.-H., Masunov, A. E., Allison, T. C., Chang, S., Lim, C., Jin, Y., and Vasu, S. S. "Molecular Dynamics of Combustion Reactions in Supercritical Carbon Dioxide. 6. Computational Kinetics of Reactions between Hydrogen Atom and Oxygen Molecule H + O2 ⇌ HO + O and H + O2 ⇌ HO2.," *Journal of Physical Chemistry A* Vol. 123, No. 50, 2019, pp. 10772-10781.

203. Akiya, N., and Savage, P. E. "Effect of Water Density on Hydrogen Peroxide Dissociation in Supercritical Water. 2. Reaction Kinetics," *Journal of Physical Chemistry A* Vol. 104, 2000, pp. 4441-4448.

204. Bao, J. L., and Truhlar, D. G. "Variational transition state theory: theoretical framework and recent developments," *Chemical Societry Reviews* Vol. 46, 2017, pp. 7548-7596.

205. Zhu, R., and Lin, M. C. "The CH3+HO2 reaction: first-principles prediction of its rate constant and product branching probabilities," *Journal of Physical Chemistry A* Vol. 105, No. 25, 2001, pp. 6243-6248.

doi: 10.1021/jp010698i

206. Yang, X., Goldsmith, C. F., and Tranter, R. S. "Decomposition and Vibrational Relaxation in CH3I and Self-Reaction of CH3 Radicals," *Journal of Physical Chemistry A* Vol. 113, 2009, pp. 8307-8317.

207. Olson, D. B., and Gardiner, W. C., Jr. "Thermal Dissociation Rate of Ethane at the High Pressure Limit from 250 to 2500 K," *Journal of Physical Chemistry* Vol. 83, No. 8, 1979, pp. 922-927.

208. Chiang, C.-C., and Skinner, G. B. "Resonance Absorption Measurements of Atom Concentrations in Reacting Gas Mixtures. 7. Pyrolysis of C2H6 and C2D6 Behind Shock Waves," *Journal of Physical Chemistry* Vol. 85, 1981, pp. 3126-3129.

209. Möller, W., Mozzhukhin, E., and Wagner, H. G. "High Temperature Reactions of CH3 1. The Reaction CH3 + H2 -> CH4 + H," *Berichte der Bunsengesellschaft für Physikalische Chemie* Vol. 90, 1986, pp. 854-861.

210. Wagner, A. F., and Wardlaw, D. M. "Study of the Recombination Reaction CH3 + CH3 -> C2H6. 2. Theory," *Journal of Physical Chemistry* Vol. 92, 1988, pp. 2462-2471.

211. Robertson, S. H., Wardlaw, D. M., and Hirst, D. M. "Potential energy function for CH3+CH3->C2H6: Attributes of the minimum energy path," *The Journal of Chemical Physics* Vol. 99, No. 10, 1993, pp. 7748-7761.

212. Yuan, T., Wang, C., Yu, C.-L., Frenklach, M., and Rabinowitz, M. J. "Determination of the Rate Coefficient for the Reaction H + O2 → OH + O by a Shock Tube/Laser Absorption/Detailed Modeling Study," *Journal of Physical Chemistry* Vol. 95, No. 3, 1991, pp. 1258-1265.

213. Masten, D. A., Hanson, R. K., and Bowman, C. T. "Shock Tube Study of the Reaction H + O2 → OH + O Using OH Laser Absorption," *Journal of Physical Chemistry* Vol. 94, No. 18, 1990, pp. 7119-7128.

214. Frank, P., and Just, T. "High Temperature Reaction Rate for H + O2 = OH + O and OH + H2 = H2O + H," *Berichte der Bunsengesellschaft für Physikalische Chemie* Vol. 89, 1985, pp. 181-187.

215. Germann, T. C., and Miller, W. H. "Quantum Mechanical Pressure-Dependent Reaction and Recombination Rates for O + OH → H + O2, HO2," *Journal of Physical Chemistry A* Vol. 101, No. 36, 1997, pp. 6358-6367.

216. Sellevåg, S. R., Georgievskii, Y., and Miller, J. A. "The Temperature and Pressure Dependence of the Reactions H + O2 (+M) → HO2 (+M) and H + OH (+M) → H2O (+M)," *Journal of Physical Chemistry A* Vol. 112, No. 23, 2008, pp. 5085-5095.

217. Duchovic, R. J., and Parker, M. A. "A Quasiclassical Trajectory Study of the Reaction H + O2 ⇌ OH + O with the O2 Reagent Vibrationally Excited," *Journal of Physical Chemistry A* Vol. 109, No. 26, 2005, pp. 5883-5896.

218. Cobos, C. J., Hippler, H., and Troe, J. "High-Pressure Falloff Curves and Specific Rate Constants for the Reactions H + O2 ⇌ HO2 ⇌ HO + O," *Journal of Physical Chemistry* Vol. 89, No. 2, 1985, pp. 342-349.

219. Smooke, M. D., Puri, I. K., and Seshadri, K. "A comparison between numerical calculations and experimental measurements of the structure of a counterflow diffusion flame burning diluted methane in diluted air," *Symposium (International) on Combustion* Vol. 21, No. 1, 1988, pp. 1783-1792.

doi: https://doi.org/10.1016/S0082-0784(88)80412-0
220. Jordà Juanós, A., and Sirignano, W. A. "Pressure effects on real-gas laminar counterflow," *Combustion and Flame* Vol. 181, 2017, pp. 54-70.

doi: https://doi.org/10.1016/j.combustflame.2017.01.030
221. Law, C. K. *Combustion physics*: Cambridge university press, 2010.
222. Ribert, G., Zong, N., Yang, V., Pons, L., Darabiha, N., and Candel, S. "Counterflow diffusion flames of general fluids: Oxygen/hydrogen mixtures," *Combustion and Flame* Vol. 154, No. 3, 2008, pp. 319-330.

doi: https://doi.org/10.1016/j.combustflame.2008.04.023
223. Huo, H., Wang, X., and Yang, V. "A general study of counterflow diffusion flames at subcritical and supercritical conditions: Oxygen/hydrogen mixtures," *Combustion and Flame* Vol. 161, No. 12, 2014, pp. 3040-3050.

doi: https://doi.org/10.1016/j.combustflame.2014.06.005
224. Banuti, D., Ma, P., Hickey, J.-P., and Ihme, M. *Thermodynamic structure of supercritical LOX–GH2 diffusion flames*, 2018.
225. Lutz, A. E., Kee, R. J., Grcar, J. F., and Rupley, F. M. "OPPDIF: A Fortran program for computing opposed-flow diffusion flames." Sandia National Labs., Livermore, CA (United States), 1997.
226. Schmitt, R. G., Butler, P. B., and French, N. B. *Chemkin real gas: a Fortran package for analysis of thermodynamic properties and chemical kinetics in nonideal systems*: University of Iowa, 1994.
227. Lucas, K. "Die Druckabhängigkeit der Viskosität von Flüssigkeiten – eine einfache Abschätzung," *Chemie Ingenieur Technik* Vol. 53, No. 12, 1981, pp. 959-960.

doi: doi:10.1002/cite.330531209
228. Poling, B. E., Prausnitz, J. M., and O'connell, J. P. *The properties of gases and liquids*: Mcgraw-hill New York, 2001.
229. Stiel, L. I., and Thodos, G. "The thermal conductivity of nonpolar substances in the dense gaseous and liquid regions," *AIChE Journal* Vol. 10, No. 1, 1964, pp. 26-30.

230. Manikantachari, K. R. V., Ladislav, V., Martin, S., Bobren-Diaz, J., and Vasu, S. "Reduced Chemical Kinetic Mechanisms for Oxy/Methane Supercritical CO2 Combustor Simulations," *Journal of Energy Resources Technology*, 2018.

doi: 10.1115/1.4039746
231. Panteleev, S. V., Masunov, A. E., and Vasu, S. S. "Molecular Dynamics Study of Combustion Reactions in a Supercritical Environment. Part 2: Boxed MD Study of CO + OH → CO2 + H Reaction Kinetics," *The Journal of Physical Chemistry A* Vol. 122, No. 4, 2018, pp. 897-908.

doi: 10.1021/acs.jpca.7b09774
232. Panteleev, S. V., Masunov, A. E., and Vasu, S. S. "Molecular Dynamics Study of Combustion Reactions in Supercritical Environment. Part 3: Boxed MD Study of CH3 + HO2 → CH3O + OH Reaction Kinetics," *The Journal of Physical Chemistry A* Vol. 122, No. 13, 2018, pp. 3337-3345.

doi: 10.1021/acs.jpca.7b12233
233. Sengers, J. V., Kayser, R., Peters, C., and White, H. *Equations of state for fluids and fluid mixtures*: Elsevier, 2000.
234. Valderrama, J. O. "The State of the Cubic Equations of State," *Industrial & Engineering Chemistry Research* Vol. 42, No. 8, 2003, pp. 1603-1618.

doi: 10.1021/ie020447b
235. Peng, D. Y., and Robinson, D. B. "A New Two-Constant Equation of State," *Ind. Eng. Chem. Fundam.* Vol. 15, 1976, p. 59.

236. Soave, G. "Equilibrium Constants from a Modified Redlich-Kwong Equation of State," *Chem. Eng. Sci.* Vol. 27, 1972, p. 1197.

237. Miller, R. S., Harstad, K. G., and Bellan, J. "Direct numerical simulations of supercritical fluid mixing layers applied to heptane–nitrogen," *Journal of Fluid Mechanics* Vol. 436, 2001.

doi: 10.1017/s0022112001003895
238. Ihme, M., and Pitsch, H. "Prediction of extinction and reignition in nonpremixed turbulent flames using a flamelet/progress variable model," *Combustion and Flame* Vol. 155, No. 1-2, 2008, pp. 90-107.

doi: 10.1016/j.combustflame.2008.04.015
239. Manikantachari, K., Martin, S., Vesely, L., Bobren-Diaz, J. O., Vasu, S., and Kapat, J. "A Strategy of Reactant Mixing in Methane Direct-Fired sCO2 Combustors," *ASME Turbo Expo 2018: Turbomachinery Technical Conference and Exposition*. American Society of Mechanical Engineers, 2018, pp. V009T38A008-V009T38A008.
240. Manikantachari, K. R. V., Martin, S., Bobren-Diaz, J. O., and Vasu, S., . "A Strategy of Mixture preparation for Methane Direct-Fired sCO2 Combustors," *Proceedings of the ASME Turbo Expo 2018: Turbine Technical Conference and Exposition*. Lillestrøm (Oslo), Norway, 2018.
241. Delimont, J., Andrews, N., and Chordia, L. "Exploration of Combustor Design for Direct Fired Oxy-fuel Application in a sCO2 Power Cycle," *Global Power and Propulsion Society, Proceedins Montreal*. , Montreal.
242. Poinsot, T., and Veynante, D. *Theoretical and numerical combustion*: RT Edwards, Inc., 2005.
243. Hirschfelder, J. O., Curtiss, C. F., Bird, R. B., and Mayer, M. G. *Molecular theory of gases and liquids*: Wiley New York, 1954.
244. Pitsch, H., and Peters, N. "A consistent flamelet formulation for non-premixed combustion considering differential diffusion effects," *Combustion and Flame* Vol. 114, No. 1-2, 1998, pp. 26-40.

245. Martin, S., Jemcov, A., and de Ruijter, B. "Modeling an Enclosed, Turbulent Reacting Methane Jet With the Premixed Conditional Moment Closure Method," *ASME Turbo Expo 2013: Turbine Technical Conference and Exposition*. American Society of Mechanical Engineers, 2013, pp. V01BT04A011-V01BT04A011.

246. Manikantachari, K., Martin, S., Rahman, R. K., Velez, C., and Vasu, S. "A general study of counterflow diffusion flames for supercritical CO2 combustion," *Journal of Engineering for Gas Turbines and Power* Vol. 141, No. 12, 2019.

247. Hasti, V. R., Kundu, P., Kumar, G., Drennan, S. A., Som, S., and Gore, J. P. "A numerical study of flame characteristics during lean blow-out in a gas turbine combustor," *2018 Joint Propulsion Conference*. 2018, p. 4955.
248. Hasti, V. R., Liu, S., Kumar, G., and Gore, J. P. "Comparison of Premixed Flamelet Generated Manifold Model and Thickened Flame Model for Bluff Body Stabilized Turbulent Premixed Flame," *2018 AIAA Aerospace Sciences Meeting*. 2018, p. 0150.
249. Hasti, V. R., Lucht, R. P., and Gore, J. P. "Large eddy simulation of hydrogen piloted CH4/air premixed combustion with CO2 dilution," *Journal of the Energy Institute* Vol. 93, No. 3, 2020, pp. 1099-1109.

250. Feyz, M., Hasti, V., Gore, J., Chowdhury, A., and Nalim, M. "Scalar predictors of premixed gas ignition by a suddenly-starting hot jet," *International Journal of Hydrogen Energy* Vol. 44, No. 42, 2019, pp. 23793-23806.

251. Masi, E., Bellan, J., Harstad, K. G., and Okong'o, N. A. "Multi-species turbulent mixing under supercritical-pressure conditions: modelling, direct numerical simulation and analysis revealing species spinodal decomposition," *Journal of Fluid Mechanics* Vol. 721, 2013, pp. 578-626.

252. Bruno, C., Sankaran, V., Kolla, H., and Chen, J. H. "Impact of multi-component diffusion in turbulent combustion using direct numerical simulations," *Combustion and Flame* Vol. 162, No. 11, 2015, pp. 4313-4330.

253. Violi, A. "Chemistry and Transport Properties for Jet Fuel Combustion." MICHIGAN UNIV ANN ARBOR DEPT OF MECHANICAL ENGINEERING, 2013.
254. CHEMKIN-PRO, R. "15112, Reaction Design," *Inc., San Diego, CA*, 2011.

255. Hirschfelder, J., Curtiss, C. F., and Bird, R. "Molecular Theory of Gases and Liquids, John Wiley & Sons, New York 1954," *N. Taxman, Phys. Rev.* Vol. 11, 1958, pp. 110, 1235.

256. Manikantachari, K., Martin, S., Bobren-Diaz, J. O., and Vasu, S. "Thermal and transport properties for the simulation of direct-fired sCO2 combustor," *Journal of Engineering for Gas Turbines and Power* Vol. 139, No. 12, 2017.

257. Manikantachari, K., Vesely, L., Martin, S., Bobren-Diaz, J. O., and Vasu, S. "Reduced Chemical Kinetic Mechanisms for Oxy/Methane Supercritical CO2 Combustor Simulations," *Journal of Energy Resources Technology* Vol. 140, No. 9, 2018.

258. Marion, J., Lariviere, B., McClung, A., and Mortzheim, J. "The STEP 10 MWe sCO2 Pilot Demonstration Status Update," *Turbo Expo: Power for Land, Sea, and Air*. Vol. 85048, American Society of Mechanical Engineers, 2021, p. V010T30A011.
259. Chehroudi, B., Talley, D., and Coy, E. "Initial growth rate and visual characteristics of a round jet into a sub-to supercritical environment of relevance to rocket, gas turbine, and diesel engines," *37th Aerospace Sciences Meeting and Exhibit*. 1999, p. 206.
260. Oschwald*, M., Smith, J., Branam, R., Hussong, J., Schik, A., Chehroudi, B., and Talley, D. "Injection of fluids into supercritical environments," *Combustion science and technology* Vol. 178, No. 1-3, 2006, pp. 49-100.

261. Chehroudi, B. "Recent experimental efforts on high-pressure supercritical injection for liquid rockets and their implications," *International Journal of Aerospace Engineering* Vol. 2012, 2012.

262. Abramovich, G. N., Girshovich, T., Krasheninnikov, S. I., Sekundov, A., and Smirnova, I. "The theory of turbulent jets," *Moscow Izdatel Nauka*, 1984.

263. Peng, J. B., Lv, Z. F., Yu, X., Meng, S. H., Dong, H., Deng, F., Chen, L., Chen, D. Y., Fan, R. W., and Dong, Z. W. "Visualization of Flow Field: Application of PLIF Technique," *Journal of Spectroscopy* Vol. 2018, 2018.

264. Grisch, F., and Orain, M. "Role of Planar Laser-Induced Fluorescence in Combustion Research," *AerospaceLab*, No. 1, 2009, pp. p. 1-14.

265. Watson, K., Lyons, K., Donbar, J., and Carter, C. "Simultaneous Rayleigh imaging and CH-PLIF measurements in a lifted jet diffusion flame," *Combustion and flame* Vol. 123, No. 1-2, 2000, pp. 252-265.

266. DeSouza, S., and Segal, C. "Sub-and supercritical jet disintegration," *Physics of Fluids* Vol. 29, No. 4, 2017, p. 047107.

267. Koroglu, B., Neupane, S., Pryor, O., Peale, R. E., and Vasu, S. S. "High temperature infrared absorption cross sections of methane near 3.4 μm in Ar and CO2 mixtures," *Journal of Quantitative Spectroscopy and Radiative Transfer* Vol. 206, 2018, pp. 36-45.

268. Pyun, S. H., Cho, J., Davidson, D. F., and Hanson, R. K. "Interference-free mid-IR laser absorption detection of methane," *Measurement Science and Technology* Vol. 22, No. 2, 2011, p. 025303.

269. Schmitt, R. G., Butler, P. B., and French, N. B. *Chemkin real gas : a Fortran package for analysis of thermodynamic properties and chemical kinetics in nonideal systems*. Iowa City: University of Iowa, 1994.
270. Martin, S. M. "The conditional moment closure method for modeling lean premixed turbulent combustion." Vol. Ph.D., Thesis, University of Washington, 2003.
271. "<116 Delimont - Simulation of a Direct Fired Oxy-Fuel Combustor (paper).pdf>."

272. Schmidt, E. *Thermodynamics -Principles and applications to engineers*. New York, 2009.
273. Turns, S. R. *An Introduction to Combustion: Concepts and Applications*: McGraw-Hill, 2012.
274. Oefelein, J. C., and Yang, V. "Modeling high-pressure mixing and combustion processes in liquid rocket engines," *Journal of Propulsion and Power* Vol. 14, No. 5, 1998, pp. 843-857.

275. Yang, V. "Modeling of supercritical vaporization, mixing, and combustion processes in liquid-fueled propulsion systems," *Proceedings of the Combustion Institute* Vol. 28, No. 1, 2000, pp. 925-942.

doi: http://dx.doi.org/10.1016/S0082-0784(00)80299-4
276. De Giorgi, M. G., and Leuzzi, A. "CFD simulation of mixing and combustion in LOx/CH4 spray under supercritical conditions," *39th AIAA Fluid Dynamics Conference*. 2009, p. 4038.
277. De Giorgi, M., Sciolti, A., and Ficarella, A. "Application and Comparison of Different Combustion Models of High Pressure LOX/CH4 Jet Flames," *Energies* Vol. 7, No. 1, 2014, pp. 477-497.

doi: 10.3390/en7010477
278. Congiunti, A., and Bruno, C. "Supercritical Combustion Properties," *41st Aerospace Sciences Meeting and Exhibit*. American Institute of Aeronautics and Astronautics, 2003.
279. Hickey, J. P., and Ihme, M. "Supercritical mixing and combustion in rocket propulsion," *Center for Turbulence Research Annual Research Briefs*, 2013.

280. Martin, S. M., Kramlich, J. C., Kosály, G., and Riley, J. J. "The Premixed Conditional Moment Closure Method Applied to Idealized Lean Premixed Gas Turbine Combustors," *Journal of Engineering for Gas Turbines and Power* Vol. 125, No. 4, 2003, p. 895.

doi: 10.1115/1.1587740
281. Metcalfe, W. K., Burke, S. M., Ahmed, S. S., and Curran, H. J. "A Hierarchical and Comparative Kinetic Modeling Study of C1− C2Hydrocarbon and Oxygenated Fuels," *International Journal of Chemical Kinetics* Vol. 45, No. 10, 2013, pp. 638-675.

doi: 10.1002/kin.20802
282. Wang, H., You, X., Joshi, A. V., Davis, S. G., Laskin, A., Egolfopoulos, F., and Law, C. K. "USC Mech Version II. High-Temperature Combustion Reaction Model of H2/CO/C1-C4 Compounds." 2007.

283. El Merhubi, H., Kéromnès, A., Catalano, G., Lefort, B., and Le Moyne, L. "A high pressure experimental and numerical study of methane ignition," *Fuel* Vol. 177, 2016, pp. 164-172.

doi: http://dx.doi.org/10.1016/j.fuel.2016.03.016
284. Waals, J. D. v. d. "On the Continuity of the Gaseous and Liquid States." Universiteit Leiden, Leiden, 1873.
285. McLinden, M., Klein, S., and Lemmon, E. "NIST REFPROP V7. 0." 2006.
286. Anderson, M. "NEUP Project 12-3318: Advanced Supercritical Carbon Dioxide Brayton Cycle Development." Univesity of Wisconsin, Madison, 2015.
287. Redlich, O., and Kwong, J. N. S. "On the Thermodynamics of Solutions. V. An Equation of State. Fugacities of Gaseous Solutions," *Chem. Rev.* Vol. 44, 1949, p. 233.

288. Patel, N. C. "The calculation of thermodynamic properties and phase equilibria using a new cubic equation of state." © Navin C. Patel, 1980.
289. Chueh, P., and Prausnitz, J. "Calculation of high-pressure vapor-liquid equilibria," *Industrial & Engineering Chemistry* Vol. 60, No. 3, 1968, pp. 34-52.

290. Soave, G., Gamba, S., and Pellegrini, L. A. "SRK equation of state: Predicting binary interaction parameters of hydrocarbons and related compounds," *Fluid Phase Equilibria* Vol. 299, No. 2, 2010, pp. 285-293.

291. Balaji, B., Raghavan, V., and Ramamurthi, K. "A Parametric Study of the Choice of Binary Interaction Parameter and Equation of State for High Pressure Vapor-Liquid Equilibrium of Nitrogen–n-Dodecane Binary System," *International Journal of Thermodynamics* Vol. 14, No. 2, 2011, pp. 79-86.

292. Wong, D. S. H., and Sandler, S. I. "A theoretically correct mixing rule for cubic equations of state," *AIChE Journal* Vol. 38, No. 5, 1992, pp. 671-680.

293. Ghosh, P. "Prediction of Vapor-Liquid Equilibria Using Peng-Robinson and Soave-Redlich-Kwong Equations of State," *Chemical engineering & technology* Vol. 22, No. 5, 1999, pp. 379-399.

294. Kim, S.-K., Choi, H.-S., and Kim, Y. "Thermodynamic modeling based on a generalized cubic equation of state for kerosene/LOx rocket combustion," *Combustion and flame* Vol. 159, No. 3, 2012, pp. 1351-1365.

295. Poschner, M. M., and Pfitzner, M. "CFD-Simulation of the injection and combustion of LOX and H2 at supercritical pressures," *Proceedings of the European Combustion Meeting*. Vol. 2010, 2009.
296. Cant, R. S., and Mastorakos, E. *An Introduction to Turbulent Reacting Flows*. London: Imperial College Press, 2008.
297. White, F. M. *Fluid Mechanics*: McGraw Hill, 2011.

298. Park, T. S., and Kim, S.-K. "A Pressure-Based Algorithm for Gaseous Hydrogen/Liquid Oxygen Jet Flame at Supercritical Pressure," *Numerical Heat Transfer, Part A: Applications* Vol. 67, No. 5, 2014, pp. 547-570.

doi: 10.1080/10407782.2014.937267
299. Baltadjiev, N. D. "An Investigation of Real Gas Effects in Spercritcal CO2 Compressors," *Department of Aeronautics and Astronautics*. Vol. Masters, MIT, Massachusetts, 2012.
300. Lucas, K. "Pressure-dependence of the viscosity of liquids-a simple estimate." Vol. 53, VCH PUBLISHERS INC 303 NW 12TH AVE, DEERFIELD BEACH, FL 33442-1788, 1981, pp. 959-960.
301. Chung, T. H., Ajlan, M., Lee, L. L., and Starling, K. E. "Generalized multiparameter correlation for nonpolar and polar fluid transport properties," *Industrial & engineering chemistry research* Vol. 27, No. 4, 1988, pp. 671-679.

302. Heidaryan, E., Hatami, T., Rahimi, M., and Moghadasi, J. "Viscosity of pure carbon dioxide at supercritical region: Measurement and correlation approach," *The Journal of Supercritical Fluids* Vol. 56, No. 2, 2011, pp. 144-151.

303. Brokaw, R. "Viscosity of Gas Mixtures, NASA Technical Note D-4496," 1968.

304. Amooey, A. A. "A simple correlation to predict thermal conductivity of supercritical carbon dioxide," *The Journal of Supercritical Fluids* Vol. 86, 2014, pp. 1-3.

305. MacPhee, D. W., and Beyene, A. "Impact of Air Quality and Site Selection on Gas Turbine Engine Performance," *Journal of Energy Resources Technology* Vol. 140, No. 2, 2017, pp. 020903-020903-7.

doi: 10.1115/1.4038118
306. Amano, R. S. "Review of Wind Turbine Research in 21st Century," *Journal of Energy Resources Technology* Vol. 139, No. 5, 2017, pp. 050801-050801-8.

doi: 10.1115/1.4037757
307. Breault, R. W., Weber, J., Straub, D., and Bayham, S. "Computational Fluid Dynamics Modeling of the Fuel Reactor in NETL's 50 kWth Chemical Looping Facility," *Journal of Energy Resources Technology* Vol. 139, No. 4, 2017, pp. 042211-042211-8.

doi: 10.1115/1.4036324
308. Du, X., Gu, M., Duan, S., and Xian, X. "The Influences of CO2 Injection Pressure on CO2 Dispersion and the Mechanism of CO2–CH4 Displacement in Shale," *Journal of Energy Resources Technology* Vol. 140, No. 1, 2017, pp. 012907-012907-9.

doi: 10.1115/1.4037687
309. Pryor, O., Barak, S., Koroglu, B., Ninnemann, E., and Vasu, S. S. "Measurements and interpretation of shock tube ignition delay times in highly CO 2 diluted mixtures using multiple diagnostics," *Combustion and Flame* Vol. 180, 2017, pp. 63-76.

310. Pryor, O., Barak, S., Lopez, J., Ninnemann, E., Koroglu, B., Nash, L., and Vasu, S. "High Pressure Shock Tube Ignition Delay Time Measurements During Oxy-Methane Combustion With High Levels of CO2 Dilution," *Journal of Energy Resources Technology* Vol. 139, No. 4, 2017, p. 042208.

311. Schmitt, R., Butler, P., and French, N. B. "CHEMKIN Real Gas," *UIME PBB*, 1993, pp. 93-006.

312. Lu, T., and Law, C. K. "Strategies for mechanism reduction for large hydrocarbons: n-heptane," *Combustion and Flame* Vol. 154, No. 1, 2008, pp. 153-163.

doi: https://doi.org/10.1016/j.combustflame.2007.11.013

313. Nicolas, G., and Metghalchi, H. "Development of the Rate-Controlled Constrained-Equilibrium Method for Modeling of Ethanol Combustion," *Journal of Energy Resources Technology* Vol. 138, No. 2, 2015, pp. 022205-022205-11.

doi: 10.1115/1.4031511

314. Petersen, E. L., and Hanson, R. K. "Reduced kinetics mechanisms for ram accelerator combustion," *Journal of Propulsion and Power* Vol. 15, No. 4, 1999, pp. 591-600.

315. Bhattacharjee, B., Schwer, D. A., Barton, P. I., and Green, W. H. "Optimally-reduced kinetic models: reaction elimination in large-scale kinetic mechanisms," *Combustion and Flame* Vol. 135, No. 3, 2003, pp. 191-208.

doi: https://doi.org/10.1016/S0010-2180(03)00159-7

316. Tomlin, A. S., Turányi, T., and Pilling, M. J. "Chapter 4 Mathematical tools for the construction, investigation and reduction of combustion mechanisms," *Comprehensive Chemical Kinetics*. Vol. 35, Elsevier, 1997, pp. 293-437.

317. Beretta, G. P., Janbozorgi, M., and Metghalchi, H. "Degree of Disequilibrium analysis for automatic selection of kinetic constraints in the Rate-Controlled Constrained-Equilibrium method," *Combustion and Flame* Vol. 168, 2016, pp. 342-364.

doi: https://doi.org/10.1016/j.combustflame.2016.02.005

318. Bobren-Diaz, J., Martin, S. M., Hitch, B. D., Manikantachari, K., and Vasu, S. "Assessment of Detailed and Reduced JetSurF 2.0 Mechanisms Using Conditional Moment Closure Method," *53rd AIAA/SAE/ASEE Joint Propulsion Conference*. 2017, p. 4854.

319. Klimenko, A. Y., and Bilger, R. W. "Conditional moment closure for turbulent combustion," *Progress in energy and combustion science* Vol. 25, No. 6, 1999, pp. 595-687.

320. Chong, S. T., Tang, Y., Hassanaly, M., and Raman, V. "Turbulent Mixing and Combustion of Supercritical Jets," *55th AIAA Aerospace Sciences Meeting*. 2017, p. 0141.

321. Manikantachari, K., Martin, S., Bobren-Diaz, J., and Vasu, S. "Thermal and transport Properties for the simulation of Direct-Fired sCO2 Combustor," *Journal of Engineering for Gas Turbines and Power*, 2017.

322. Abdul-Sater, H., Lenertz, J., Bonilha, C., Lu, X., and Fetvedt, J. "A CFD Simulation of Coal Syngas Oxy-Combustion in a High-Pressure Supercritical CO2 Environment," *ASME Turbo Expo 2017: Turbomachinery Technical Conference and Exposition*. American Society of Mechanical Engineers, 2017, pp. V04AT04A051-V04AT04A051.
323. Delimont, J., McClung, A., and Portnoff, M. "Direct Fired Oxy-Fuel Combustor for sCO2 Power Cycles: 1MW Scale Design and Preliminary Bench Top Testing," *ASME Turbo Expo 2017: Turbomachinery Technical Conference and Exposition*. American Society of Mechanical Engineers, 2017, pp. V009T38A027-V009T38A027.
324. Turns, S. R. *An introduction to combustion*: McGraw-hill New York, 1996.
325. Beer, J., and Lee, K. "The effect of the residence time distribution on the performance and efficiency of combustors," *Symposium (International) on Combustion*. Vol. 10, Elsevier, 1965, pp. 1187-1202.
326. Andreini, A., and Facchini, B. "Gas turbines design and off-design performance analysis with emissions evaluation," *ASME Turbo Expo 2002: Power for Land, Sea, and Air*. American Society of Mechanical Engineers, 2002, pp. 271-281.
327. Syed, M. S., Punuru, J. R., Dooley, K. M., and Knopf, F. C. "A readily accessible platform for detailed combustion emissions calculations," *International Journal of Mechanical Engineering Education* Vol. 40, No. 4, 2012, pp. 289-304.
328. Bongartz, D., Shanbhogue, S. J., and Ghoniem, A. F. "Formation and Control of Sulfur Oxides in Sour Gas Oxy-Combustion: Prediction Using a Reactor Network Model," *Energy & Fuels* Vol. 29, No. 11, 2015, pp. 7670-7680.
329. Glarborg, P., Kee, R., Grcar, J., and Miller, J. "PSR: A FORTRAN program for modeling well-stirred reactors," *Sandia Report SAND86-8209*, 1986.
330. Larson, R. S. "PLUG: A Fortran program for the analysis of plug flow reactors with gas-phase and surface chemistry." Sandia Labs., Livermore, CA (United States), 1996.
331. Dostal, V., Hejzlar, P., and Drscoll, M. J. *The supercritical carbon dioxide power cycle : Comparison to other advanced power cycles*. La Grange Park, IL, ETATS-UNIS: American Nuclear Society, 2006.
332. Kancherla, R. V. M., Martin, S. M., Bobren-Diaz, J., and Vasu, S. "A Counter-flow Diffusion Flame study for the Supercritical CO2 Combustion," *AIAA Scitech 2019 Forum*. 2019, p. 0673.
333. Strakey, P. A. "Oxy-Combustion Modeling for Direct-Fired Supercritical CO2 Power Cycles," *Journal of Energy Resources Technology* Vol. 141, No. 7, 2019, pp. 070706-070706-8.

doi: 10.1115/1.4043124
334. Kancherla, R. V. M., Martin, S. M., Bobren, J. O., and Vasu, S. "The Influence of Elevated Pressures on the Methane Combustion in N2 and Co2 Dilutions," *53rd AIAA/SAE/ASEE Joint Propulsion Conference*. 2017.
335. Manikantachari, K. R. V., Martin, S., Rahman, R. K., Velez, C., and Vasu, S. "A General Study of Counterflow Diffusion Flames for Supercritical CO2 Mixtures," *ASME Turbo*

Expo 2019: Turbomachinery Technical Conference and Exposition. Vol. Volume 4A: Combustion, Fuels, and Emissions, 2019.

336. Manikantachari, K., Vesely, L., Martin, S., Bobren-Diaz, J. O., and Vasu, S. "Reduced Chemical Kinetic Mechanisms for Oxy/Methane Supercritical CO2 Combustor Simulations," *Journal of Energy Resources Technology* Vol. 140, No. 9, 2018, p. 092202.

337. Manikantachari, K. R. V., Martin, S., Vesely, L., Bobren-Diaz, J. O., Vasu, S., and Kapat, J. "A Strategy of Mixture Preparation for Methane Direct-Fired sCO2 Combustors," No. 51180, 2018, p. V009T38A009.

doi: 10.1115/GT2018-75557

338. Andrews, J. D. N. "Computational Modeling of a Direct Fired Oxy-Fuel Combustor for sCO2 Power Cycles," *sCO2 symposium* Pittsburgh, 2018.

339. Delimont, J., Andrews, N., and Chordia, L. "Computational Modeling of a 1MW Scale Combustor for a Direct Fired sCO2 Power Cycle," No. 51180, 2018, p. V009T38A025.

doi: 10.1115/GT2018-77087

340. Menon, S., Yeung, P.-K., and Kim, W.-W. "Effect of subgrid models on the computed interscale energy transfer in isotropic turbulence," *Computers & fluids* Vol. 25, No. 2, 1996, pp. 165-180.

341. Amsden, A. A., and Findley, M. "KIVA-3V: A block-structured KIVA program for engines with vertical or canted valves." Lawrence Livermore National Lab.(LLNL), Livermore, CA (United States), 1997.

342. Lemmon, E. W., Huber, M. L., and McLinden, M. O. "NIST reference fluid thermodynamic and transport properties–REFPROP," *NIST standard reference database* Vol. 23, 2002, p. v7.

343. Manikantachari, K. R. V., Martin, S., Bobren-Diaz, J. O., and Vasu, S. "Thermal Properties for the Simulation of Direct-Fired sCO2 Combustor," No. 50961, 2017, p. V009T38A008.

doi: 10.1115/GT2017-63311

344. Jones, W., and Lindstedt, R. "Global reaction schemes for hydrocarbon combustion," *Combustion and flame* Vol. 73, No. 3, 1988, pp. 233-249.

345. Westbrook, C. K., and Dryer, F. L. "Simplified reaction mechanisms for the oxidation of hydrocarbon fuels in flames," *Combustion science and technology* Vol. 27, No. 1-2, 1981, pp. 31-43.

346. Persis, S. p. d., Cabot, G., Pillier, L., Gökalp, I., and Boukhalfa, A. M. "Study of Lean Premixed Methane Combustion with CO2 Dilution under Gas Turbine Conditions," *Energy and Fuels*, 2012.

347. Glarborg, P., and Bentzen, L. L. "Chemical effects of a high CO2 concentration in oxy-fuel combustion of methane," *Energy & Fuels* Vol. 22, No. 1, 2007, pp. 291-296.

348. Vasu, S. S., Davidson, D. F., and Hanson, R. K. "Shock tube study of syngas ignition in rich CO2 mixtures and determination of the rate of H+ O2+ CO2→ HO2+ CO2," *Energy & Fuels* Vol. 25, No. 3, 2011, pp. 990-997.

349. Barak, S., Pryor, O., Lopez, J., Ninnemann, E., Vasu, S., and Koroglu, B. "High-Speed Imaging and Measurements of Ignition Delay Times in Oxy-Syngas Mixtures With High CO2 Dilution in a Shock Tube," No. 50848, 2017, p. V04AT04A023.

doi: 10.1115/GT2017-63316

350. Almansour, B., Thompson, L., Lopez, J., Barari, G., and Vasu, S. S. "Ignition and Flame Propagation in Oxy-Methane Mixtures Diluted With CO2," No. 56697, 2015, p. V04BT04A021.

doi: 10.1115/GT2015-43355

351. Andersen, J., Rasmussen, C. L., Giselsson, T., and Glarborg, P. "Global combustion mechanisms for use in CFD modeling under oxy-fuel conditions," *Energy & Fuels* Vol. 23, No. 3, 2009, pp. 1379-1389.

352. Metcalfe, W. K., Burke, S. M., Ahmed, S. S., and Curran, H. J. "A Hierarchical and Comparative Kinetic Modeling Study of C1 − C2 Hydrocarbon and Oxygenated Fuels," *International Journal of Chemical Kinetics* Vol. 45, No. 10, 2013, pp. 638-675.

doi: 10.1002/kin.20802

353. Pryor, O., Barak, S., Koroglu, B., Ninnemann, E., and Vasu, S. S. "Measurements and interpretation of shock tube ignition delay times in highly CO2 diluted mixtures using multiple diagnostics," *Combustion and Flame* Vol. 180, 2017, pp. 63-76.

doi: https://doi.org/10.1016/j.combustflame.2017.02.020

354. "ANSYS Chemkin-Pro." http://www.ansys.com/products/fluids/ansys-chemkin-pro, San Diego, CA., 2019.

355. Koroglu, B., Pryor, O. M., Lopez, J., Nash, L., and Vasu, S. S. "Shock tube ignition delay times and methane time-histories measurements during excess CO 2 diluted oxy-methane combustion," *Combustion and flame* Vol. 164, 2016, pp. 152-163.